


9-1-2020

## Study of the Role of Biologically-Relevant, Labile Nickel Pools in the Maturation of Nickel-Dependent Enzymes

Priyanka Basak  
*University of Massachusetts Amherst*

Follow this and additional works at: [https://scholarworks.umass.edu/dissertations\\_2](https://scholarworks.umass.edu/dissertations_2)

 Part of the [Biochemistry Commons](#), and the [Inorganic Chemistry Commons](#)

---

### Recommended Citation

Basak, Priyanka, "Study of the Role of Biologically-Relevant, Labile Nickel Pools in the Maturation of Nickel-Dependent Enzymes" (2020). *Doctoral Dissertations*. 1995.  
<https://doi.org/10.7275/18847822> [https://scholarworks.umass.edu/dissertations\\_2/1995](https://scholarworks.umass.edu/dissertations_2/1995)

This Open Access Dissertation is brought to you for free and open access by the Dissertations and Theses at ScholarWorks@UMass Amherst. It has been accepted for inclusion in Doctoral Dissertations by an authorized administrator of ScholarWorks@UMass Amherst. For more information, please contact [scholarworks@library.umass.edu](mailto:scholarworks@library.umass.edu).

**STUDY OF THE ROLE OF BIOLOGICALLY – RELEVANT, LABILE NICKEL  
POOLS IN THE MATURATION OF NICKEL-DEPENDENT ENZYMES**

A Dissertation Presented

by

**PRIYANKA BASAK**

Submitted to the Graduate School of the University of Massachusetts in partial fulfillment of the  
requirements for the degree of

**DOCTOR of PHILOSOPHY**

September 2020

Department of Chemistry

© Copyright by Priyanka Basak 2020

All Rights Reserved

STUDY OF THE ROLE OF BIOLOGICALLY – RELEVANT, LABILE NICKEL POOLS IN  
THE MATURATION OF NICKEL-DEPENDENT ENZYMES

A Dissertation Presented

By

PRIYANKA BASAK

Approved as to style and content by:

---

Michael J. Maroney, Chair

---

Michael J. Knapp, Member

---

Min Chen, Member

---

Scott C. Garman, Member

---

Ricardo Metz, Department Head

Department of Chemistry

## ACKNOWLEDGEMENTS

First and foremost, I would like to deeply thank my advisor, Prof. Mike Maroney for accepting me into his group and letting me pursue my interest in metals in biology that I had developed during my undergraduate research internship. He has been immensely kind, patient and supportive throughout the past six and a half years. His invaluable guidance and experience have not only helped me grow as a researcher but also taught me the tactics to handle and cope up with difficult times in a productive way. Thank you, Mike for everything! I am also grateful to my dissertation committee members, Prof. Mike Knapp, Dr. Min Chen and Prof. Scott Garman who took out time from their busy schedules and participated in my research progress meetings and provided useful research insights.

I would like to extend my gratitude to Steve Eyeles and Mass spectrometry Core facility where I collected the MS data and Lizz Bartlett and IALS Biophysical Characterization Core facility where I collected my ITC, SEC-MALS and CD data for my research. I am also thankful to our collaborators, the Merrell lab, at the Uniformed Services University of Health Sciences (Bethesda, Maryland) for their work on the acid survival of hypA variant strains, and Dr. Dianne Cabelli for the pulse radiolytic experiments on the NiSOD samples at the National Brookhaven Laboratory. I also acknowledge the beamline scientist, Matthew Latimer and Erik Nelson, who helped us run and collect our XAS data at SSRL beamline 7-3 and 9-3.

I would also like to thank my colleagues and friends at the LSL and LGRT, especially the Knapp Lab, the Kittlestved lab and the labs in the entire 3<sup>rd</sup> floor (North Wing) including the Vachet Lab, the Kaltashov lab, the Vierling lab, the Gierasch lab, the Chien Lab, Hebert Lab, for sharing their equipment, space, and expertise. My past lab members, Heidi and Tiffany have been immensely helpful and supportive in teaching me the technical laboratory and experimental skills.

I must also thank Manju Sharma for her help and expertise and having my back whenever I needed her till date even outside the lab. Her empathy and positive attitude had helped me overcome some of the most difficult times during my graduate studies.

I express my sincere gratitude to my undergraduate research advisor Prof. Shyamalava Mazumdar who, during my summer research internship, introduced me to the colorful world of metalloenzymes. I am also grateful to Dr. Manas Kumar Ghosh, who was my research mentor during my time in Prof. Mazumdar's lab and taught me valuable research skills.

Finally, I would like to thank my parents and my beloved sister, who despite their intrinsic reluctance, allowed me to pursue my graduate studies in a foreign land away from them. I appreciate their understanding, support and motivation that has kept me going and enabled me to finish my studies.

## ABSTRACT

### STUDY OF THE ROLE OF BIOLOGICALLY – RELEVANT, LABILE NICKEL POOLS IN THE MATURATION OF NICKEL-DEPENDENT ENZYMES

September 2020

PRIYANKA BASAK, M.Sc. INDIAN INSTITUTE OF TECHNOLOGY BOMBAY

Ph.D., UNIVERSITY OF MASSACHUSETTS AMHERST

Directed by: Professor Michael J. Maroney

Nickel is a critical micronutrient for various organisms (microbes, fungi, and plants), which utilize it as a cofactor of one or more nickel enzymes that catalyze specific reactions and are essential for their proper growth and survival in various ecological niches. Like other metals, a tight regulation of cellular nickel levels is critical to prevent toxic effects of nickel deprivation, nickel overload and ‘free’ nickel. Two cellular nickel pools, comprised of more static and labile pools of nickel complexes, play important roles in maintaining nickel homeostasis in microorganisms. While more static nickel pools include nickel tightly bound to nickel-dependent enzymes, nickel in the labile pool is reversibly and more weakly bound to either nickel chaperones or low-molecular weight (LMW) ligands, as is the case for many other transition metals. The role of nickel chaperones in enzyme maturation and activation is being extensively investigated, but the importance of cellular LMW complexes in the process remains largely unknown.

In this work, we investigate the role of labile nickel pools (both non-proteinaceous and proteinaceous ligands) in the maturation of nickel-dependent enzymes - Nickel Superoxide Dismutase (NiSOD) from *Streptomyces coelicolor*, and urease and Ni,Fe-hydrogenase from *Helicobacter pylori*. For the maturation of NiSOD, no chaperone has been characterized for nickel delivery to the active site, and in our work, using biochemical assays, mass spectrometry and

spectroscopic methods, we provide compelling evidence that biologically relevant, non-proteinaceous, LMW ligand complexes of nickel with L-histidine is inevitable for the proper maturation of the enzyme. Studies on the maturation process of NiSOD also revealed the role of structural components in NiSOD, such as cis-trans isomerization of proline residue in the formation of ‘Ni-hook’ in the enzyme.

In *Helicobacter pylori*, which is a human pathogen, there are two nickel dependent enzymes – urease and Ni, Fe hydrogenase both of which require a common nickel-chaperone (proteinaceous labile nickel ligand), HypA for its maturation. It interacts with HypB for maturation of Ni, Fe hydrogenase and with UreE for maturation of urease, but what factors determine its differential interaction with its downstream partner proteins is unknown. In our studies, we interrogated the flexibility and dynamics of HypA by glycine mutations to perturb the maturation of the two nickel enzymes in the pathogen. Our *in vitro* assays indicate that the mutations do not affect the urease maturation, but it does affect the maturation of Ni, Fe – hydrogenase in the pathogen. Using X-ray absorption Spectroscopy, we also characterized the recently discovered high-affinity nickel site in HypA•UreE complex which surprisingly revealed an octahedral nickel site in the complex.



## TABLE OF CONTENTS

	Page
ACKNOWLEDGMENTS .....	iv
ABSTRACT .....	vi
LIST OF TABLES .....	xiii
LIST OF FIGURES .....	xiv
CHAPTER	
<b>1. BIOLOGICALLY RELEVANT LABILE NICKEL COMPLEXES IN NICKEL TRAFFICKING.....</b>	<b>1</b>
1.1 Components of Cellular Nickel Trafficking.....	1
1.2 Environmental Nickel Bioavailability and Extracellular Low-Molecular Weight Ligands for Nickel Acquisition.....	5
1.3 Intracellular Proteinaceous Labile Nickel Pool.....	6
1.4 Intracellular Non-Proteinaceous Labile Nickel Pool.....	8
1.4.1 Histidine .....	11
1.4.2 2-methyl-2,4- thiazolidine-dicarboxylic acid .....	15
1.5 Experimental Techniques to Study cellular Labile Nickel Pools .....	16
1.6 References .....	18
<b>2. SUPEROXIDE DISMUTASES: A REVIEW .....</b>	<b>27</b>
2.1 Superoxide: A consequence of Earth's Great Oxidation Event.....	27
2.2 Superoxide Dismutases .....	29
2.2.1 Nickel Superoxide Dismutase .....	31
2.2.2 Cu, Zn Superoxide Dismutase.....	37
2.2.3 Fe/Mn Superoxide Dismutase.....	38
2.3 References .....	42

<b>3. <i>IN VITRO</i> MATURATION OF NISOD REVEALS A ROLE OF CYTOPLASMIC LIGANDS</b> .....	<b>46</b>
3.1 Introduction .....	46
3.2 Experimental Methods .....	49
3.2.1 Cloning, Protein Expression and Purification .....	49
3.2.2 Mutagenesis .....	53
3.2.3 Mass Spectrometry for Protein Characterizations .....	54
3.2.4 Periodic-Acid Schiff (PAS) test .....	55
3.2.5 DTNB test .....	55
3.2.6 SEC-MALS .....	56
3.2.7 Circular Dichroism .....	57
3.2.8 UV-Visible Spectroscopy .....	57
3.2.9 Isothermal Titration Calorimetry .....	57
3.2.10 X-ray Absorption Spectroscopy .....	59
3.2.11 SodX Homology Modelling .....	63
3.2.12 Pulse Radiolysis .....	64
3.2.13 In vitro processing assays .....	64
3.2.14 In vitro processing assays in presence of L-histidine or D-histidine .....	65
3.2.15 Mass Spectrometry for in vitro processing assays .....	65
3.2.16 In gel activity assay .....	66
3.3 Results .....	67
3.3.1 Protein Characterizations .....	67
3.3.1.1 WT-SodN .....	67
3.3.1.2 SodN variants (H15A-SodN and P19A-SodN) .....	73
3.3.1.3 WT-SodX and S28A SodX .....	74
3.3.2 Proteolytic Processing .....	76
3.3.2.1 WT-SodX processes WT-SodN and does not require Ni(II) .....	76
3.3.2.2 Ser28 is catalytic residue for SodX .....	78
3.3.2.3 Metals including Ni(II) inhibit proper processing of SodN .....	78
3.3.2.4 L-Histidine rescues proper processing of WT-SodN by WTSodX in presence of Ni(II) .....	81

3.3.2.5 D-Histidine cannot rescue proper processing of WT-SodN by WTSodX in presence of Ni(II) .....	84
3.4 Discussion .....	85
3.5 Conclusion .....	90
3.6 References .....	92
<b>4. ROLE OF PROLINE 5 IN THE MATURATION OF NICKEL SUPEROXIDE DISMUTASE .....</b>	<b>99</b>
4.1 Introduction .....	99
4.2 Experimental Methods .....	102
4.2.1 Site Directed Mutagenesis, Protein Expression and Purification .....	102
4.2.2 Isothermal Titration Calorimetry .....	104
4.2.3 Metallation of P5A-SOD .....	106
4.2.4 UV-Visible Spectroscopy .....	106
4.2.5 Electronic Paramagnetic Spectroscopy .....	107
4.2.6 Pulse Radiolysis .....	107
4.3 Results .....	108
4.3.1 Isothermal Titration Calorimetry .....	108
4.3.2 Electronic Structure .....	109
4.3.3 Redox Catalysis .....	112
4.4 Discussion .....	113
4.5 References .....	119
<b>5. NICKEL TRAFFICKING IN <i>HELICOBACTER PYLORI</i>: A REVIEW .....</b>	<b>123</b>
5.1 Introduction .....	123
5.2 Nickel regulation .....	126
5.3 Nickel import .....	127
5.4 Nickel storage .....	129
5.5 Nickel delivery .....	129
5.6 Nickel Export .....	133
5.7 Conclusion .....	133
5.8 References .....	135

<b>6. CHARACTERIZATION OF THE HIGH-AFFINITY NICKEL BINDING SITE IN THE HYPA•UREE COMPLEX FROM <i>H. PYLORI</i></b> .....	143
6.1 Introduction .....	143
6.2 Experimental Methods .....	146
6.2.1 X-ray Absorption Spectroscopic Data Collection .....	146
6.2.2 X-ray Absorption Spectroscopic Data Reduction & Analysis .....	146
6.3 Results .....	149
6.3.1 XANES & EXAFS Analysis of Ni-site .....	149
6.3.2 XANES & EXAFS Analysis of Zn-site .....	154
6.4 Discussion .....	154
6.5 Conclusion .....	155
6.6 References .....	156
<b>7. PERTURBATION OF PROTEIN DYNAMICS BY GLYCINE MUTATIONS IN HYPA: THE ROLE OF HYPA CONFORMATIONS IN MATURATION OF UREASE AND Ni, Fe- HYDROGENASE IN <i>H. PYLORI</i></b> .....	159
7.1 Introduction .....	159
7.2 Experimental Methods .....	163
7.2.1 Site-directed mutagenesis of Glycine residues in HypA from <i>H. pylori</i> .....	163
7.2.2 Expression and Purification of Gly-to-Ala HypA variant proteins .....	164
7.2.3 Acid Viability assays .....	165
7.2.4 <i>In vitro</i> urease activity assay .....	166
7.2.5 <i>In vitro</i> hydrogenase activity assay .....	168
7.2.6 Circular Dichroism Spectroscopy .....	169
7.2.7 XAS Data Collection, Data Reduction and Analysis .....	169
7.3 Results .....	173
7.3.1 Gly-to-Ala substitutions in HypA do not affect the acid viability of <i>H. pylori</i> or urease activity .....	173
7.3.2 Gly-to-Ala substitutions in <i>H. pylori</i> HypA affects Ni, Fe - Hydrogenase activity .....	175

7.3.3 Circular Dichroism Spectroscopy: Perturbed secondary structure of selected Gly-to-Ala HypA variants .....	177
7.3.4 Unperturbed Zn- or Ni-site of HypA by XAS .....	179
7.4 Discussion .....	184
7.5 References .....	188
APPENDICES .....	194
A. SUPPORTING INFORMATION FOR THE ROLE OF CYTOPLASMIC LIGANDS IN THE <i>IN VITRO</i> MATURATION OF NISOD .....	194
B. SUPPORTING INFORMATION FOR NICKEL BINDING TO HYP A-UREE <sub>2</sub> COMPLEX .....	210
C. SUPPORTING INFORMATION FOR ROLE OF GLYCINE-TO-ALANINE MUTATION IN HYP A FOR THE MATURATION OF UREASE AND NI, FE-HYDROGENASE IN <i>H.PYLORI</i> .....	228
BIBLIOGRAPHY .....	235

## LIST OF TABLES

<b>Table</b>	<b>Page</b>
3.1 Oligonucleotides used in Chapter 3 .....	54
3.2 Protein Characterization parameters determined using mass spectrometry, ITC and UV-Visible Spectroscopy.....	68
4.1 Amounts of Ni(III) and $k_{cat}$ in all studied NiSOD variants .....	117
6.1. Selected EXAFS fits for the Ni-site in the HypA-UreE <sub>2</sub> complex at pH 7.2 .....	152
7.1 Primers and plasmids used for the studies in Chapter 7 .....	164
7.2 Optimized conditions used for maximal expression of glycine variants of HypA and the corresponding mass of purified proteins .....	165
7.3 Strains of <i>H. pylori</i> used for the studies in Chapter 7 .....	166
7.4 <i>In – vitro</i> Ni, Fe- hydrogenase activity of <i>H. pylori</i> strains .....	176
7.5 Calculated helix propensity of conserved Gly-to-Ala <i>HpHypA</i> proteins .....	180
7.6. Best EXAFS fits of Zn- site in non- conserved Gly-to-Ala HypA variants .....	181
7.7. Selected EXAFS fits of Ni- site in non- conserved Gly-to-Ala HypA variants .....	181

## LIST OF FIGURES

<b>Figure</b>	<b>Page</b>
1.1 Representation of cellular nickel pools .....	1
1.2 Schematics showing classification of cellular nickel pools .....	3
1.3 Molecular structures of known biological nickel ligands .....	9
1.4 Crystal structures showing nickel complexes bound to nickel transporters .....	13
2.1 Crystal structure of Nickel Superoxide Dismutase .....	32
2.2 Crystal structure of Copper, Zinc Superoxide Dismutase .....	38
2.3. Crystal structure of Iron Superoxide Dismutase .....	39
2.4 Crystal structure of Manganese Superoxide Dismutase .....	40
3.1 Nickel active site in Nickel Superoxide Dismutase .....	46
3.2 ITC thermograms of WT-SOD and WT-SodN titrated with nickel .....	60
3.3. UV-Visible spectra of WT-Ni(II) SodN overlaid with dithionite reduced WTNiSOD ...	71
3.4 X-ray Absorption spectroscopic data (XANES and EXAFS) of WT-NiSodN .....	73
3.5 Deconvoluted ESI-MS spectra of proteolytic assays with WT- and mutant- SodN with WT-SodX or SodX variant with or without Ni(II), Co(II), and Zn(II).....	80
3.6. Kinetic traces showing the SOD activity in WTNiSOD overlaid with that of proteolytic assays mixtures .....	82

3.7	Deconvoluted ESI-MS spectra of proteolytic assays with WT- SodN and WT-SodX in presence of nickel and L-Histidine .....	83
3.8	High-resolution deconvoluted ESI-MS spectra of proteolytic assays with WT- SodN and WT-SodX in presence of nickel and D-Histidine .....	85
3.9	Schematics showing processing and maturation of NiSOD .....	91
4.1	Crystal structure of WT-NiSOD showing the position of Proline 5 in the ‘Ni-hook’..	100
4.2	Conformations of Cis- and Trans- proline in peptides .....	101
4.3	ITC thermograms of P5A-SOD titrated with nickel .....	109
4.4	UV-Visible spectra of as-isolated P5A-NiSOD overlaid with as-isolated WTNiSOD.	110
4.5	EPR spectrum of as-isolated P5A-NiSOD .....	111
4.6	Energy diagram showing stability of cis-trans isomers of X-Proline imide and X-non-proline amide bonds .....	113
5.1	Nickel trafficking components in <i>Helicobacter pylori</i> .....	125
6.1	NMR solution structure of <i>H. pylori</i> HypA (PDB ID: 6G81) .....	144
6.2	Crystal structure of <i>H. pylori</i> UreE (PDB ID: 3TJ8) .....	145
6.3	X-ray Absorption spectroscopic data (XANES and EXAFS) of Ni,Zn-WTHypA•UreE <sub>2</sub> complex at pH 7.2 .....	151
7.1	NMR solution structure of nickel metallochaperone HypA from <i>H. pylori</i> (PDB ID: 6G81) .....	161



7.2	A. Acid Viability assay of Gly-to-Ala-HypA expressing <i>H. pylori</i> strains .....	174
	B. <i>In vitro</i> urease activity of Gly-to-Ala-HypA expressing <i>H. pylori</i> strains .....	174
7.3	<i>In vitro</i> Ni,Fe- hydrogenase activity of Gly-to-Ala-HypA expressing <i>H. pylori</i> strains	175
7.4	CD Spectra of apo (dotted line) and Ni-bound (solid line) conserved and non-conserved Gly -to -Ala <i>H. pylori</i> HypA variant proteins at pH 7.2 .....	178

## CHAPTER 1

### LABILE NICKEL COMPLEXES IN NICKEL TRAFFICKING

#### 1.1 Components of Cellular Nickel Trafficking

Nickel is a critical micronutrient for various organisms (microbes, fungi, and plants), which utilize it as a cofactor of one or more nickel enzymes that catalyze specific reactions and are essential for their proper growth and survival in various ecological niches.<sup>1-2</sup> Environmental nickel exists mostly as divalent nickel (Ni(II)) coordinated to different inorganic and organic ligands, and depending on geographical locations, its concentrations can range from  $\mu\text{M}$  to  $\text{nM}$ .<sup>3</sup> Plants and microbes acquire bioavailable environmental Ni(II), into the cells through transmembrane transporters (**Figure 1.1**), although whether cellular nickel acquisition occurs as a nickel complex

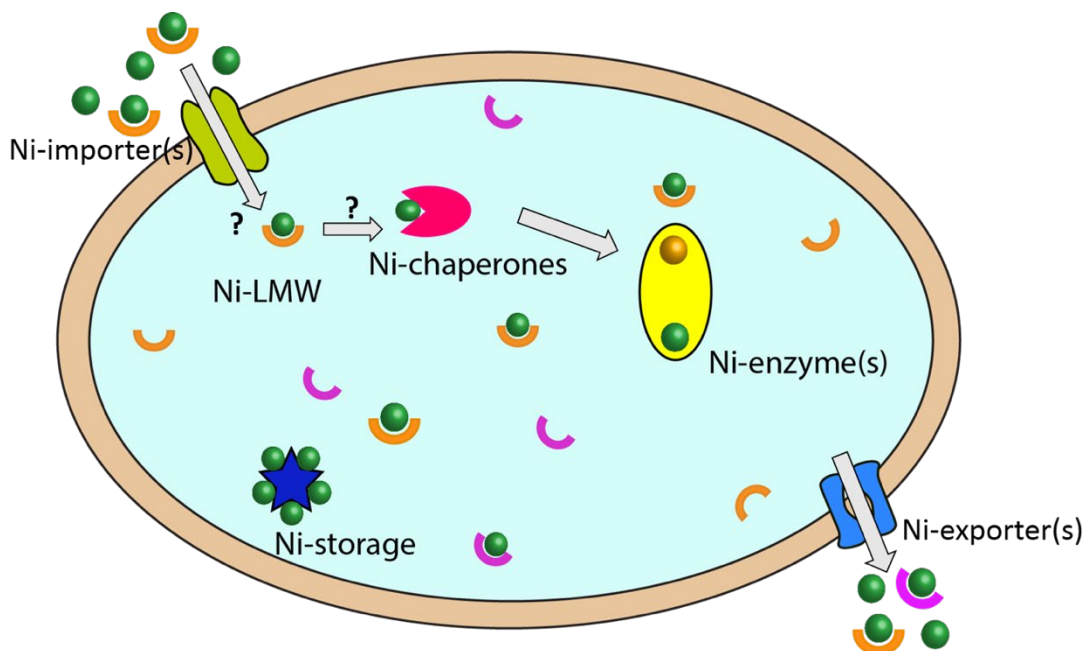


**Figure 1.1: Diagram showing classification of cellular nickel pools: nickel is shown in green spheres, colored half-brackets denote free cellular ligands.**

or ‘free’ nickel (defined as aqua complexes of nickel) is just beginning to be understood. Excess nickel or ‘free’ nickel in cells is lethal, as it can adventitiously bind to non-specific biomolecules or replace other metals from their cognate sites and cause unwanted outcomes.<sup>4</sup> Like other metals,

nickel deprivation, nickel overload and ‘free’ nickel is toxic, and so intracellular nickel levels are under tight regulation. In a typical nickel trafficking pathway (**Figure 1.1**), specific nickel regulators (or nickel responsive transcription factors) control nickel import and export and also maintain optimal intracellular nickel levels, nickel chaperones deliver nickel to target enzymes and nickel storage proteins bind more than one nickel and release it when required by the cell. In addition, low molecular weight (LMW) complexes of nickel in the cytosol might also play a key role in cellular nickel homeostasis.

Low molecular weight ligands are compounds that can be multidentate and can form stable complexes with metals. The role of these ligands in metal homeostasis lies before, in between, and after cellular metal transport, and hence can be grouped into different categories: extracellular LMW ligands, and intracellular LMW ligands (**Figure 1.2**). Extracellular LMW ligands are secreted by organisms into the extracellular space and influence the bioavailability of metal ions<sup>5</sup>, which can either be increased (*e.g.*, Fe acquisition by siderophores<sup>5-6</sup>) or decreased (organic acids for Al immobilization by plants<sup>7</sup>). Siderophores are excellent examples of extracellular LMW ligands that are secreted by bacteria to acquire environmental Fe, which exists in its nearly insoluble Fe(III) form. Siderophores specifically bind the insoluble Fe (III) with high affinity, and it has low affinity for Fe(II).<sup>6</sup> The Fe(III)-siderophore complex (generally FeO<sub>6</sub> complexes employing hydroxamate or catecholate ligands) is actively transported across the cell membrane.<sup>8</sup> Iron from the siderophore complex is released in the cell via many mechanisms including reduction, pH reduction, changes of redox potential, and degradation of the ligand to soluble Fe (II) and makes it available for cellular acquisition in bacteria and plants.

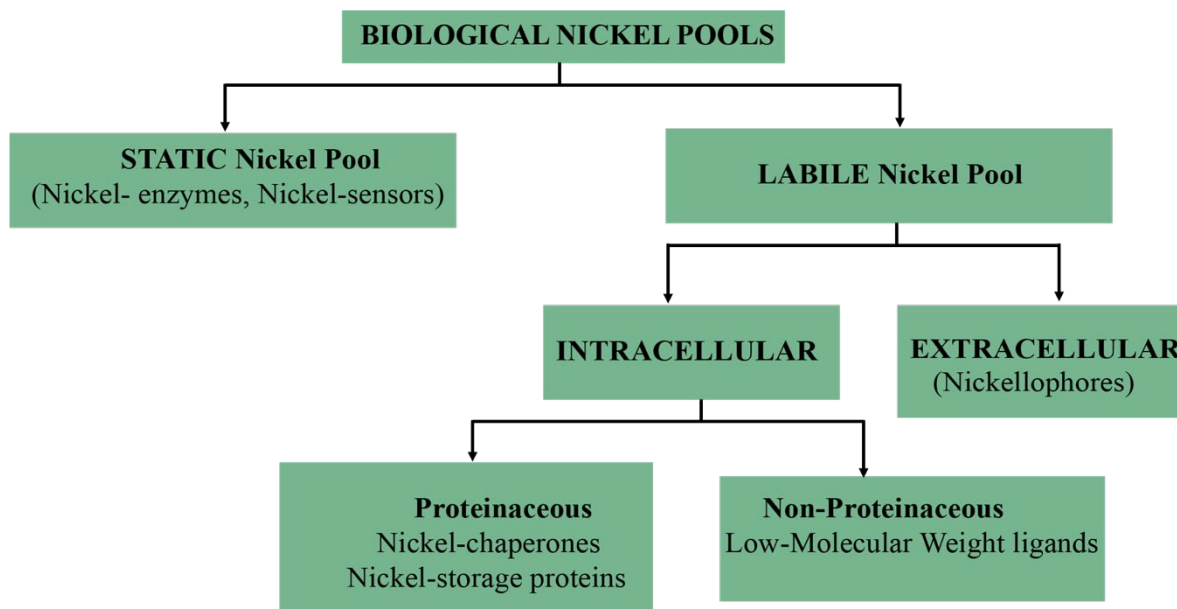


**Figure 1.2: Schematic showing classification of cellular nickel pools.**

Intracellular LMW ligands can function to buffer metals in cytosol or other cellular compartments. According to the Irving – William ( $\text{Mn(II)} < \text{Fe(II)} < \text{Co(II)} < \text{Ni(II)} < \text{Cu(II)} > \text{Zn(II)}$ ) series that describes the stability of complexes between divalent metal ions and organic ligands, irrespective of the chemical nature (S, N, O), Cu(II) always forms the most stable complexes, followed by Zn(II) and Ni(II).<sup>9</sup> This implies that in biological systems, in order to prevent displacement of metals such as Mn(II) and Fe(II) (which form less stable complexes) from their respective cognate binding sites, free Cu, Zn and Ni, should practically be not available. Such a scenario is applicable during protein folding of nascent polypeptides, which are vulnerable to being metallated with the wrong metal.<sup>10-11</sup> This problem is solved in cells by maintaining a very low level of these metal ions in cytosol which is achieved by chelating the metals with either proteinaceous moieties such as metallochaperones, or low-molecular weight ligands, both of which can undergo ligand exchange reactions and ensure the non- existence of free metal in cytosol.<sup>12-14</sup> Generally, ligand exchange reactions in cytosol are not determined by absolute affinities, instead

by relative affinities.<sup>13</sup> A cellular ligand can complex a metal further down in the Irving – William series, such as Fe, provided that the metals further up in the Irving – William series are tightly bound to other molecules with higher affinity.

Depending on the organism, cellular nickel levels can range from nM (in microbes) to mM (in hyperaccumulating plants), and exist as both static and labile nickel pools, both of which form the total cellular nickel pool, similar to other metals. Nickel – dependent enzymes, which tightly bind nickel are considered as the thermodynamic nickel sink, and constitute a major cellular static nickel pool. On the other hand, nickel, weakly bound to proteinaceous or non – proteinaceous moieties, generally LMW ligands inside the cell, that can be easily exchanged on demand constitute the cellular labile nickel pool. Typically, delivery of a specific metal, such as nickel, to the respective enzyme active sites is ensured by the interplay of a complex array of nickel – binding proteins, and essentially involves exchange of nickel between these proteins with varying nickel affinities. These proteins are either nickel metallochaperones or nickel storage proteins, and form the proteinaceous labile nickel pool.<sup>15</sup> The mechanisms with which these proteinaceous nickel pools participate in cellular nickel mobilization and enzyme maturation is being extensively explored and is discussed in section 1.3. Besides these proteinaceous nickel (or metal) pools, an emerging theme in metal trafficking is the importance of non - proteinaceous labile (or bioavailable or exchangeable) metal pool, which comprises metal that is weakly bound to cytosolic ligands. While the identities of the ligands involved in labile Fe, Cu and Zn pools (cytoplasmic or mitochondrial) are emerging,<sup>16-20</sup> knowledge regarding the ligands involved and exact functions of labile cytoplasmic pools of transition metals, including nickel, is limited and require further investigation. Selected amino acids, their derivatives, ATP, GSH etc., are promising low-molecular weight candidates for cellular metal – buffering.

## 1.2 Environmental Nickel Bioavailability and Extracellular LMW ligands for nickel Acquisition

Nickel is present in all three biospheres – air, water and soil. According to World Health Organization (WHO), in natural waters, at pH 5 - 9, nickel predominantly occurs as  $\text{Ni}(\text{H}_2\text{O})_6^{2+}$ , but complexes of nickel with  $\text{OH}^-$ ,  $\text{SO}_4^{2-}$ ,  $\text{HCO}_3^-$ ,  $\text{Cl}^-$ ,  $\text{NH}_3$  also form in this pH range.<sup>21</sup> Compared to other transition metals, such as, Cu(II), Fe(II), Mn(II) that have rapid water exchange rates in the order of  $\sim 10^6 - 10^9 \text{ s}^{-1}$ , water exchange rate of Ni is  $3.4 \times 10^4 \text{ s}^{-1}$ , which is relatively slower than other transition metals.<sup>22</sup> Particularly in marine waters, the solubility and reactivity of nickel is affected by strong organic ligands that can impact the bioavailability of nickel.<sup>23-24</sup> Electrochemical studies show that 30 - 50% of dissolved nickel is bound to strong organic ligands of unknown chemical composition and suggest a diversity in ligand composition, source and binding affinities.<sup>25-26</sup> A wide – variety of nickel chelators, such as phytochelatins, glutathione, and staphylopines are produced by marine organisms and are believed to contribute toward the natural ligand pool.<sup>23</sup> Degradation products of organic matter, known as humic compounds, can also produce a structurally heterologous collection of molecules that can complex nickel. The metal binding stability constants and turnover rates are determined by the chemical composition of the ligands.<sup>23</sup> In general, according to Irving – William series, there is a competition between Cu and Ni for ligand binding sites, with  $\text{Cu}^{2+}$  forming more stable organic complexes. As the ligand concentrations are always in excess of Cu concentration,  $\text{Cu}^{2+}$  tends to saturate stronger ligands, leaving weaker ligands to coordinate  $\text{Ni}^{2+}$ .<sup>23</sup> Owing to low concentrations, large number of potential ligands, and heterogeneity, the chemical composition and identity of such ligands are difficult to characterize. Recently, molecular formulae of some nickel and copper binding marine compounds found in Eastern Pacific Ocean was determined using a combination of Liquid

Chromatography - Inductively Coupled Plasma Mass Spectrometry (LC-ICPMS), Liquid Chromatography - high resolution Electrospray Ionization Mass Spectrometry (LC-ESIMS) and Fourier Transform Ion Cyclotron Resonance Mass spectrometry (FT-ICRMS).<sup>23</sup> These are low molecular weight (masses ranging between 600 – 700 Da), multi – dentate ligands with hard Lewis-bases (electron pair donor) that bind Ni in +2 oxidation state, but their structure and source remains elusive.<sup>23</sup>

Soil is another area where nickel is found in appreciable concentrations. Both plants and soil bacteria require nickel uptake from soil. Bioavailability of nickel in soil is largely modulated by pH and soil type.<sup>27-28</sup> While the pH regulates the chemical speciation and ligand binding properties, organic matter - rich soil binds Ni more tightly than clay silicates and oxides or hydroxides within the acidic pH range.<sup>28</sup>

### **1.3 Intracellular Proteinaceous Labile Nickel Pool**

Protein species in the cytosol that bind nickel and can exchange it constitute the proteinaceous labile nickel pool. Typically, these proteins are either nickel metallochaperones that directly shuttle nickel and/or participate in nickel insertion into nickel -dependent enzymes or nickel storage proteins. The basic feature of these nickel metallochaperones, similar to other metallochaperones, is their specificity and lability. The binding affinity of nickel chaperones are in micromolar range, and are labile enough to exchange nickel with partner proteins. For instance, HypA, which is a nickel metallochaperone for the maturation of Ni, Fe hydrogenase in *E. coli*, has a nickel binding affinity of 1 $\mu$ M, and it delivers nickel to HypB in a GTPase dependent manner.<sup>29-</sup>  
<sup>33</sup> The latter then inserts nickel to large subunit (HydB) of Ni, Fe – hydrogenase.<sup>30, 34</sup>

In bacteria that utilize other nickel – dependent enzymes for survival, there are several other enzyme specific nickel chaperones. For example, in the human pathogen *H. pylori*, which in addition to Ni, Fe – hydrogenase contains urease, a cascade of urease - specific accessory proteins, UreEFGH, which includes the nickel chaperone, UreE ensures proper maturation of this enzyme.<sup>35-</sup>  
<sup>36</sup> The dimer of UreE (UreE<sub>2</sub>) binds nickel with relatively higher affinity with an apparent dissociation constant (K<sub>d</sub>) of  $0.15 \pm 0.01 \mu\text{M}$ . Interestingly, previous studies highlighted a critical role of HypA in urease maturation in *H. pylori*.<sup>37</sup> Recent studies revealed that in *H. pylori*, HypA interacts with UreE to form a complex (HypA•UreE<sub>2</sub> ) whose nickel affinity is thousand and ten-thousand fold higher than that of either HypA or UreE<sub>2</sub>, respectively.<sup>38</sup> It is possible that the nickel - bound HypA•UreE<sub>2</sub> complex is most likely involved in nickel delivery to urease, but its experimental verification is required. Similarly, biophysical and calorimetric characterization of a novel nickel chaperone, CooT from *Rhodospirillum rubrum* required for the maturation of Carbon monoxide dehydrogenase (CODH) revealed its binding affinity for nickel to be 9 nM.<sup>39-40</sup> The molecular details of its role in the activation of CODH is being investigated.<sup>41</sup>

Storage proteins for nickel in *E. coli* are unknown, but Hpn1 and Hpn1- like proteins in *H. pylori* are considered to be storage proteins which are small (7-8 kDa), His-rich (and Gln-rich for Hpn2) proteins that can bind 2-5 nickel ions per monomer with a dissociation constant of 7  $\mu\text{M}$  and 3 $\mu\text{M}$ , respectively.<sup>42</sup> Hpn interacts with Hpn2, with accessory proteins, HypA and HypB and also with the UreA subunit of urease.<sup>42</sup> Information on how these storage proteins function during nickel trafficking is lacking.



#### 1.4 Intracellular Non – Proteinaceous Labile Nickel Pool

Low molecular weight compounds in the cell that can loosely bind nickel and exchange it with other LMW compounds and/or proteins or enzymes can be categorized as non-proteinaceous labile nickel pool. Irrespective of cell – type (plants or bacterial), these compounds have similar properties, but their regulation is likely dependent on the environmental and growth factors. Nickel enzymes are widely distributed in both lower and higher plants. Lower plants, such as, algae contain ureases, and Nickel Superoxide Dismutase.<sup>36, 43</sup> In germinating plants, including legumes (*Rhizobium*, *Bradyrhizobium*, etc.), urease, Glyoxalase I, and hydrogenases are known nickel enzymes, which utilize similar accessory proteins for their maturation as their bacterial counterparts.<sup>44-45</sup> Besides, there are a number of other plants such as *Sebartica acuminata*, *Alyssum lesbiacum*, which are not known to contain any nickel-dependent enzyme, but can hyperaccumulate nickel as a strategy to acquire nickel-tolerance in a nickel-rich growth environment, such as the soils of New Caledonia.<sup>46</sup> The Ni concentration in the latex of *Sebartica acuminata* is about 25% of the dry mass, which is in stark contrast to the value of < 0.001% in other plants, and is the highest recorded nickel content in any species.<sup>46</sup>

Plant ligands play an important role in the sequestration of nickel from soil, transport to above – ground tissue and finally storage.<sup>46</sup> The first stage of nickel uptake in plants is its interaction with soil.<sup>46</sup> Plants produce a number of low-molecular weight compounds, including organic acids, amino acids, peptides and proteins, some of which are possible nickel – coordinating ligands shown in **Figure 1.3**.<sup>46</sup> Among these, histidine (**Figure 1.3A**) has a higher affinity for Ni(II) and, in fact, exposure of hyperaccumulator to Ni either elicited a large and proportional increase in the levels of free His (*A. lesbiacum*) or increased Ni tolerance in nonaccumulators (*e.g.*, *A. montanum* L.) and Ni transport capacity to shoots (*e.g.*, *Pisum sativum* and *Brassica juncea*).<sup>46-</sup>

<sup>47</sup> Nickel import from the environment in bacteria is facilitated by two types of transmembrane transporters: ATP- dependent transporters (such as NikABCDE in *E. coli*), and nickel permeases (such as Ni/Co permeases (NiCoTs), e.g.NixA in *H. pylori*, and HoxN in *R. eutropha*). Recent studies identified L-His as a potential ligand required for specific nickel uptake by ATP-dependent nickel importers in a variety of organisms including *E. coli*, *Y. pestis*, *S. aureus*, *C. jejuni*, and *H.*

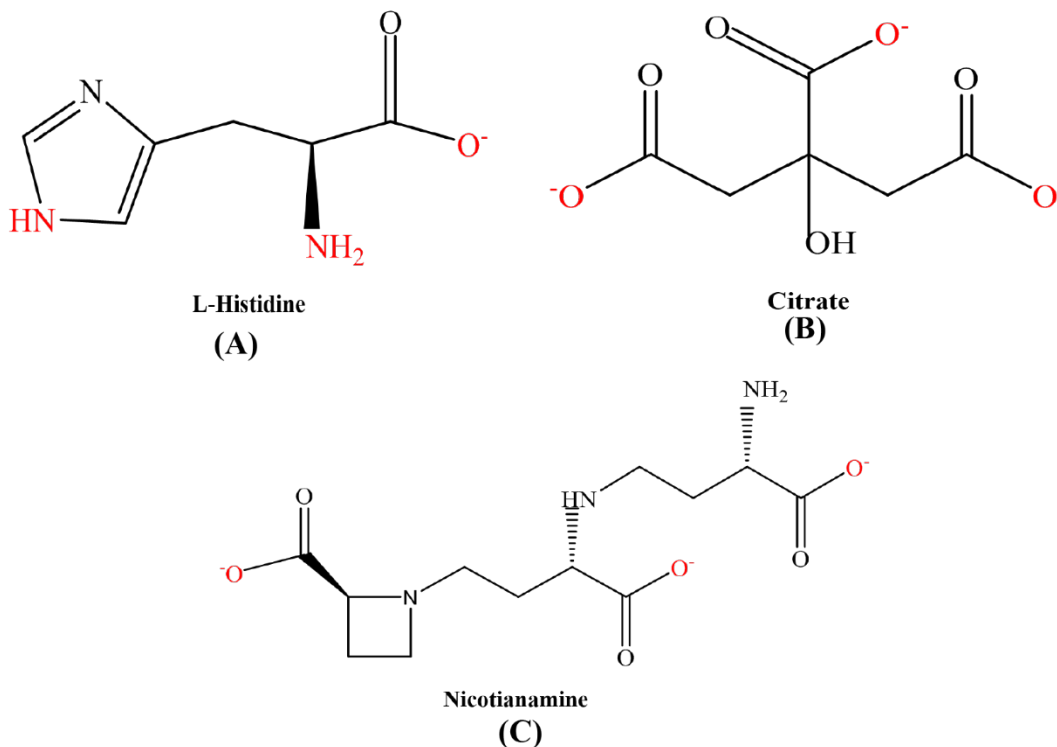


**Figure 1.3: Molecular structure of known biological nickel-ligands and binding ligands shown in red A) Histidine, B) Citrate, C) Nicotianamine**

*pylori* (described below).<sup>1, 48</sup> Other studies have established that competition between metallosensors and ligands involved in the labile nickel pool (*i.e.*, nickel buffer), particularly L-His, are important to specific metal sensing.<sup>49</sup> A histidine - dependent nickel complex, distinct from Ni-(L-His)<sub>2</sub> was found to bind to a solute – binding protein (SBP), CntA, involved in nickel import in *S. aureus*.<sup>50</sup> This complex is essentially a metallophore, called staphylopine, which is assembled by proteins encoded by *cntKLM* gene cluster found in *S. aureus*, *Y. pestis*, and *P.*

*aeruginosa*.<sup>50</sup> Staphylopin also modulates the uptake of metal ions other than nickel and hence its specificity to nickel remains to be established.<sup>50</sup> Besides histidine, NikA from *S. aureus* was found to bind a nickel complex in histidine - depleted cultures, which was modeled as Ni-(L-His)(2 - methyl - 2,4 - thiazolidine - dicarboxylic acid).<sup>50</sup>

In addition to histidine, the weak organic acid – citrate (**Figure 1.3B**), is also a likely candidate for forming a biological nickel-complex. Analysis of the Ni – rich latex and leaves of *S. acuminata* revealed a nickel – citrate complex, and is the only example of a biological nickel-citrate complex.<sup>46</sup> Citrate is a weak ligand for nickel with an association constant ( $\log \beta$ ) of 5.4.<sup>51</sup> With histidine present, the factors affecting preferential binding of nickel to citrate are unknown, and no such bacterial complex has been isolated so far. Another biologically relevant small – molecule bound nickel complex is Ni-Nicotianamine (NA, **Figure 1.3C**), identified by mass spectrometry in extracts of the Ni hyperaccumulating plants (*T. caerulescens* and *S. acuminata*).<sup>46</sup> NA is the precursor to a group of multidentate ligands, mugineic acid and avenic acid, which are the phytosiderophores (PS) in graminaceous plants.<sup>46</sup> NA was first isolated from the leaves of tobacco plant *Nicotiana tabacum L.* in 1971 and is ubiquitously found in all naturally occurring multicellular plants.<sup>46</sup> NA binds Ni(II) more strongly than Fe(II), and hence it is not surprising that complexes of NA with nickel were isolated from the nickel hyperaccumulators.

It is possible that the nickel-LMW complexes identified in plants also exist, with/without modifications, in bacteria. The cellular LMW ligands identified for nickel import in bacteria are also likely candidates that constitute the cellular labile nickel pool. In any event, the role of these ligands for nickel import raise several questions relevant to nickel trafficking. Do these ligands provide nickel specificity and distinguish between the transport of nickel or other metal ions? Are these ligands specifically secreted by these organisms to import nickel? Are these complexes

transported intact or are the ligands stripped away during the transport process? Once imported, what is the fate of these nickel complexes – are these ligands metabolized or form a part of cellular non – proteinaceous labile nickel pool? If these complexes remain intact, do metallochaperones acquire nickel from these complexes or acquire the whole complex until it is inserted into the correct nickel enzyme? What factors inside the cell determines the partitioning of nickel in the two labile nickel pools? Can these nickel-complexes play a direct role in enzyme maturation?

### ***1.4.1 Histidine***

Histidine is one of the twenty standard amino acids present in proteins of all living organisms. Its side-chain is an imidazole, and it is the only amino acid whose side-chain can switch from unprotonated to protonated state under neutral conditions due to the  $pK_a$  value of 6.0 of its side-chain. Histidine is a versatile ligand that binds metals with a number of coordination modes using its carboxylato-, amine-, and imidazole groups (**Figure 1.3A**), and similar to other amino acids, there are two stereoisomers of histidine: L-, and D-, with L-His being the biologically active form (**Figure 1.3A**). With nickel, L-His forms 1:1 and 1: 2 complexes with stability constants ( $\log \beta$ ) of 6.7 and 4.8 respectively, and Ni(II) - (L-His)<sub>2</sub> crystallizes in the trans-imidazole configuration (**Figure 1.3A**).<sup>52-53</sup> Uptake of nickel in *E. coli* by NikABCDE requires L-His, which is co-transported with Ni(II).<sup>48</sup> *E. coli* strains grown without L-His in growth medium had decreased nickel uptake rate and intracellular nickel concentrations.<sup>48</sup> No other molecule, such as polycarboxylic acids, L-His derivatives, such as histidinol, L-His-CONH<sub>2</sub>, and L-His methyl ester, or even D-His could reproduce the same Ni-uptake rate as L-His, and in fact, D- His was inhibitory.<sup>48</sup> The concentration dependence of Ni-uptake and binding to NikA suggested a ternary complex with a stoichiometry of Ni:2L-His:NikA.<sup>48</sup>

Crystal structures of NikA: Ni(II)-(L-His)<sub>2</sub> complex revealed several interesting features related to Ni-recognition by NikA (**Figure 1.4A**).<sup>54</sup> First, the Ni(II) atom in protein complex is not ‘free’, i.e. not bound to water ligands, instead Ni(II) is bound to the two extraneous L-His molecules that are co-transported, which provides five of the six ligands. The COO<sup>-</sup> ligand from one of the co-transported L-His is displaced by His<sub>416</sub> in NikA, that was previously shown to be important for nickel transport,<sup>55</sup> and forms the sixth ligand in the six – coordinate Ni(II) complex. The displaced COO<sup>-</sup> ligand from L-His interact with the highly conserved Arg residues of NikA, that presumptively forms the cation binding pocket in NikA. These Arg residues also promote the formation of a unique stereoisomer of Ni(II)-(L-His)<sub>2</sub> configuration, previously unobserved that is different from its usual trans-imidazole in (**Figure 1.3A**),<sup>52</sup> and most closely resembles the trans- COO<sup>-</sup> species observed in Co(III)-(L-His)<sub>2</sub> complex.<sup>56-57</sup> It is unknown if NikA initially binds the usual trans-imidazole Ni-(L-His)<sub>2</sub> and then undergoes ligand rearrangements to form the observed Ni-isomer in NikA. The functional relevance of such a Ni-isomer is also unknown.

The role of His<sub>416</sub> in discrimination of Ni(II) versus other metals for transport has not been studied. It is likely that the interactions observed for *E. coli* NikA:Ni – (L-His)<sub>2</sub> will not be observed for Cu – (L-His)<sub>2</sub> and Zn – (L-His)<sub>2</sub> as these complexes display lower coordination numbers. The only divalent metal tested for specificity is Co, which shows inhibition of Ni-accumulation, suggesting a similar interaction of *Ec*NikA:Co – (L-His)<sub>n</sub>. However, as suggested by the Irving-William series, association of L-His with Co(II) is weaker, which means that a higher concentration of Co(II) will be required to attain Co-(L-His)<sub>2</sub> concentration required for binding to *Ec*NikA. Thus, relative abundance of metal – (L-His)<sub>2</sub> complexes which binds to *Ec*NikA is also a determining factor for selectivity of Ni(II) over Co(II) or other metals.

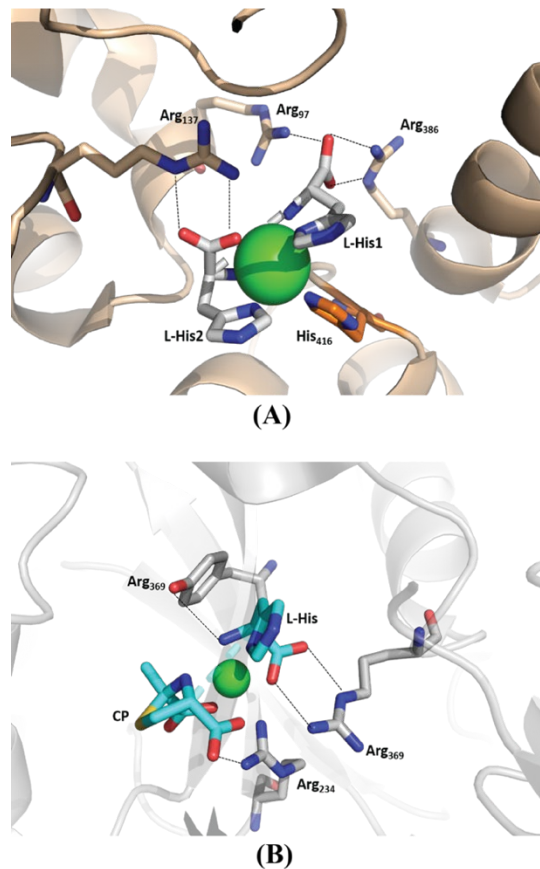


**Figure 1.4: Crystal structures showing nickel complexes bound to nickel transporters: A) Ni(II)-(L-His)<sub>2</sub> complex bound to the nickel-binding site in *EcNikA* (PDB ID: 4I8C). Free histidines (L-His1 and L-His2) are shown in grey and nickel is shown as green sphere. His<sub>416</sub> is shown in orange and protein residues making H-bond interactions (dashed-lines) with free histidines are shown in pale orange. B) Ni(II)-(L-His)-CP complex bound to nickel-binding site in *SaNikA* (PDB ID: 4XKR). Free L-His and CP are shown in cyan. Protein residues making H-bond interactions with free histidine and CP are depicted in grey.**

Similar structures were obtained for *YpYntA*, which is homologous to *EcNikA*, but has distinct amino acid sequence and position of nickel binding residues. In *YpYntA*: Ni-(L-His)<sub>2</sub> complex, the amine-ligand (-NH<sub>2</sub>) from one of the co-transported L-Histidine molecule is displaced by His<sub>482</sub>, and results in the same trans- COO<sup>-</sup> stereoisomer of nickel-histidine, with

only one Arg interaction. In *Sa*NikA, however, there are no histidine residues in the nickel binding pocket, and as a result, the nickel-histidine complex in *Sa*NikA: Ni-(L-His)<sub>2</sub> complex exists in a trans- NH<sub>2</sub> configuration. Similarly, an all cis-Ni-(L-His)<sub>2</sub> stereoisomer was observed for *H. pylori* CeuE, which displaces a Nδ - atom of the L-His ligand by His103. In contrast, NikZ from *C. jejuni*, shows a Ni-L-His complex bound to the transporter and is possibly due to the abundance of His residues in the protein.

It is possible that complexation of nickel solely with L-His or in combination with other cellular ligands tunes the affinity of Ni(II) and provide molecular interactions, which determine transport specificity through the promiscuous nickel/metal transporters. However, whether these organisms deliberately secrete their own L-His or utilize the extraneous L-His as a means to specifically import nickel is unknown. The importance of L-His in maintaining nickel or cellular metal homeostasis, in general, is far reaching and is also reported in higher organisms such as, yeast (*S. cerevisiae*), and humans. While L-His confers nickel tolerance to *S. cerevisiae*, it stimulates uptake of divalent metals in human erythrocytes and in the erythroleukaemic cell lines.<sup>58-59</sup> Transport of nickel in human blood serum is facilitated by nickel-binding to human serum albumin and a ternary complex with L-histidine.<sup>60</sup> In fact, Cu(II)-(L-His)<sub>2</sub> complex is used as a therapeutic agent to treat Menkes disease and Infantile hypertrophic cardioencephalomyopathy, which are the diseases associated with defective copper transport.<sup>61</sup> Biosynthesis of L-His is conserved across all living organisms and occurs via ten enzymatic reactions afforded by proteins encoded by *his* operon which convert phosphoribosyl pyrophosphate to L-His.<sup>62</sup> However, no histidine export system has been described in any organism.<sup>62</sup>

#### ***1.4.2 2-methyl-2,4-thiazolidine-dicarboxylic acid***

Apart from histidine, cellular metabolites can also function as nickel chelators for cellular nickel import or labile nickel pool. One such known metabolites identified from *S. aureus* is 2-methyl-2,4-thiazolidine-dicarboxylic acid (also called CP).<sup>63</sup> This small organic compound, in conjunction with a free histidine, formed a six-coordinate octahedral nickel complex that bound SaNikA derived from histidine-depleted cultures (**Figure 1.4B**).<sup>1, 63</sup> CP provided three of the six interactions with nickel via its two carboxylate groups, and amine group at the 3-position of the thiazolidine ring, while the free-histidine molecule provided the remaining three interactions to nickel arising from its carboxylate group, amine group, and N $\delta$  atom of its imidazole group. CP is the by-product of non-enzymatic condensation reaction of L-cysteine and pyruvic acid in cysteine pathway *in vivo*, and is also identified in the culture supernatants of *E. coli*.<sup>63-64</sup> Free cysteines are the precursor to the 2-methyl-2,4-thiazolidine-dicarboxylic acid in *Salmonella typhimurium*, and it is possible that a similar processing of free cysteines in *S. aureus* occurs to import the nickel complex.<sup>50</sup> Efflux of metabolites of cysteine pathway, such as CP, in *E. coli*, is known to involve the major facilitator protein Orf299 (or YdeD).<sup>64</sup> In *S. aureus*, two homologues of Orf299 are predicted to be SAV0107 (22% identity with *E. coli* Orf299) and an unknown protein (42% identity with YdeD putative protein from *B. subtilis*).<sup>63</sup> These proteins belong to EamA family, many of the members of which are predicted to be integral membrane proteins.<sup>63</sup>

It appears that in the absence of exogenous histidine, *S. aureus* secretes its endogenous metabolites, such as free histidine or CP to acquire nickel from its environment. Notably, under normal growth conditions, SaNikA does bind Ni-(L-His)<sub>2</sub> in a configuration different than that for EcNikA, but what forms the basis of using a heterogenous nickel complex, such as Ni-CP-(L-His), and not Ni-(L-His)<sub>2</sub> or Ni-(CP)<sub>2</sub>, in histidine depleted cultures, is unclear. Whether CP is a



substitute for a second histidine under growth conditions lacking histidine or histidine -based bioavailability of nickel or if a mix of CP and histidine is the natural complex for nickel acquisition and/or transport remains elusive.

### **1.5 Experimental Techniques to study cellular labile nickel or metal pools**

While the total cellular metal content (which comprises of both static and labile metal pool) and its distributions has been measured using a variety of techniques, such as ICP-MS, synchrotron radiation X-ray fluorescence imaging, proton/particle-induced X-ray emission spectrometry, secondary-ion MS (SIMS), and laser ablation ICP-MS (LA-ICP-MS), there has been an increasing interest in measuring the labile metal pool in cells using *in vivo* metal – specific fluorescent sensors.<sup>13, 15, 19, 65-66</sup> Synthetic compounds or genetically encoded fluorescent proteins targeting specific intracellular metals are designed that most likely displace the natural metal-LMW complex and bind to the labile metal pools, and the read out is either a fluorescence which is measured as FRET or imaging, which is correlated with the levels of that labile metal pool.<sup>65-66</sup> Such studies are emerging for Zn, and Cu, but information on nickel is not available yet.<sup>19, 67-68</sup> It is important to note that these sensors explicitly undergo ligand exchange reactions with the natural labile metal pool that leads to identity-loss of natural labile intracellular metal-LMW complexes, and hence, characterizing such intracellular metal-LMW complexes is inherently difficult and challenging. So, experimental techniques where these natural LMW complexes from cytosol can be retained need to be developed.

Recently, a modified LC – ICP-MS technique was cleverly employed to isolate and identify LMW complexes of iron in mitochondria.<sup>17</sup> Soluble mitochondrial extracts were passed through a 10 - kDa cut-off membrane, and the flow - through was injected into a size exclusion column that

can resolve metal complexes  $\leq 10$  – kDa.<sup>17</sup> An on-line ICP – MS on the eluted fractions was then performed to identify the metal bound complexes.<sup>17</sup> This technique clearly resolved the labile LMW metal complexes, but the identity of the ligands bound to those metals remains unknown. Subsequent NMR or XAS studies on the same fractions can provide information on the nature of ligands bound to the metals. While this technique is exclusively used for mitochondrial Fe, Zn, and Mo, it appears promising for cytosolic Ni also. The challenge however is to obtain practical concentrations of these complexes relevant for structural studies.

Another minimally destructive technique to identify cellular ligands for metals, including nickel can be ICP – MS with metals of interest being either radio-labelled or analyzed with advanced metal – specific techniques such as XAS. Recent studies were used to characterize the Zn-metallome in whole bacterial cell using high – resolution XAS.<sup>69</sup> Whole – cell XAS on other metals such as Cu, Co and Cd has also been reported previously that identified the potential ligands around the respective metals.<sup>70-72</sup> The ligands involved in the nickel proteome using these methods is unknown so far. The major drawback in these studies is its inability to distinguish between the static and labile identity of the metals of interest. Prior fractionation of the cells to specifically isolate the labile metal pool, followed by its analysis either/or ICP-MS or XAS or NMR can be helpful in determining the complete identity of these labile nickel pool or metal pool in general and awaits further investigation.

## 1.6 References

1. Chivers, P. T., Nickel recognition by bacterial importer proteins. *Metallomics : integrated biometal science* **2015**, 7 (4), 590-595.
2. Boer, J. L.; Mulrooney, S. B.; Hausinger, R. P., Nickel-dependent metalloenzymes. *Arch. Biochem. & Biophys.* **2014**, 544, 142-152.
3. M. Cempel, G. N., Nickel: A Review of its sources and environmental toxicology. *Polish J Environ. Stud.* **2006**, 15 (3), 375-382.
4. Macomber, L.; Hausinger, R. P., Mechanisms of nickel toxicity in microorganisms. *Metallomics : integrated biometal science* **2011**, 3 (11), 1153-1162.
5. Kraemer, S. M., Iron oxide dissolution and solubility in the presence of siderophores. *Aquatic Sci.* **2004**, 66 (1), 3-18.
6. Hider, R. C.; Kong, X., Chemistry and biology of siderophores. *Nat. Prod. Rep.* **2010**, 27 (5), 637-657.
7. Kochian, L. V.; Pineros, M. A.; Liu, J.; Magalhaes, J. V., Plant Adaptation to Acid Soils: The Molecular Basis for Crop Aluminum Resistance. *Ann. Rev. Plant Biol.* **2015**, 66, 571-598.
8. Schalk, I. J.; Mislin, G. L.; Brillet, K., Structure, function and binding selectivity and stereoselectivity of siderophore-iron outer membrane transporters. *Curr. Top Membr.* **2012**, 69, 37-66.
9. Irving, H.; Williams, R. J. P., 637. The stability of transition-metal complexes. *J. Chem. Soc. (Resumed)* **1953**, (0), 3192-3210.
10. Foster, A. W.; Osman, D.; Robinson, N. J., Metal preferences and metallation. *J. Biol. Chem.* **2014**, 289 (41), 28095-28103.

11. Waldron, K. J.; Robinson, N. J., How do bacterial cells ensure that metalloproteins get the correct metal? *Nat. Rev. Microbiol.* **2009**, *7* (1), 25-35.
12. Metals in Cells: Control of Cellular Metal Concentration. In *Encyclopedia of Inorganic and Bioinorganic Chemistry*, pp 1-12.
13. Clemens, S., Metal ligands in micronutrient acquisition and homeostasis. *Plant Cell Environ.* **2019**, *42* (10), 2902-2912.
14. Finney, L. A.; O'Halloran, T. V., Transition metal speciation in the cell: insights from the chemistry of metal ion receptors. *Science* **2003**, *300* (5621), 931-936.
15. New, E. J., Tools to study distinct metal pools in biology. *Dalt.Trans.* **2013**, *42* (9), 3210-3219.
16. Lv, H.; Shang, P., The significance, trafficking and determination of labile iron in cytosol, mitochondria and lysosomes. *Metallomics : integrated biometal science* **2018**, *10* (7), 899-916.
17. Lindahl, P. A.; Moore, M. J., Labile Low-Molecular-Mass Metal Complexes in Mitochondria: Trials and Tribulations of a Burgeoning Field. *Biochemistry* **2016**, *55* (30), 4140-4153.
18. Ma, Z.; Chandrangsu, P.; Helmann, T. C.; Romsang, A.; Gaballa, A.; Helmann, J. D., Bacillithiol is a major buffer of the labile zinc pool in *Bacillus subtilis*. *Mol. Microbiol.* **2014**, *94* (4), 756-770.
19. Muylle, F. A.; Adriaensen, D.; De Coen, W.; Timmermans, J. P.; Blust, R., Tracing of labile zinc in live fish hepatocytes using FluoZin-3. *Biometals* **2006**, *19* (4), 437-450.
20. Krężel, A.; Maret, W., The biological inorganic chemistry of zinc ions. *Arch. Biochem. Biophys.* **2016**, *611*, 3-19.
21. *Nickel in Drinking water*. World Health Organization: 2019.

22. Helm, L.; Merbach, A. E., Inorganic and Bioinorganic Solvent Exchange Mechanisms. *Chem. Rev.* **2005**, *105* (6), 1923-1960.
23. Boiteau, R. M.; Till, C. P.; Ruacho, A.; Bundy, R. M.; Hawco, N. J.; McKenna, A. M.; Barbeau, K. A.; Bruland, K. W.; Saito, M. A.; Repeta, D. J., Structural Characterization of Natural Nickel and Copper Binding Ligands along the US GEOTRACES Eastern Pacific Zonal Transect. *Front. in Marine Sci.* **2016**, *3* (243).
24. Vraspir, J. M.; Butler, A., Chemistry of marine ligands and siderophores. *Ann. Rev. of Marine Sci.* **2009**, *1*, 43-63.
25. Saito, M. A.; Moffett, J. W.; DiTullio, G. R., Cobalt and nickel in the Peru upwelling region: A major flux of labile cobalt utilized as a micronutrient. *Glob. Biogeochem. Cycles* **2004**, *18* (4).
26. Van Den Berg, C. M. G.; Nimmo, M., Determination of interactions of nickel with dissolved organic material in seawater using cathodic stripping voltammetry. *Science of The Total Environ.* **1987**, *60*, 185-195.
27. Echevarria, G.; Massoura, S. T.; Sterckeman, T.; Becquer, T.; Schwartz, C.; Morel, J. L., Assessment and control of the bioavailability of nickel in soils. *Environ. Toxicol. Chem.* **2006**, *25* (3), 643-651.
28. Weng, L. P.; Wolthoorn, A.; Lexmond, T. M.; Temminghoff, E. J. M.; van Riemsdijk, W. H., Understanding the Effects of Soil Characteristics on Phytotoxicity and Bioavailability of Nickel Using Speciation Models. *Environ. Sci. & Tech.* **2004**, *38* (1), 156-162.
29. Lacasse, M. J.; Summers, K. L.; Khorasani-Motlagh, M.; George, G. N.; Zamble, D. B., Bimodal Nickel-Binding Site on Escherichia coli [NiFe]-Hydrogenase Metallochaperone HypA. *Inorg. Chem.* **2019**, *58* (20), 13604-13618.

30. Lacasse, M. J.; Zamble, D. B., [NiFe]-Hydrogenase Maturation. *Biochemistry* **2016**, *55* (12), 1689-1701.
31. Hu, H. Q.; Johnson, R. C.; Merrell, D. S.; Maroney, M. J., Nickel Ligation of the N-Terminal Amine of HypA Is Required for Urease Maturation in *Helicobacter pylori*. *Biochemistry* **2017**, *56* (8), 1105-1116.
32. Herbst, R. W.; Perovic, I.; Martin-Diaconescu, V.; O'Brien, K.; Chivers, P. T.; Pochapsky, S. S.; Pochapsky, T. C.; Maroney, M. J., Communication between the zinc and nickel sites in dimeric HypA: metal recognition and pH sensing. *J. Am. Chem. Soc.* **2010**, *132* (30), 10338-10351.
33. Atanassova, A.; Zamble, D. B., *Escherichia coli* HypA is a zinc metalloprotein with a weak affinity for nickel. *J. Bacteriol.* **2005**, *187* (14), 4689-4697.
34. Miki, K.; Atomi, H.; Watanabe, S., Structural Insight into [NiFe] Hydrogenase Maturation by Transient Complexes between Hyp Proteins. *Acc. Chemical Res.* **2020**, *53* (4), 875-886.
35. Farrugia, M. A.; Macomber, L.; Hausinger, R. P., Biosynthesis of the urease metallocenter. *J. Biol. Chem.* **2013**, *288* (19), 13178-13185.
36. Maroney, M. J.; Ciurli, S., Nonredox nickel enzymes. *Chem. Rev.* **2014**, *114* (8), 4206-4228.
37. Benoit, S. L.; Mehta, N.; Weinberg, M. V.; Maier, C.; Maier, R. J., Interaction between the *Helicobacter pylori* accessory proteins HypA and UreE is needed for urease maturation. *Microbiology* **2007**, *153* (Pt 5), 1474-1482.
38. Hu, H. Q.; Huang, H. T.; Maroney, M. J., The *Helicobacter pylori* HypA.UreE2 Complex Contains a Novel High-Affinity Ni(II)-Binding Site. *Biochemistry* **2018**, *57* (20), 2932-2942.

39. Alfano, M.; Perard, J.; Miras, R.; Catty, P.; Cavazza, C., Biophysical and structural characterization of the putative nickel chaperone CooT from *Carboxydotherrmus hydrogenoformans*. *J. Biol. Inorg. Chem.* **2018**, *23* (5), 809-817.
40. Timm, J.; Brochier-Armanet, C.; Perard, J.; Zambelli, B.; Ollagnier-de-Choudens, S.; Ciurli, S.; Cavazza, C., The CO dehydrogenase accessory protein CooT is a novel nickel-binding protein. *Metallomics : integrated biometal science* **2017**, *9* (5), 575-583.
41. Alfano, M.; Veronesi, G.; Musiani, F.; Zambelli, B.; Signor, L.; Proux, O.; Rovezzi, M.; Ciurli, S.; Cavazza, C., A Solvent-Exposed Cysteine Forms a Peculiar Ni(II) -Binding Site in the Metallochaperone CooT from *Rhodospirillum rubrum*. *Chemistry (Weinheim an der Bergstrasse, Germany)* **2019**, *25* (67), 15351-15360.
42. Vinella, D.; Fischer, F.; Vorontsov, E.; Gallaud, J.; Malosse, C.; Michel, V.; Cavazza, C.; Robbe-Saule, M.; Richaud, P.; Chamot-Rooke, J.; Brochier-Armanet, C.; De Reuse, H., Evolution of *Helicobacter*: Acquisition by Gastric Species of Two Histidine-Rich Proteins Essential for Colonization. *PLoS Pathog.* **2015**, *11* (12), e1005312.
43. Dupont, C. L.; Neupane, K.; Shearer, J.; Palenik, B., Diversity, function and evolution of genes coding for putative Ni-containing superoxide dismutases. *Environ. Microbiol.* **2008**, *10* (7), 1831-1843.
44. Dalton, D. A.; Russell, S. A.; Evans, H. J., Nickel as a micronutrient element for plants. *Biofactors* **1988**, *1* (1), 11-16.
45. Eskew, D. L.; Welch, R. M.; Cary, E. E., Nickel: an essential micronutrient for legumes and possibly all higher plants. *Science* **1983**, *222* (4624), 621-623.
46. Callahan, D. L.; Baker, A. J.; Kolev, S. D.; Wedd, A. G., Metal ion ligands in hyperaccumulating plants. *J. Biol. Inorg. Chem.* **2006**, *11* (1), 2-12.

47. Ingle, R. A.; Mugford, S. T.; Rees, J. D.; Campbell, M. M.; Smith, J. A. C., Constitutively High Expression of the Histidine Biosynthetic Pathway Contributes to Nickel Tolerance in Hyperaccumulator Plants. *The Plant Cell* **2005**, *17* (7), 2089.
48. Chivers, P. T.; Benanti, E. L.; Heil-Chapdelaine, V.; Iwig, J. S.; Rowe, J. L., Identification of Ni-(L-His)<sub>2</sub> as a substrate for NikABCDE-dependent nickel uptake in *Escherichia coli*. *Metallomics : integrated biometal science* **2012**, *4* (10), 1043-1050.
49. Foster, A. W.; Pernil, R.; Patterson, C. J.; Scott, A. J. P.; Palsson, L. O.; Pal, R.; Cummins, I.; Chivers, P. T.; Pohl, E.; Robinson, N. J., A tight tunable range for Ni(II) sensing and buffering in cells. *Nat. Chem. Biol.* **2017**, *13* (4), 409-414.
50. Zeer-Wanklyn, C. J.; Zamble, D. B., Microbial nickel: cellular uptake and delivery to enzyme centers. *Curr. Opin. Chem. Biol.* **2017**, *37*, 80-88.
51. Smith, R. M., Martell, A. E., *Critical Stability Constants*. Plenum: New York, 1989; Vol. 6.
52. Fraser, K. A.; Harding, M. M., The crystal and molecular structure of bis(histidino)nickel(II) monohydrate. *J. Chem.Soc. A: Inorganic, Physical, Theoretical* **1967**, (0), 415-420.
53. Zhang, Y.; Akilesh, S.; Wilcox, D. E., Isothermal Titration Calorimetry Measurements of Ni(II) and Cu(II) Binding to His, GlyGlyHis, HisGlyHis, and Bovine Serum Albumin: A Critical Evaluation. *Inorg. Chem.* **2000**, *39* (14), 3057-3064.
54. Lebrette, H.; Iannello, M.; Fontecilla-Camps, J. C.; Cavazza, C., The binding mode of Ni-(L-His)<sub>2</sub> in NikA revealed by X-ray crystallography. *J. Inorg. Biochem.* **2013**, *121*, 16-18.



55. Cavazza, C.; Martin, L.; Laffly, E.; Lebrette, H.; Cherrier, M. V.; Zeppieri, L.; Richaud, P.; Carrière, M.; Fontecilla-Camps, J. C., Histidine 416 of the periplasmic binding protein NikA is essential for nickel uptake in Escherichia coli. *FEBS Lett.* **2011**, *585* (4), 711-715.
56. Zompa, L. J., The preparation and tentative structural assignment of the geometrical isomers of bis-(L-histidinato)cobalt(III) ion. *J. Chem.Soc. D: Chem.Comm.* **1969**, (14), 783-783.
57. Sundberg, R. J.; Martin, R. B., Interactions of histidine and other imidazole derivatives with transition metal ions in chemical and biological systems. *Chem. Rev.* **1974**, *74* (4), 471-517.
58. Farcasanu, I. C.; Mizunuma, M.; Nishiyama, F.; Miyakawa, T., Role of L-histidine in conferring tolerance to Ni<sup>2+</sup> in *Sacchomyces cerevisiae* cells. *Biosci. Biotechnol. Biochem.* **2005**, *69* (12), 2343-2348.
59. Oakley, F.; Horn, N. M.; Thomas, A. L., Histidine-stimulated divalent metal uptake in human erythrocytes and in the erythroleukaemic cell line HEL.92.1.7. *J. Physiol.* **2004**, *561* (Pt 2), 525-534.
60. Glennon, J. D.; Sarkar, B., Nickel(II) transport in human blood serum. Studies of nickel(II) binding to human albumin and to native-sequence peptide, and ternary-complex formation with L-histidine. *Biochem. J.* **1982**, *203* (1), 15-23.
61. Deschamps, P.; Kulkarni, P. P.; Gautam-Basak, M.; Sarkar, B., The saga of copper(II)-L-histidine. *Coordination Chemistry Reviews* **2005**, *249* (9), 895-909.
62. Kulis-Horn, R. K.; Persicke, M.; Kalinowski, J., Histidine biosynthesis, its regulation and biotechnological application in *Corynebacterium glutamicum*. *Microbial biotech.* **2014**, *7* (1), 5-25.
63. Lebrette, H.; Borezée-Durant, E.; Martin, L.; Richaud, P.; Boeri Erba, E.; Cavazza, C., Novel insights into nickel import in *Staphylococcus aureus*: the positive role of free histidine and

structural characterization of a new thiazolidine-type nickel chelator. *Metallomics* **2015**, *7* (4), 613-621.

64. Dassler, T.; Maier, T.; Winterhalter, C.; Böck, A., Identification of a major facilitator protein from *Escherichia coli* involved in efflux of metabolites of the cysteine pathway. *Mol. Microbiol.* **2000**, *36* (5), 1101-1112.

65. Hao, Z.; Zhu, R.; Chen, P. R., Genetically encoded fluorescent sensors for measuring transition and heavy metals in biological systems. *Curr. Opin. Chem. Biol.* **2018**, *43*, 87-96.

66. Ackerman, C. M.; Lee, S.; Chang, C. J., Analytical Methods for Imaging Metals in Biology: From Transition Metal Metabolism to Transition Metal Signaling. *Anal. Chem.* **2017**, *89* (1), 22-41.

67. Morgan, M. T.; Bourassa, D.; Harankhedkar, S.; McCallum, A. M.; Zlatic, S. A.; Calvo, J. S.; Meloni, G.; Faundez, V.; Fahrni, C. J., Ratiometric two-photon microscopy reveals attomolar copper buffering in normal and Menkes mutant cells. *Proc. Natl. Acad. Sci. U. S. A.* **2019**, *116* (25), 12167-12172.

68. Chung, C. Y.-S.; Posimo, J. M.; Lee, S.; Tsang, T.; Davis, J. M.; Brady, D. C.; Chang, C. J., Activity-based ratiometric FRET probe reveals oncogene-driven changes in labile copper pools induced by altered glutathione metabolism. *Proc. Natl. Acad. Sci. U.S.A.* **2019**, *116* (37), 18285.

69. Thomas, S. A.; Mishra, B.; Myneni, S. C. B., High Energy Resolution-X-ray Absorption Near Edge Structure Spectroscopy Reveals Zn Ligation in Whole Cell Bacteria. *J. Phys. Chem. Lett.* **2019**, *10* (10), 2585-2592.

70. Kretschmer, X. C.; Meitzner, G.; Gardea-Torresdey, J. L.; Webb, R., Determination of Cu environments in the cyanobacterium *Anabaena flos-aquae* by X-ray absorption spectroscopy. *Appl. and environ. microbiol.* **2004**, *70* (2), 771-780.

71. Belviso, B. D.; Italiano, F.; Caliandro, R.; Carrozzini, B.; Costanza, A.; Trotta, M., Cobalt binding in the photosynthetic bacterium *R. sphaeroides* by X-ray absorption spectroscopy. *Biometals* **2013**, *26* (5), 693-703.
72. Penen, F.; Isaure, M. P.; Dobritsch, D.; Bertalan, I.; Castillo-Michel, H.; Proux, O.; Gontier, E.; Le Coustumer, P.; Schaumlöffel, D., Pools of cadmium in *Chlamydomonas reinhardtii* revealed by chemical imaging and XAS spectroscopy. *Metallomics : integrated biometal science* **2017**, *9* (7), 910-923.

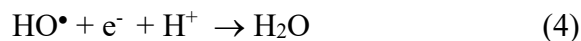
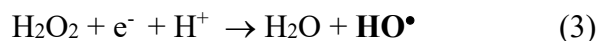
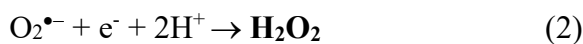
## CHAPTER 2

### SUPEROXIDE DISMUTASES: A REVIEW

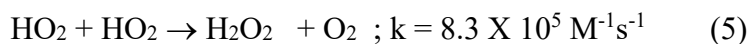
#### 2.1 Superoxide: A consequence of earth's great oxidation event

Superoxide radical ( $O_2^{\bullet-}$ ) is a reactive oxygen species formed by one electron reduction of oxygen and exists in all aerobic organisms as a consequence of their aerobic life processes. Depending on its biological context, it can be a toxic radical or decompose harmlessly, or can also act as a signaling molecule.<sup>1</sup> Evolution of oxygenic photosynthesis by cyanobacteria, some 2.4 billion years ago led to the Great Oxidation Event that resulted in increase of oxygen in earth's biosphere.<sup>1-2</sup> Consequently, as an adaptation strategy, organisms developed oxygen – utilizing metabolic pathways which produced reactive oxygen species - hydroxyl ( $OH^{\bullet}$ ), superoxide, and hydrogen peroxide ( $H_2O_2$ ) as byproducts that are capable of causing oxidative damage. Hence, antioxidant systems including antioxidant enzymes evolved to protect organisms from growing levels of oxidative damage by such reactive oxygen species.<sup>1</sup>

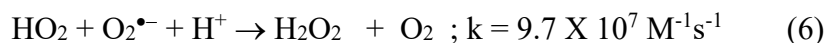
Dioxygen is a strong four – electron oxidant and is reduced to water in four sequential one electron reduction steps (**Equations 1 - 4**), each of which generates intermediates, characterized as reactive oxygen species and are potential oxidizing agents<sup>1</sup>:



Superoxide radical ( $O_2^{\bullet-}$ ) is a highly soluble, small anion, solvated by tightly hydrogen – bonded water molecules. Its protonated form ( $HO_2$ ) is a weak acid with a  $pK_a$  of 4.8, and hence, at physiological pH of 7.0,  $O_2^{\bullet-}$  is the predominant species.<sup>1</sup> At low pH, there is only  $HO_2$  present in solution, which is a poor reductant, and thus undergoes slow disproportionation (**Equation 5**).<sup>1,3</sup>



One - electron reduction of  $O_2^{\bullet-}$  to  $O_2^{2-}$  is an energetically uphill reaction, but presence of proton or metal makes the reaction thermodynamically favorable, and thermodynamic stabilization of the  $O_2^{2-}$  after one electron reduction of superoxide is one of the prerequisites for a successful disproportionation reaction that can be achieved by either protons or metals, as seen in Superoxide Dismutases (SODs) or Superoxide Reductases (SORs).<sup>1</sup> In case of  $HO_2$  at low pH, its proton serve as the  $O_2^{2-}$  stabilization moiety.<sup>1</sup> The rate of disproportionation is fastest at  $pH = pK_a = 4.8$ , where the concentration of both  $HO_2$  and  $O_2^{\bullet-}$  are equal, and the former acts as oxidant and latter acts as better reductant (**Equation 6**).<sup>1</sup> At high pH, however, no superoxide disproportionation occurs as the charge repulsion between two  $O_2^{\bullet-}$  prevent the reaction.<sup>1</sup> Furthermore, in case of such a disproportion occurring at high pH, the  $O_2^{2-}$  generated will also be unstable in absence of proton or metal.<sup>1</sup>



In cells,  $O_2^{\bullet-}$  is a selective oxidant as its major targets are labile Fe-S clusters and not the common cellular components such as peptides, carbohydrates, nucleic acids, or lipids, although it leads to production of other ROS, such as  $HO^{\bullet}$  that reacts with these biomacromolecules.  $O_2^{\bullet-}$  rapidly and irreversibly oxidizes the labile Fe-S clusters present in the biosynthetic enzymes that

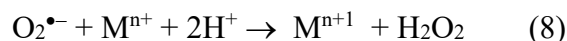
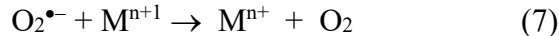
are required for essential metabolic pathways synthesizing branched-chain, aromatic – and sulfur containing amino acids. Such oxidation leads to inactivation of these enzymes and causes cellular toxicity. To prevent this oxidative damage by  $O_2^{\bullet-}$ , there are two main strategies: 1) conversion of superoxide directly to water via a four- electron reduction step, a process speculated to be performed by flavodiiron proteins or 2) catalytic disproportionation of  $O_2^{\bullet-}$  by enzymes such as SODs. The latter does not require any external reducing equivalents and/ or external energy and hence, is the dominant pathway for cellular superoxide detoxification.

## 2.2 Superoxide Dismutases

Superoxide Dismutases (SOD) are a ubiquitous group of antioxidant enzymes that evolved to catalyze the disproportionation of superoxide radical to oxygen and hydrogen peroxide and regulate the cellular levels of superoxide radical. These SODs are essentially metal – containing enzymes and depending on the type of metal - active center, are classified in three different categories – 1) Copper and Zinc containing SOD (Cu, Zn – SOD), 2) Manganese or Iron containing SOD (Mn/Fe – SOD), and 3) Nickel containing SOD (Ni – SOD). The presence of metals in these enzymes also suggest the pattern of bioavailable metals before and after the Great Oxidation Event.<sup>1</sup> It is possible that prior to GOE, when earth's atmosphere was reducing, metals such as  $Fe^{2+}$ ,  $Mn^{2+}$  and  $Ni^{2+}$  were more soluble and bioavailable for cellular enzymatic processes than  $Cu^{2+}$  or  $Zn^{2+}$ , which might have existed as their insoluble sulfide salts. Brief encounters with low/negligible oxygen levels in atmosphere, in part, due to cyanobacterial photosynthesis, likely necessitated the need for SOD, and as iron was plentiful, it formed the first SOD (Fe-SOD) and hence is the most primitive of all SODs. Gradual rise of oxygen during or after GOE altered the bioavailability of metals, particularly, iron, that precipitated as Fe(III)-oxides (or rust), and that necessitated the evolution of other alternatives of Fe-SOD. Likewise, Mn – SOD, and Ni – SOD

came into play and are found in prokaryotes, particularly in cyanobacteria, and archaea.<sup>1</sup> Subsequently, high levels of oxygen in atmosphere diminished the bioavailable Mn and Ni being mostly present as their insoluble salts and Cu being more bioavailable as Cu<sup>2+</sup>.<sup>1</sup> Thus, Cu, Zn-SODs are the most recent forms of nature's antioxidant enzymes and are widespread in organisms including humans.<sup>1</sup>

Catalytic disproportionation of superoxide radical by SODs occurs via a two - step ping - pong mechanism (**Equation 7 - 8**) where the superoxide radical alternatively oxidizes and reduces the catalytic metal and produces O<sub>2</sub> and hydrogen peroxide. In the first step, the oxidized form of catalytic metal (M<sup>n+1</sup>) oxidizes superoxide radical to oxygen and is itself reduced to M<sup>n+</sup>. In the second step, another superoxide radical reduces the catalytic metal and generates peroxide, which is protonated by H<sup>+</sup>, which most likely, is provided by enzyme residues.



The reduction potentials (E°) for one electron reduction and oxidation of O<sub>2</sub><sup>•-</sup> are - 0.18 V and +0.91 V, respectively. So, for an optimum enzymatic turnover, the reduction potential of SOD enzymes should be near the average of the two half reactions (Equation 7 – 8). In fact, the four SODs do have E° that are close to this intermediate value: Fe - SOD (~ 0.22 V), Ni - SOD (0.29 V) Mn - SOD (0.3 V), and Cu, Zn – SOD (0.32 V for bovine and 0.36 V for humans).<sup>4</sup>

The spontaneous rate of O<sub>2</sub><sup>•-</sup> disproportionation is bimolecular and is dependent on the concentration of O<sub>2</sub><sup>•-</sup>, but in the presence of SOD, superoxide disproportionation is split into two half reactions with each being first order in O<sub>2</sub><sup>•-</sup>. SOD – catalyzed superoxide disproportionation

occurs at a rate which is close to the diffusion – controlled limit and varies little over the physiologically relevant pH range.

### 2.2.1 Nickel Superoxide Dismutase

Nickel Superoxide Dismutase (NiSOD) is the most recently discovered, and structurally the most distinct member of SOD family of enzymes and is found in cyanobacteria (*P. maritima*) and actinomycetes species such as *Streptomyces*.<sup>5-6</sup> The active site metal in this SOD is nickel, which performs the catalytic conversion of superoxide radical to oxygen and hydrogen peroxide.<sup>7-8</sup> While aqueous Cu (II), Fe (II) and Mn (II) can spontaneously disproportionate superoxide in solution, aqueous Ni (II) is inert towards such redox reaction,<sup>9</sup> and hence is a unique choice for redox disproportionation that is achieved by a unique protein ligand environment to stabilize the Ni(II)/Ni(III) redox process and give rise to SOD catalysis.<sup>1</sup> In order to perform both the half reactions in the superoxide disproportionation reaction, **(Equations 5 and 6)**, the redox potential of the active site metal should be ideally between the two half reactions, i.e., 0.36V.<sup>1</sup> Although, the redox potentials of both iron and copper do not allow for both half reactions, superoxide can be reduced to peroxide level even in absence of protein environment due to proton-coupled electron transfer.<sup>1</sup> On the other hand, while aqueous Mn(II) itself, owing to its high redox potential (1.51V vs NHE), cannot disproportionate superoxide in aqueous media, with proper mixture of N/O ligands, its redox potential is tuned to disproportionate superoxide in aqueous media.<sup>1</sup> Theoretical calculations estimate that the redox potential of nickel in aqueous media is 2.26V,<sup>10</sup> which is well above that of manganese also, and cannot be fine-tuned with only N/O ligands.<sup>1</sup> Instead, a mix of N/O - and S - ligands perfectly tune the redox potential of nickel for redox activity as observed in NiSOD, CO dehydrogenase and Ni,Fe-hydrogenases.<sup>1, 11</sup>



### 2.2.1.1 Enzyme Structure

Crystal structures of NiSOD obtained under a variety of conditions show that the enzyme is 88 - kDa homohexamer, with six 13.2 – kDa monomers (**Figure 2.1**).<sup>5, 12</sup> Each of the monomeric subunits is composed of antiparallel 4-helix bundles, with the nickel binding site at its N-terminus, protruding out of each of these  $\alpha$ -helical bundles.<sup>5, 12</sup> The homohexameric structure of apo-NiSOD and holo- NiSOD are essentially similar except for the N-terminus, which is disordered in absence of Ni.<sup>5</sup> The hexamer forms a hollow sphere with a 60 Å diameter and an interior void of 20 Å in diameter.<sup>5</sup> This architecture of NiSOD is distinct from other SODs, which are typically dimers or tetramers and predominantly have  $\beta$ -barrel folds (Cu, Zn – SOD) or a mix of both  $\alpha$ - and  $\beta$ -structure (Mn/Fe – SOD).<sup>1, 5</sup>

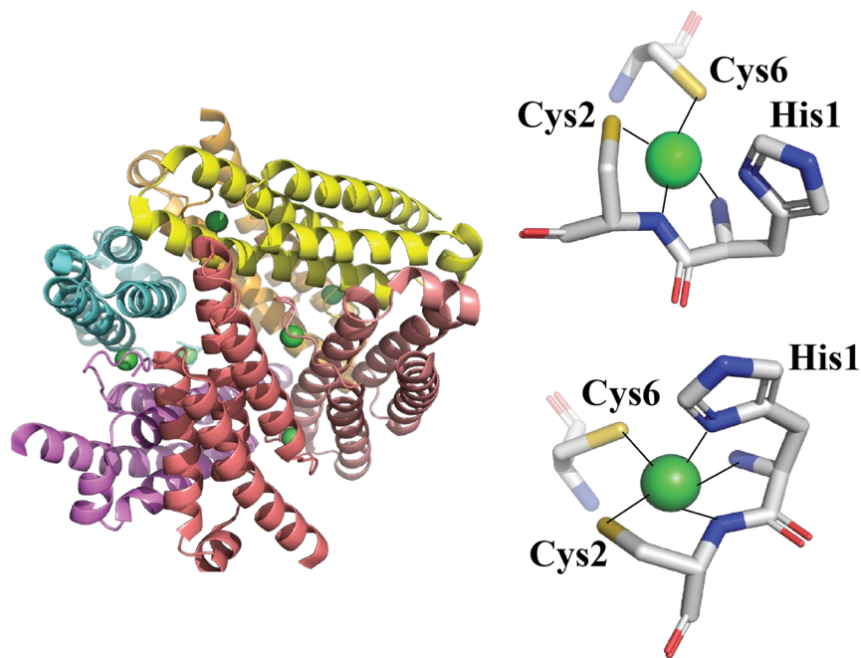


**Figure 2.1: Ribbon structure of hexameric NiSOD (left, PDB ID: 1T6U) and close-up view of the Ni-active site (right) in its reduced Ni(II) (top) and oxidized Ni(III) (bottom) states.**

### 2.2.1.2 Ni-active site structure

The N-terminus of apo – WT - NiSOD is disordered as revealed by crystal structures, but in the resting state of the active as - isolated WT - NiSOD, binding of nickel orders the N-terminus, and the nickel in the active site exists in two oxidation states – Ni(II) and Ni(III) in a 50 : 50 ratio as confirmed by electron paramagnetic resonance spectroscopy.<sup>5, 8, 12</sup> Reconstitution of WT - NiSOD with Ni(II)(H<sub>2</sub>O)<sub>6</sub> under an anoxic environment predominantly produces a Ni(II) active site.<sup>8</sup> Exposure of the anoxically reconstituted WT - NiSOD to air results in the formation of a 50% Ni(III) site suggesting a one electron oxidation of the nickel site in presence of air. However, what prevents the one electron oxidation of the rest (50% ) of the Ni(II) sites in the enzyme, and the basis for this apparent redox cooperativity is unknown. Furthermore, sodium dithionite (Na<sub>2</sub>S<sub>2</sub>O<sub>5</sub>) completely reduces Ni(III) - containing sites in the enzyme to a Ni(II) – site but attempts to increase Ni(III) by strongest oxidizing agents (potassium ferricyanide, iridium chloride) had minimal effect.<sup>5</sup>

The highly conserved N-terminal residues (**HCXXPCXXY**) form the ‘nickel – hook’ like motif at the N-terminus of the enzyme. The oxidation state of the nickel center determines the structure of the resting active site, with Ni(II) adopting a four – coordinate planar geometry or Ni(III) in five – coordinate geometry. The N-terminal amine (-NH<sub>2</sub>), backbone amidate (-NH) of Cys2, two thiolates (-SH) from Cys2 and Cys6 are nickel – ligands for both Ni(II) and Ni(III) in the enzyme, but an axial ε-N from imidazole of His1 is an additional ligand for the Ni(III) state, which is known to stabilize this oxidation state of the enzyme. Substitution of His1 to Ala results in a NiSOD variant (H1A – NiSOD) which is isolated with only Ni(II), but shows 6% activity as compared to WT-NiSOD and suggests that the oxidized state of Ni (i.e Ni(III)) is still accessible in this variant.<sup>13</sup> Kinetic studies of the oxidation of the as-isolated H1A-NiSOD variant enzyme

show the formation of a Ni(III)-like species that is unstable and rapidly decays.<sup>13</sup> Insertion of Ala or Met prior to His 1 (Ala0 - NiSOD or Met0 - NiSOD) extends the N-terminus of the enzyme by one amino acid and renders the enzyme inactive.<sup>5, 14</sup> Similarly, transforming the amidate ligand of the nickel – site to a secondary amine by native chemical ligation resulted in only 1% of the WT - NiSOD activity.<sup>15</sup> Mixed amine - amidate ligands from N-terminus and backbone amide of Cys2 are crucial to prevent the oxidation of the thiol residues (Cys 2 and Cys 6) to sulfinato or sulfenato species by peroxide.<sup>14</sup> The two thiol residues are important to the formation of the low spin nickel (II) – site, and substitution of either or both of these Cys residues to Ser produces a NiSOD variant which contains a high- spin Ni(II) site and is catalytically inactive.<sup>11</sup> Cys 2, particularly was also shown to be important for maintaining the hexameric structure of the enzyme.<sup>11</sup> Notably in WT-NiSOD, the two cysteine residues binding nickel are in cis-configuration, the relevance of which is unknown. Also, whether the mixed amine/amide ligands in NiSOD confer resistance to oxidation of both the Cys residue by superoxide is also unknown.

### ***2.2.1.3 Activity/Kinetics and Mechanism of SOD***

Like all SODs, redox titration established that Ni<sup>3+</sup>/Ni<sup>2+</sup> redox couple in WT - NiSOD has a reduction potential of approximately 290 mV, which is close to the optimum potential for catalytic disproportionation of superoxide radical.<sup>16</sup> The catalytic rate constant,  $k_{cat}$ , of WT - NiSOD for the disproportionation of pulse radiolytically generated superoxide radical is  $\approx 10^9$  M<sup>-1</sup>s<sup>-1</sup> per nickel site), which is similar to other SODs and the reaction is diffusion – limited and pH independent suggesting that protons for H<sub>2</sub>O<sub>2</sub> are provided by the protein residues.<sup>1, 8</sup> Azide and cyanide inhibit superoxide disproportionation by 50%.<sup>16</sup>

The exact mechanism of superoxide disproportionation by NiSOD is unclear and is still a matter of debate.<sup>1, 16</sup> Both inner- and outer- sphere mechanisms or a mixture of the two are possible for each of the two half reaction of superoxide catalysis.<sup>1</sup> Theoretical calculations agree in favor of an inner – sphere mechanism involving a Ni – O<sub>2</sub><sup>•-</sup> bond formation and is supported by the presence of an open coordination position on Ni<sup>3+</sup> - site, inhibition by other anions and electrostatic steering. However, unlike other SODs, as activity of NiSOD is independent of ionic strength, and the active site is more solvent – accessible, binding of superoxide to nickel is probably not important, and instead supports an outer – sphere mechanism. In fact, azide, a close mimic of superoxide radical, does not bind to nickel center directly, but makes electrostatic interactions with nearby residues in such a way that it causes small perturbations in the spectroscopic feature of nickel site.<sup>5</sup> Furthermore, crystallographic studies on mutant NiSOD (Y9F - NiSOD) show that Cl<sup>-</sup> and Br<sup>-</sup> bind at the same site modeled for azide binding , but not to the nickel center directly.<sup>16</sup> Also, Asp3 and Tyr9 were shown to cooperatively control the accessibility of anion radical such as, superoxide.<sup>16</sup>

#### **2.2.1.4 Assembly**

The active NiSOD enzymes (WT- or variants) for the above mentioned spectroscopic, crystallographic and functional studies were obtained by heterologous purification of *sodN* truncated at His15 and fused to either pelB sequence or a sequence with factor Xa cleavage site.<sup>5</sup> <sup>17</sup> Attempts to purify a construct with a Methionine (Met0) before the His1, failed to show SOD activity and highlighted the importance of free N-terminus of His1 in forming the active site of NiSOD.<sup>5</sup> NiSOD is a post-translationally modified product of *sodN* which encodes an inactive precursor with an extended N – terminal sequence (also called a leader sequence or signal peptide) upstream of nickel binding site.<sup>6, 17-18</sup> Although the functional relevance of this leader sequence is

elusive, its proteolytic processing at the invariant Ala- His peptide bond is crucial to the formation of the nickel - hook in active NiSOD.<sup>18</sup> In native organisms which produce NiSOD, the proteolytic processing of the leader sequence is performed by a putative cognate protease that lies upstream of *sodN* and is properly oriented for divergent transcription.<sup>6, 18</sup> While expression of either *sodN* or  $\Delta$ *sodN* failed to produce active NiSOD in cell lysates of *E. coli.*, heterologous co-expression of *sodN* and *sodX* from *Prochlorococcus maritima* showed NiSOD activity in a nickel - dependent manner, and highlighted a crucial role of SodX and nickel in the biosynthesis of active NiSOD, but its details remain largely unknown.<sup>6</sup>

One of the goals of this dissertation is to elucidate the biosynthetic mechanism of formation of active NiSOD from its precursor, SodN and its putative cognate protease, SodX and also identify the role of nickel in this process. Based on the previous *in vivo* and crystallographic studies, an interesting model for the formation of active NiSOD was proposed by Barondeau et. al.<sup>5</sup> According to this model, nickel binding and proteolysis by SodX is likely coupled.<sup>5</sup> A pre-active nickel site is first formed by binding nickel to His15 and Cys16 of the precursor, SodN, which also might serve as a SodX recognition motif and aids in specifically processing the leader sequence of SodN at the invariant Ala - His site.<sup>5</sup> Once processed, a cis - trans isomerization of Pro5 was also proposed to account for a conformational change that might lead to proper positioning of the two thiolates in cis configuration and, facilitate the binding of the remaining thiolate ligand from Cys6, thereby completing the formation of active nickel site.<sup>5</sup> However, an experimental verification of each of the proposed steps is lacking and requires further investigation.

A detailed investigation of the biosynthetic machinery for the formation of an active NiSOD might reveal unexpected insights into its maturation mechanism, such as a nickel-dependent proteolysis, similar to that required for maturation of Ni, Fe - hydrogenases.

Furthermore, this study will also advance the current repertoire of the biosynthesis of redox active nickel - dependent enzymes in nature.

### 2.2.2 Cu, Zn – Superoxide Dismutase<sup>1</sup>

Cu, Zn – SOD is found in bacterial periplasm, almost all eukaryotes (also known as SOD1) and its genes have also been identified in archaea. In bacteria, Cu, Zn - SOD can exist as a monomer or a dimer, but in eukaryotes, it exists exclusively as a 32 – kDa homodimer with each subunit containing a copper and zinc binding site in close proximity and intramolecular disulfide bond between two cysteine residues (Cys57 and Cys146, human Cu, Zn – SOD numbering) **(Figure 2.2)**.<sup>19-20</sup> Each subunit of Cu, Zn – SOD folds as an eight stranded Greek key  $\beta$ -barrel with seven connecting loops, of which loop IV and VII are functionally important zinc, and electrostatic loops, respectively. The Zn – loop contains all the Cys residues required for Zn – binding, while the electrostatic loop contains second sphere active site residues such as the catalytically important Arg143, which limits solvent access to metal binding sites, and acts as an active – site lid. The positive charge of Arg143 ensures the electrostatic steering of  $O_2^{\bullet-}$  to the active site. Neutralization of this charge by Arg143Ile mutation or charge reversal (Arg143Glu or Arg143Asp) led to a drop in the catalytic rates by 1-2 orders of magnitude.<sup>21-23</sup>

The oxidation state of copper in Cu, Zn – SOD determines the active site structure of the resting enzyme.<sup>1</sup> In the reduced state ( $Cu^+$ ), copper is bound to three histidine residues (His46, His48 and His120) in trigonal planar geometry and zinc is bound to three histidine (His63, His71, His80) and one aspartate residue (Asp83) in a tetrahedral geometry.<sup>24</sup> Upon oxidation, the copper active site structure adopts a five - coordinate distorted pyramidal structure where  $Cu^{2+}$  binds an

additional water molecule and an imidazole from His63 that bridges copper and zinc, and the zinc site remains unchanged.<sup>24</sup>

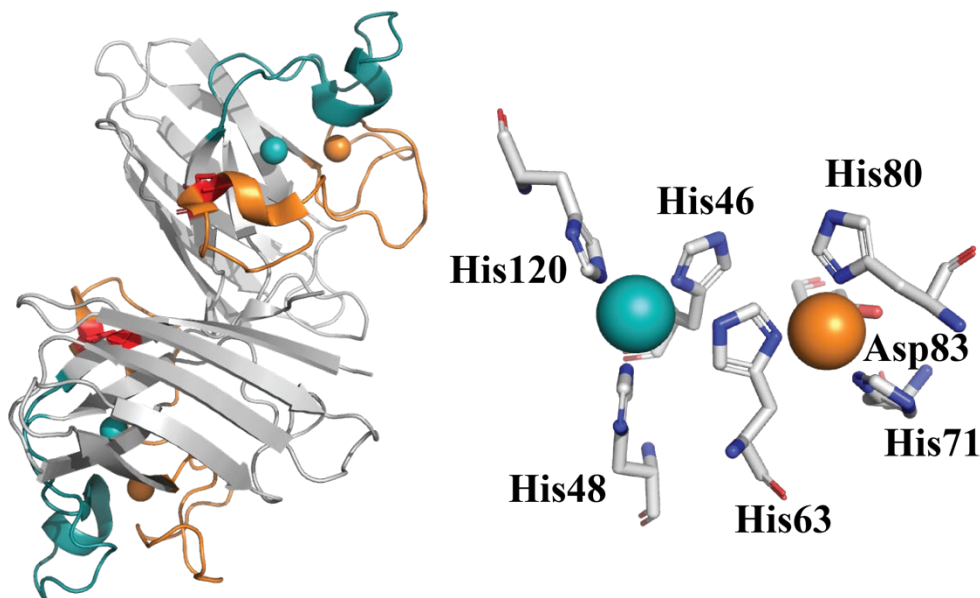


**Figure 2.2: Ribbon structure of dimeric human SOD1 (left, PDB ID: 1PU0) and close-up view of the reduced Cu<sup>I</sup>, Zn-active site (right). Copper and Zinc are shown as teal and orange sphere, respectively. Zinc-loop is shown in orange and the electrostatic loop is shown in teal. The intrasubunit disulfide bond is shown in red.**

### 2.2.3 Fe/Mn – Superoxide Dismutase

Fe - SOD is believed to be the most primitive among all SODs and is found in all domains of life (bacteria, archaea and eukaryotes).<sup>1</sup> Crystal structures of Fe - SOD show that each of its monomer is a mixture of  $\beta$  - sheets and  $\alpha$  - helices and contains a Fe - active site, which is coordinated to N/O-donor ligands in a trigonal bipyramidal geometry (**Figure 2.3**).<sup>1,25</sup> His 73, His 160 and Asp156 (*E. coli* Fe-SOD numbering) form the equatorial ligands, and slow – exchanging H<sub>2</sub>O/OH<sup>-</sup> and His 26 form the axial ligands to the resting Fe<sup>3+</sup> - SOD active site.<sup>25-26</sup> Superoxide

disproportionation in Fe - SOD occurs via a mix of inner sphere and outer -sphere mechanisms:  $O_2^{\bullet-}$  radical first binds to  $Fe^{3+}$ - SOD, and reduces it to  $Fe^{2+}$  - SOD, leading to the formation of  $O_2$ , which is released. Subsequently, Tyr34 and Gln69 facilitate the outer sphere coordination of another superoxide radical to  $Fe^{2+}$ - SOD, oxidizing  $Fe^{2+}$ - SOD to  $Fe^{3+}$ - SOD, and forming peroxide  $O_2^{2-}$ . The axial  $H_2O$  ligand of the active – site provides the first proton for the peroxide anion generating a hydroperoxide, which is further protonated by hydroxyl of Tyr34 and forms the hydrogen peroxide that is released from the site.<sup>1</sup>

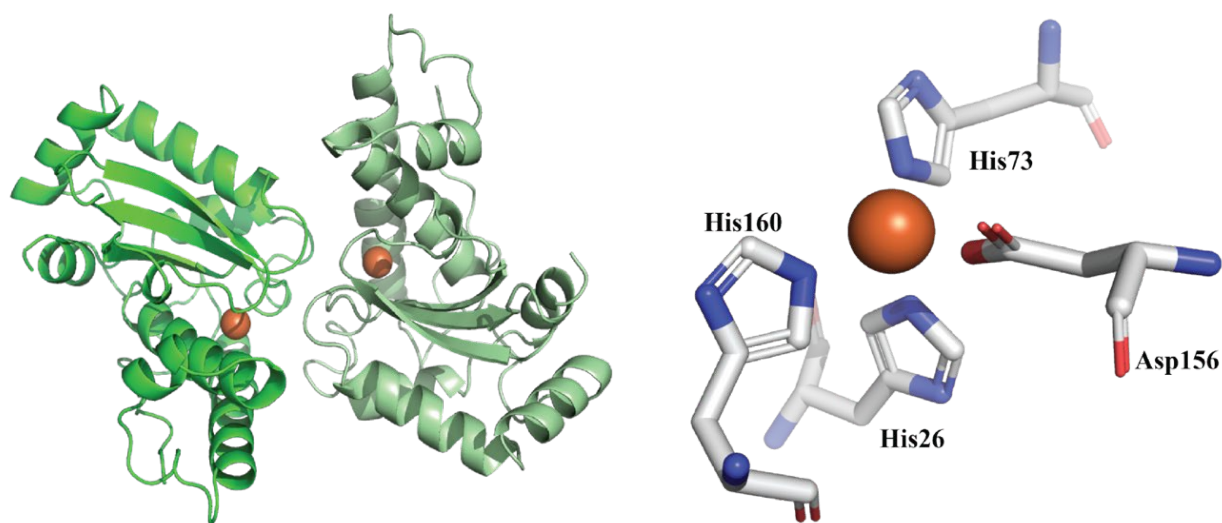


**Figure 2.3: Ribbon structure of *E. coli* FeSOD (left, PDB ID: 1ISB) and close-up view of the Fe-active site (right).**

Mn - SOD can be subdivided into two groups: the cambialistic Fe/Mn – SOD in which substitution of either Fe with Mn or vice versa does not affect SOD activity, and exclusively Mn - SODs, which despite structural similarity to Fe-SOD is highly Mn - specific.<sup>1, 27</sup> The latter is prevalent in eukaryotic mitochondrion and has a distinct amino acid sequence from the bacterial/archeal Mn – SOD.<sup>1</sup> Eukaryotic Mn - SOD is tetrameric, and bacterial Mn - SOD is



dimeric (**Figure 2.4**).<sup>28</sup> The active site structure of Mn – SOD is the same as that of Fe – SOD, with three histidines, one aspartate, and a water or hydroxyl ligand are arranged in distorted trigonal bipyramidal geometry.<sup>1</sup> Most Mn – SODs are isolated as Mn<sup>3+</sup> - SODs, but the fungal MnSODs are isolated as the reduced form (Mn<sup>2+</sup> - SOD).<sup>1</sup> The active site Mn in Mn-SOD is protected from the solvent by several important residues that are hydrogen – bonded to each other, and electrostatic guidance draws the superoxide radical to the enzyme active site for one electron – two proton catalysis to produce hydrogen peroxide.<sup>1</sup> Hydrogen - bonded secondary sphere residues (Tyr34, His30) and particularly Gln 146 (or Gln 143 in humans) play an important role in the structure and activity of MnSODs.<sup>1</sup>

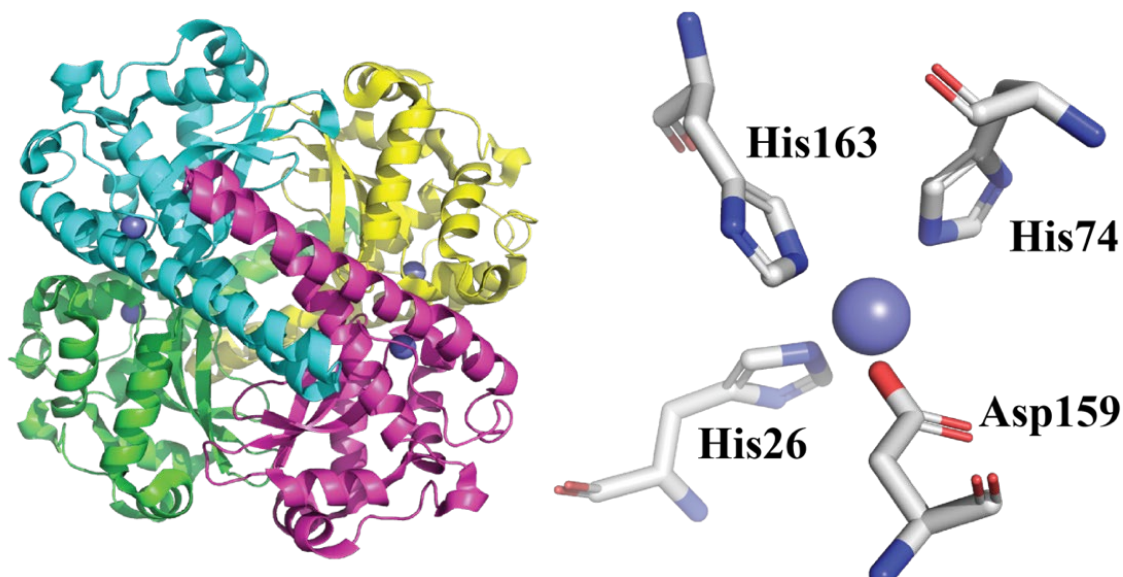


**Figure 2.4: Ribbon structure of *E. coli* MnSOD (left, PDB ID: 1LUV) and close-up view of the Mn-active site (right).**

It is interesting to note that despite structural and active site similarity, MnSODs are able to specifically acquire manganese in presence of large concentration of iron in cells, the basis of which is largely unknown.<sup>1</sup> Besides, the acquisition of manganese by MnSOD *in vivo* is also not clear. In eukaryotes, MnSOD is found in mitochondria and inevitably, manganese must be

transported to this organelle for metal acquisition by apo – Mn- SOD. There are several genes (Smfp1 and Smfp2) that are identified as the manganese transporters,<sup>29</sup> and deletion of these genes led to the loss of MnSOD activity.<sup>30</sup> However, the gene knockouts did not entirely deplete the cells of manganese suggesting the existence of alternative transporters for manganese trafficking.<sup>30</sup>

*In vitro* maturation studies of MnSOD from *E. coli* and *Thermus thermophilus* show that metalation of apo – MnSOD by manganese is ‘thermally – gated’ and occurs at elevated temperatures, due to destabilization of the protein that allows the non – specific metal incorporation.<sup>31-32</sup>

## 2.3 References

1. Sheng, Y.; Abreu, I. A.; Cabelli, D. E.; Maroney, M. J.; Miller, A. F.; Teixeira, M.; Valentine, J. S., Superoxide dismutases and superoxide reductases. *Chem. Rev.* **2014**, *114* (7), 3854-3918.
2. Raymond, J.; Segre, D., The effect of oxygen on biochemical networks and the evolution of complex life. *Science* **2006**, *311* (5768), 1764-1767.
3. Bielski, B. H. J.; Allen, A. O., Mechanism of the disproportionation of superoxide radicals. *J Phys. Chem.* **1977**, *81* (11), 1048-1050.
4. Grove, L. E.; Xie, J.; Yikilmaz, E.; Miller, A. F.; Brunold, T. C., Spectroscopic and computational investigation of second-sphere contributions to redox tuning in Escherichia coli iron superoxide dismutase. *Inorg. Chem.* **2008**, *47* (10), 3978-3992.
5. Barondeau, D. P.; Kassmann, C. J.; Bruns, C. K.; Tainer, J. A.; Getzoff, E. D., Nickel superoxide dismutase structure and mechanism. *Biochemistry* **2004**, *43* (25), 8038-8047.
6. Eitinger, T., In vivo production of active nickel superoxide dismutase from Prochlorococcus marinus MIT9313 is dependent on its cognate peptidase. *J. Bacteriol.* **2004**, *186* (22), 7821-7825.
7. Youn, H. D.; Kim, E. J.; Roe, J. H.; Hah, Y. C.; Kang, S. O., A novel nickel-containing superoxide dismutase from Streptomyces spp. *Biochem. J.* **1996**, *318* ( Pt 3), 889-896.
8. Choudhury, S. B.; Lee, J. W.; Davidson, G.; Yim, Y. I.; Bose, K.; Sharma, M. L.; Kang, S. O.; Cabelli, D. E.; Maroney, M. J., Examination of the nickel site structure and reaction mechanism in Streptomyces seoulensis superoxide dismutase. *Biochemistry* **1999**, *38* (12), 3744-3752.
9. Bielski, B. H. J.; Cabelli, D. E.; Arudi, R. L.; Ross, A. B., Reactivity of HO<sub>2</sub>/O<sup>-2</sup> Radicals in Aqueous Solution. *J. Physical and Chemical Reference Data* **1985**, *14* (4), 1041-1100.

10. Zilbermann, I.; Maimon, E.; Cohen, H.; Meyerstein, D., Redox chemistry of nickel complexes in aqueous solutions. *Chem. Rev.* **2005**, *105* (6), 2609-2625.
11. Ryan, K. C.; Johnson, O. E.; Cabelli, D. E.; Brunold, T. C.; Maroney, M. J., Nickel superoxide dismutase: structural and functional roles of Cys2 and Cys6. *J. Biol. Inorg. Chem.* **2010**, *15* (5), 795-807.
12. Wuerges, J.; Lee, J. W.; Yim, Y. I.; Yim, H. S.; Kang, S. O.; Djinovic Carugo, K., Crystal structure of nickel-containing superoxide dismutase reveals another type of active site. *Proc. Natl. Acad. Sci. U. S. A.* **2004**, *101* (23), 8569-8574.
13. Ryan, K. C.; Guce, A. I.; Johnson, O. E.; Brunold, T. C.; Cabelli, D. E.; Garman, S. C.; Maroney, M. J., Nickel superoxide dismutase: structural and functional roles of His1 and its H-bonding network. *Biochemistry* **2015**, *54* (4), 1016-1027.
14. Huang, H. T.; Dillon, S.; Ryan, K. C.; Campecino, J. O.; Watkins, O. E.; Cabelli, D. E.; Brunold, T. C.; Maroney, M. J., The Role of Mixed Amine/Amide Ligation in Nickel Superoxide Dismutase. *Inorg. Chem.* **2018**, *57* (20), 12521-12535.
15. Campecino, J. O.; Dudycz, L. W.; Tumelty, D.; Berg, V.; Cabelli, D. E.; Maroney, M. J., A Semisynthetic Strategy Leads to Alteration of the Backbone Amidate Ligand in the NiSOD Active Site. *J. Am. Chem. Soc.* **2015**, *137* (28), 9044-9052.
16. Herbst, R. W.; Guce, A.; Bryngelson, P. A.; Higgins, K. A.; Ryan, K. C.; Cabelli, D. E.; Garman, S. C.; Maroney, M. J., Role of conserved tyrosine residues in NiSOD catalysis: a case of convergent evolution. *Biochemistry* **2009**, *48* (15), 3354-3369.
17. Bryngelson, P. A.; Arobo, S. E.; Pinkham, J. L.; Cabelli, D. E.; Maroney, M. J., Expression, reconstitution, and mutation of recombinant *Streptomycescoelicolor* NiSOD. *J. Am. Chem. Soc.* **2004**, *126* (2), 460-461.

18. Kim, E. J.; Chung, H. J.; Suh, B.; Hah, Y. C.; Roe, J. H., Transcriptional and post-transcriptional regulation by nickel of sodN gene encoding nickel-containing superoxide dismutase from *Streptomyces coelicolor* Muller. *Mol. Microbiol.* **1998**, *27* (1), 187-195.
19. Valentine, J. S.; Doucette, P. A.; Zittin Potter, S., Copper-zinc superoxide dismutase and amyotrophic lateral sclerosis. *Annu. Rev. Biochem.* **2005**, *74*, 563-593.
20. Perry, J. J.; Shin, D. S.; Getzoff, E. D.; Tainer, J. A., The structural biochemistry of the superoxide dismutases. *Biochim. Biophys. Acta* **2010**, *1804* (2), 245-262.
21. Borders, C. L., Jr.; Johansen, J. T., Identification of Arg-143 as the essential arginyl residue in yeast Cu,Zn superoxide dismutase by use of a chromophoric arginine reagent. *Biochem. Biophys. Res. Commun.* **1980**, *96* (3), 1071-1078.
22. Fisher, C. L.; Cabelli, D. E.; Tainer, J. A.; Hallewell, R. A.; Getzoff, E. D., The role of arginine 143 in the electrostatics and mechanism of Cu,Zn superoxide dismutase: computational and experimental evaluation by mutational analysis. *Proteins* **1994**, *19* (1), 24-34.
23. Cudd, A.; Fridovich, I., Electrostatic interactions in the reaction mechanism of bovine erythrocyte superoxide dismutase. *J. Biol. Chem.* **1982**, *257* (19), 11443-11447.
24. Hart, P. J.; Balbirnie, M. M.; Ogihara, N. L.; Nersissian, A. M.; Weiss, M. S.; Valentine, J. S.; Eisenberg, D., A structure-based mechanism for copper-zinc superoxide dismutase. *Biochemistry* **1999**, *38* (7), 2167-2178.
25. Lah, M. S.; Dixon, M. M.; Patridge, K. A.; Stallings, W. C.; Fee, J. A.; Ludwig, M. L., Structure-function in *Escherichia coli* iron superoxide dismutase: comparisons with the manganese enzyme from *Thermus thermophilus*. *Biochemistry* **1995**, *34* (5), 1646-1660.

26. Dooley, D. M.; Jones, T. F.; Karas, J. L.; McGuirl, M. A.; Brown, R. D.; Koenig, S. H., Azide and fluoride binding to E. coli iron superoxide dismutase as studied by solvent proton magnetic relaxation dispersion. *J. Am. Chem. Soc.* **1987**, *109* (3), 721-725.
27. Abreu, I. A.; Cabelli, D. E., Superoxide dismutases-a review of the metal-associated mechanistic variations. *Biochim. Biophys. Acta* **2010**, *1804* (2), 263-274.
28. Hunter, G. J.; Trinh, C. H.; Bonetta, R.; Stewart, E. E.; Cabelli, D. E.; Hunter, T., The structure of the Caenorhabditis elegans manganese superoxide dismutase MnSOD-3-azide complex. *Protein Sci.* **2015**, *24* (11), 1777-1788.
29. Culotta, V. C.; Yang, M.; Hall, M. D., Manganese transport and trafficking: lessons learned from Saccharomyces cerevisiae. *Eukaryot Cell* **2005**, *4* (7), 1159-1165.
30. Luk, E.; Carroll, M.; Baker, M.; Culotta, V. C., Manganese activation of superoxide dismutase 2 in Saccharomyces cerevisiae requires MTM1, a member of the mitochondrial carrier family. *Proc. Natl. Acad. Sci. U. S.A* **2003**, *100* (18), 10353-10357.
31. Whittaker, M. M.; Whittaker, J. W., Thermally triggered metal binding by recombinant Thermus thermophilus manganese superoxide dismutase, expressed as the apo-enzyme. *J. Biol. Chem.* **1999**, *274* (49), 34751-34757.
32. Whittaker, M. M.; Lerch, T. F.; Kirillova, O.; Chapman, M. S.; Whittaker, J. W., Subunit dissociation and metal binding by Escherichia coli apo-manganese superoxide dismutase. *Arch. Biochem. Biophys.* **2011**, *505* (2), 213-225.

## CHAPTER 3

### *IN VITRO* MATURATION OF NISOD REVEALS A ROLE FOR CYTOPLASMIC LIGANDS IN PROCESSING AND METALLATION

#### 3.1 Introduction

Nickel Superoxide Dismutase (NiSOD), the nickel-specific member of the superoxide dismutase family of enzymes, catalyzes the disproportionation of toxic superoxide radical to oxygen and hydrogen peroxide.<sup>1-2</sup> So far, NiSOD is found in actinobacteria (*e.g.*, *Streptomyces sp.*) and cyanobacteria (*e.g.* *Prochlorococcus sp.*) and it has been shown to express in response to Ni(II) in *Streptomyces lividans*.<sup>3-4</sup> The active site in NiSOD resides at the protein N-terminus and compared to other SOD active sites, employs a unique mix of N- and S-donor ligands to create a redox-active Ni(II)/Ni(III) center that is required for catalysis. The N-terminal amine from His1, the amidate N of Cys2, and the side chains of Cys2 and Cys6 constitute nickel ligands in both oxidation states,<sup>1-2, 5-7</sup> and coordination of the imidazole from His1 is found in the Ni(III) state (Figure 3.1).<sup>1, 6</sup>

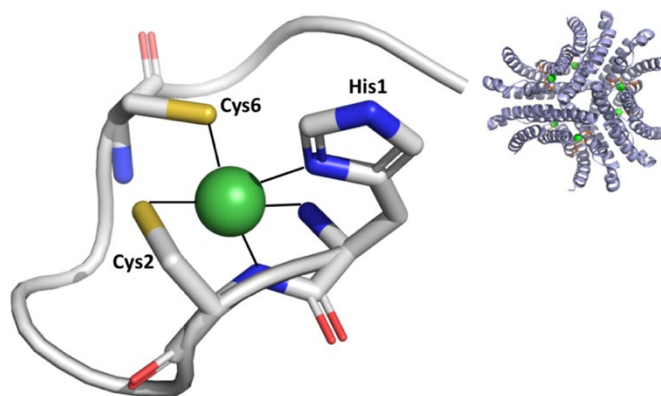


**Figure 3.1:** The nickel active site in NiSOD (PDB ID: 1T6U). The inset shows the hexameric enzyme. Green sphere represents nickel.

Although the structural, spectroscopic and enzymatic properties of NiSOD are well characterized,<sup>8-9</sup> the maturation of this enzyme is elusive and is predicted to be a nickel-dependent process,<sup>10-11</sup> with potential similarities to the process of Ni, Fe-hydrogenase maturation that catalyzes the reversible oxidation of molecular hydrogen.<sup>12-13</sup> In Ni, Fe-hydrogenases, there are two subunits – a large subunit that accommodates the hetero-bimetallic active site with nickel and iron cofactors, and a smaller subunit that contains the Fe-S clusters.<sup>12, 14</sup> Maturation of Ni, Fe-hydrogenases requires sequential insertion of the metal cofactors (iron followed by nickel) by their respective metallo-chaperones in the pre-active site of the large subunit (HydB) which is expressed as a precursor protein with an extension at its C-terminus.<sup>13</sup> Proper insertion of metal co-factors in the pro-enzyme provides the necessary recognition motif for the cognate protease (HycI or HybD), which then cleaves the C-terminal extension resulting in a conformational change of the cofactor-loaded large subunit (HydB) that ensures proper docking of the small-subunit, thereby completing the maturation process.<sup>13-16</sup>

WT-NiSODs are products of *sodN* genes, which encode an inactive pro-enzyme (SodN), transcription of which in native organisms is regulated by nickel (facultative expression).<sup>10, 17</sup> Similar to Ni, Fe- hydrogenase, maturation of NiSOD also requires post-translational modification of SodN.<sup>10</sup> SodN has a variable N-terminal leader sequence that in *S. coelicolor* features 14 amino acids upstream of the His15 residue (which becomes the first amino acid and the N-terminus of the mature NiSOD), the functional role of which is still unknown.<sup>10</sup> In the native organism, SodN produces active NiSOD in presence of nickel, but heterologous expression of SodN in *E.coli*, fails to produce active NiSOD in presence of nickel. However, expression of  $\Delta$ *sodN* (a modified construct of SodN where the first 14 residues are truncated) in *E.Coli*, produces active NiSOD in presence of nickel suggesting that proteolysis of the SodN leader peptides immediately prior to the



conserved His15 residue is an absolute requirement for active WT-NiSOD formation, and native organisms but not *E.coli* have the necessary proteolytic machinery for proper processing of the precursor.<sup>10, 17</sup> This led to the development of SodN constructs with factor-Xa or pelB cleavage sites to effect N-terminal cleavage of recombinant SodN *in vitro*.<sup>1, 17</sup> Following N-terminal cleavage, the resulting recombinant apo-NiSOD was readily nickelated by Ni(II) salts in solution, suggesting that no nickel metallochaperone is required, and no metallochaperone for NiSOD maturation has yet been characterized. In an attempt to identify accessory proteins involved in maturation of NiSOD, one study demonstrated that in *S. seoulenesis*, overexpression of a metal-binding protein CbiX-hp, which is homologous (87%) to its cobaltochelate protein (CbiX) increased the expression and activity of NiSOD, but its deletion did not abolish NiSOD activity.<sup>18</sup>

The identification of the putative cognate protease involved in native N-terminal processing of NiSODs (SodX) was achieved by co-expression of *P. marinus* *sodN* and *sodX* in *E.coli*, which resulted in production of active NiSOD *in vivo*.<sup>11</sup> The lack of a specific nickel metallochaperone in this study also supports the notion that none is involved in nickelation of apo-NiSOD. In-gel SOD activity assays performed on the *E. coli* cell lysates showed increasing NiSOD activity as a function of Ni(II) concentration.<sup>11</sup> Later, a nickel-dependent proteolytic model for the maturation of NiSOD was proposed based on the aforementioned *in vivo* studies,<sup>10-11</sup> structural studies of Met0 (insertion of a Met residue before His1 in the recombinant construct of apo-NiSOD) and CN-treated apo-NiSOD,<sup>1</sup> and by analogy with the maturation of Ni, Fe-hydrogenase, which requires nickel insertion prior to proteolysis of the large subunit,<sup>12-13</sup> a nickel-dependent model for the maturation of NiSOD was proposed.<sup>1</sup> It was postulated that chelation of Ni(II) by His15 and Cys16 in SodN (becomes His1 and Cys2 in NiSOD) promotes proteolytic maturation followed by a trans-cis isomerization of Pro5, (or Pro19 in SodN ) that positions Cys6 in such a

way that the two thiols (Cys2 and Cys6) can bind nickel in a cis-orientation, thereby completing the nickel site coordination and forming the ‘nickel-hook’ feature of the mature enzyme.<sup>1</sup>

One of the objectives of this research is to examine and elucidate the steps involved in *in vitro* processing, nickel incorporation, and ‘Ni-hook’ formation in purified recombinant SodN proteins using recombinant SodX from *S. coelicolor* for N-terminal processing resulting in the formation of active NiSOD. The role of Pro19 in the proteolytic reaction and formation of Ni-hook was also analyzed using the variant P19ASodN.

## **3.2 Experimental Methods**

### **3.2.1 Cloning, Protein Expression, and Purification**

The *sodN* gene from *S. coelicolor* in the pET3a plasmid carrying a resistance gene for ampicillin for selection was generously provided by J. H. Roe from Seoul National University. The pET3a-SodN plasmid was used to transform BL21(DE3) plysS cells carrying a resistance gene for chloramphenicol. The transformed cells were grown in 0.5 mL Luria Bertini (LB) media in 5 ml tubes at 37°C for 1 hour and aliquots were plated on agar plates containing the chloramphenicol and ampicillin antibiotics. A single colony was picked and grown overnight in LB media (200 mL) supplemented with chloramphenicol and ampicillin at 37°C with shaking at 200 rpm. A 10 mL aliquot of the overnight culture was added to 1 L of the pre-warmed fresh LB media, grown to an OD<sub>600</sub> of 0.6-0.8, and then induced by addition of a solution of isopropyl – β-D-1-thiogalactopyranoside to a final concentration of 0.8mM, followed by incubation for 3-4 hours at 37°C. Cells were harvested by centrifugation at 8000 rpm for 15 min and frozen at -80°C.

The harvested cells were thawed at 37°C and re-suspended in Buffer A (50 mM Tris, 1 mM TCEP, pH 8.8). DNase I solution (100 μL of 10 mg/ml DNase, 10 mM MgCl<sub>2</sub>, 20mM Tris, pH

7.5 and 40% glycerol), and 380  $\mu$ L of 0.2 M PMSF were added and the mixture incubated at 37°C until the viscosity of the solution was sufficiently reduced. The cells were then sonicated using SONICS (Vibracell) using 3 s pulses at 40 % power with a 12 s interval to further lyse the cells. Lysed cells were centrifuged at 10,000 rpm for 45 minutes at 4°C, and the clear supernatant was used for protein purification.

All chromatographic purification steps were carried out using AKTA-FPLC system (Amersham Biosciences). The supernatant was loaded onto a pre-equilibrated Q-Sepharose column (GE Health Sciences) at a rate of 2.00 ml/min with buffer A. Once the absorbance returned to baseline value, the protein was eluted with a linear gradient of Buffer B (50 mM Tris, 1 mM TCEP, 1 M NaCl, pH 8.8). All the fractions containing protein was collected and analyzed using SDS-PAGE. Fractions containing SodN (MW 14,702 kDa) were pooled and buffer-exchanged against Buffer C (50mM HEPES, 1mM TCEP, pH 7.0) using a PD-10 column (GE Healthcare) and loaded on a pre-equilibrated SP-Sepharose column at a rate of 2.00 ml/min. The column was washed with five column volumes of Buffer C, and protein was eluted with Buffer C containing 1 M NaCl. The purity of collected protein fractions were analyzed by SDS-PAGE and the fractions containing SodN were pooled and concentrated. Protein concentrations were determined using the absorbance at 280 nm and a theoretical extinction coefficient of 17,085  $M^{-1}cm^{-1}$  obtained from web-based ExPASy Protein Parameters tool. EDTA (up to a final concentration of 1 mM) and 10 % glycerol were added to the concentrated protein stock, which was stored frozen at -20°C until needed.

The *sodX* gene from genomic DNA of *S. coelicolor* (obtained from Wellcome Sanger Institute, United Kingdom) was amplified using PCR with forward and reverse primers (**Table 3.1**). The purified PCR product was obtained from a 1% agarose gel and digested with BspEI and

XhoI to create overhangs complementary to the pET23bSUMO vector. The insert was ligated to pET23bSUMO vector using Quick Ligase (New England Biolabs) and the ligated DNA was used to transform GC10 cells, which were then plated on LB-agar media containing 100 mg/ml ampicillin for selection, and incubated overnight at 37°C. Single colonies were picked and grown overnight in 2 mL LB-Amp media at 37°C and the pET23bSUMO-SodX plasmid was then extracted using a Thermo Scientific miniprep Kit. The plasmid was further digested using XmaI, AvaI, BstII, NheI, and ApaI to confirm the insertion of *sodX* at the correct position of the vector. The gene sequence was confirmed by DNA sequencing (IDT, Inc.).

The pET23bSUMO-SodX plasmid containing chloramphenicol and ampicillin resistance genes for selection was used to transform BL21(DE3) plysS cells. A single colony was picked and grown overnight in LB media supplemented with both antibiotics at 37°C with shaking at 200 rpm. A 10 mL aliquot of the overnight culture was added to per litre of the pre-warmed fresh LB media, and then grown to an OD<sub>600</sub> of 0.6-0.8, followed by induction with 0.95 mM of isopropyl – β-D-1-thiogalactopyranoside and incubation for 3 hours at 37°C. Cells were harvested by centrifugation at 8000 rpm for 15 min and frozen at -80 °C. However, this construct exhibited several purification problems and hence *sodX* was sub-cloned into the pET22b vector as follows.

The *sodX* gene from M108 forward was cloned out of the pET23bSUMO plasmid using PCR amplification with forward and reverse primers (**Table 3.1**). The purified PCR product was obtained from an 0.8% agarose gel. The product was digested with NdeI and XhoI to create overhangs complementary to the pET22b vector. The insert was ligated to the pET22b vector using ligase, and DH5α *E. coli* cells were transformed with the pET22b vector containing the SodX gene (pET22b/SodX). The DH5α cells were grown in 0.5 mL LB media at 37 °C for 1 hour and aliquots of the culture were plated on LB media containing 100 mg/ml of ampicillin and incubated

overnight at 37°C. Single colonies were picked and grown overnight in 5 mL LB-Amp media at 37°C for pET22b-SodX plasmid extraction using the GeneJET plasmid miniprep Kit (Thermo Fisher). The gene sequence was confirmed by Genewiz, Inc. (**Appendix A, Figure A.1**). The pET22b-SodX plasmid was then used to transform BL21 (DE3) plysS cells. The transformed cells were grown in 0.5 mL LB media in 5 ml tubes at 37 °C for 1 hour and aliquots were plated on agar plates containing the chloramphenicol and ampicillin antibiotics. A 10 mL aliquot of the overnight culture was added to per litre of the pre-warmed fresh LB media, grown to an OD<sub>600</sub> of 0.6-0.8 and then induced with 0.95 mM of isopropyl –  $\beta$ -D-1-thiogalactopyranoside for 3 hours at 37°C. Cells were harvested by centrifugation at 8000 rpm for 15 min and frozen at -80°C for storage.

The harvested cells were thawed at 37 °C and re-suspended in Buffer A (50 mM HEPES, pH 8.5). 100  $\mu$ L of DNase I solution (containing 10 mg/ml DNase, 10 mM MgCl<sub>2</sub>, 20 mM Tris, pH 7.5 and 40 % glycerol) was added and the mixture was incubated at 37°C until the viscosity of the solution was sufficiently reduced. The cells were then sonicated with SONICS (Vibracell) using 3s pulses at 40 % power with a 12s interval to further lyse the cells. Lysed cells were then centrifuged at 10,000 rpm for 45 minutes at 4°C and the supernatant was filtered using a 0.22  $\mu$ M syringe filter. The clear filtrate was used for protein purification.

All chromatographic purification steps were carried out using AKTA-FPLC system (Amersham Biosciences). The filtrate was loaded onto an SP-Sepharose column (GE Health Sciences) at a rate of 3.00 ml/min with buffer A. Once the absorbance returned to baseline value, the protein was eluted with a linear gradient of Buffer B (50 mM HEPES, 1 M NaCl, pH 8.5). All the fractions containing protein were collected and analyzed using SDS-PAGE. Fractions containing pure SodX (MW 16,157 Da) were pooled, and the protein concentration was determined using its theoretical molar extinction coefficient value of 24,960 M<sup>-1</sup> cm<sup>-1</sup> determined

using web-based ExPASy Protein Parameters tool. Portions (200  $\mu$ l) of the 0.15 mM purified protein solution were aliquoted and frozen at -20  $^{\circ}$ C until used for experiments.

### 3.2.2 Mutagenesis

Site-directed mutagenesis was used to introduce Ala substitutions at His15 and Pro19 of SodN. The pET3a vector encoding wild - type *sodN* sequence from *S. coelicolor* and carrying an ampicillin-resistance gene was used as the template DNA for the single point mutations using polymerase chain reaction (PCR) and PCR primers (listed in **Table 3.1**) were designed to incorporate the desired mutations. For each 50  $\mu$ L volume of PCR reaction mixture, 0.5  $\mu$ M (25 picomoles) of each primer was used for 2 ng of template DNA. Successful PCR amplifications were determined using 0.8% agarose gel and the amplicons were subsequently digested with DpnI for 1 hr at 37 $^{\circ}$ C to remove any methylated template DNA. The digested PCR mixture was then used to transform DH5 $\alpha$  competent cells carrying no resistance gene for selection, and the cells were plated on LB-agar media supplemented with 100 mg/mL ampicillin (Fisher Scientific), followed by incubation at 37  $^{\circ}$ C for 12-16 hours. Single colonies from the plates were grown to saturation in 5ml LB-miller broth supplemented with ampicillin at 37  $^{\circ}$ C. Cells were pelleted at 13,000 g for 5 minutes and the plasmids were isolated using GeneJET plasmid miniprep kit (Thermo Fisher Scientific). Gene sequencing (Genewiz, Inc.) confirmed the successful mutations. The protein expression for these variants was found similar to that of WT-SodN and these proteins were purified as described for WT-SodN.

Site-directed mutagenesis was used to introduce Ala substitutions at Ser28 of SodX. pET 22b (+) vector encoding wild-type *sodX* sequence from *S.coelicolor* and carrying an ampicillin-resistance gene was used as the template DNA for the single point mutations using polymerase chain reaction (PCR) and PCR primers (listed in **Table 3.1**) were designed to incorporate the

desired mutations. Ser28ASodX plasmid was obtained using the PCR protocol for His15ASodN as described above. Gene sequencing (Genewiz, Inc.) confirmed the successful mutations. The protein expression for S28A-SodX was found similar to WT-SodX, and the overexpressed protein was purified similarly to WT-SodX.

**Table 3.1: Oligonucleotides used for obtaining plasmids in this study.\***

Plasmid	Template	Forward Primer (5'→3')	Reverse Primer (5'→3')
<b>pET3a-H15AsodN</b>	pET3a-WT <i>sodN</i>	AGCGCC <u>GCAT</u> TGCG	CAGGTCGCAT <u>G</u>
		ACCTG	<u>C</u> GGCGCT
		TAATTCGGAGGT	TAATCTCGAGC
<b>pET23bSUMO</b>	Genomic <i>ScsodX</i>	GTGATGCCGGAGC	TACCGCGCTCG
<b>WT<i>sodX-1</i></b>		AACTGTCGCAGGA	CAAGCGCCTGG
		GACCGA	AGGCGGAC
		TAAGGACAT <u>ATGA</u>	TAATCTCGAG <u>C</u>
<b>pET22b (+)</b>	pET23bSUMO	TGCCGGAGCAAC	<u>T</u> ACCGCGCTCG
<b>WT<i>sodX-2</i></b>	WT <i>sodX-1</i>		C
<b>pET22b (+)</b>	pET22b (+)	GCCGG <u>CTAT</u> GGTG	ACCAT <u>AGCC</u> GG
<b>S28A<i>sodX</i></b>	WT <i>sodX-2</i>	CCCAC	CCC <u>GGTC</u>

\*Mutagenic bases are underlined

### 3.2.3 Mass Spectrometry for Protein Characterization

Molecular weights of all purified proteins were determined using LC-MS, where the purified protein samples were passed through a C-8 BioBasic column (Thermo Scientific) that was pre-equilibrated with solution A (0.1% formic acid in water). The protein samples were eluted

using 95% solution B (0.1% formic acid in acetonitrile) and injected into an AB Sciex QStar XL ESI-Q- TOF mass spectrometer, which was previously calibrated with PfHA.

SodX – MS/MS: For Collision Induced Dissociation (CID) on WT-SodX, the protein was diluted in 50% MeOH solution and then directly injected into Synapt G2Si HDMS. The parent peak with  $m/z$  of 1296 was used for MS/MS.

SodX - LC/MS/MS: Purified WT-SodX was buffer exchanged in 50mM  $\text{NH}_4\text{HCO}_3$ . A portion of this sample was diluted to a final concentration of 25 $\mu\text{M}$  which was digested with 20  $\mu\text{g}$  trypsin (Sigma Aldrich) in 50mM  $\text{NH}_4\text{HCO}_3$  and incubated for 16h at 37°C. The reaction was stopped by addition of 10% formic acid. The tryptic digest was passed through nano-LC (Easy nLC 1000) pre-equilibrated with solution A (0.1% formic acid in water). The protein samples were eluted using 95% solution B (0.1% formic acid in acetonitrile). MS/MS spectra with high intensity in each peptide of the protein were selected from 800 – 6000  $m/z$  and fed into the ExPASy GlycoMod tool, which generated theoretical O-glycosylated modification of varying masses. One such predicted modification corresponded to the difference in mass observed for WT-SodX ( $\Delta m = + 691.5 \text{ Da}$ ).

### **3.2.4 Periodic Acid Schiff (PAS) test**

Periodic Acid Schiff test with slight modification from the microtiter -based protocols<sup>19-20</sup> was done on WT-SodX or S28ASodX. Briefly, 25  $\mu\text{L}$  of 1mg/mL of WT-SodX or S28ASodX, was oxidized with 120  $\mu\text{L}$  of 0.06% periodate solution made in 7% acetic acid, and the mixture was incubated for 1.5 hours. 100  $\mu\text{L}$  of the Schiff's reagent was then added to the mixture and incubated for additional 30 minutes. Absorbance for these samples were recorded from 350 – 750nm.

### **3.2.5 DTNB test**



DTNB test was performed on SodX (WT- and S28A variant) using the standard protocol (Thermo Scientific). Briefly, a stock of DTNB solution was made by dissolving 26.34 mg in reaction buffer (0.1mM sodium phosphate, 1mM EDTA, pH 8.0). A set of cysteine standard solutions (0 mM-1.5 mM) were made using Cysteine hydrochloride in reaction buffer. The protein stock samples were diluted to 50  $\mu$ M. 250  $\mu$ l of cysteine standard or protein sample was added to a solution containing 50  $\mu$ l DTNB solution and 2.5 mL reaction buffer. The mixture was incubated at room temperature for 15 minutes and the absorbances of each solution was measured at 412 nm using Agilent 8453 Diode-array spectrophotometer. A standard curve was made using the absorbance values of the standards and the concentration of the protein sample was obtained from this curve.

### **3.2.6 SEC-MALS**

A stock of purified protein samples (apo-WT-NiSOD, apo-WT-SodN and WT-SodX) was buffer exchanged in gel filtration (GF) buffer (50 mM Tris, 200 mM NaCl, pH 8.0). A TSKgel G2000SWxL column (Tosoh Bioscience) was attached to Agilent HPLC system that was coupled to DAWN HELEOS II light scattering detector (Wyatt Technology) and the Optilab T-rEX refractometer (Wyatt Technology). The system was equilibrated with GF buffer at 0.5 mL/min and experiments were performed at 25°C. 25  $\mu$ L aliquots of 50  $\mu$ M apo-WT-NiSOD, apo-WT-SodN and 100  $\mu$ M of WT-SodX protein solution were injected for SEC-MALS analysis at a flow rate of 1.5 mL/min. Eluted proteins were monitored by multiple components of the instrument: UV at 280 nm, light scattering at 664 nm with detectors at multiple angles (13 - 157.8°) and refractive index at 658 nm. Each chromatogram was processed using Astra 6 software package (Wyatt Technology) as described previously<sup>21</sup>. The absolute mass of Bovine Serum Albumin (BSA, expected 66.5 kDa, SEC-MALS 64.7 kDa) was used to calibrate the system and the software.

### **3.2.7 Circular Dichroism**

The purified proteins (apo-WT-NiSOD and apo-WT-SodN) were buffer exchanged in CD buffer (25 mM Tris, 100 mM NaCl, pH 8.0). The protein stock solutions were transferred to an anaerobic chamber (Coy Laboratories), reduced with 5 equivalents of DTT and incubated for 1 hour at room temperature. The reduced protein samples were then buffer exchanged in CD buffer, followed by the addition of three equivalents of Ni(II)Cl<sub>2</sub> and incubation for additional three hours. Chelex beads were added to remove excess metal, and the metallated proteins (holo-WT-NiSOD and holo-WT-SodN) were buffer exchanged for an additional three times with CD buffer. The metal content of the sample were checked using ICP-OES. 20 μM of each these protein samples (apo-WT-NiSOD, holo-WT-NiSOD, apo-WT-SodN, holo-WT-SodN) was used to obtain their CD spectrum on Jasco J-1500 Circular Dichroism Spectrophotometer.

### **3.2.8 UV-Vis Spectroscopy**

Stock solutions of purified WT-SodN or P19A-SodN were buffer exchanged in buffer C (containing 50 mM Tris, 1 mM TCEP, 200 mM NaCl, pH 8.0). A 120 μL sample containing 100 μM of each of apo-WT-SodN (or P19A-SodN) in Buffer C was scanned from 250 nm to 1100 nm using an Agilent 8453 Diode-array spectrophotometer. For nickel-bound WT-SodN or its variants, the purified and buffered exchanged apo-protein solutions were incubated with an equivalent amount of nickel for 15 minutes and scanned similarly.

### **3.2.9 Isothermal Titration Calorimetry**

Isothermal titration calorimetry (ITC) was used to measure the heat released by Ni-binding to SodN and WT-SOD proteins using an Auto-ITC200 model microcalorimeter

(Microcal/Malvern). The instrument has a cell volume of 200  $\mu\text{L}$  and a syringe volume of 40  $\mu\text{L}$ , which were filled by robotic arms from plates stored at 4  $^{\circ}\text{C}$  prior to the start of the experiment. All titrations were performed in ITC Buffer (20 mM Tris, 1 mM TCEP, 200 mM NaCl, pH 8.0) at 25  $^{\circ}\text{C}$  with the reference cell filled with water. A stock of purified proteins (SodN or its variants or WT-SOD) were buffer exchanged in ITC buffer (20 mM Tris, 1 mM TCEP, 200 mM NaCl, pH 8.0) using Amicon Ultra – 0.5 mL centrifugal filters with 3-kDa MWCO pre-equilibrated with ITC Buffer and then diluted to 150  $\mu\text{M}$  for titration immediately before the ITC experiments.  $\text{NiCl}_2$  was dissolved in MilliQ water from a 10 mM stock solution and its exact concentration was checked by ICP-OES. An aliquot of this solution was diluted in ITC Buffer to a final concentration of 2.0 mM and was used for titrations.

For each ITC experiment, 20 injections were made from the syringe into the cell and the change in heat was monitored by the instrument. The initial injection contained only 0.4  $\mu\text{L}$  and was used to minimize the equilibration artifacts sometimes observed with the first injection and was not included in fitting the data. All subsequent injections at 2.0  $\mu\text{L}$  each were used for fitting the titration curve in each experiment. For titration of WT-SOD or SodN (WT- or variants) with  $\text{NiCl}_2$ , the spacing between injections were set to 300 sec. Experimental titrations were accompanied by corresponding reference/control titrations of  $\text{NiCl}_2$  into ITC Buffer in the cell, the resulting heats of which were used to establish the corresponding baseline corrections used for fitting the  $\Delta H$  data. Experimental titrations were performed thrice using separately prepared proteins, and each replicate produced similar results.

The resulting data were fitted using the MicroCal analysis module in Origin 7.0. First, the heat released from titration experiments were baseline corrected and then integrated to produce the

corresponding  $\Delta H$  curve. The  $\Delta H$  curve for each experiment was corrected by subtracting the average  $\Delta H$  from the reference titration. The  $\Delta H$  curve was fitted with the OneSites model to find the apparent  $K_a$  (multiple fitting models were attempted for each set of experimental data and in each case the OneSites model produced the best  $\chi^2$  value). The apparent  $K_d$  values reported are the inverse of the  $K_a$  values obtained from each fit.

### **3.2.10 X-ray Absorption Spectroscopy, Data Reduction, and Analysis**

A stock solution of 300  $\mu\text{M}$  SodN protein was reduced with 3-fold excess of DTT under anaerobic conditions for three hours and then buffer exchanged in Buffer D (50 mM Tris, 200 mM NaBr, pH 8.0) using an Amicon Ultra – 0.5 mL centrifugal filters with 3-kDa MWCO pre-equilibrated with Buffer D. Aliquots of a  $\text{NiCl}_2$  solution from stock (9.34 mM) were added to the SodN sample at an interval of 15 minutes until a 3-fold excess of nickel was reached, and then incubated for an additional 1 hour. Excess nickel from this sample was removed using Chelex beads (Sigma) and the sample was then concentrated to 100  $\mu\text{l}$ . An aliquot from this sample was used to determine the nickel content using ICP-OES and protein concentration using UV-vis. The ratio of nickel per SodN protein was found to be 0.8. The remaining sample of Ni-SodN was mixed glycerol to 11% by volume and loaded into kapton-taped polycarbonate holders and then rapidly frozen in liquid nitrogen. XAS data on the frozen samples were collected at Stanford Synchrotron Radiation Lightsource (SSRL) at the SLAC National Accelerator Laboratory using dedicated ring conditions (3 GeV and 450-500 mA) on beamline 9-3 using a Si (220) double crystal monochromator. The frozen samples were immobilized on aluminum prongs and cooled to  $\sim 10$  K using a liquid helium cryostat (Oxford Instruments). A 30-element Ge detector (Canberra) was used for collecting X-ray fluorescence data. To minimize scattering, a 3  $\mu\text{m}$  Z-1 filter and Soller

slits were installed between the detector and sample. X-ray fluorescence data on the Ni K-edge of Ni-WT-SodN were collected concurrently with spectra of Ni metal foil in transmission mode for energy calibration. Extended X-ray Absorption Fine Structure (EXAFS) were collected to 15k above the K-edge.

Data reduction and analyses were performed according to previously published procedures for Ni K-edge XAS data.<sup>22-25</sup> The Sixpack<sup>26</sup> software package was used to process and normalize the XAS data. Fluorescence channels from each scan were visually checked for bad channels, which were deleted. For each scan, Ni K-edge energy calibration was performed by assigning the first maximum in the first derivative spectrum of the Ni-foil to 8331.6 eV. The energy calibrated XAS data (shown in Figure 3.4) for NiSodN is an average of 8 scans that were normalized and corrected for background. For normalization and background correction, the K-edge energy of Ni was set to 8340 eV with an  $R_{\text{bkg}}$  of 1. A Gaussian function was used for fitting the pre-edge range of -200 to -50 eV and quadratic polynomial functions with 7-8 spline points were used to fit the post-edge range of +100 to +975 eV relative to  $E_0$ . The edge jump was normalized by setting the difference between the corrected pre-edge and post-edge baselines to 1. The EXAFS data were converted to k-space using the relationship  $[2m_e (E-E_0)/\hbar^2]^{1/2}$ , where  $m_e$  is the mass of an electron and  $\hbar$  is the Plank's constant divided by  $2\pi$ . The  $k^3$ -weighted EXAFS data were Fourier-transformed over the k-range 2-12.5  $\text{\AA}^{-1}$  using a Hanning window and fit in r-space using an  $S_0$  value of 0.9. The r-space data shown in the figures was not corrected for phase shifts.

The Artemis software program<sup>26</sup> was used for EXAFS analysis with parameters for scattering atoms generated by FEFF6. Multiple-scattering paths for histidine imidazole and backbone amide (BBAm) ligands were generated as previously described.<sup>21</sup> The EXAFS fitting equation used was:

$$\chi(k) = \sum_i \frac{N_i f_i(k) e^{-2k^2 \sigma_i^2}}{kr_i^2} \sin[2kr_i + \delta_i(k)]$$

where  $f(k)$  is the scattering amplitude,  $\delta(k)$  is the phase-shift,  $N$  is the number of neighboring atoms,  $r$  is the distance to the neighboring atoms, and  $\sigma_i^2$  is a Debye-Waller factor reflecting the mean square deviation in the distance to the nearest neighbor (thermal and static disorder).

To compare the different models fit to the data set, ifeffit utilizes three goodness of fit parameters:  $\chi^2$ , reduced  $\chi^2$ , and the R-factor.  $\chi^2$  is given by equation 1, where  $N_{idp}$  is the number of independent data points,  $N_{\varepsilon^2}$  is the number of uncertainties to minimize,  $Re(fi)$  is the real part of EXAFS function and  $Im(fi)$  is the imaginary part of the EXAFS fitting function.

$$\chi^2 = \frac{N_{idp}}{N_{\varepsilon^2}} \sum_{i=1}^N Re(fi) + Im(fi) \quad (1)$$

Reduced  $\chi^2$  represents the degree of freedom in the fit and is given by equation (2)

$$red.\chi^2 = \frac{\chi^2}{N_{idp} - N_{var}} \quad (2)$$

where  $N_{var}$  is the number of refining parameters and  $N_{var}$  is the number of adjustable parameters. Additionally, ifeffit calculates the R-factor for the fit, which is given by equation (3) and is scaled to the magnitude of the data making it proportional to  $\chi^2$ .

$$R = \frac{\sum_{i=1}^N \{[Re(fi)^2] + [Im(fi)^2]\}}{\sum_{i=1}^N \{[Re(xdatai)^2] + [Im(xdatai)^2]\}} \quad (3)$$

In comparing different models, the R-factor and reduced  $\chi^2$  parameter were used to determine the model that was the best fit for the data. The R-factor will generally improve with an increasing

number of adjustable parameters, while reduced  $\chi^2$  will go through a minimum and then increase, indicating that the model is overfitting the data. The resolution of the data was determined by equation (4).

$$resolution = \frac{\pi}{2 \times \Delta k} \quad (4)$$

**XANES:** X-ray absorption near edge structure (XANES) analysis provides information about the coordination number and the oxidation state of metal complexes. Ni(II) complexes show features associated with high-energy electronic transitions in the pre-edge XANES region of XAS spectra. These transitions involve the promotion of the core 1s electron to either a 3d manifold (1s→3d), which occurs near 8331 eV, or to a 4p<sub>z</sub> orbital (1s→4p<sub>z</sub>), which occurs at 8336 eV. The Ni K-edge XANES spectra of reduced WT-NiSOD shows a shoulder at 8337eV with a peak area of X eV (Figure 3.4A). This peak is associated with a 1s→4p<sub>z</sub> transition and is characteristic of a four-coordinate nickel complex. The Ni K-edge XANES analysis of NiSodN complex show a small 1s→3d feature at 8331.6 eV (Figure 3.4A) with a peak area of 0.036(±0.002) eV<sup>2</sup>, which is representative of a six-coordinate complex.

**EXAFS:** Analysis of the Extended X-ray Absorption Fine Structure (EXAFS) region of metal complexes provides information on the identity of ligand-donor atoms around the metal center. The Ni K-edge EXAFS spectrum of Ni(II) site in Ni-WT-SodN complex is shown in Figure 3.4B, with the fits leading to best fit, shown in black and summarized in Table 2. Single scattering analysis of EXAFS data of this complex yields a nickel site composed of 5-6 N/O-donor ligands. A six-coordinate nickel site agrees with the coordination number/geometry determined from its XANES analysis. Including one or two sulfur shells with 5 or 4 N/O shells improves the R-factor but increases the disorder parameter for the S-donor ligands beyond an acceptable value.

Systematic splitting of the six-coordinate N/O shell of the nickel site into two N/O shells with 5N/O at 2.08 Å and 1 N/O at 2.28 Å improved the Debye-Waller factor and also lowered the R-factor. Further substituting the long N/O ligand with 1 imidazole ligand further improves the fit with respect to R-factor and accounts for scattering in the second and third coordination sphere of the Ni center, but increases the disorder parameter for 5N/O shell. Modeling two of the N/O ligands as a bidentate amidate (BBAm), as has been done for other complexes where backbone N coordination leads to the formation of a five-membered chelate ring<sup>21</sup> and is a known feature of Ni coordination in WT-NiSOD, further improved the fit with acceptable values for the disorder parameter,  $\sigma^2$ . Incorporation of two imidazole ligands in the model further improved the R-factor, but results in higher  $\sigma^2$  value for the long N/O ligand. Finally, adjusting the single the imidazole to an angle of  $\alpha = 5^\circ$  in the model with bidentate amidate coordination further lowers the R-factor with acceptable values for the disorder parameter of each shell, and hence was the best fit model. Including S-donors in the model results in better R-factors, but features high disorder ( $\sigma^2$ ) for these donors. The best fit model is consistent with the absence of thiolates from cysteines (16 or 20) in the coordination sphere of the Ni(II) site, and with a Ni binding site composed of six N/O-donor ligands, with one of them contributed by an imidazole from histidine, most likely the His15 in SodN.

### 3.2.11 SodX Homology Modelling

The *S. coelicolor* SodX model structure was generated using PHYRE2<sup>27</sup>. The resulting model was aligned using all atoms to the *E. coli* signal peptidase (1T7D<sup>28</sup>) in Pymol. A heptapeptide (A-HCDLPC) corresponding to the N-terminus of apoSodN and including the last residue of the pro-sequence) was built in Pymol and manually positioned in the active site of SodX.



### 3.2.12 Pulse radiolysis

The protein samples (WT-NiSOD, Ni-WT-SodN, Ni-P19A-SodN, and the nickel containing proteolytic mixtures with or without L-histidine) were buffer exchanged in buffer P containing 10 mM phosphate, 30 mM formate, pH 7.5. The nickel content of each sample was determined using ICP-MS, which were then sent to National Brookhaven Laboratory for pulse radiolytic experiments that were run by Dr. Diane Cabelli. The catalytic removal of superoxide radicals ( $O_2^-$ ) by the various species described above was measured directly using pulse radiolysis at Brookhaven National Laboratory. The disappearance of  $O_2^-$  was followed optically at 260 nm. All the solutions contained micromolar concentrations of WT-NiSOD, SodN, SodX or mixtures thereof, sometimes with added  $NiCl_2$  and/or added L-His. The buffer was always 30 mM sodium phosphate and 10 mM sodium formate (pH 7.4) and 15  $\mu$ M EDTA (ethylenediaminetetraacetate). All rate constants are given relative to the concentration of Ni determined by ICP in the carefully buffer-exchanged sample. EDTA was added a few minutes prior to generation of  $O_2^-$  and sequential pulses generating different amount of  $O_2^-$  were administered during 5-10 minutes. There was no significant change in rate from the initial to the final pulse. This procedure was used to ensure that EDTA was not removing Ni from an active site in SodN or SodX. However, unlike in CuSOD, Ni ion is not catalytically active for the removal of  $O_2^-$  so there is no way to confirm that all of the Ni measured in the sample is properly bound.

### 3.2.13 *In Vitro* Processing assays

All metal stock solutions were made in ultrapure water obtained from Milli-Q (EMD Millipore) and the metal content was quantified using ICP-OES (Perkin Elmer). For metal-dependent processing assays, these metal solutions were diluted in assay buffer (50 mM Tris, pH 8.0) to 1.3 mM. WT-SodN was reduced with a 3-fold excess of DTT under anaerobic conditions

and then buffer exchanged using Amicon Ultra – 0.5 mL centrifugal filters with 3-kDa MWCO pre-equilibrated with assay buffer. Metal-dependence of processing assays of SodN by SodX was carried out by mixing DTT reduced SodN with purified SodX in the absence or presence of metals in buffer solutions under anaerobic conditions. DTT reduced SodN (40  $\mu$ M) was incubated with 80  $\mu$ M metals (Ni, Co, and Zn in assay buffer) for 15 minutes. SodX (40  $\mu$ M) was finally added to the reaction mixture and the samples were incubated at 30°C for 12 hours, prior to analysis for protein composition by ESI-MS (*vide infra*).

### **3.2.14 *In Vitro* Processing assays in the presence of nickel and L-Histidine or D-Histidine**

For L-Histidine or D-Histidine dependent processing assays in presence of nickel, varying concentrations of L-His (0.01, 0.1, 1.0 and 10.0 mM) in assay buffer M (50 mM Tris, 1 mM TCEP, pH 8.0) were made. A stock solution of SodN was buffer exchanged in assay buffer M and diluted to 40  $\mu$ M in each L-His containing buffer. A stock solution of NiCl<sub>2</sub> was also made in assay buffer M. An aliquot of this nickel solution was added to 40  $\mu$ M SodN so that the final concentration of the metal is 80  $\mu$ M and the assay mixture was incubated for 15 minutes. Then, an aliquot of 40  $\mu$ M SodX from a stock solution was then added to the assay mixture and the mixture was incubated at 30°C for 12 hours. The protein content of each reaction mixture was then analyzed using ESI-MS (AB Sciex QStar XL).

### **3.2.15 Mass Spectrometry for proteolytic assay characterization**

*Characterization of metal-dependent processing assay mixtures:* 100  $\mu$ L of each of the metal-dependent processing assay samples was buffer exchanged in 5 mM ammonium acetate using Amicon Ultra – 0.5 mL centrifugal filters with 3-kDa MWCO pre-equilibrated with the same solvent. These samples were then directly injected into AB Sciex Qstar XL ESI-Q-TOF mass

spectrometer, which was previously calibrated with PfHA. Analyst Software was then used to deconvolute the mass spectrum of each sample.

*Characterization of L-His or D-His dependent processing assay mixtures in presence of nickel:*

100  $\mu$ L of each of the L-His (or D-His) dependent processing assay samples was buffer exchanged in 5 mM ammonium acetate using Amicon Ultra – 0.5 mL centrifugal filters with 3-kDa MWCO pre-equilibrated with the same solvent. These samples were then directly injected into a pre-calibrated Thermo Orbitrap Fusion Tribrid Mass Spectrometer. The data was deconvoluted using ThermoX Calibur Software from Thermo scientific.

### **3.2.16 In-gel activity Assays**

In-gel SOD activity staining, as described elsewhere<sup>29</sup>, was used to qualitatively assess the SOD-activity of the metal-dependent processing assay samples containing nickel or other metal salts. Briefly, 150  $\mu$ M of DTT-reduced SodN was incubated with 300  $\mu$ M of metals (Mn, Fe, Co, Ni, Cu, and Zn) in assay buffer for 15 minutes, and an equivalent amount of SodX was added to the samples. These assay samples further incubated at 30°C for 12 hours. Native sample buffer (62.5mM Tris.HCl pH 6.8, 40% glycerol, 0.01% bromophenol blue) was added to these assay samples, which were then loaded on 12% native polyacrylamide gels and run at constant voltage (120V) for 6 hours at 4°C. The gels were washed thrice with ultra-pure water and then soaked in 50 mM phosphate buffer containing 28  $\mu$ M NBT and 28  $\mu$ M Riboflavin for 30min and kept in the dark. The staining solution was removed, and the gel was washed again twice with ultra-pure water and incubated in phosphate buffer containing 28 mM TEMED for 30 minutes in the dark. The gels were exposed to white light for 20 minutes and then scanned.

### 3.3 Results

#### 3.3.1 Protein Characterizations

**3.3.1.1 Ni-binding to Apo-SodN.** The *sodN* gene from *Streptomyces coelicolor* was obtained from Prof. J. H. Roe at Seoul National University.<sup>17</sup> The correct gene sequence was confirmed by DNA sequence analysis (Genewiz, Inc., **Appendix A, Figure A.1**) and SodN was recombinantly expressed in *E. coli* BL21(DE3) plysS and purified as described in the Experimental Methods section (**Appendix A, Figure A.2**, lane 4; apo-WT-NiSOD, lane 3). The molecular weight of the recombinant protein was confirmed using ESI-MS (WT-SodN calculated: 14,702 Da, found 14,701 Da; **Appendix A, Figure A.3A**, and **Table 3.2**), which does not show apparent dimer formation, as is the case for WT-NiSOD. A +32 Da modification of SodN was also observed in its mass spectrum, which is attributed to the formation of sulfoxxygenate species (bis-sulfenate or sulfinate) similar to that observed for Ala0-NiSOD (where an Alanine is inserted prior to His1 in the recombinant construct of apo-WT-NiSOD)<sup>25</sup>. In addition to the expected WT-SodN species at 14,701 Da, a truncated species of WT-SodN at 14,236 Da and 14,101 Da (denoted as N $\Delta$ 4-SodN N $\Delta$ 5-SodN, in which the first four and five residues, respectively were truncated, **Appendix A, Figure A.3A & Figure A.3B**) was also detected in the purified protein samples. This species occurs in all batches of purification and is also detected in the two variants of SodN used in this study (H15A-SodN, and P19A-SodN; *vide infra*), and is possibly a product of spontaneous cleavage that might result from changing pH from 8.8 to a pH 7.0 during purification, commonly observed for proteins with unstable sequences.<sup>30</sup>

**Table 3.2: Protein Characterization parameters determined using mass spectrometry<sup>a</sup>, ITC<sup>b</sup> and UV-Visible Spectroscopy<sup>c</sup>.**

Protein	Theoretical Monomeric Mass (Da)	<sup>a</sup> Observed Monomeric Mass (Da)	<sup>b</sup> Ni-binding parameters		<sup>c</sup> LMCT (S→Ni(III))	<sup>a</sup> Processing
			K <sub>d</sub> (μM)	N		
WT-NiSOD	13,200.1	13,199.1	0.68 ± 0.20	0.95 ± 0.02	Yes	NA*
WT-SodN	14,702.8	14,701.8	21.1 ± 1.7	1.03 ± 0.02	No	Yes (13,199)
P19A-SodN	14,676.8	14,676.8	37.3 ± 3.5	0.52 ± 0.06	No	Yes (13,171.5)
H15ASodN	14,636.8	14,635.3	20.7 ± 2.3	0.47 ± 0.02	No	No

\*NA = Not Applicable

In order to determine the oligomeric state and the associated molecular weight of purified apo-WT-SodN, size exclusion chromatography coupled to multiple angle light scattering (SEC-MALS) was performed and compared with that of the recombinantly purified apo-WT-NiSOD (**Appendix A, Figure A.3C**). As determined from the size-exclusion chromatogram, apo-WT-SodN and apo-WT-NiSOD eluted as single peaks. Using MALS analysis on these protein peaks, the apparent molecular masses of apo-WT-SodN and apo-WT-NiSOD were calculated to be  $95.38 \pm 0.04$  kDa and  $89.69 \pm 0.05$  kDa, respectively, values that are consistent with a homohexameric quaternary structure for SodN, as previously observed for apo-WT-NiSOD.<sup>1, 6</sup> Therefore, the presence of the N-terminal leader sequence upstream of the nickel binding region has no effect on the oligomeric state of the pro-enzyme.

The leader sequence also had negligible effect on the secondary structural features of SodN. Circular Dichroism was performed on purified apo- and Ni-bound WT-SodN and compared with the spectrum obtained for WT-NiSOD. Both apo-WT-SOD and Ni-WT-NiSOD, show spectra with  $\alpha$ -helical features that are consistent with its 4-helix bundle structure (**Appendix A, Figure A.3D**). Apo-WT-SodN and Ni-WT-SodN show similar  $\alpha$ -helical features demonstrating that the secondary structural features of SodN are not significantly altered by the presence of the 14-amino acid N-terminal extension or Ni(II) ions, and indicating that the precursor likely also contains a 4-helix bundle, as expected from the formation of the hexameric oligomer.

Ni(II)-binding to purified pro-enzyme, apo-WT-SodN, was measured using isothermal titration calorimetry and compared with that of the recombinantly purified apo-WT-NiSOD (**Figure 3.2, Table 3.2**). Titration of apo-WT-NiSOD with a solution of NiCl<sub>2</sub> as detailed in the Experimental Methods section, was exothermic (**Figure 3.2A**), and the analysis of the resulting binding isotherm is consistent with a single binding event involving 0.95(2) nickel per subunit with an apparent  $K_d$  of 0.68(2)  $\mu$ M. Apo-WT-SodN bound 1.03(2) nickel per subunit with an apparent  $K_d$  of 21.1(1.7)  $\mu$ M (**Figure 3.2B**, and Experimental Methods), which is thirty-fold lower than that for apo-WT-NiSOD. Thus, despite the presence of metal binding residues (His15, amide of Cys16, and thiols from Cys16 and Cys20), the pro-enzyme is less competent for nickel binding than the processed enzyme, which is also supported by the differences observed in the spectroscopic properties of the nickel-bound complexes of SodN and WT-NiSOD (see below).

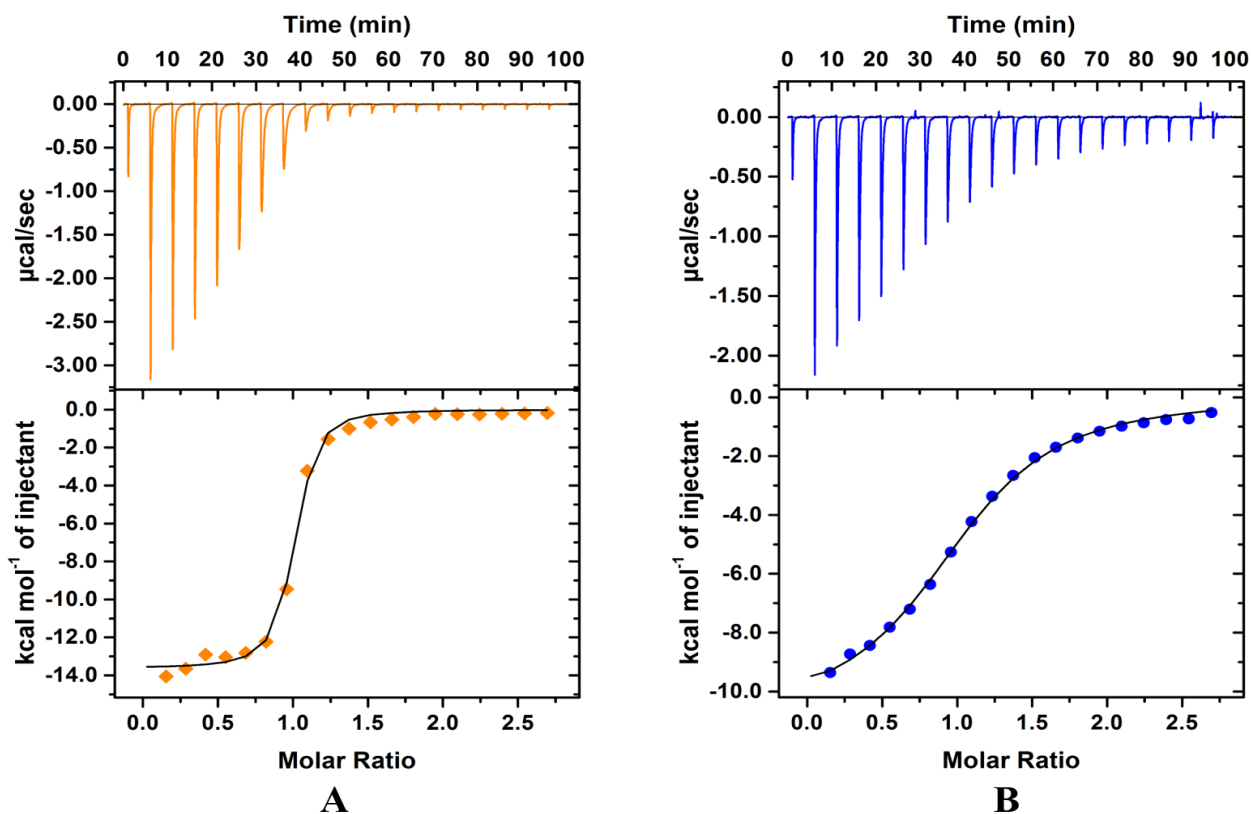


**Figure 3.2:** ITC thermograms (top) and binding isotherms (bottom) for titrations of A) 0.15 mM apo-WT-SOD (orange), and B) 0.15 mM of apo-WT-SodN (blue) with 2 mM Ni<sup>2+</sup> in buffer containing 20 mM Tris, 200 mM NaCl, 1 mM TCEP, pH 8.0. A one-site binding model was used to fit the binding of Ni to apo-WT-SOD and apo-WT-SodN (solid black lines) to give binding stoichiometries of 0.95(2) and 1.03(2) and  $K_d$  values of 0.68(2)  $\mu\text{M}$  and 21.1(1.7)  $\mu\text{M}$ , respectively.

The structural features of the Ni(II) binding site in SodN was probed using UV-Vis and K-edge X-ray absorption spectroscopy (XAS), as described in the Experimental Methods section. The UV-vis spectra of Ni-WT-SodN, as-isolated NiSOD, and dithionite-reduced NiSOD are compared in **Figure 3.3**. The spectrum of Ni-WT-SodN does not exhibit the  $S \rightarrow \text{Ni(III)}$  LMCT absorption found in the as-isolated WT-NiSOD spectrum ( $\lambda_{\text{max}} = 372 \text{ nm}$ ,  $\epsilon = 7600 \text{ M}^{-1}\text{cm}^{-1}$ )<sup>31</sup>, consistent with the Ni(II) formulation for the WT-SodN complex and/or the lack of thiolate

ligation, and the spectrum is similar to apo-WT-SodN (**Appendix A, Figure A.4**). Further, the spectrum of Ni-WT-SodN lacks the higher energy absorptions associated with  $S \rightarrow Ni(II)$  LMCT in dithionite-reduced NiSOD<sup>31</sup>, suggesting the absence of thiolate ligands in the pro-enzyme Ni(II) complex.

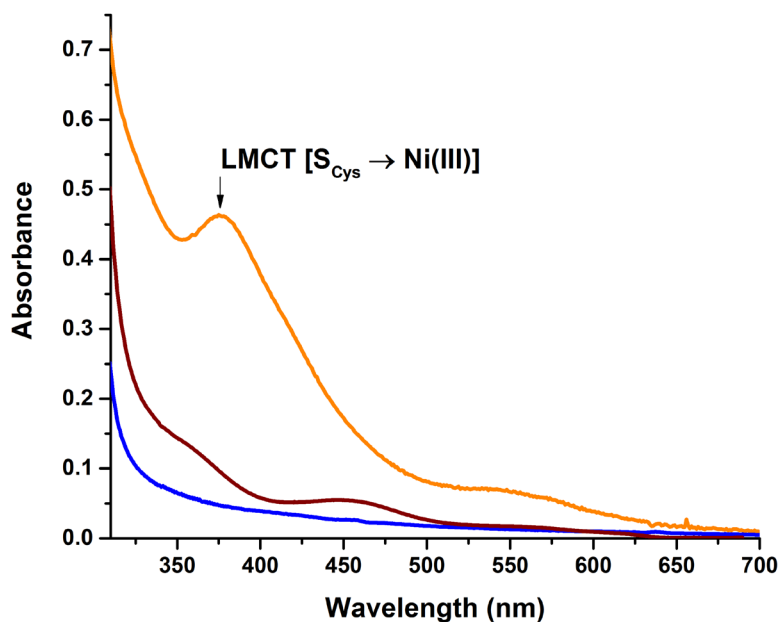


**Figure 3.3: Overlay of UV-Vis spectra of 100 μM Ni(II)-WT-SodN (blue), as-isolated recombinant WT-NiSOD (orange) and dithionite-reduced recombinant NiSOD (wine).**

To get more detailed structural information about the Ni(II) binding site in WT-SodN and address the absence of S-donor ligands, including Cys thiol ligation, XAS was performed on the Ni(II)-WT-SodN complex and compared with the reported spectrum of dithionite-reduced Ni(II)-SOD in **Figure 3.4**. The XANES spectrum of Ni(II)-WT-SodN (**Figure 3.4A**) does not show the pre-edge maximum associated with a  $1s \rightarrow 4p_z$  electronic transition near 8336 eV that is diagnostic for a planar four-coordinate geometry<sup>32</sup> and that is present in the spectrum of dithionite-reduced NiSOD.<sup>5</sup> The Ni(II)-WT-SodN spectrum does show a small peak near 8331 eV that is associated



with a  $1s \rightarrow 3d$  electronic absorption.<sup>32</sup> The area under this peak,  $0.036(2) \text{ eV}^2$  is consistent with a six-coordinate distorted octahedral geometry<sup>32</sup>.

The extended x-ray absorption fine structure (EXAFS) spectrum shows no evidence of S-coordination (max intensity at  $\sim k = 6 \text{ \AA}^{-1}$ ) and can be fit by six-coordinate models that do not contain S-donor ligands in the primary coordination sphere of the Ni(II) center (**Appendix A, Table A.1**). The spectrum does have features that arise from scattering atoms outside the primary coordination sphere that could be fit by multiple-scattering from histidine imidazole ligands and scattering from ordered C atoms that arise from chelate rings formed by coordination of backbone N-donors, like those found in NiSOD.<sup>5, 24</sup> The best fit (**Figure 3.4B**), as judged by  $R \leq 5\%$ , decreasing red  $\chi^2$  and acceptable values of  $\sigma^2$ , was obtained for a model that features six N/O-donor ligands and includes one imidazole ligand (likely from His15, *vide infra*) and one bidentate amidate-type chelate. In summary, the XAS data are consistent with a high spin six-coordinate Ni(II) site with a  $(\text{N/O})_5\text{His}$  ligand donor set that is quite distinct from the low-spin  $\text{N}_2\text{S}_2$  planar site found in dithionite-reduced Ni(II)SOD.

Spectroscopic characterization of Ni-WT-SodN complex clearly shows that the nickel site in the proenzyme is distinct than that of the WT-NiSOD, especially absence of thiolate coordination to the nickel site. In WT-NiSOD, binding of sulfurs (from Cys2 and Cys6) is ‘all or none’ phenomenon, meaning that both sulfurs are required to support the native low-spin Ni(II) configuration, and the loss of even one sulfur leads to the conversion to high spin Ni(II) center and loss of remaining sulfur-donor ligand.<sup>22</sup> Examples of high spin, six-coordinate mono-thiolate nickel complex are rare and features very long Ni-S distances ( $2.46\text{-}2.54 \text{ \AA}$ ), such as in Ni(tren)(1,3-dtsq)(H<sub>2</sub>O), Ni(tren)(1,3-dtsq)(H<sub>2</sub>O), and RcnR (nickel-responsive transcriptional regulator).<sup>22, 33-34</sup> In absence of thiolate coordination, as histidine has relatively higher affinity for

nickel, the imidazole coordination in NiSodN likely arises from His15, which is also one of the constituents of the invariant cleavage site in the SodN.

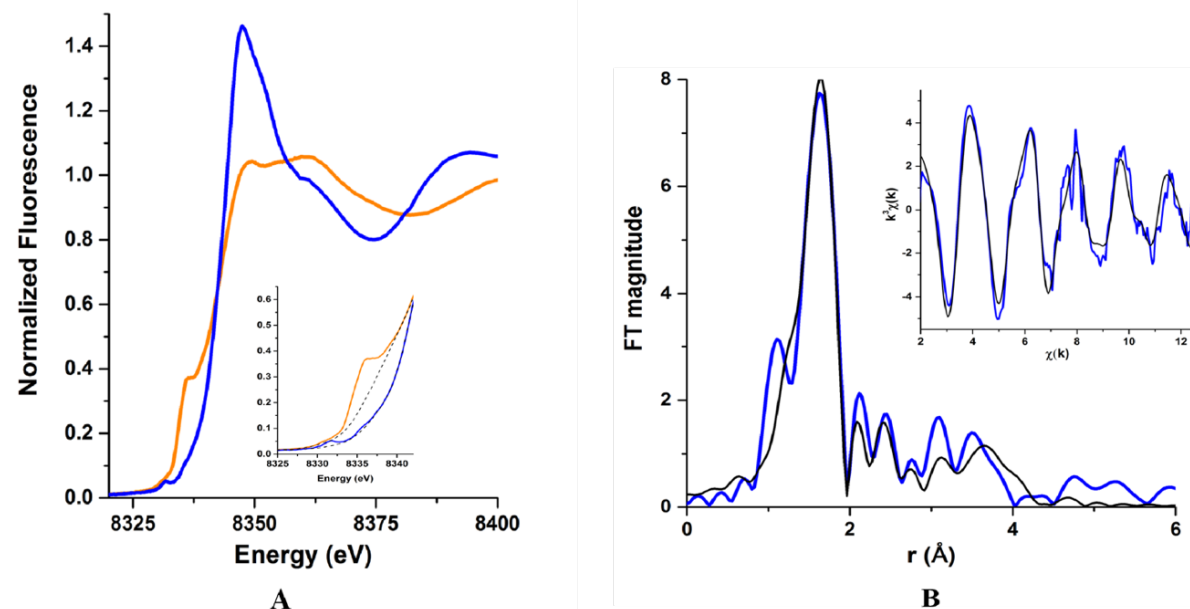


**Figure 3.4.** A) Overlay of the Ni K-edge XANES region of the XAS spectra of Ni-WT-SodN (blue), dithionite-reduced NiSOD<sup>5</sup> in 50mM Tris, 200mM NaBr, pH 8.0. B) Fourier-transformed EXAFS ( $k = 2 - 12.5 \text{ \AA}^{-1}$ ) data (blue) uncorrected for phase-shifts and the best fit model (black) from Table -2 SI (2N/O (2.04Å), 1BBAm (1.99 Å, 2.04 Å), 1N/O (2.25 Å), 1Im5° (2.13 Å)) for Ni-WT-SodN in 50mM Tris, 200mM NaBr, pH 8.0. The inset shows the in  $k^3$ -weighted unfiltered EXAFS data (blue) and best fit model (black).

**3.3.1.2 SodN variants, H15A-SodN and P19A-SodN were produced to examine the role of these residues in the maturation process.** To further assess the role of His 15 in nickel binding properties of SodN, nickel binding affinity of a variants of SodN – H15ASodN and P19ASodN were obtained, expressed and purified as described in Experimental Methods. The molecular weights of these purified SodN variants (**Table 3.2**) were determined using ESI-MS (**Appendix A, Figure A.3A**).

Similar nickel binding affinities were also observed for SodN variants - H15A-SodN ( $K_d = 20$  (2)  $\mu\text{M}$ ,  $n = 0.5$ ) and P19ASodN ( $K_d = 37$  (3)  $\mu\text{M}$ ,  $n = 0.5$ ), respectively, but the nickel binding stoichiometry ( $n$ ) for both these variants is less than 1:1 (**Table 3.2 and Appendix A, Figure A.5A**). The low stoichiometry possibly reflects the loss of a ligand in H15A-SodN and interference with the binding site formation in P19A-SodN (*vide infra*). Additionally, for H15A-SodN, detailed analysis of the thermodynamic parameters derived from the binding isotherms suggest nickel binding to H15A-SodN is associated with more favorable enthalpy ( $\Delta H = -21$  kcal/mol) and entropy ( $-T\Delta S = 14.8$  kcal/mol) as compared to that of WT-SodN ( $\Delta H = -8.5$  kcal/mol,  $-T\Delta S = 2.3$  kcal/mol) or WT-NiSOD ( $\Delta H = -13.0$  kcal/mol,  $-T\Delta S = 4.7$  kcal/mol) (**Appendix A, Table A.2**). Favorable enthalpy change arises due to strong hydrogen bonding and/or Van der Waals interactions, while favorable entropy changes are associated with desolvation of non-polar groups. Higher enthalpy-entropy contributions during nickel binding in H15A-SodN are compensated that gives rise to comparable Gibbs free energy and hence similar nickel binding affinity with respect to WT-SodN. Thus, loss of His15 in SodN perturbs the nickel binding energetics in H15A-SodN and reflects a significant role of His15 in the nickel binding process of SodN. Similar to Ni-bound WT-SodN, P19A-SodN variant did not show any UV-Vis spectral features associated with the presence of S-donor ligands (**Appendix A, Figure A.4**).

**3.3.1.3 SodX is a serine protease that is expressed in modified form in *E. coli*.** SodX from *S. coelicolor* is the predicted cognate protease for SodN and is presumed to belong to S26A class of serine proteases,<sup>35</sup> that utilize a Ser-Lys catalytic dyad for its proteolytic activity. This class of serine proteases,<sup>35</sup> are involved in proteolytic processing of N-terminal signal sequences (*e.g.*, *E. coli* SPase I, which is a membrane-bound protease),<sup>36</sup> and SodX has significant sequence homology (**Appendix A, Figure A.6**). In *S. coelicolor* (and most other microorganisms expressing

NiSOD), *sodX* is found downstream of *sodN* (**Appendix A, Figure A.7A**) and encodes a polypeptide of 16,157 Da with 146 amino acids (**Appendix A, Figure A.1**).<sup>37</sup>

The recombinant *sodX* gene from *Streptomyces coelicolor* was obtained as described in Experimental Methods, expressed in *E. coli* BL21(DE3) plysS (**Appendix A, Figure A.2B**) and purified by cation-exchange column chromatography (**Appendix A, Figure A.2A, lane 2**). The molecular weight of the purified protein was determined using ESI-MS (SodX calculated: 16,157 Da, Found 16,848 Da) (**Appendix A, Figure A.7B**). A Collision-Induced-Dissociation (CID)-MS (**Appendix A, Figure A.7C**) performed on this purified protein confirmed the absence of any extra residues at the C- or N-terminus and eliminated the possibility of modification at the terminals. However, LC-MS/MS on the tryptic digest (**Appendix A, Figure A.7D**) followed by its analysis using the web - based ExPASy Glycomod tool identified a peptide from residues 125 -142 of WT – SodX, to contain a (Deoxyhexose)<sub>2</sub>(Sulf)<sub>5</sub> moiety whose mass accounts for increased mass of WT- SodX. A modified periodic acid - Schiff (PAS) test<sup>19</sup> and a DTNB (5, 5 – dithio – bis - (2-nitrobenzoic acid)) test<sup>38</sup> were both positive and hence confirm the likely identity of this modification. Despite the modification, purified WT-SodX showed the expected proteolytic activity of Ala14-His15 cleavage site in WT-SodN (**Figure 3.5, top, A**). Proteolytic assays performed in the presence of PMSF and EDTA (to rule out metalloproteases) did not inhibit processing, which is consistent with the feature of the Ser-Lys class of serine proteases.<sup>35</sup>

The conserved Ser28 in SodX from *S. coelicolor* is predicted as the catalytic residue in the protease. Hence, a protein variant of SodX, Ser28A-SodX was obtained, expressed and purified (as described in the Experimental Methods section) to test the role of this residue in proteolysis. The MW characterized by ESI-MS shows a protein with similar mass as the WT-SodX (**Appendix**

**A, Figure A.7B**) that also tested positive in the PAS and DTNB assays, but is devoid of proteolytic activity (**Figure 3.5D**), suggesting that Ser28 is the catalytic residue in SodX.

To determine the oligomeric state and the associated molecular weight of purified WT-SodX, SEC-MALS was performed (**Appendix A, Figure A.8A**). WT-SodX eluted as single peak on the size-exclusion chromatogram. Using MALS analysis on this protein peak, the apparent molecular mass of WT-SodX was calculated to be  $116.38 \pm 0.04$  kDa, a value that is consistent with a homoheptameric quaternary structure for SodX.

To examine the secondary structural features of SodX, circular dichroism (CD) spectroscopy was performed on purified WT-SodX, which showed predominantly  $\alpha$ -helical features (**Appendix A, Figure A.8B**). To check whether SodX can bind Ni(II) or not, the purified WT – SodX was metallated with NiCl<sub>2</sub>, and excess metal was removed by Chelex beads, and the sample was analyzed for its nickel content by ICP-OES. No nickel was found to bind the protein.

Based on the reported structure of inhibitor bound *E. coli* SPaseI (PDB: 1T7D)<sup>28</sup>, a homology model for WT-SodX bound to a peptide (A-HCDLPC) resembling the leader peptide of SodN was obtained (**Appendix A, Figure A.8C**). This model shows the positioning of Ala14-His15 site of SodN with the catalytic site (Ser28) of the protease.

### 3.3.2 Proteolytic Processing

**3.3.2.1 SodX can cleave WT-SodN yielding apo-WT-SOD in a process that does not require Ni(II).** Processing of SodN by SodX was studied under a variety of conditions (See Experimental Methods) and the reaction products were identified by ESI-MS (**Figure 3.5**). Reaction of a mixture of 40  $\mu$ M SodN and 40  $\mu$ M SodX in assay buffer (50mM Tris, pH 8.0) for 16 h showed the production of N $\Delta$ 14-SodN, or apo-NiSOD, by cleavage of SodN between Ala14

and His15 (**Figure 3.5A & Appendix A, Figure A.3B**). That the resulting apo-NiSOD is functional was confirmed by first adding 150  $\mu\text{M}$   $\text{NiCl}_2$  (made in assay buffer) to the product mixture (containing 150  $\mu\text{M}$  each of apo-WT-SodN and WT-SodX), and then demonstrating catalysis in the mixture by kinetic analysis using pulse radiolytic generation of superoxide<sup>7</sup> (**Figure 3.6**), and by native electrophoresis gels that were stained for activity using the in-gel-SOD activity assay method<sup>29</sup> (**Appendix A, Figure A.9, lanes 1-10**). Although the catalytic activity of the cleavage product mixture is small (specific activity =  $4.5 \times 10^7 \text{ M}^{-1}\text{s}^{-1}$ ), it is not observed for unprocessed SodN + Ni (specific activity =  $2.1 \times 10^6 \text{ M}^{-1}\text{s}^{-1}$ ) under the same reaction conditions (**Figure 3.6**).

In addition to the correct SodX cleavage product, an N $\Delta$ 6-WT-SodN species was also present in WT-SodN - SodX proteolytic mixture (**Figure 3.5A**), which represents the peptide hydrolysis at Phe6-Ala7 site (**Figure 3.6**). This species appears to be a non-specific cleavage product. Other protein species observed in the WT-SodN - SodX proteolytic mixtures were the unprocessed WT-SodN, N $\Delta$ 4-WT-SodN, and N $\Delta$ 5-WT-SodN in the mass spectrum (**Figure 3.5A**) that are a feature of samples of SodN alone (**Appendix A, Figure A.3A, top**) and presumably represents an auto-cleavage product formed during sample preparation (*vide supra*).

The SodN variants H15A-SodN and P19A-SodN were also examined by this protein processing assay. Under identical conditions, H15A-SodN did not show the formation of the correct cleavage product (apo-His1Ala-SOD, MW = 13,134 Da) in the product mixture (**Figure 3.5B**). This result indicates that the presence of H15 in the protein is essential for generating proper cleavage by SodX, presumably because it is required for recognition by SodX. The corresponding N $\Delta$ 4-, N $\Delta$ 5- H15ASodN species, similar to that of WT assay (and pure protein, **Appendix A, Figure A.3A, middle**), are also observed here.

In the case of P19A-SodN, the analysis of the reaction products shows the presence of the correct N $\Delta$ 14 cleavage product (apo-P5A-NiSOD, M.W. = 13,174 Da, **Figure 3.5C**), indicating that the N $\Delta$ 14 cleavage is unaffected by the substitution of the Pro19 residue. The only other proteins observed are uncleaved P19A-SodN and the N $\Delta$ 5-P19A-SodN protein which are also observed in the mass spectrum of purified P19A-SodN protein (**Appendix A, Figure A.3A, bottom**). Addition of Ni(II) to the proteolytic mixture containing P19A-SodN and WT-SodX failed to produce SOD activity in In-gel SOD activity assay (**Appendix A, Figure A.9, lane 11**), but kinetic analysis of the mixture (containing P19A-SodN, WT-SodX and Ni(II)) using pulse radiolytic generation of superoxide showed SOD activity (specific activity =  $2.3 \times 10^7 \text{ M}^{-1}\text{s}^{-1}$  **Appendix A, Figure A.11A-B**) which is  $\sim 49\%$  less as compared to the proteolytic mixture containing WT-SodN, WT-SodX and Ni(II) (specific activity =  $4.5 \times 10^7 \text{ M}^{-1}\text{s}^{-1}$ ) suggesting that the processed product (P5A-NiSOD) has a reduced catalytic SOD activity.

**3.3.2.2. Ser28 is the catalytic Ser residue in SodX.** The protein processing assay described above was repeated using S28A-SodX (**Figure 3.5D**). The reaction product mixture does not show the properly cleaved product (apo-WT-NiSOD), demonstrating that Ser28 is essential for catalysis by SodX. Only the N $\Delta$ 5-WT-SodN and N $\Delta$ 6-WT-SodN (MW = 13,954 Da) proteins are observed. The latter apparently results from a mis-cut of the N-terminal leader of SodN by SodX.

**3.3.2.3 Metals, including Ni(II) inhibit cleavage of SodN by SodX.** To examine the role of metals, particularly nickel, in proteolysis, the same proteolytic assay as above involving SodN and SodX was performed with metal ions (Ni(II), Co(II), and Zn(II)) added. The reaction products were again identified using ESI-MS and the deconvoluted mass spectra are shown in **Figure 3.5 (E – H)**. Addition of NiCl<sub>2</sub> (up to a final concentration of 80  $\mu\text{M}$  in assay buffer) to the buffered

solution of WT-SodN in the absence of SodX results in a reaction product spectrum that is essentially that of purified WT-SodN (**Appendix A, Figure A.3A**), indicating that Ni(II) alone does not induce processing nor does it strongly affect auto-proteolysis of the leader sequence. Addition of WT- SodX to preincubated solutions of SodN + NiCl<sub>2</sub> (80μM), CoCl<sub>2</sub> (80 μM) or ZnCl<sub>2</sub> (80 μM) produces a predominant peak at 13,954 Da that corresponds to the NΔ6-WT-SodN mis-cleaved product (**Figure 3.5 F - H**) with only small amounts of the correct NΔ14 cleavage product. The relative intensities for the NΔ14 cleavage products are only 8% for Ni- or Co- and 24% for Zn-containing proteolytic assays relative to the metal-free samples. Furthermore, WT-SodN (MW 14, 702 Da) completely disappeared in the Zn-containing proteolytic assay.

A plausible reason for this is the precipitation of Zn(OH)<sub>2</sub> and/or Zn-WT-SodN complex that occurred upon addition of Zn to apo-WT-SodN under these assay conditions (pH 8.0). (This may also affect the cleavage results for this metal ion, which appear higher, but might result from a loss of Zn from the reaction mixture.). Hence, these proteolytic assays suggest that presence of metals (Ni, Co or Zn) inhibit the proper proteolysis of the leader sequence in SodN, probably due to binding of these metals at the Ala-His processing site via His15, which is an essential residue for processing.



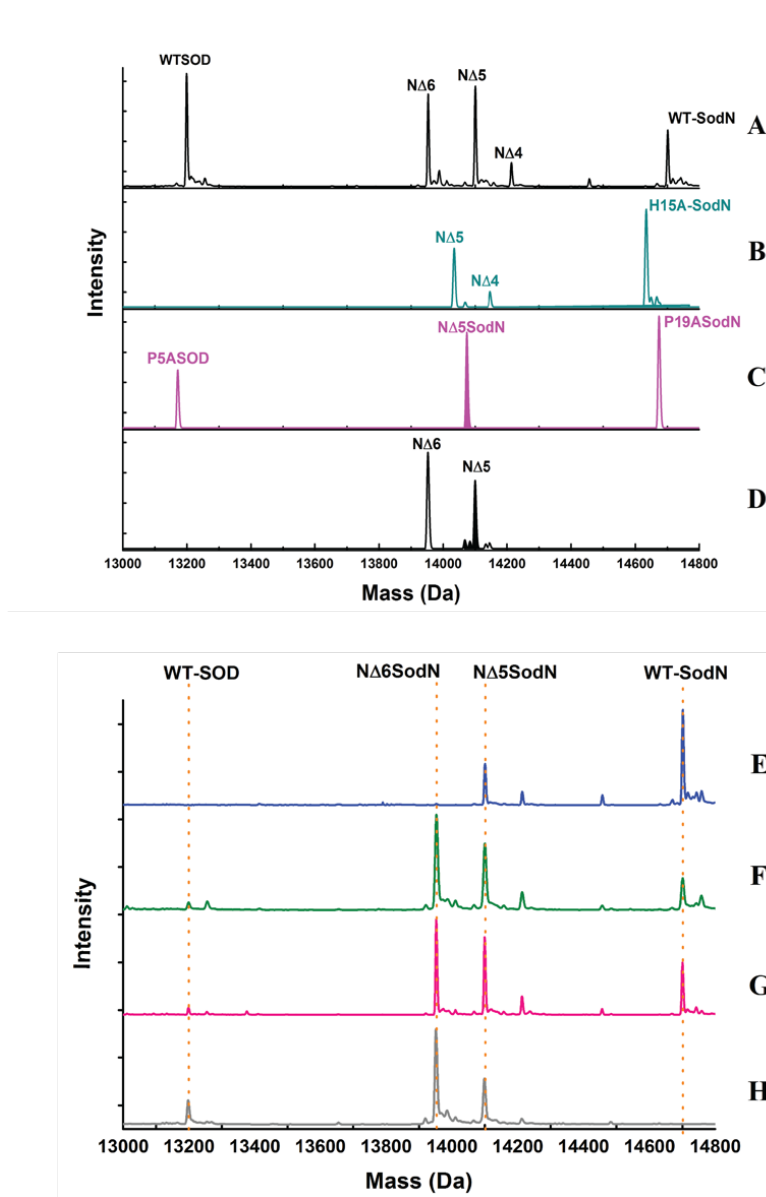


**Figure 3.5: Deconvoluted ESI-MS spectra of proteolytic assays in buffers containing 50mM Tris, pH 8.0 (A-D), A: 40  $\mu$ M apo-WT-SodN with 40  $\mu$ M WT-SodX; B: 40  $\mu$ M apo-H15A-SodN with 40  $\mu$ M WT-SodX; C: 40  $\mu$ M apo-P19A-SodN with 40  $\mu$ M WT-SodX; D: 40  $\mu$ M apo-WT-SodN with 40  $\mu$ M S28A-SodX; and proteolytic assays in buffers containing 50mM Tris, pH 8.0 in the presence of metals (E - H), E: 40  $\mu$ M WT-SodN incubated with 80  $\mu$ M NiCl<sub>2</sub>; F: 40  $\mu$ M WT-SodX added to WT-SodN pre-incubated with 80  $\mu$ M NiCl<sub>2</sub>; G: 40  $\mu$ M WT-SodX added to WT-SodN pre-incubated with 80  $\mu$ M CoCl<sub>2</sub>, H: 40  $\mu$ M WT-SodX added to WT-SodN pre-incubated with 80 $\mu$ M ZnCl<sub>2</sub>.**

**3.3.2.4 L-Histidine promotes proper proteolysis in the presence of Ni(II).** Histidine has been proposed as a cellular ligand for Ni(II) in *Syncheocystis*.<sup>39</sup> To investigate the possibility that a ternary complex of a small ligand, WT-SodN, and Ni(II) might allow for processing of WT-SodN, the proteolytic assays with Ni(II) added were repeated in the presence of L-His. Nickel speciation curves for SodN, NiSOD, and L-His (**Appendix A, Figure A.10A**), were calculated using the known binding affinities of Ni(II) to L-His,<sup>40-41</sup> apo-WT – SodN, and apo -WT-NiSOD (*vide supra*) to identify Ni(II) and Histidine concentrations that would not inhibit but allow SodX-dependent cleavage of SodN. Furthermore, these simulated nickel speciation curves would also reveal if a specific Ni-His complex (Ni-(L-His) or Ni-(L-His)<sub>2</sub>) was important for SodX-dependent cleavage in presence of nickel. Based on nickel speciation curve (**Appendix A, Figure A.10A**), a concentration of 80  $\mu\text{M}$  Ni(II) was chosen, and L-His was added to the standard processing assays at concentrations of 0, 0.01, 0.1, 1.0, and 10 mM. The results summarized in **Figure 3.7** show that adding 0.01, 0.1 or 1.0 mM L-His allows N $\Delta$ 14 processing to occur in the presence of 80  $\mu\text{M}$  Ni(II), which is inhibitory in the absence of L-His (**Figure 3.5F**). Thus, preventing the formation of the Ni(II) complex of WT-SodN by complexation with L-His enables correct processing. The product of processing (i.e. N $\Delta$ 14-SodN or WT-NiSOD at 13,199 Da) obtained in the presence of Ni(II) and selected L-His concentrations demonstrate NiSOD activity (specific activity = 1.3 – 3.3  $\times 10^7 \text{ M}^{-1}\text{s}^{-1}$ ), as shown by the catalytic kinetic curves in the assay using pulse-radiolytic generation of O<sub>2</sub><sup>-</sup> (**Figure 3.6; Appendix A, Figure A.11C-D**). This demonstrates that L-His is able to prevent inhibition of N-terminal processing but provides a source of Ni(II) for maturation of the enzyme.

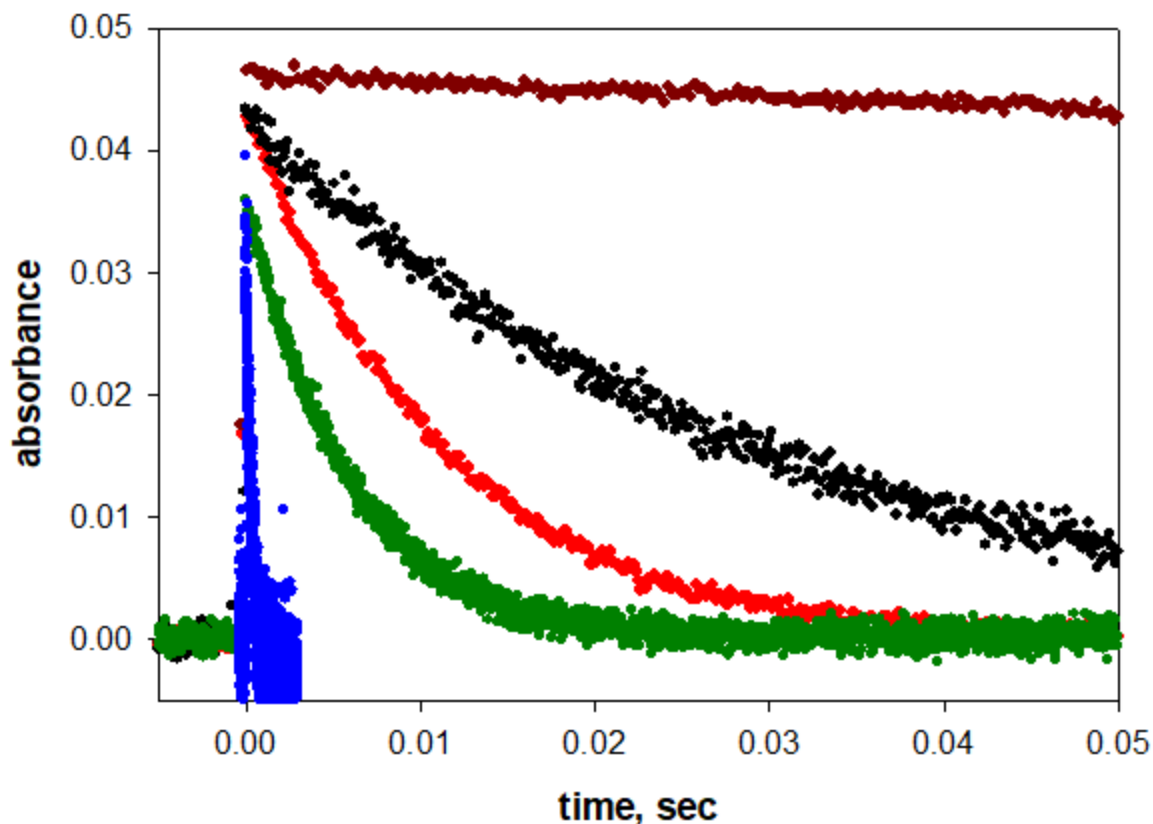
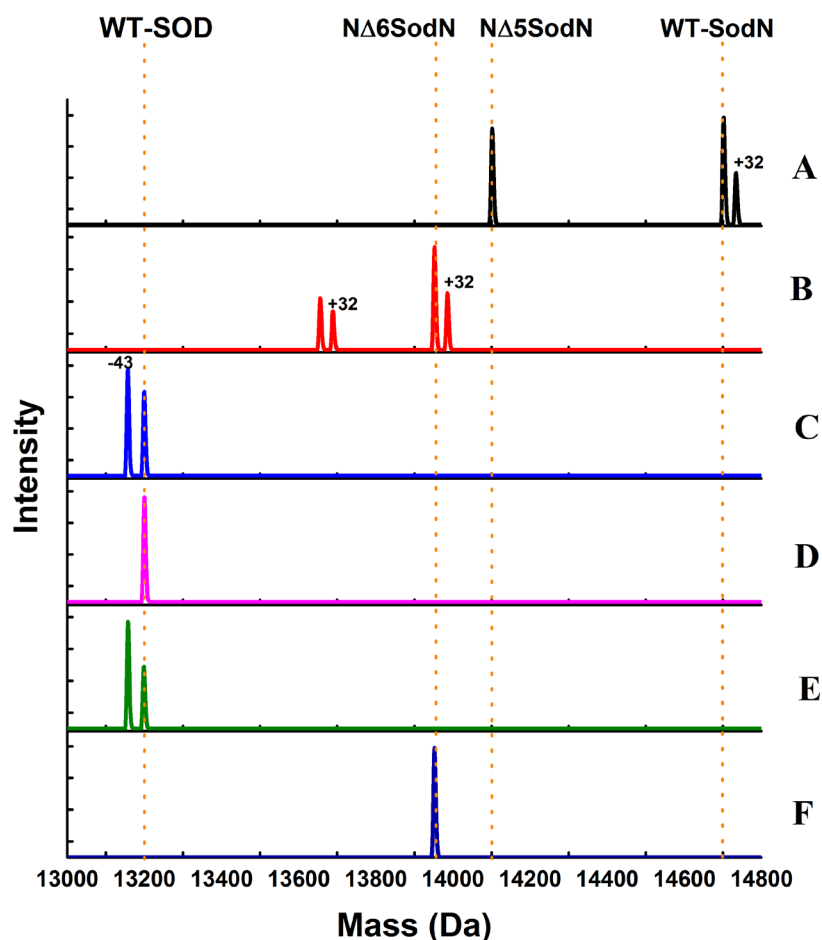


Figure 3.6: Kinetic traces showing disappearance of pulse-radiolytically generated superoxide radical by monitoring absorbance at 260 nm for buffer (brown), and catalytic curves for WT-NiSOD (blue;  $[\text{Ni}] = 3.7 \mu\text{M}$ ), Ni-WT-SodN (black;  $[\text{Ni}] = 9.5 \mu\text{M}$ ), The reaction mixture: WT-SodN + WT-SodX with Ni(II) added after cleavage (green;  $[\text{Ni}] = 4.7 \mu\text{M}$ ), and the reaction mixture: WT-SodN + WT-SodX + Ni in 1 mM L-His (red;  $[\text{Ni}] = 2.8 \mu\text{M}$ ). The trace for buffer reflects the uncatalyzed rate of the bimolecular disproportionation reaction at the relevant  $[\text{O}_2^-]$ , while the red and green traces clearly demonstrate catalysis. The black trace for SodN reflects a small amount of catalysis that may be due to trace impurities. [Note: The samples have varying concentrations of nickel, but only the SodN sample is significantly higher than the others. For WT-NiSOD and WT-SodN samples, the assumption that a single 1:1 complex is present and all the Ni contributes equally to catalysis is valid. In case of reaction mixtures, the concentration of Ni represents the total conc. of Ni complexes, only a fraction of which may be bound productively to correctly processed protein.] (Figure courtesy of Diane E. Cabelli, Brookhaven National Laboratory)



**Figure 3.7: Deconvoluted ESI- MS traces of proteolytic assays containing 40  $\mu\text{M}$  WT-SodX and 40  $\mu\text{M}$  WT-SodN in assay buffer (50mM Tris, 1mM TCEP, pH 8.0): A: apo-WT-SodN incubated with denatured WT-SodX, (SodX was denatured using 1M HCl); B: WT-SodX + WT-SodN pre-incubated with 80  $\mu\text{M}$  NiCl<sub>2</sub>; C: WT-SodX + WT-SodN pre-incubated with 80  $\mu\text{M}$  NiCl<sub>2</sub> + 0.01 mM L-Histidine D: + 0.1 mM L-Histidine; E: + 1.0 mM L-Histidine; F: + 10.0 mM L-Histidine.**

This is consistent with the  $K_d$  values measured for SodN ( $K_d = 21.1\mu\text{M}$ ) and for apo-Ni-SOD ( $K_d = 0.68\mu\text{M}$ ) by ITC (*vide supra*), the SodN value being weaker than that for L-His ( $K_d = 0.2\mu\text{M}$  for Ni(II)-(L-His), and  $K_d = 15\mu\text{M}$  for Ni(II)-(L-His)<sub>2</sub>)<sup>40-42</sup> and the apo-WT-NiSOD value being tighter than Ni(II)-(L-His)<sub>2</sub>. The L-His concentration dependence of processing in presence of 80  $\mu\text{M}$  nickel can be explained by considering the formation of a specific ternary complex (SodN•Ni-

(L-His)) between SodN, Ni, and L-His (Supplementary Fig. 10b), which might promote proper proteolysis. According to this curve, for nickel at 80  $\mu\text{M}$ , the ternary complex can form at 0.01, 0.1 and 1.0 mM of L-His, but not at 0.0 or 10 mM L-His. The fact that no N-terminal processing of SodN was observed for 10 mM L-His (**Figure 3.7F**), further supports the idea that the processing is sensitive to specific L-His concentrations, which form specific nickel-histidine complexes at lower concentrations, such as a 1:1 Ni-(L-His), and that driving the formation of Ni(L-His)<sub>2</sub> with excess L-His (10 mM) is deleterious to processing.

Interestingly, the peaks for WT-SodN and for the other cleavage products are not observed in these spectra. However, high-resolution ESI-MS spectra of these assays (**Appendix A, Figure A.12**), do show the peaks for WT-SodN, N $\Delta$ 6WT-SodN and N $\Delta$ 9WT-SodN, in addition to N $\Delta$ 5-WT-SodN, confirming the presence and less abundance of the precursor and the other truncated species.

### **3.3.2.5 D-Histidine does not rescue *in vitro* processing of SodN by SodX in presence of Ni(II).**

The processing assays conducted in the presence of 0.01, 0.1, and 1.0 mM L-His were repeated only using D-His. The results are summarized in (**Figure 3.8**) and show that, in contrast to the results obtained with L-His, N $\Delta$ 14 processing is not observed in the presence of 80  $\mu\text{M}$  Ni(II) and 0.01 and 0.1 mM D-His, and only a trace of the apo-WT-SOD product is observed at 1.0 mM D-His. This result suggests that a specific chiral ternary complex formed between Ni(II), one L-His and either SodX, SodN, or a SodN-SodX complex might be involved in N-terminal processing of SodN which will not only keep nickel away from interfering with the cleavage site in WT SodN, but will also ensure specific nickel insertion into the pre-active site.

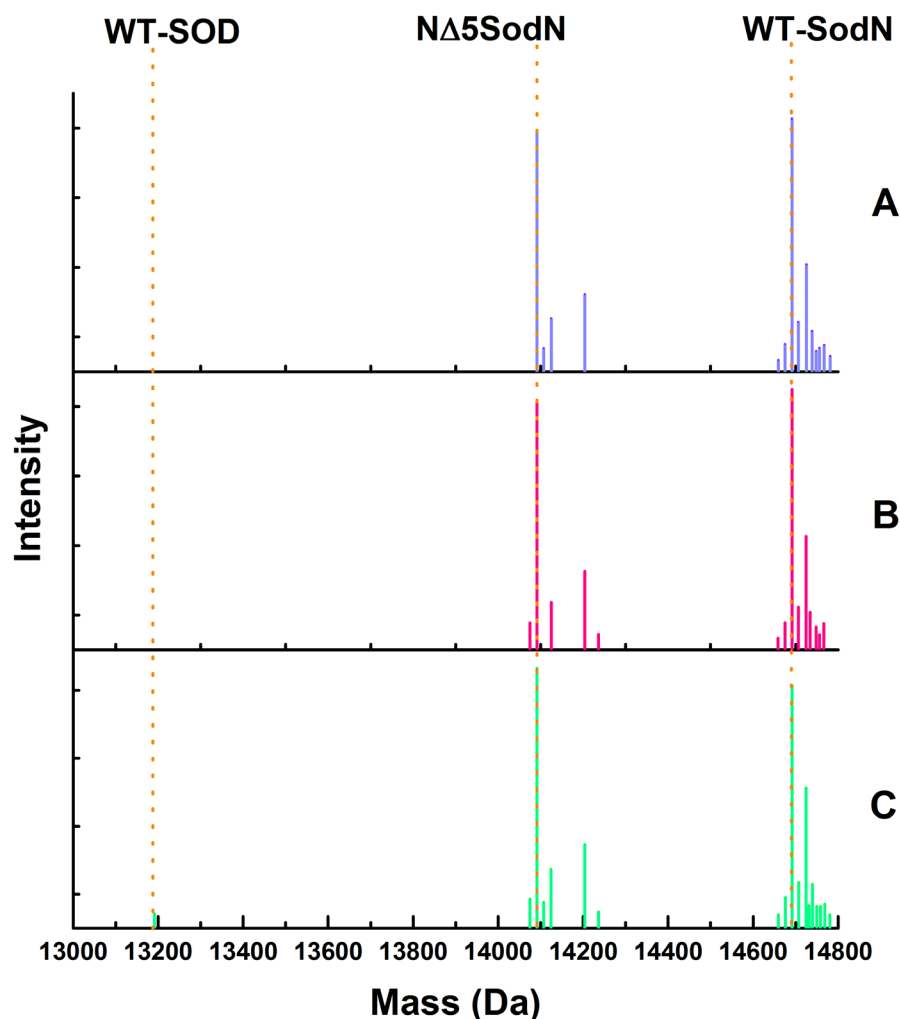


**Figure 3.8. High-resolution deconvoluted ESI- MS traces of proteolytic assays containing 40  $\mu$ M WT-SodX with 40 $\mu$ M WT-SodN pre-incubated with 80 $\mu$ M NiCl<sub>2</sub> in assay buffers containing 50mM Tris, 1mM TCEP, pH 8.0, and A: 0.01 mM D-Histidine; B: 0.1 mM D-Histidine; C: 1.0 mM D-Histidine.**

### 3.4 Discussion

NiSODs constitute a unique class of SOD enzyme that likely evolved in response to the appearance of O<sub>2</sub> in the Earth's atmosphere that made iron less bio-available.<sup>43</sup> Its presence in cyanobacteria makes it the most common SOD in the ocean.<sup>43</sup> In order to utilize Ni(II) as a catalytic metal, the enzyme adopted unique structural features (*e.g.*, Cys ligation, Figure 3.1) that optimize

the normally inaccessible Ni(II/III) redox couple for catalysis,<sup>5, 9, 44</sup> and impart functional properties that are similar to those of the other SOD enzymes, which utilize Mn, Fe, or Cu as catalytic centers.<sup>9</sup> How these metals are recognized *in vivo* and specifically inserted to form active enzyme still remains largely unknown.

NiSOD is expressed as a pro-enzyme, SodN, that requires N-terminal processing in order to produce protein that can subsequently bind nickel by an unknown mechanism *in vivo* to form a nickel-site in the required coordination geometry that can catalyze superoxide disproportionation. The N-termini of SodN proteins from a variety of sources reveal an extension of variable length that contains an invariant Ala-His peptide bond.<sup>11</sup> Previous studies employing cell lysates from *E.coli* expressing *sodN* and *sodX* from cyanobacteria suggested that formation of active NiSOD is nickel- and SodX-dependent with a putative role of SodX as the cognate protease for processing the N-terminus of SodN via hydrolysis of the invariant Ala-His bond and an undefined role of nickel. Processing of SodN by SodX reveals the critical N-terminal residue in NiSOD, His1, which provides two of the nickel ligands in the mature enzyme: the N-terminal amine and the imidazole sidechain.<sup>1,6</sup>

Heterologous expression and purification of *S. coelicolor* WT- SodX in *E. coli* produced a protein with a +691 Da modification, which is proposed to result from O-linked-glycosylation (Deoxyhexose-sulfur), possibly at Ser128, using mass spectroscopic data (*vide supra*). Notably, *E.coli* expresses SPase I, which is a membrane bound protease, where its N-terminal residues (2-75) are expected to be associated with the membrane by an unknown mechanism.<sup>45-46</sup> Membrane bound proteins are often glycosylated, so it is possible that the biosynthetic machinery of *E.coli* glycosylates SodX probably due to sequence and/or structural homology. The glycan modification does not eliminate the activity of SodX in N-terminal processing experiments using ESI-MS for

detection. SodX was found to have no discernible affinity for Ni(II) by ICP, thus excluding the possibility of it being a nickel source (or chaperone) for NiSOD.

The work presented here shows that SodN does not bind Ni(II) as tightly as the processed protein (apo-WT-NiSOD) (Figure 3.2), and does so utilizing a set of ligands that includes an imidazole residue, but lacks the S-donor Cys2 and Cys6 ligands (Figure 3.3 and Figure 3.4) as in the mature NiSOD, and which therefore explains the weaker affinity and weak SOD catalytic activity (Figure 3.6) as well. Our studies show that SodX alone is sufficient for N-terminal processing of SodN (Figure 3.4A), which yields active enzyme upon subsequent nickel addition (**Figure 3.9A**). However, *in vivo*, where cytosolic nickel is buffered to  $10^{-10}$  M<sup>47-48</sup>, given the weak nickel binding affinity of WT-NiSOD, thermodynamic flow of nickel from the buffered nickel pool to newly formed enzyme after the N-terminal proteolysis will be negligible. We also find that proper proteolytic cleavage of SodN by SodX at Ala14-His15 cleavage site is *inhibited* by metals, including Ni(II), (**Figure 3.9B**) which excludes the possibility of nickel-assisted proteolysis as observed in Ni, Fe- hydrogenase. This result was unexpected because maturation of the recombinantly-expressed, apo-WT-NiSOD is readily achieved *in vitro* using processed protein and buffered solutions of Ni(II).<sup>17</sup>

Using a protein variant, H15A-SodN (*S. coelicolor* sequence numbering), we were able to demonstrate that the His residue involved in the Ala14-His15 cleavage site is required for cleavage by SodX (Figure 3.4B). Given this requirement and the role of a His imidazole sidechain in metal binding by SodN (Appendix A, Figure A.5A), the results suggest a possible mechanism for inhibition of N-terminal processing by metal ions: If a metal ion binds to this specific imidazole sidechain, the resulting metal-coordination might impair recognition of the Ala-His bond by SodX. and thus its cleavage by giving non-specific processing products such as NΔ6SodN (**Figure 3.9B**).



This in turn raises a question about *in vivo* maturation of the enzyme, which takes place in the presence of a LMW pool of available Ni(II) that could potentially prevent N-terminal processing. On the other hand, SodX processed P19A-SodN variant to its corresponding P5A-SOD, but the cleaved product did not show activity in the in-gel activity assay. This suggests that Pro19 is not involved in providing the necessary proteolytic-recognition motif for SodX, but may be required for structural rearrangement required for Ni-hook formation (Chapter 4).

Work on the trans-membrane transport of Ni(II) and on the specific metal responses and binding properties of Ni(II)-responsive metalloregulators, such as InrS, point to the importance of L-His to Ni(II) binding in the function of these proteins.<sup>39-40, 49</sup> A complex of Ni(II)-L(His)<sub>2</sub>, and not D-His, was found to specifically bind the nickel importer, NikA in *E.coli* or its homologues in *S. aureus*, and *Y. pestis*.<sup>40, 49</sup> L-His was also found to compete with InrS for Ni(II) in molar ratios similar to that found in cyanobacteria.<sup>39</sup> L-His is found at concentrations of 45 – 180 μM in the cytoplasm of *E.coli*, and *Synechocystis*,<sup>39-40, 50-51</sup> and therefore might also play a role in metallocenter assembly in enzymes. To test this role for NiSOD maturation, we carried out N-terminal processing in the presence of L-His and found that in the presence of biologically relevant concentrations of L-His (10 μM, 100 μM and 1 mM), N-terminal processing was no longer inhibited by Ni(II) and resulted in production of active enzyme (Figure 3.7C-E, Appendix A, Figure A.12C-E, **Figure 3.9C**). This result is consistent with the Ni-binding properties of SodN, L-His, and apo-NiSOD, where the Ni affinity from measured K<sub>d</sub> values has the order: SodN < Ni-(L-His)<sub>2</sub> < apo-NiSOD < Ni-(L-His). Thus, L-His would be expected to compete with SodN for Ni(II) binding, but serve as a source of Ni for apo-NiSOD.

However, very high concentrations (10 mM) of L-His showed that N-terminal processing was again inhibited by presence of Ni(II) ions (**Figure 3.7F, Appendix A, Figure A.12F**). This

suggested that a specific complex, such as Ni(L-His) might be formed by 1 L-His complexed with one Ni(II) ion, may be involved, and that higher concentrations of L-His that would drive the equilibria toward formation of a 2:1 complex might be deleterious. The notion that a specific 1:1 Ni(L-His) complex is involved, is consistent with the result that D-His does not promote N-terminal cleavage of SodN in the presence of Ni(II). If a competition resulting from simple equilibria involving just the chelation of Ni(II) by L-His were involved, D-His would behave the same as L-His. The fact that it does not, implies the existence of a ternary complex formed with either SodN, SodX or a quaternary complex of Ni(L-His) formed with SodN and SodX, where the stereochemical properties of the Ni(His) complex are essential.

A likely structure for this ternary complex is suggested by the ligands available from SodN and the final coordination of Ni(II) in holo-NiSOD. The 1:1 L-His:Ni complex may change the nickel binding affinity so that it binds to Cys16 and/or Cys20 on SodN rather than imidazole of His15, and therefore positions the Ni so that it does not interfere with SodN processing and would also potentially assist in Ni-hook formation in a process involving displacement of the L-His ligand by the N-terminal amine, His1 imidazole, and Cys2 amidate following N-terminal processing. The pH- and microenvironment independent stability constants ( $\log\beta$ ) of Ni(II)-L-His is 8.8, and that of Ni(II)-L-Cys is 9.1, while the stability constant of the ternary complex of Ni(II) with L-His and L-Cys (Ni(II)-(L-His)(L-Cys)) is 18.4, which indicates that the ternary species are comparatively more stabilized than their corresponding binary complexes Ni(II)-L-His or Ni(II)-L-Cys.<sup>42, 52</sup>

Early work showed several potential parallels between mechanisms of NiSOD maturation and another redox active nickel enzyme: Ni,Fe-hydrogenase (H<sub>2</sub>ase), which also uses a thiolate ligation to confer redox activity on the nickel site in order to catalyze the reversible oxidation dihydrogen.<sup>12</sup>

The heterometallic active site of Ni<sub>2</sub>Fe-H<sub>2</sub>ase is buried inside the large subunit, HydB, which is also expressed as a pro-protein, but requires C-terminal processing.<sup>12</sup> The proteolytic processing of Ni<sub>2</sub>Fe-H<sub>2</sub>ase is dependent on the sequential insertion of active site metals – Fe insertion first, along with the non-protein CN<sup>-</sup> and CO ligands, involving the HypCDEF accessory proteins, followed Ni insertion by HypA and HypB.<sup>12-13</sup> Once the metals are inserted into the pre-active site, the cognate endopeptidase (such as, HycI (an aspartyl protease) for large subunit of hydrogenase 3 in *E. coli*)<sup>16</sup> recognizes the C-terminal extension and cleaves it, which facilitates the docking of small subunit containing Fe-S clusters and completes the maturation of Ni, Fe hydrogenase.<sup>12-13</sup> Metal specificity is conferred by the incorporation of the correct metals. Ni(II) cannot be bound to the pro-enzyme prior to the construction of the Fe site, and substitution of other metals (*e.g.*, Zn(II)) for Ni(II) prevents C-terminal processing.<sup>15</sup>

The details of NiSOD maturation are quite distinct from this mechanism, and reveal that the maturation of the two enzymes are similar only in the fact that post-translational processing of a pro-protein are involved. (Maturation of NiSOD does not involve accessory proteins and is inhibited by the presence of the active site metal). Metal specificity in this process is conferred by the availability of other metals, some of which are unavailable due to the high affinity of their metallosensors,<sup>39,47</sup> and by the nature of the L-His complex involved. This latter feature has much in common with specific Ni transport by NikABCDE, which involves recognition by NikA of a 1:1 L-His: Ni(II) complex.<sup>49,53</sup>

### **3.5 Conclusion**

In conclusion, our studies highlighted the role of a potential kinetically labile nickel complex in the maturation of NiSOD that does not have any known metallochaperone for specific

nickel delivery to its active site. ‘Free’ – metals (Co(II), Ni(II), and Zn(II)) bind to NiSOD precursor, SodN, using the histidine at its conserved Ala-His cleavage site and hinder the proper proteolytic processing of its N-terminal leader peptide by its cognate protease, SodX (Figure 3.9A). Proper proteolytic processing of SodN by SodX to yield apo-NiSOD can be promoted either in complete absence of ‘free’-metals (Figure 3.9B), which is an unfeasible cellular condition or by complexing metals, particularly Ni, with biologically relevant nickel-ligands, such as L-Histidine (Figure 3.9C), concentrations of which, should correspond to the formation of a labile nickel-complex. The latter ensures that nickel does not interfere during the proteolytic processing but is available for insertion upon the formation of the ‘Ni-hook’ in apo-SOD. Alternatively, given the stability constants of binary and ternary complexes of Ni with L-Histidine and L-Cysteine, it is possible that nickel insertion to the pre-active site in SodN occurs by the formation of a ternary complex between the labile Ni-L(His) and Cys16 (or Cys20) before the proteolytic processing. However, this model awaits further investigation.

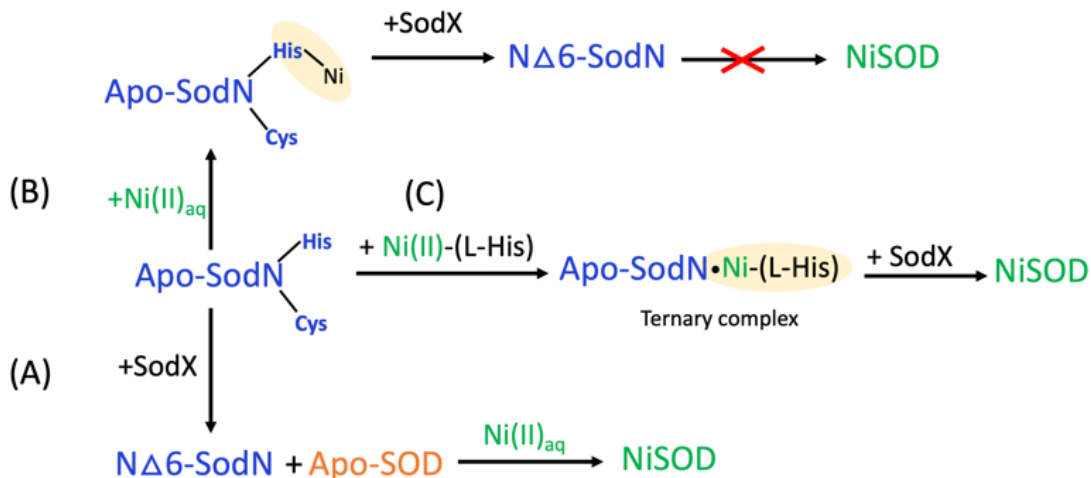


**Figure 3.9: Scheme showing processing and maturation of NiSOD**

### 3.6 References

1. Barondeau, D. P.; Kassmann, C. J.; Bruns, C. K.; Tainer, J. A.; Getzoff, E. D., Nickel superoxide dismutase structure and mechanism. *Biochemistry* **2004**, *43* (25), 8038-8047.
2. Youn, H. D.; Kim, E. J.; Roe, J. H.; Hah, Y. C.; Kang, S. O., A novel nickel-containing superoxide dismutase from *Streptomyces* spp. *Biochem. J.* **1996**, *318* ( Pt 3), 889-896.
3. Ahn, B. E.; Cha, J.; Lee, E. J.; Han, A. R.; Thompson, C. J.; Roe, J. H., Nur, a nickel-responsive regulator of the Fur family, regulates superoxide dismutases and nickel transport in *Streptomyces coelicolor*. *Mol. Microbiol.* **2006**, *59* (6), 1848-1858.
4. Miller, A.-F., Superoxide dismutases: ancient enzymes and new insights. *FEBS Lett.* **2012**, *586* (5), 585-595.
5. Choudhury, S. B.; Lee, J. W.; Davidson, G.; Yim, Y. I.; Bose, K.; Sharma, M. L.; Kang, S. O.; Cabelli, D. E.; Maroney, M. J., Examination of the nickel site structure and reaction mechanism in *Streptomyces seoulensis* superoxide dismutase. *Biochemistry* **1999**, *38* (12), 3744-3752.
6. Wuerges, J.; Lee, J. W.; Yim, Y. I.; Yim, H. S.; Kang, S. O.; Djinovic Carugo, K., Crystal structure of nickel-containing superoxide dismutase reveals another type of active site. *Proc. Natl. Acad. Sci. U. S. A.* **2004**, *101* (23), 8569-8574.
7. Herbst, R. W.; Guce, A.; Bryngelson, P. A.; Higgins, K. A.; Ryan, K. C.; Cabelli, D. E.; Garman, S. C.; Maroney, M. J., Role of conserved tyrosine residues in NiSOD catalysis: a case of convergent evolution. *Biochemistry* **2009**, *48* (15), 3354-3369.
8. Campecino, J. O., Maroney, M. J., Reinventing the Wheel: The NiSOD Story. In *The Biological Chemistry of Nickel*, Deborah Zamble, M. R.-Z., Henryk Kozlowski, Ed. Royal Society of Chemistry: Metallobiology Series No. 10, 2017; Vol. 10, Ch. 9.

9. Sheng, Y.; Abreu, I. A.; Cabelli, D. E.; Maroney, M. J.; Miller, A. F.; Teixeira, M.; Valentine, J. S., Superoxide dismutases and superoxide reductases. *Chem. Rev.* **2014**, *114* (7), 3854-3918.
10. Kim, E. J.; Chung, H. J.; Suh, B.; Hah, Y. C.; Roe, J. H., Transcriptional and post-transcriptional regulation by nickel of sodN gene encoding nickel-containing superoxide dismutase from *Streptomyces coelicolor* Muller. *Mol. Microbiol.* **1998**, *27* (1), 187-195.
11. Eitinger, T., In vivo production of active nickel superoxide dismutase from *Prochlorococcus marinus* MIT9313 is dependent on its cognate peptidase. *J. Bacteriol.* **2004**, *186* (22), 7821-7825.
12. Lacasse, M. J.; Zamble, D. B., [NiFe]-Hydrogenase Maturation. *Biochemistry* **2016**, *55* (12), 1689-1701.
13. Senger, M.; Stripp, S. T.; Soboh, B., Proteolytic cleavage orchestrates cofactor insertion and protein assembly in [NiFe]-hydrogenase biosynthesis. *J. Biol. Chem.* **2017**, *292* (28), 11670-11681.
14. Alfano, M.; Cavazza, C., Structure, function, and biosynthesis of nickel-dependent enzymes. *Protein Sci.* **2020**, *29* (5), 1071-1089.
15. Magalon, A.; Blokesch, M.; Zehelein, E.; Bock, A., Fidelity of metal insertion into hydrogenases. *FEBS Lett.* **2001**, *499* (1-2), 73-76.
16. Theodoratou, E.; Paschos, A.; Magalon, A.; Fritsche, E.; Huber, R.; Bock, A., Nickel serves as a substrate recognition motif for the endopeptidase involved in hydrogenase maturation. *Eur. J. Biochem.* **2000**, *267* (7), 1995-1999.

17. Bryngelson, P. A.; Arobo, S. E.; Pinkham, J. L.; Cabelli, D. E.; Maroney, M. J., Expression, reconstitution, and mutation of recombinant *Streptomycescoelicolor* NiSOD. *J. Am. Chem. Soc.* **2004**, *126* (2), 460-461.
18. Kim, I. K.; Yim, Y. I.; Kim, Y. M.; Lee, J. W.; Yim, H. S.; Kang, S. O., CbiX-homologous protein (CbiXhp), a metal-binding protein, from *Streptomyces seoulensis* is involved in expression of nickel-containing superoxide dismutase. *FEMS Microbiol. Lett.* **2003**, *228* (1), 21-26.
19. Kilcoyne, M.; Gerlach, J. Q.; Farrell, M. P.; Bhavanandan, V. P.; Joshi, L., Periodic acid-Schiff's reagent assay for carbohydrates in a microtiter plate format. *Anal. Biochem.* **2011**, *416* (1), 18-26.
20. Dahlqvist, A.; Olsson, I.; Nordén, Å., The periodate-schiff reaction: Specificity, kinetics, and reaction products with pure substrates. *J. Histochem. & Cytochem.* **1965**, *13* (6), 423-430.
21. Hu, H. Q.; Johnson, R. C.; Merrell, D. S.; Maroney, M. J., Nickel Ligation of the N-Terminal Amine of HypA Is Required for Urease Maturation in *Helicobacter pylori*. *Biochemistry* **2017**, *56* (8), 1105-1116.
22. Ryan, K. C.; Johnson, O. E.; Cabelli, D. E.; Brunold, T. C.; Maroney, M. J., Nickel superoxide dismutase: structural and functional roles of Cys2 and Cys6. *J. Biol. Inorg. Chem.* **2010**, *15* (5), 795-807.
23. Campecino, J. O.; Dudycz, L. W.; Tumelty, D.; Berg, V.; Cabelli, D. E.; Maroney, M. J., A Semisynthetic Strategy Leads to Alteration of the Backbone Amidate Ligand in the NiSOD Active Site. *J. Am. Chem. Soc.* **2015**, *137* (28), 9044-9052.
24. Ryan, K. C.; Guce, A. I.; Johnson, O. E.; Brunold, T. C.; Cabelli, D. E.; Garman, S. C.; Maroney, M. J., Nickel superoxide dismutase: structural and functional roles of His1 and its H-bonding network. *Biochemistry* **2015**, *54* (4), 1016-1027.

25. Huang, H. T.; Dillon, S.; Ryan, K. C.; Campecino, J. O.; Watkins, O. E.; Cabelli, D. E.; Brunold, T. C.; Maroney, M. J., The Role of Mixed Amine/Amide Ligation in Nickel Superoxide Dismutase. *Inorg. Chem.* **2018**, *57* (20), 12521-12535.
26. Webb, S. M., SIXPack a Graphical User Interface for XAS Analysis Using IFEFFIT. *Physica Scripta* **2005**, 1011-1014.
27. Kelley, L. A.; Mezulis, S.; Yates, C. M.; Wass, M. N.; Sternberg, M. J., The Phyre2 web portal for protein modeling, prediction and analysis. *Nat. Protoc.* **2015**, *10* (6), 845-858.
28. Paetzel, M.; Goodall, J. J.; Kania, M.; Dalbey, R. E.; Page, M. G., Crystallographic and biophysical analysis of a bacterial signal peptidase in complex with a lipopeptide-based inhibitor. *J. of Biol. Chem.* **2004**, *279* (29), 30781-30790.
29. Weydert, C. J.; Cullen, J. J., Measurement of superoxide dismutase, catalase and glutathione peroxidase in cultured cells and tissue. *Nat. Protoc.* **2010**, *5* (1), 51-66.
30. Butre, C. I.; Buhler, S.; Sforza, S.; Gruppen, H.; Wierenga, P. A., Spontaneous, non-enzymatic breakdown of peptides during enzymatic protein hydrolysis. *Biochim. Biophys. Acta* **2015**, *1854* (8), 987-994.
31. Fiedler, A. T.; Bryngelson, P. A.; Maroney, M. J.; Brunold, T. C., Spectroscopic and computational studies of Ni superoxide dismutase: electronic structure contributions to enzymatic function. *J. Am. Chem. Soc.* **2005**, *127* (15), 5449-5462.
32. Colpas, G. J.; Kumar, M.; Day, R. O.; Maroney, M. J., Structural investigations of nickel complexes with nitrogen and sulfur donor ligands. *Inorg. Chem.* **1990**, *29* (23), 4779-4788.
33. Milan Melnik; Tibor Sramko; Michal Dunaj--Jurco; Anton Sirota; Clive E. Hollow Ay, Nickel coordination compounds: Classification and analysis of crystallographic and structural data. *Rev. Inorg.Chem.* **1994**, *14* (1-4), 1.



34. Rosenfield, S. G.; Berends, H. P.; Gelmini, L.; Stephan, D. W.; Mascharak, P. K., New octahedral thiolato complexes of divalent nickel: syntheses, structures, and properties of (Et<sub>4</sub>N)[Ni(SC<sub>5</sub>H<sub>4</sub>N)<sub>3</sub>] and (Ph<sub>4</sub>P)[Ni(SC<sub>4</sub>H<sub>3</sub>N<sub>2</sub>)<sub>3</sub>].CH<sub>3</sub>CN. *Inorg. Chem.* **1987**, *26* (17), 2792-2797.
35. Paetzel, M.; Dalbey, R. E.; Strynadka, N. C., Crystal structure of a bacterial signal peptidase in complex with a beta-lactam inhibitor. *Nature* **1998**, *396* (6707), 186-190.
36. M., P., Bacterial Signal Peptidases. *Subcell Biochem.* **2019**, *92*, 187-219.
37. UniProt: a worldwide hub of protein knowledge. *Nucleic Acids Res.* **2019**, *47*, D506-515.
38. Riener, C. K.; Kada, G.; Gruber, H. J., Quick measurement of protein sulfhydryls with Ellman's reagent and with 4,4'-dithiodipyridine. *Anal. and Bioanal. Chem.* **2002**, *373* (4-5), 266-276.
39. Foster, A. W.; Pernil, R.; Patterson, C. J.; Scott, A. J. P.; Palsson, L. O.; Pal, R.; Cummins, I.; Chivers, P. T.; Pohl, E.; Robinson, N. J., A tight tunable range for Ni(II) sensing and buffering in cells. *Nat. Chem. Biol.* **2017**, *13* (4), 409-414.
40. Chivers, P. T.; Benanti, E. L.; Heil-Chapdelaine, V.; Iwig, J. S.; Rowe, J. L., Identification of Ni-(L-His)<sub>2</sub> as a substrate for NikABCDE-dependent nickel uptake in Escherichia coli. *Metallomics : integrated biometal science* **2012**, *4* (10), 1043-1050.
41. Zhang, Y.; Akilesh, S.; Wilcox, D. E., Isothermal Titration Calorimetry Measurements of Ni(II) and Cu(II) Binding to His, GlyGlyHis, HisGlyHis, and Bovine Serum Albumin: A Critical Evaluation. *Inorg. Chem.* **2000**, *39* (14), 3057-3064.
42. Smith, R. M., Martell, A. E., *Critical Stability Constants*. Plenum: New York, 1989; Vol. 6.

43. Cuvelier, M. L.; Allen, A. E.; Monier, A.; McCrow, J. P.; Messié, M.; Tringe, S. G.; Woyke, T.; Welsh, R. M.; Ishoey, T.; Lee, J.-H.; Binder, B. J.; DuPont, C. L.; Latasa, M.; Guigand, C.; Buck, K. R.; Hilton, J.; Thiagarajan, M.; Caler, E.; Read, B.; Lasken, R. S.; Chavez, F. P.; Worden, A. Z., Targeted metagenomics and ecology of globally important uncultured eukaryotic phytoplankton. *Proc. Natl. Acad. Sci. U.S.A.* **2010**, *107* (33), 14679-14684.
44. Deborah Zamble, M. R.-Z., Henryk Kozłowski, *The Biological Chemistry of Nickel*. Royal Society of Chemistry: Cambridge, U.K., 2017.
45. Paetzel, M., Structure and mechanism of Escherichia coli type I signal peptidase. *Biochim. Biophys. Acta* **2014**, *1843* (8), 1497-1508.
46. Auclair, S. M.; Bhanu, M. K.; Kendall, D. A., Signal peptidase I: cleaving the way to mature proteins. *Protein Sci.* **2012**, *21* (1), 13-25.
47. Foster, A. W.; Osman, D.; Robinson, N. J., Metal preferences and metallation. *J. Biol. Chem.* **2014**, *289* (41), 28095-28103.
48. Frausto da Silva, J. J. R., and Williams, R. J. P. , *The Biological Chemistry of the Elements: The Inorganic Chemistry of Life*. Oxford University Press: Oxford, 1991.
49. Chivers, P. T., Nickel recognition by bacterial importer proteins. *Metallomics : integrated biometal science* **2015**, *7* (4), 590-595.
50. Bennett, B. D.; Kimball, E. H.; Gao, M.; Osterhout, R.; Van Dien, S. J.; Rabinowitz, J. D., Absolute metabolite concentrations and implied enzyme active site occupancy in Escherichia coli. *Nat. Chem. Bio.* **2009**, *5* (8), 593-599.
51. Trumbo, P.; Yates, A. A.; Schlicker, S.; Poos, M., Dietary reference intakes: vitamin A, vitamin K, arsenic, boron, chromium, copper, iodine, iron, manganese, molybdenum, nickel, silicon, vanadium, and zinc. *J. Am. Dietetic Assoc.* **2001**, *101* (3), 294-301.

52. M.Sivasankar Nair, P. T. A., M. Sankaranarayana Pillai, Chidambaram Natarajan, Mixed-ligand complexes involving sulfur-containing ligands. Part1. Nickel(II) ternary complexes of L-cysteine, D-penicillamine and L-cysteic acid with imidazoles *J. Chem. Soc., Dal. Trans.* **1993**, (6), 917-921.
53. R. M. Howlett, B. M. H., A. Hitchcock, D. J. Kelly, *Microbiology* **2012**, *158*, 1645-1655.

## CHAPTER 4

### ROLE OF PROLINE5 IN STRUCTURE AND FUNCTION OF NICKEL SUPEROXIDE DISMUTASE

#### 4.1 Introduction

Nickel Superoxide Dismutase is a distinct representative of the Superoxide Dismutase (SOD) family of enzymes. It is a product of *sodN*, which encodes a precursor with an extended N-terminal sequence (leader/signal sequence), that is proteolytically cleaved at the invariant Ala-His peptide bond to form active NiSOD upon nickel incorporation.<sup>1-2</sup> The nickel active site in NiSOD is located at the N-terminus where the highly conserved N-terminal HCXXPCXXY motif forms the ‘Ni-hook’ (**Figure 4.1**), which is disordered in absence of nickel.<sup>3-4</sup> In as-isolated resting oxidized WT-NiSOD, nickel in the active site occurs as a 50 : 50 mixture of Ni(II) and Ni(III), and nickel, depending on its oxidation state, is coordinated to a unique mix of N- and S- ligands that tune the redox potential of Ni(II)/Ni(III) couple (~290 mV) in such a way that it can catalyze the superoxide disproportionation reaction.<sup>4-7</sup> The nickel ligands in the active site of NiSOD are the N-terminal amine (-NH<sub>2</sub>), backbone amidate N atom (-N<sup>-</sup>) of Cys2, and two thiolates (-S<sup>-</sup>) from Cys2 and Cys6 (in cis- configuration).<sup>3-4, 6, 8-11</sup> An additional ε-N- ligand from the imidazole of His1 binds axially to the Ni(III) site and stabilizes it.<sup>5-6</sup> Site – directed mutagenesis of the primary coordination sphere of NiSOD, and extensive biophysical and spectroscopic studies have highlighted the specific role of each of the nickel binding residues in its structure and catalytic properties.<sup>7-12</sup>

An interesting and unexplored feature of NiSOD is the role of the conserved Proline 5 (Pro5, in WT-NiSOD) in the formation of the Ni-hook. Recent studies on a Pro5 to Ala variant of NiSOD model peptide suggested a possible role of this residue in providing the accessibility to Cys6 for nickel binding.<sup>13</sup> Although the initial configuration of Pro5 in apo - WTSOD or the

corresponding Pro19 in its precursor SodN is unknown, crystal structure of WT - NiSOD reveals that Pro5 in the active enzyme is in cis – conformation (a condition which is observed only in 5% of the proteins<sup>14</sup>). Previous studies had postulated a trans – cis isomerization of Pro5 post proteolysis that mediates the correct positioning of the active site residues,<sup>3</sup> but an experimental verification of this hypothesis is lacking. Interestingly, in-gel activity of the nickel-added proteolytic mixture containing P19ASodN variant and SodX failed to show NiSOD activity which may be due to the inability of the corresponding P5A-NiSOD variant to form the classic ‘Ni-hook’(Chapter 3) caused by hindering the trans-cis isomerization by an Ala substitution in the variant , but molecular details of this process is unknown.

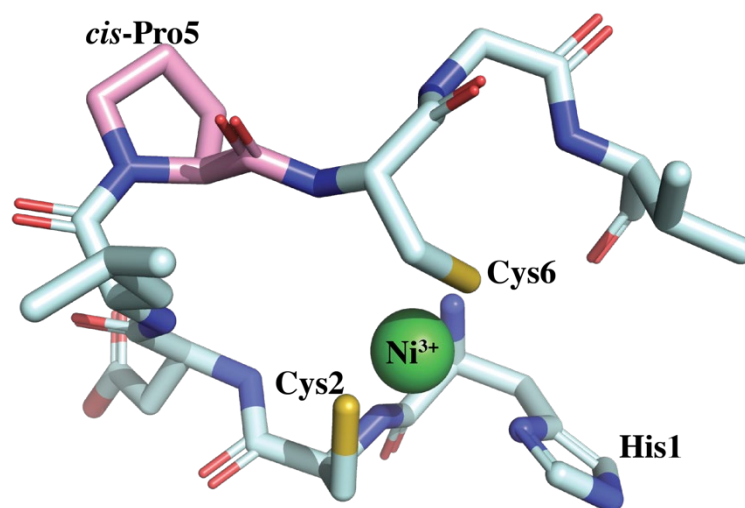


**Figure 4.1: Ball & Stick representation of residues 1 – 7 of Ni-hook in as-isolated WT-NiSOD (PDB ID: 1T6U). His1 is shown in His<sub>on</sub> and His<sub>off</sub> configuration observed in Ni(III) and Ni(II) sites, respectively. Side chain of Pro5 is shown in magenta.**

Proline is a non-polar, aliphatic, and the only proteinogenic amino acid with a secondary amine. In proline, the alpha amino group is directly attached to -CH<sub>2</sub> of the side - chain from  $\alpha$ -carbon, forming a five-membered cyclic structure (**Figure 4.2**). An amide bond between any amino acid (X) and proline using its secondary amine N-atom lacks the H-donor moiety but can

act as a H-acceptor. Compared to other amino acids, the distinct cyclic structure of proline makes it an exceptional, conformationally rigid amino acid that affects the secondary structure of proteins. The secondary structure of proteins is explained by the dihedral angles ( $\phi$ ,  $\psi$ , and  $\omega$ ) of protein backbone. Due to the cyclic nature of Pro, it is one of the two special amino acids which do not follow a typical Ramachandran's plot with only few allowed degrees of rotation of its  $\psi$  and  $\phi$  angles where its  $\phi$  angle is locked at  $-65^\circ$ . Consequently, compared to other amino acids, the free entropy of proline is significantly less, and hence it is predominantly found in 'turns' of the protein structure where there is a small difference in the entropy of its folded and unfolded states.

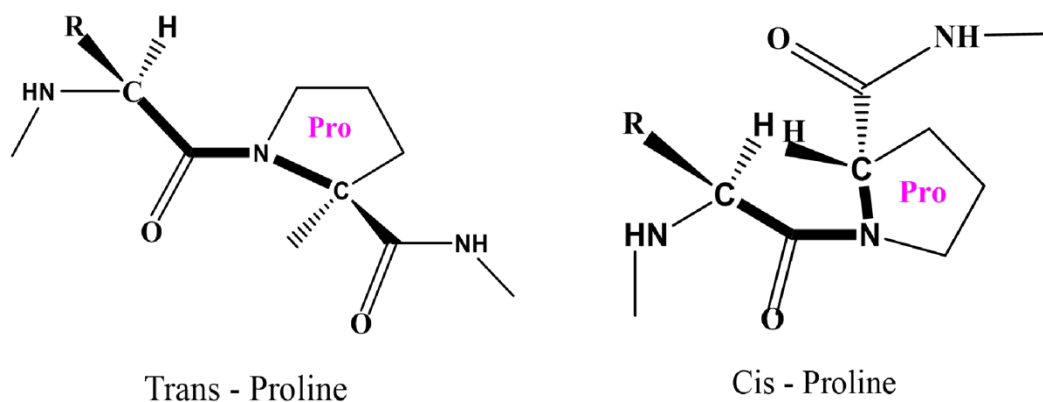


**Figure 4.2: Trans - & Cis - configuration of proline in peptides**

Typically, amino acids including prolines, are preferentially translated in trans-conformation to avoid steric effects. However, unlike other amino acids, proline can populate both its cis- and trans – configurations, and is one of the important ways to achieve large conformational changes and reach various macrostates of multidomain proteins without modification of covalent structures.<sup>15-19</sup> Many crucial biological processes such as, cell signaling, neurodegeneration, channel gating, gene regulation, epigenetic modifications, and others are controlled by conformational changes mediated by proline switching.<sup>15</sup> The cis-trans isomerization of proline in

X-Pro peptides can be defined as the two distinct states of the backbone dihedral angle  $\omega$  ( $C\alpha-C-N-C\alpha$ ) at  $0^\circ$  for cis and  $\pm 180^\circ$  for trans (**Figure 4.2**).<sup>15</sup> The free energy barriers to rotation about the torsion angle is  $\sim 13$  kcal/mol, which can be altered due to different substitutions and side chain effects.<sup>20-21</sup> As shown by experimental, theoretical, and statistical investigations, the population of the trans – conformation of proline predominates ( $> 95\%$ ) in short peptides containing only one proline residue, polyproline peptides, and in large proteins with nonredundant chains from Protein Data Bank.<sup>15</sup> This trans state preference is attributed to steric and electronic effects of ring atoms. Changes in the local and global environments of short peptides or large proteins can lead to substantial variation in the equilibria and exchange rates between macrostates. Although the trans-state of proline is predominant among large proteins, recent studies identified increased population of cis-state in some systems such as staphylococcal nuclease, 5-HT3 receptor and Crk adaptor proteins.<sup>15</sup>

In this chapter, using site directed mutagenesis and spectroscopic techniques, we investigate and elucidate the role of Pro5 in the structure and function of NiSOD.

## 4.2 Experimental Procedures

### 4.2.1 Site-Directed Mutagenesis, Protein Purification and characterization

A pET22b (+) vector (with Ampicillin resistance) encoding wild-type *NiSOD* sequence (from *S. coelicolor*) preceded by a *pelB* sequence was used as the template DNA for the single point mutation using polymerase chain reaction (PCR) and the following primers: Forward - 5' GACCTGGCCCTGCGGCGTGTAC 3', and Reverse - 5' GTACACGCCGCAGGCCCAGGTC 3' were designed to incorporate the desired mutation (indicated by the underline). For each 50  $\mu$ L volume of PCR reaction mixture, 0.5  $\mu$ M of each primer was used for 2 ng of template DNA.

Successful PCR amplifications were determined using an 0.8% agarose gel, and the amplicons were subsequently digested with DpnI for 1 hr at 37°C to remove any methylated template DNA. The digested PCR mixture was then used to transform DH5 $\alpha$  competent cells. The transformed cells were grown in 0.5 mL Luria Bertini (LB) media in 5 ml tubes at 37°C for 1 hour and aliquots were plated on agar plates containing ampicillin antibiotic followed by a 12-16 hour incubation at 37°C. Single colonies were grown to saturation in 5ml LB-miller broth supplemented with ampicillin at 37°C. Cells were pelleted at 13,000 g for 5 minutes and the plasmids were isolated using GeneJET plasmid miniprep kit (Thermo Fisher Scientific). Gene sequencing (Genewiz, Inc.) confirmed the successful mutation.

The pET22b-peIB-P5ANiSOD plasmid construct was used to transform BL21(DE3) cells. The transformed cells were grown in 0.5 mL Luria Bertini (LB) media in 5 ml tubes at 37°C for 1 hour and aliquots were plated on agar plates containing ampicillin antibiotic followed by a 12-14 hour incubation at 37°C. A single colony was picked and grown overnight in LB media (200 mL) supplemented with ampicillin at 37°C with shaking at 200 rpm. A 10 mL aliquot of the overnight culture was added to 1 L of the pre-warmed fresh LB media containing ampicillin, grown to an OD<sub>600</sub> of 0.6 - 0.8, and then induced with 0.8mM of isopropyl –  $\beta$ -D-1-thiogalactopyranoside for 3 - 4 hours at 37°C. Cells were harvested by centrifugation at 4000 g for 15 min and then re-suspended in 100 mL of osmotic shock buffer (20% sucrose, 1 mM EDTA, 30 mM Tris.HCl, pH 8.0) per liter of culture. The cell suspension was shaken at 180 rpm for 15 minutes at room temperature and centrifuged at 4000 g for 10 minutes. The supernatant was discarded, and the cells were then re-suspended in 100 mL ice-cold 5mM MgSO<sub>4</sub> per liter of culture. The resuspended cells were shaken at 4°C for 10 minutes and then centrifuged at 10,000 g for 10 minutes. The pellet was discarded, and the supernatant was collected for further purification.



All chromatographic purification steps were carried out using AKTA-FPLC system (Amersham Biosciences). The supernatant was loaded onto a pre-equilibrated Q-Sepharose column (GE Health Sciences) at a rate of 2.00 ml/min with buffer A (50 mM Tris, pH 8.0). Once the absorbance returned to baseline value, the protein was eluted with a linear gradient of Buffer B (50 mM Tris, 1 M NaCl, pH 8.0). All the fractions containing protein was collected and analyzed using SDS-PAGE. Fractions containing P5A-SOD (MW 13,676 Da) were pooled and loaded on a 120 mL HiLoad 16/60 Superdex 75 (GE Life Sciences) column equilibrated with Buffer C (50 mM Tris, 200 mM NaCl, pH 8.0). Protein fractions were collected on the basis of absorbance values at 280 nm and the purity of collected protein fractions were analyzed by SDS-PAGE. Fractions containing P5A-NiSOD were pooled, concentrated and frozen at -20°C until ready to use.

The molecular weight of the purified protein was confirmed using electrospray - ionization mass spectrometry (ESI-MS) using a Thermo Orbitrap Fusion Tribrid instrument. The molecular weight of P5A-NiSOD was calculated as 13,676.12 Da, found 13,674.12 Da.

#### **4.2.2 Isothermal Titration Calorimetry**

Isothermal titration calorimetry (ITC) was used to measure the heat released by Ni-binding to apo-WT-SOD and apo-P5A-SOD proteins using an Auto-ITC200 model microcalorimeter (Microcal/Malvern). The instrument has a cell volume of 200  $\mu$ L and a syringe volume of 40  $\mu$ L, which were filled by robotic arms from plates stored at 4°C prior to the start of the experiment. All titrations were performed in ITC Buffer (20 mM Tris, 1 mM TCEP, 200 mM NaCl, pH 8.0) at 25°C with the reference cell filled with water. A stock of purified proteins (WT- or P5A - SOD) were buffer exchanged in ITC buffer (20 mM Tris, 1 mM TCEP, 200 mM NaCl, pH 8.0) using Amicon Ultra – 0.5 mL centrifugal filters with 3-kDa MWCO pre-equilibrated with ITC Buffer

and then diluted to 150  $\mu\text{M}$  for titration immediately before the ITC experiments.  $\text{NiCl}_2$  was dissolved in MilliQ purified water from a 10 mM stock solution, and its exact concentration was checked by ICP-OES. An aliquot of this solution was diluted in ITC Buffer to a final concentration of 2 mM and was used for titrations.

For each ITC experiment, 20 injections were made from the syringe into the cell and the change in heat was monitored by the instrument. The initial injection contained only 0.4  $\mu\text{L}$  and was used to minimize the equilibration artifacts sometimes observed with the first injection and was not included in fitting the data. All subsequent injections at 2.0  $\mu\text{L}$  each were used for fitting the titration curve in each experiment. For titration of apo-WT-SOD or apo-P5A-SOD with  $\text{NiCl}_2$ , the spacing between injections was set to 300 sec. Experimental titrations were accompanied by corresponding reference/control titrations of  $\text{NiCl}_2$  into ITC Buffer in the cell, the resulting heats of which were used to establish the corresponding baseline corrections used for fitting the  $\Delta\text{H}$  data. Experimental titrations were performed thrice using separately prepared proteins, and each replicate produced similar results.

The resulting data were fitted using the MicroCal analysis module in Origin7.0. First, the thermograms from the titration experiments were baseline corrected and then integrated to produce the corresponding  $\Delta\text{H}$  curve. The  $\Delta\text{H}$  curves for each experiment were corrected by subtracting the average  $\Delta\text{H}$  from the reference titration. The  $\Delta\text{H}$  curves were fitted with the OneSites model to find the apparent  $K_a$  (multiple fitting models were attempted for each set of experimental data and in each case the OneSites model produced the best  $\chi^2$  value). The apparent  $K_d$  values reported are the inverse of the  $K_a$  values obtained from each fit.

### 4.2.3 Metalation of P5A-SOD

All metalation steps on the purified P5A-SOD protein was performed inside the anaerobic glovebox (Coy Laboratory Products, Inc.). The purified protein was reduced with 5-fold excess of DTT (Dithiothreitol), and excess DTT was removed by buffer exchanging the protein with degassed Buffer C in Zeba spin columns (Amicon, 3kDa MWCO). The reduced and buffer exchanged protein was then reconstituted with 3-fold excess of NiCl<sub>2</sub>, and excess nickel was removed by Chelex (Sigma Aldrich), followed by buffer exchange in degassed Buffer C. ICP-MS was used to quantify the nickel content of the reconstituted P5A-NiSOD. Briefly, an aliquot from a stock solution of ICP-MS standard QC 21 (Analytical West) was used to make standard solutions (5mL each) containing nickel from 0 ppb - 40 ppb. 250 μL of aqua-regia was added to each of these solutions and the final volume was adjusted to 5 mL. The standards were injected into ICP-MS (Perkin Elmer Nexion). Deionized water was used as the blank, and the intensity of <sup>58</sup>Ni obtained from the blank was subtracted from each reading. A calibration curve using the intensity values of each of the standard solutions was prepared. A sample of P5A-NiSOD was made similarly and its nickel content was determined using the standard calibration curve.

### 4.2.4 UV-Visible Spectroscopy

UV-Visible Spectroscopy was used to determine protein concentration as well as for the spectral characterization and comparison of the as-isolated, P5A-NiSOD with as-isolated WT Ni-SOD. Reconstituted (nickel added) P5A-NiSOD was diluted to 100μM with Buffer C and its spectra was recorded on Hewlett-Packard 8453 UV-visible spectrophotometer. Three molar equivalents of sodium dithionite were added for reduction of P5A-NiSOD in anaerobic glove bag

and mixed by inversion. Spectra for 100 $\mu$ M reduced P5A-NiSOD sample in gas-tight quartz cuvette (FireflySci) was recorded using the same UV-Visible spectrophotometer.

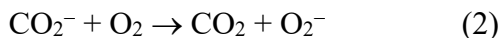
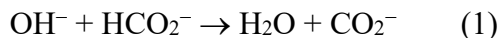
#### **4.2.5 Electron Paramagnetic Resonance**

A 200 $\mu$ L sample of as-isolated holo-P5A-NiSOD (0.5 mM based on nickel concentration) in 50 mM Tris, 200 mM, pH 8.0 was used for EPR experiments. As a standard, solution of Cu-EDTA (0.5 mM) was also made in water. The samples were transferred to EPR tubes and flash frozen in liquid nitrogen. EPR samples were run using finger dewar on a Bruker Elexsys E-500 EPR instrument equipped with DM4116 cavity at 9.609 GHz frequency, 6.0131 mW power, 10G modulation amplitude, 100 GHz modulation frequency, 327 ms time constant, 77K.

Processing and double integration of EPR signals from Cu-EDTA or P5A-NiSOD were performed using the in-built integration software in the Xepr program. The number of spins from 0.5 mM Cu-EDTA was taken as standard and were used to determine the number of spins in as-isolated P5A-NiSOD.

#### **4.2.6 Pulse radiolysis for kinetics**

A 100  $\mu$ M nickel-loaded P5A-NiSOD was diluted with Buffer C and buffer exchanged in a solution containing 10 mM phosphate, 30 mM formate, pH 7.5. Pulse radiolysis to generate superoxide to study catalysis by holo-P5A-NiSOD samples was carried out by Dr. Diane Cabelli at Brookhaven National laboratory using a 2-meV Van de Graff accelerator. Superoxide radicals were generated upon pulse radiolysis of an aqueous air/O<sub>2</sub>-saturated solution containing 10 mM phosphate, 30 mM formate, and 5 $\mu$ M EDTA, pH 7.5.



Catalytic rate constants were obtained by monitoring the disappearance of  $\text{O}_2^-$  at 260 nm in presence of micromolar concentrations of P5A-NiSOD. The path length of the quartz cell used was 2.0 cm and a 100 – 700 ns pulse width was chosen, resulting in the generation of 1-7  $\mu\text{M}$   $\text{O}_2^-$  per pulse. The reported rate constants are based on metal concentration, with the assumption that all nickel ions are specifically bound and contribute equally to  $\text{O}_2^-$  dismutation.

## 4.3 Results

### 4.3.1 Isothermal Titration Calorimetry

The nickel binding profile of P5A-NiSOD was evaluated using Isothermal Titration Calorimetry (ITC) (**Figure 4.3**) and compared with that of WT-NiSOD (Chapter 3). Titration of apo-WT-SOD with a solution of  $\text{NiCl}_2$ , as detailed in the Methods section, was exothermic and the analysis of the resulting binding isotherm is consistent with a single binding event involving 0.95(2) nickel per protein with an apparent  $K_d$  of 0.68(2)  $\mu\text{M}$ . Apo-P5A-SOD, on the other hand, bound 0.76(2) nickel per subunit but with an apparent  $K_d$  of 0.16 (0.02)  $\mu\text{M}$ , which is six-fold tighter than that for apo-WT-SOD.

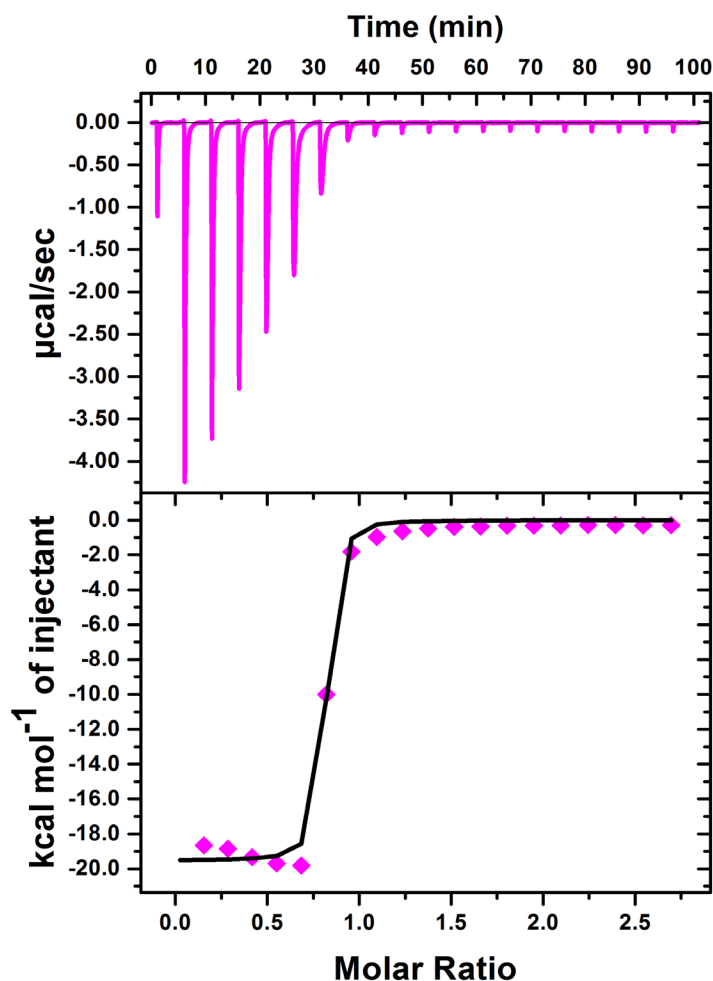


**Figure 4.3:** ITC thermogram (top) and Ni binding isotherm (bottom) for 0.15 mM apo-P5A-SOD (magenta) titrated with 2 mM Ni(II) in buffer containing 20 mM Tris, 200mM NaCl, 1mM TCEP, pH 8.0. A one-site binding model was used to fit (solid black line) the binding of Ni(II) to P5A-SOD.

### 4.3.2 Electronic Structure

UV - Vis absorption spectra of recombinant, as - isolated P5A - NiSOD and WT - NiSOD samples from *S. coelicolor* are shown in **Figure 4.4**. The as - isolated P5A - NiSOD spectrum is similar to as - isolated WT - NiSOD spectrum, and features the transition near 370 nm, which is characteristic of a  $S_{Cys} \rightarrow Ni(III)$  Ligand to Metal Charge Transfer (LMCT) transition and also confirms the presence of a Ni(III)-site in the variant.<sup>22</sup>

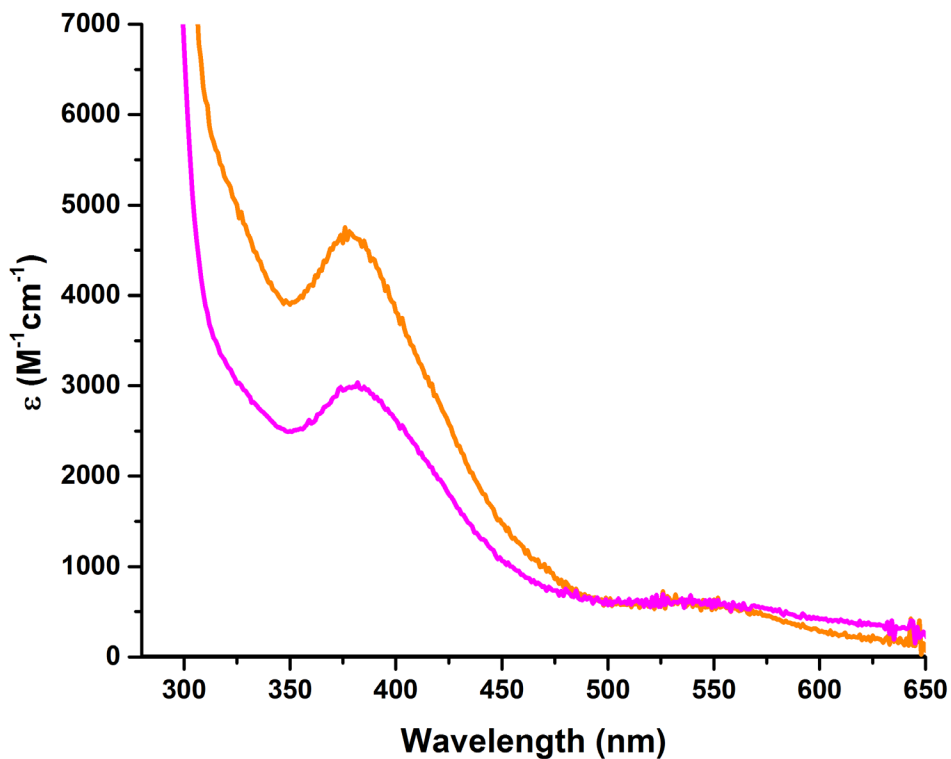
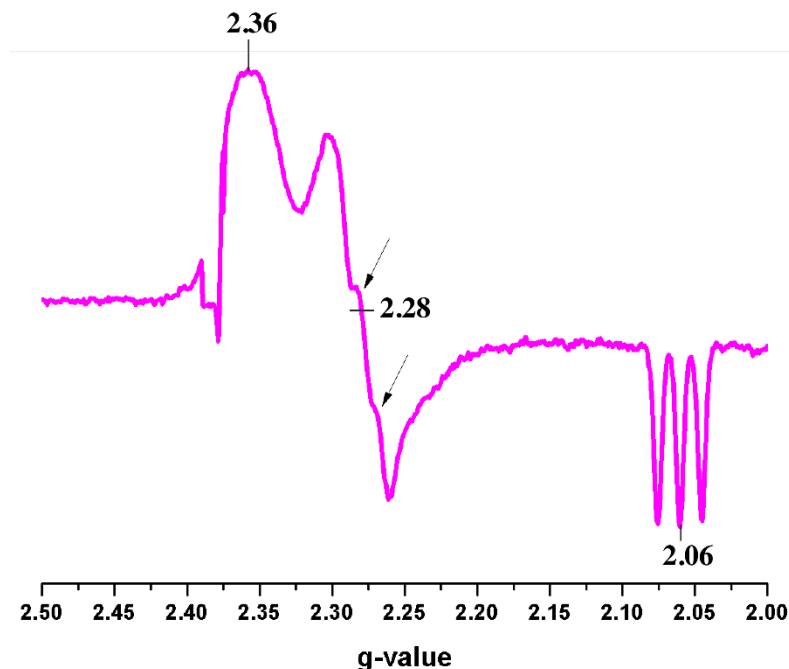


**Figure 4.4:** UV-Vis spectra of 100  $\mu\text{M}$  (in total nickel concentration that includes Ni(II) and Ni(III)) as – isolated WT-NiSOD (orange) and as – isolated P5A-NiSOD (magenta).

Previous studies suggested that the molar extinction coefficient ( $\epsilon$ ) of the charge transfer (CT) transition at 370 nm in as-isolated WT- NiSOD (containing a 50:50 mixture of Ni(II) and Ni(III)) should be  $\sim 4600 \text{ M}^{-1}\text{cm}^{-1}$  and that of  $\text{S} \rightarrow \text{Ni(III)}$  (where Ni(III) content is 50%, based on EPR spin quantization) is  $7600 \text{ M}^{-1}\text{cm}^{-1}$ .<sup>23</sup> UV-Visible absorption spectra of as-isolated P5A-NiSOD (**Figure 4.4**) shows that  $\epsilon$  of the CT transition at 370 nm of this variant is  $\sim 3000 \text{ M}^{-1}\text{cm}^{-1}$ , which is less than that for the as-isolated WT-NiSOD. Using the reported molar extinction coefficient ( $\epsilon_{370}$ ) of  $\text{S} \rightarrow \text{Ni(III)}$  CT of WT-NiSOD, the calculated Ni(III) content in P5A-NiSOD is expected to be  $\sim 32.6\%$ . However, spin integration of EPR spectra of as-isolated P5A-NiSOD (**Figure 4.5**) reveal that 40% of the nickel in the variant is Ni(III), which does not match the expected Ni(III) content derived from the UV-visible absorption spectra, and thus indicates a

different molar extinction coefficient for  $S \rightarrow Ni(III)$  CT in the variant. The difference in the absorbances at 378 nm for as-isolated P5A-NiSOD and dithionite reduced P5A-NiSOD yields the absorbance associated with  $S \rightarrow Ni(III)$  CT in P5A-NiSOD, and as Ni(III) content in P5A-NiSOD is 40%, the estimated molar extinction coefficient for  $S \rightarrow Ni(III)$  CT in P5A-NiSOD is  $4850 \text{ M}^{-1}\text{cm}^{-1}$ .



**Figures 4.5: X-band EPR spectra obtained at 77K for as-isolated sample of P5A-NiSOD. The arrows show the additional hyperfine features ( $A_{yy} = 8.8 \text{ G}$ ) on the  $g_y$  tensor of P5A-NiSOD.**

The EPR of recombinant, as - isolated WT – NiSOD shows a  $S = \frac{1}{2}$  signal and reveals a rhombic spectrum with  $g_x = 2.30$ ,  $g_y = 2.22$ ,  $g_z = 2.01$ , and a hyperfine coupling on  $g_z$  tensor ( $A_{zz} = 24.9 \text{ G}$ ) which is assigned to the interaction of  $Ni^{3+}$  with one axial N- donor ligand (nuclear spin for  $^{14}\text{N}$  is 1) from His1.<sup>3, 6</sup> EPR spectrum of as-isolated P5A-NiSOD also reveals a  $S = \frac{1}{2}$  signal, and a rhombic spectrum, but with subtle differences in the corresponding g-values and hyperfine



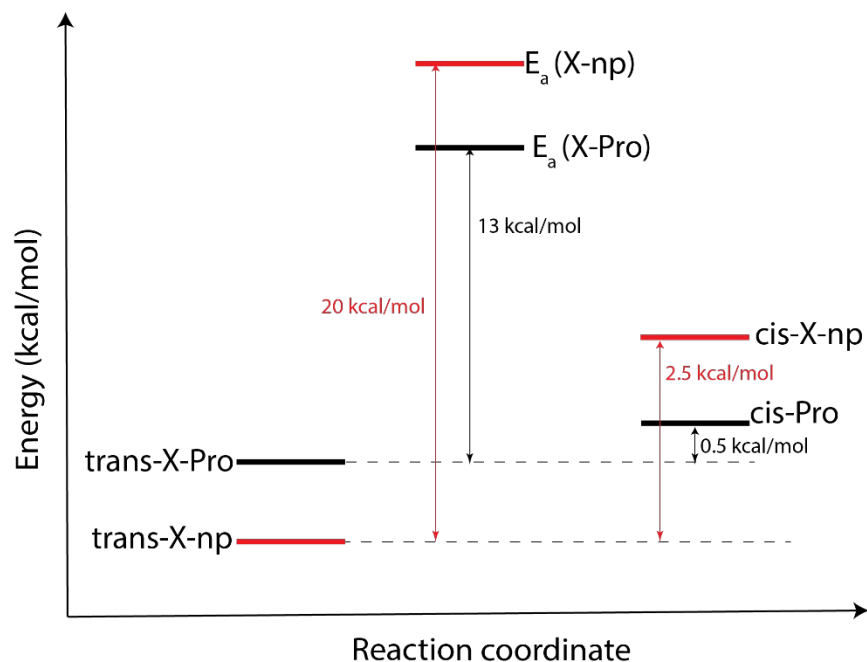
coupling than the as-isolated WT – NiSOD. The observed  $g$ -values for as-isolated P5A-NiSOD are:  $g_x = 2.36$ ,  $g_y = 2.28$ , and  $g_z = 2.06$ , and hyperfine couplings are resolved on the  $g_y$  tensor ( $A_{yy} = 8.8$  G) as well as on the  $g_z$  tensor ( $A_{zz} = 25.9$  G). The additional small and distinct hyperfine coupling on the  $g_y$  feature ( $A_{yy}=8.8$  G) of P5A - NiSOD presumably arises from the interaction of the  $Ni^{3+}$  with one of the equatorial N-donor ligands provided by either the N-terminal amine or the backbone amide. Similar hyperfine splitting at the  $g_y$  tensor was observed for the azide-treated sample of WT NiSOD and was reasoned to be due to the structural perturbation caused by the interaction of azide with Ni-macrocycle in as-isolated WT-NiSOD and not directly with its Ni (III) center.<sup>3</sup> Similar to the as-isolated WT-NiSOD, the observation of hyperfine coupling on the  $g_z$  tensor of as-isolated P5A-NiSOD is associated with the apical imidazole N-donor from His1, which also indicates that this His1 is also a ligand to the Ni-site in P5A-NiSOD. The subtle changes observed in the EPR parameters of P5A-NiSOD indicate that the structure of the Ni site in P5A-NiSOD is slightly but not strongly perturbed from that in the WT enzyme.

### 4.3.3 Redox Catalysis

The structural and electronic perturbation caused by the substitution of Pro5 to Ala in NiSOD does affect the catalytic properties of the as-isolated P5A - NiSOD variant. The catalytic rate constant ( $k_{cat}$ ) of as-isolated P5A – NiSOD, determined by monitoring the disappearance of superoxide radical (generated pulse-radiolytically) at 260 nm was  $2.3 \times 10^8$   $M^{-1}s^{-1}$  at pH 7.5, which is 35% of the reported value of as-isolated WT – NiSOD ( $0.71 \times 10^9$   $M^{-1}s^{-1}$ ). This modest loss of activity is likely due to an altered redox potential for the Ni site that is not optimum for SOD catalysis.

## 4.4 Discussion

*Cis-trans* isomerization of proline (*cis*-Pro  $\Leftrightarrow$  *trans*-Pro) is one of the common routes to induce conformational changes in proteins and in most cases, are critical to protein function.<sup>15-17, 24-26</sup> The *trans*- isomer of X-Pro peptide is favored over the *cis*- isomer by only 0.5 kcal/mol (**Figure 4.6**), and the activation barrier for *cis*-Pro  $\Leftrightarrow$  *trans*-Pro is lower ( $\sim 13$  kcal/mol) as compared to that of *cis*-X-non-proline (X-np)  $\Leftrightarrow$  *trans*-X-non-proline ( $\sim 20$  kcal/mol), where the *trans*- isomer is favored over the *cis*- isomer by 2.5 kcal/mol.<sup>20-21, 27-29</sup> Thus, X-Pro imide bond have higher propensity for *cis*-  $\Leftrightarrow$  *trans*- isomerization than the X-np amide bonds and hence a higher abundance (10-30%) of *cis*-form for X-Pro peptide bonds is observed at equilibrium as compared to X-np peptide bonds (1.5% occurrence of *cis*-form).



**Figures 4.6:** Energy diagram showing stability of *cis*- and *trans*- isomers of X-proline (X-Pro) imide and X-non-proline (X-np) amide bond and activation energy barriers ( $E_a$ ) associated with respective *cis*-  $\Leftrightarrow$  *trans*- isomerization.

The N-terminal of apo-WT-NiSOD which contains the ‘nickel-hook’ residues (HCDLPCGVY) is disordered<sup>3</sup> and resembles an ‘unfolded’ state, where a slow *trans*-Pro5  $\leftrightarrow$  *cis*-Pro5 isomerization can occur readily with the higher abundance of *trans*-isomer, as observed in ribonuclease A<sup>21</sup>. Upon Ni(II) binding, the N-terminal of NiSOD becomes ordered or ‘folded’, and Pro5 in holo-NiSOD is locked in a sterically unfavored *cis*-conformation (with 100% abundance), which was proposed to be required for proper positioning of the nickel-ligand residues, especially the *cis* - configuration of two thiolate donors, Cys2 and Cys6, in the nickel active site of WT-NiSOD that is formed after the processing of the N – terminal extension of NiSOD precursor, SodN.<sup>3</sup> Our studies show that binding of Ni(II) to apo-WT-NiSOD is exothermic and enthalpically driven with an apparent  $\Delta H = -13$  kcal/mol. The total Gibbs free energy ( $\Delta G$ ) associated with Ni(II) binding to apo-WT-NiSOD obtained from ITC is -8.3 kcal/mol, which is the sum of the free energies associated with *trans*-Pro5  $\rightarrow$  *cis*-Pro5 isomerization (+0.5 kcal/mol) and nickel complexation. Thus, the deduced free energy for nickel complexation to apo-WT-NiSOD is -8.8 kcal/mol, which is also consistent with the range of free energy values (-5 to -12 kcal/mol) obtained for Ni(II) complexes with other proteins, such as UreE<sup>30-31</sup>. Hence, it is reasonable to expect that the nickel complex drives *trans*-Pro  $\rightarrow$  *cis*-Pro isomerization.

Substitution of Pro5 with an Ala in NiSOD changes the imide of Leu4-Pro5 to an amide bond (Leu4-Ala5), which in the apo- P5A-NiSOD polypeptide can be translated either as *cis*-Leu4-Ala5 or preferably a *trans*- Leu4-Ala5 (based on energy considerations, **Figure 4.6**). Due to high energy barrier (~17.5 kcal/mol) and steric factors, the *trans*-Leu4-Ala5  $\leftrightarrow$  *cis*-Leu4-Ala5 isomerization is unfavorable under equilibrium conditions, and can lead to protein destabilization, and therefore, Leu4-Ala5 amide bond should predominantly exist as its *trans*-isomer in apo- P5A-NiSOD. If a *cis*-isomer at the fifth position of NiSOD polypeptide is required for proper

positioning of the nickel binding residues in mature enzyme, a *trans*-isomer at that position may disrupt nickel hook formation and/or abolish nickel binding in the variant enzyme. In case of P5A-NiSOD, as the free energy for *trans*-Ala5  $\rightarrow$  *cis*-Ala5 isomerization is higher (+2.5 kcal/mol), the free energy associated with nickel complexation in P5A-NiSOD will be higher (-10.8 kcal/mol), and will require a complex with tighter affinity. In fact, Ni(II) binding affinity for apo-P5A-NiSOD is 0.16  $\mu$ M which is six-fold tighter than that of apo-WT-NiSOD. Thus, in the light of these results, it is clear that the nickel complex formation will drive the *trans*-  $\leftrightarrow$  *cis*- isomerization of Pro5 and Ala5 in WT-NiSOD and P5A-NiSOD, respectively. A crystal structure of P5A-NiSOD might reveal the actual configuration of Ala5 in the variant enzyme.

Close examination and analysis of UV-Vis spectrum of as-isolated P5A-NiSOD suggest a 42% decrease in molar extinction coefficient of S $\rightarrow$ Ni(III) CT in the variant enzyme, which might arise either due to lower Ni(III) content or lower intensity of charge transfer from sulfur to Ni(III) or a combination of both. Ni(III) content in as-isolated P5A-NiSOD is 40% as revealed by EPR spin quantization, which is 20% less than that of as-isolated WT-NiSOD (which has 50% Ni(III) character). Recent study on peptide mimics of NiSOD suggested that in absence of Pro5, the peptide mimic of P5A-NiSOD coordinates Ni(II) by all the N-donors (provided by NH<sub>2</sub>, N<sub>im</sub>, N<sup>-</sup>) as in WT-NiSOD enzyme, but only one thiolate donor (possibly by Cys2) instead of two thiolates (from Cys2 and Cys6) as in the active WT-enzyme. While this further underscores a role for Pro5 in positioning one of the thiolate coordination (possibly Cys6) to the active site,<sup>13</sup> it is important to note that nickel center in the WT-NiSOD enzyme is low spin which requires the coordination of thiolates from both Cys2 and Cys6.<sup>11</sup> In absence of either Cys2 or Cys6, the nickel center in the enzyme changes to a high-spin nickel site with no-thiolate coordination, a fact that was not accounted for in the aforementioned peptide mimic study. Hence, the lower intensity of

charge transfer from sulfur to Ni(III) in P5A-NiSOD might arise from a longer thiolate coordination from either Cys2 or Cys6, which can be deduce either from its crystal structure or XAS.

Spectroscopic and kinetic studies revealed interesting features of this variant of NiSOD, which bears similarities to WT-NiSOD, to azide - treated sample of WT- NiSOD,<sup>3</sup> and to the D3A-NiSOD<sup>7</sup> variant. Similar to as - isolated WT- NiSOD, as-isolated P5A-NiSOD contains a mixture of Ni(II) and Ni(III), but as deduced from its EPR spin – integration studies, the Ni(III) content of this variant is a little lower, about 40% vs. 50% for WT-NiSOD. This value is even less than that of D3A- or Y9F/Y62F- NiSOD which have 48-52% Ni(III) character. The remaining 60% of the bound nickel in P5A-NiSOD exists as Ni(II), which is EPR-silent in these experiments. Several secondary coordination-sphere variants of NiSOD (**Table 4.2**) demonstrated 3-5% reduction in its Ni(III) content, or no Ni(III) content by alteration of primary sphere residues, such as H1A, H1\*(amidate to secondary amine), C2S, C6S, C2S/C6S etc. It is interesting to note that alteration of a non – coordinating residue, such as Pro5 in NiSOD, which is also not involved in secondary sphere coordination (like D3-, E17- or R47-, Y9- or Y62-, **Table 4.2**), raises the redox potential of the nickel site to a value that is less accessible to air oxidation, resulting in lower amounts of Ni(III) in as – isolated samples of P5A - NiSOD. Assuming Nerstian behavior, and given that the  $E^0$  value of WT- NiSOD is  $\sim 0.29$  V vs NHE, based on the Ni(III)/Ni(II) content of P5A-NiSOD, the  $E^0$  of the variant is calculated to be  $\approx 0.30$  V. A higher redox potential of P5A-NiSOD is expected to decrease the catalytic activity of the variant. The small,  $\sim 10$ mV, increase in this potential is consistent with the observed activity of P5A-NiSOD, which is 35% of WT- NiSOD. The increased redox potential makes Ni(III) hard to access and this inhibits the reduction of  $O_2^-$  to  $H_2O_2$ . In H1\*NiSOD variant (where the amidate ligand was converted to a secondary amine),

**Table 4.2: Amounts of Ni(III) and  $k_{cat}$  in all studied NiSOD variants**

NiSOD	% Ni(III)	$k_{cat}$ ( $M^{-1}s^{-1}$ )
WT <sup>6</sup>	51	$5.3 \times 10^9$
Recombinant WT <sup>7</sup>	51	$7.1 \times 10^8$
D3A <sup>7</sup>	48	$2.1 \times 10^8$
Y9F <sup>7</sup>	53	$3.7 \times 10^8$
Y62F <sup>7</sup>	48	$6.4 \times 10^8$
Y9F/Y62F <sup>7</sup>	46	$2.4 \times 10^8$
H1A <sup>10</sup>	0	$4.7 \times 10^7$
Ala0 <sup>8</sup>	0	$1.0 \times 10^6$
C2S <sup>11</sup>	0	$5.0 \times 10^6$
C6S <sup>11</sup>	0	$3.0 \times 10^6$
C2S/C6S <sup>11</sup>	0	$1.0 \times 10^6$
R47A <sup>10</sup>	15	$1.2 \times 10^8$
E17A/R47A <sup>10</sup>	0	$3.6 \times 10^7$
E17R/R47E <sup>10</sup>	8	$9.5 \times 10^7$
H1* <sup>9</sup>	11	$5.6 \times 10^6$
H53A <sup>32</sup>	50	$3.5 \times 10^8$
P5A	40	$2.5 \times 10^8$

which contains 11% Ni(III), an estimated decrease in redox potential of 20mV was associated with an activity that was only 1% of the WT-NiSOD.<sup>9</sup> The subtle perturbation of Ni(III)/Ni(II) ratio in

P5A-NiSOD effects its rate of superoxide disproportionation, which is reduced by 65%, and is in agreement with expectations based on studies of other NiSOD variants, such as D3A-NiSOD.

The *cis* – conformation of a conserved Pro5 in WT- NiSOD ( which is the N- terminally processed product of a precursor – SodN) is among the only 5% cases where proline predominantly populates its *cis* - conformation in protein structures. As the N - terminus, which contains the Pro is disordered<sup>3</sup>, the conformation of Pro5 from the crystal structures of the apo – WTNiSOD cannot be discerned and hence, whether Pro5 occurs in *cis* – or *trans* – orientation in apo–NiSOD is unknown. Similarly, the N-terminal sequence of apo – WT-SodN (Met1 – Val23) which includes the pre-active site residues of WT-SOD and Pro19 (Pro5 in WTSOD) is expected to be disordered. However, as SodN binds nickel in a 1:1 stoichiometry with His15 (Chapter 3) as one of the possible ligands, the N-terminus might possibly get ordered in NiSodN and a crystal structure of this complex might show the original orientation of Pro5 in the precursor and/or the processed protein (SOD), that may resolve the conundrum of initial configuration of Pro5 in WT-SOD.

#### 4.5 References

1. Eitinger, T., In vivo production of active nickel superoxide dismutase from *Prochlorococcus marinus* MIT9313 is dependent on its cognate peptidase. *J. Bacteriol.* **2004**, *186* (22), 7821-7825.
2. Kim, E. J.; Chung, H. J.; Suh, B.; Hah, Y. C.; Roe, J. H., Transcriptional and post-transcriptional regulation by nickel of *sodN* gene encoding nickel-containing superoxide dismutase from *Streptomyces coelicolor* Muller. *Mol. Microbiol.* **1998**, *27* (1), 187-195.
3. Barondeau, D. P.; Kassmann, C. J.; Bruns, C. K.; Tainer, J. A.; Getzoff, E. D., Nickel superoxide dismutase structure and mechanism. *Biochemistry* **2004**, *43* (25), 8038-8047.
4. Wuerges, J.; Lee, J. W.; Yim, Y. I.; Yim, H. S.; Kang, S. O.; Djinovic Carugo, K., Crystal structure of nickel-containing superoxide dismutase reveals another type of active site. *Proc. Natl. Acad. Sci. U. S. A.* **2004**, *101* (23), 8569-8574.
5. Bryngelson, P. A.; Arobo, S. E.; Pinkham, J. L.; Cabelli, D. E.; Maroney, M. J., Expression, reconstitution, and mutation of recombinant *Streptomyces coelicolor* NiSOD. *J. Am. Chem. Soc.* **2004**, *126* (2), 460-461.
6. Choudhury, S. B.; Lee, J. W.; Davidson, G.; Yim, Y. I.; Bose, K.; Sharma, M. L.; Kang, S. O.; Cabelli, D. E.; Maroney, M. J., Examination of the nickel site structure and reaction mechanism in *Streptomyces seoulensis* superoxide dismutase. *Biochemistry* **1999**, *38* (12), 3744-3752.
7. Herbst, R. W.; Guce, A.; Bryngelson, P. A.; Higgins, K. A.; Ryan, K. C.; Cabelli, D. E.; Garman, S. C.; Maroney, M. J., Role of conserved tyrosine residues in NiSOD catalysis: a case of convergent evolution. *Biochemistry* **2009**, *48* (15), 3354-3369.
8. Huang, H. T.; Dillon, S.; Ryan, K. C.; Campecino, J. O.; Watkins, O. E.; Cabelli, D. E.; Brunold, T. C.; Maroney, M. J., The Role of Mixed Amine/Amide Ligation in Nickel Superoxide Dismutase. *Inorg. Chem.* **2018**, *57* (20), 12521-12535.



9. Campecino, J. O.; Dudycz, L. W.; Tumelty, D.; Berg, V.; Cabelli, D. E.; Maroney, M. J., A Semisynthetic Strategy Leads to Alteration of the Backbone Amidate Ligand in the NiSOD Active Site. *J. Am. Chem. Soc.* **2015**, *137* (28), 9044-9052.
10. Ryan, K. C.; Guce, A. I.; Johnson, O. E.; Brunold, T. C.; Cabelli, D. E.; Garman, S. C.; Maroney, M. J., Nickel superoxide dismutase: structural and functional roles of His1 and its H-bonding network. *Biochemistry* **2015**, *54* (4), 1016-1027.
11. Ryan, K. C.; Johnson, O. E.; Cabelli, D. E.; Brunold, T. C.; Maroney, M. J., Nickel superoxide dismutase: structural and functional roles of Cys2 and Cys6. *J. Biol. Inorg. Chem.* **2010**, *15* (5), 795-807.
12. Johnson, O. E.; Ryan, K. C.; Maroney, M. J.; Brunold, T. C., Spectroscopic and computational investigation of three Cys-to-Ser mutants of nickel superoxide dismutase: insight into the roles played by the Cys2 and Cys6 active-site residues. *J. Biol. Inorg. Chem.* **2010**, *15* (5), 777-793.
13. Lihi, N.; Csire, G.; Szakacs, B.; May, N. V.; Varnagy, K.; Sovago, I.; Fabian, I., Stabilization of the Nickel Binding Loop in NiSOD and Related Model Complexes: Thermodynamic and Structural Features. *Inorg. Chem.* **2019**.
14. Lorenzen, S.; Peters, B.; Goede, A.; Preissner, R.; Frömmel, C., Conservation of cis prolyl bonds in proteins during evolution. *Proteins* **2005**, *58* (3), 589-595.
15. Xia, J.; Levy, R. M., Molecular dynamics of the proline switch and its role in Crk signaling. *J. Phys. Chem. B* **2014**, *118* (17), 4535-4545.
16. Lu, K. P.; Finn, G.; Lee, T. H.; Nicholson, L. K., Prolyl cis-trans isomerization as a molecular timer. *Nat. Chem. Biol.* **2007**, *3* (10), 619-629.

17. Andreotti, A. H., Native state proline isomerization: an intrinsic molecular switch. *Biochemistry* **2003**, *42* (32), 9515-9524.
18. Wedemeyer, W. J.; Welker, E.; Scheraga, H. A., Proline cis-trans isomerization and protein folding. *Biochemistry* **2002**, *41* (50), 14637-14644.
19. Dugave, C.; Demange, L., Cis-trans isomerization of organic molecules and biomolecules: implications and applications. *Chem. Rev.* **2003**, *103* (7), 2475-2532.
20. Pierson, N. A.; Chen, L.; Russell, D. H.; Clemmer, D. E., Cis-trans isomerizations of proline residues are key to bradykinin conformations. *J. Am. Chem. Soc.* **2013**, *135* (8), 3186-3192.
21. Schultz, D. A.; Baldwin, R. L., Cis proline mutants of ribonuclease A. I. Thermal stability. *Protein Sci.* **1992**, *1* (7), 910-916.
22. Fiedler, A. T.; Bryngelson, P. A.; Maroney, M. J.; Brunold, T. C., Spectroscopic and computational studies of Ni superoxide dismutase: electronic structure contributions to enzymatic function. *J. Am. Chem. Soc.* **2005**, *127* (15), 5449-5462.
23. Fiedler, A. T.; Brunold, T. C., Spectroscopic and computational studies of Ni<sup>3+</sup> complexes with mixed S/N ligation: implications for the active site of nickel superoxide dismutase. *Inorg. Chem.* **2007**, *46* (21), 8511-8523.
24. Schmidpeter, P. A.; Koch, J. R.; Schmid, F. X., Control of protein function by prolyl isomerization. *Biochim. Biophys. Acta.* **2015**, *1850* (10), 1973-1982.
25. Joseph, A. P.; Srinivasan, N.; de Brevern, A. G., Cis-trans peptide variations in structurally similar proteins. *Amino Acids* **2012**, *43* (3), 1369-1381.
26. Schmidt, M.; Zahn, S.; Carella, M.; Ohlenschlager, O.; Gorlach, M.; Kothe, E.; Weston, J., Solution structure of a functional biomimetic and mechanistic implications for nickel superoxide dismutases. *Chembiochem : a European journal of chemical biology* **2008**, *9* (13), 2135-2146.

27. Stewart, D. E.; Sarkar, A.; Wampler, J. E., Occurrence and role of cis peptide bonds in protein structures. *J. Mol. Biol.* **1990**, *214* (1), 253-260.
28. Pal, D.; Chakrabarti, P., Cis peptide bonds in proteins: residues involved, their conformations, interactions and locations. *J. Mol. Biol.* **1999**, *294* (1), 271-288.
29. Ramachandran, G. N.; Sasisekharan, V., Conformation of polypeptides and proteins. *Adv. Protein Chem.* **1968**, *23*, 283-438.
30. Grosseohme, N. E.; Mulrooney, S. B.; Hausinger, R. P.; Wilcox, D. E., Thermodynamics of Ni<sup>2+</sup>, Cu<sup>2+</sup>, and Zn<sup>2+</sup> Binding to the Urease Metallochaperone UreE. *Biochemistry* **2007**, *46* (37), 10506-10516.
31. Wilcox, D. E., Isothermal titration calorimetry of metal ions binding to proteins: An overview of recent studies. *Inorg. Chim. Acta* **2008**, *361* (4), 857-867.
32. Carr, C. Relationship between structure and function in nickel proteins and enzymes. Electronic Resource, University of Massachusetts Libraries, 2017.

## CHAPTER 5

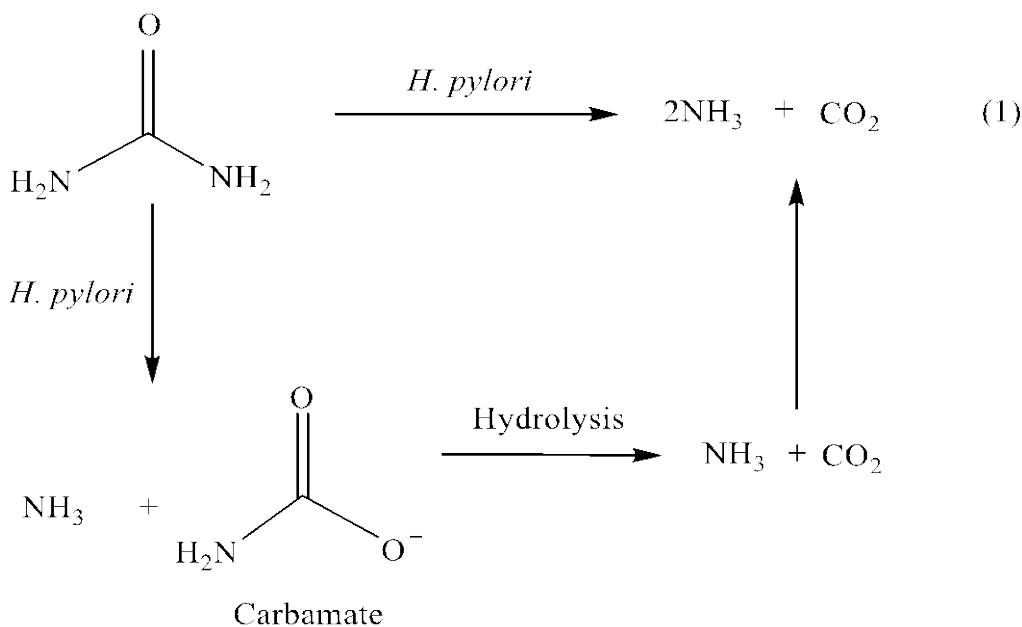
### NICKEL TRAFFICKING IN *HELICOBACTER PYLORI* : A REVIEW

#### 5.1 Introduction

*Helicobacter pylori* is a gram negative, microaerophilic bacterium associated with peptic ulcers, gastritis and gastric cancers in humans.<sup>1</sup> More than 50% of the world's population is infected by this pathogen with the risks being higher for developing countries.<sup>2-3</sup> The World Health Organization (WHO) has listed this pathogen as 'high priority' on global priority list of antibiotic-resistant bacteria.<sup>4</sup> Despite being a neutrophile, *H. pylori* has a unique ability to survive and colonize under the acidic conditions (pH<2) of the human stomach. *H. pylori* invades the highly acidic gastric mucosal layer and utilizes its pH sensing (chemotaxis) machinery to reach the less acidic epithelial lining of the stomach.<sup>5</sup> In fact, the pathogen is widely present in the mucus layer of the gastric lining, the mucus gland of the stomach cavity, the surface of and even within the gastric epithelial cells.<sup>1</sup> Due to such a differential presence in the stomach, it is difficult to completely eradicate the pathogen. The most common therapy utilized to treat *H. pylori* infection include a combination of two antibiotics (Clarithromycin and Amoxicillin/Metronidazole), and a proton-pump inhibitor or a bismuth – based colloidal drug.<sup>6-7</sup> However, increasing *H. pylori* resistance to clarithromycin necessitates the need to develop new therapies that can be effective in eradicating this pathogen completely.

One of the major mechanisms of acid acclimatization of *H. pylori* is its potential to maintain a near-neutral internal and external pH. This ability is provided by a nickel-dependent enzyme, urease, which hydrolyzes host urea to ammonia (Equation 1) that eventually neutralizes its internal and immediate external environment.<sup>8-9</sup> In fact, the efficiency of this pH homeostasis in the

pathogen was recently quantified using a ratiometric pHluorin (RpH) sensor.<sup>10</sup> Upon acid exposure (pH 2), the cytoplasmic pH of *H. pylori* dropped down to 5.1, but was restored to pH 6.0 after an hour.<sup>10</sup>



*H. pylori* urease is a tetramer of trimers  $[(\alpha\beta)_3]_4$  composed of UreA and UreB subunits which contain the dinuclear nickel-active site with the two Ni centers bridged by oxygen atoms of carbamylated lysine residue.<sup>9</sup> Deletion of structural genes for urease, *ureA* and *ureB*, results in complete loss of its acid viability and under acidic conditions, is lethal for the pathogen. Although urease is constitutively expressed in high amounts accounting for up to 10% of the total cellular protein pool in *H. pylori*, the activity of this enzyme is critically nickel-dependent.<sup>11</sup> In the absence of added nickel, only 2% of the active sites contain nickel and the strain is severely deficient in colonization, thus establishing nickel as one of the critical virulence factor for this pathogen.<sup>12-13</sup>

In addition to urease, another important nickel-containing enzyme in *H. pylori* required for host colonization is Ni, Fe–hydrogenase – a membrane bound enzyme, which catalyzes the reversible oxidation of molecular hydrogen and has been proposed to generate energy (H<sub>2</sub>) for the pathogen to colonize.<sup>14</sup> Additionally, oxidation of H<sub>2</sub> by hydrogenases was implicated to be crucial for the translocation of the carcinogenic toxin CagA from the pathogen to the host gastric epithelial cells, which is another crucial factor determining the virulence of *H. pylori*.<sup>15</sup> In this chapter, recent developments in nickel trafficking in *H. pylori* are highlighted with a major emphasis on the factors that contribute to high fidelity delivery of nickel to urease and Ni, Fe – hydrogenase in the pathogen.

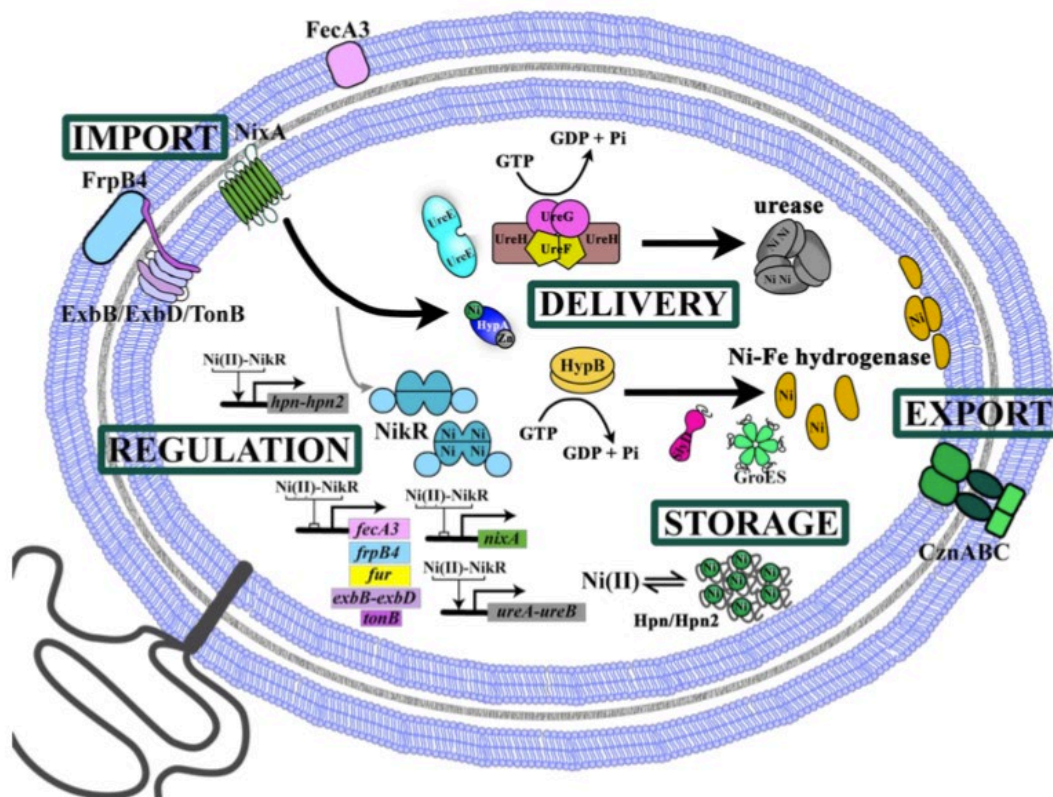


Figure 5.1. Nickel trafficking components in *H. pylori* (adapted with permission from Hu, Heidi, “The Role of the Metallochaperone HypA in the Acid Survival and Activities of Nickel Enzymes in *Helicobacter pylori*” (2018). *Doctoral Dissertations*. 1174)

## 5.2 Nickel Regulation

Nickel forms the enzymatic cofactor of nine enzymes found in different bacteria, but excess nickel can be toxic by either interfering with other metalloenzymes or by inducing oxidative stress.<sup>16</sup> Thus, uptake, utilization and efflux of nickel ions in the cells should be tightly regulated. Nickel homeostasis in bacteria, including the ureolytic and gastric pathogens, such as *H. pylori*, is of prime importance as it uses two important nickel – dependent enzymes - urease and Ni, Fe–hydrogenase for colonization and virulence. NikR is one of the main regulatory factors of nickel homeostasis and so far, the only well characterized nickel - responsive transcriptional regulator in *H. pylori*.<sup>17</sup> Depending on nickel availability and/or acid stress, NikR activates or represses several targeted genes involved in nickel import, delivery and storage.<sup>10, 18-21</sup>

NikR is a homo-tetrameric protein made of two dimers, where the N-terminus of each subunit is a DNA-binding domain (DBD) and its C-terminus binds metals (MBD) and are involved in tetramerization.<sup>22-23</sup> The DBD and MBD are connected with a flexible linker and can adopt variable conformations facilitated by nickel binding.<sup>8</sup> NikR binds nickel with high affinities (nM-pM), although it can also bind other metals (Zn, Co).<sup>24</sup> Binding of nickel to NikR has been extensively characterized using spectroscopic methods.<sup>8</sup> The DNA binding affinity of nickel - bound NikR is in the nM range.<sup>22, 25</sup> Homo-tetrameric Ni-NikR binds to AT-rich promoter regions of *H. pylori* genome that can activate or repress several genes. For example, binding of nickel to NikR promotes the transcription of the structural genes for urease, *ureA* and *ureB*, but downregulates the structural genes for Ni, Fe-hydrogenase.<sup>26</sup> However, it does not affect the transcription of accessory proteins required for the maturation of either urease or hydrogenase.<sup>26</sup> In fact, HypA, HypB, SlyD and UreE have been shown to compete with NikR for nickel binding to prevent pre-mature downregulation of nickel importer genes.<sup>27</sup> Ni-NikR represses the

transcription of nickel-importer genes, *nixA*, *fecA3*, *frpB4*, *exbBD/tonB* as well as the gene encoding the iron-responsive regulator, *fur*.

### 5.3 Nickel Import

The requirement of nickel in *H. pylori* as a cofactor for urease and Ni, Fe- hydrogenase, necessitates import of nickel into its cytoplasm from the extracellular environment. However, due to relatively low availability of extracellular nickel (30 nM in seawater<sup>8</sup>, 5nM in fresh water<sup>8</sup> and 1-11 nM in human body<sup>28</sup>) acquisition of nickel is challenging for *H. pylori*. Therefore, the pathogen has evolved to recruit specific nickel importers to scavenge the relatively less abundant nickel from outside.

Nickel import in *H. pylori* is facilitated by both outer<sup>29</sup> and inner membrane transporters which either import Ni(II)<sup>30</sup> or nickel complexes<sup>31</sup> in periplasm or cytoplasm of *H. pylori*, respectively. In the inner membrane, two types of nickel transporters in *H. pylori* have been discovered so far - a single component secondary transporter, NixA, that belongs to nickel/cobalt transporter family<sup>29, 32</sup> and 2) a multicomponent transporter involving the ATP-binding cassette (ABC)-type transporter, NiuBDE<sup>28, 33</sup>. NixA is a high- affinity, low capacity nickel importer in *H. pylori*.<sup>32-33</sup> It is an eight -transmembrane domain protein whose expression is regulated by NikR.<sup>29</sup> Deletion of NixA in *H. pylori* abolished only 50% of urease activity and did not affect the colonization of pathogen in mouse model, suggesting the presence of alternative nickel transporters in *H. pylori*.<sup>8, 28, 30, 33</sup> The other inner membrane nickel transporter in *H. pylori* is NiuBDE, which is a novel ABC-type transporter and consists of three proteins: NiuB, the periplasmic solute-binding protein, and NiuD and NiuE, which are predicted to be permease and ATPase subunits, respectively.<sup>28</sup> NiuDE is predicted to be a possible NikR target as it was pulled



out with NikR-ChIP seq experiments.<sup>34</sup> Inactivation of both NixA and NiuD resulted in 1) high tolerance of *H. pylori* toward nickel, 2) severely diminished intracellular nickel levels, and 3) compromised urease activities and 4) acid vulnerability.<sup>28</sup> Although both NixA and NiuBDE import nickel in *H. pylori*, these are two different types of nickel uptake transporters in *H. pylori* where NiuBDE functions at pH 5 and 7, while NixA is much more active at acidic pH.<sup>28</sup> Also, while NixA is highly selective for nickel, NiuBDE is also involved in transport of cobalt and bismuth.<sup>28</sup> The structures of both these nickel importers is currently unknown and requires further investigation.

Outer membrane nickel-importers in *H. pylori* include FecA3, FrpB4<sup>28</sup> and CeuE<sup>28, 31</sup>. FecA3 and FrpB4 are TonB/ExbB/ExbD-dependent transporters, which were originally identified as transporters of iron-siderophore complexes.<sup>29</sup> However, in *H. pylori*, these genes were differentially regulated by Ni and NikR, by acid and by the iron-responsive regulator, Fur.<sup>29</sup> Ni-, Fe- and pH dependent studies on deletion strains of these outer membrane proteins show that under neutral conditions, iron-siderophore complexes are imported by these outer membrane transporters, but nickel or nickel complexes are imported under low nickel or acid stress conditions.<sup>29</sup> *H. pylori* CeuE protein (HP1561) was previously annotated as periplasmic component of an ATP-binding cassette (ABC-type) transporter responsible for Fe- or Fe-complex acquisition, but recent X-ray crystallographic and biophysical studies identified this protein to be involved in uptake of nickel, specifically, as a nickel-L(His)<sub>2</sub> complex<sup>31</sup>, similar to that reported for NikABCDE in *E. coli*<sup>35-36</sup>.

## 5.4 Nickel Storage

Hpn and Hpn2 (or Hpn1 for Hpn-like) are two paralogous nickel storage proteins encoded by *hpn* and *hpn2* in the *H. pylori* genome.<sup>37</sup> Both these proteins were shown to be essential for colonization of the pathogen in mouse models.<sup>37</sup> In presence of *hpn* and *hpn2*, the whole cell nickel content of the pathogen was found to increase substantially and mutant *H. pylori* strains lacking these genes exhibited higher sensitivity to nickel and the metal-drug, ranitidine – bismuth citrate, which are used to treat *H. pylori* infections.<sup>8, 37</sup> Transcription of *hpn* and *hpn2* are up - regulated by Ni and NikR<sup>18</sup>, and only Hpn2 is also upregulated by acid<sup>38</sup>. Hpn and Hpn2 are small (7-8 kDa), His-rich (and Gln-rich for Hpn2) proteins that can bind 2-5 Ni(II) ions per monomer with a dissociation constant of 7  $\mu$ M and 3 $\mu$ M, respectively.<sup>37</sup> Hpn interacts with Hpn2, with accessory proteins, HypA and HypB and also with the UreA subunit of urease.<sup>37</sup> A recent cross-linking study, however, diversified the protein - interaction profile for Hpn and Hpn2, and reported their associations with over a hundred proteins. These proteins include, but is not restricted to, nickel-enzymes or their associated proteins.<sup>39</sup>

## 5.5 Nickel Delivery

The two nickel targets in *H. pylori*, urease and Ni, Fe-hydrogenase, require the orchestration of specific accessory proteins for proper delivery of nickel to their respective active sites. Delivery and incorporation of nickel to the active site of apo-urease is facilitated by a cascade of accessory proteins, UreEFGH<sup>40</sup> (encoded by *ureEFGH* operon downstream of *ureA* and *ureB* structural genes) each of which has distinct function in maturation of the enzyme. For example, UreE - dimer binds nickel with micromolar affinity and interacts with UreG, a P-loop GTPase that dimerizes upon nickel binding and provides energy for nickel delivery to active site of urease.<sup>8</sup>

UreF and UreH binds to apo-urease and is suggested to induce conformational changes in the immature enzyme to allow nickel and carbon dioxide access to the active site. Crystallographic studies show that nickel induces dimerization of UreG, and UreF-UreH can bind nickel and GTP-bound UreG-dimer. Hydrolysis of GTP in the complex is triggered by bicarbonate and then facilitates nickel insertion into the active site.<sup>41-42</sup> Furthermore, recent studies further elucidated the molecular details of GTP-dependent UreG dimerization and highlighted the role of UreE as the sole nickel donor.<sup>43</sup> As GTPase activity of UreG is essential for urease activation, the GTP-binding domain of UreG has been targeted for development of GTP analogues that can function as GTPase inhibitors to prevent urease activity and treat *H. pylori* infection.<sup>44</sup> A two-plasmid system has been developed to aid in testing urease inhibitors in-cell.<sup>45</sup>

Similar to *E.coli*, maturation of Ni, Fe – hydrogenase in *H. pylori* is established by the cascade of accessory proteins including HypAB<sup>13, 46</sup>, HypCDEF<sup>47</sup> and SlyD<sup>48</sup> with each performing specific functions to sequentially insert the fully liganded Fe-center first followed by the insertion of nickel.<sup>49</sup> Assembly and insertion of the iron center, FeCO(CN)<sub>2</sub> into its catalytic core is performed by HypCDEF<sup>50</sup>, where HypF, a carbamoyl-transferase, carbamoylates HypE, which acts as a ATP-dependent dehydratase, to produce a thiocyanate product<sup>49</sup>. The HypC-HypD complex ensures the incorporation of the iron complex into the catalytic core.<sup>49</sup> Once the Fe-center is properly assembled into the large subunit precursor, HypA and HypB transfer nickel to the active site in a concerted process, the exact mechanism of which is still unclear.<sup>8,49</sup> HypA, is a small 13.2 kDa monomeric protein that binds nickel at its N-terminus with micromolar affinity and also contains an intrinsic structural Zn-site.<sup>51-54</sup> The nickel site in HypA is paramagnetic and the N-terminus plays a crucial role in nickel binding.<sup>52, 54</sup> HypB is a metallo-GTPase and unlike UreG, requires nickel binding to activate its GTPase activity.<sup>55</sup> HypA and HypB forms a heterodimeric

complex in solution<sup>55-56</sup>, and the interaction between nickel-bound HypA and HypB is required for nickel transfer from HypA to HypB, leading to self-dimerization of HypB and its subsequent GTPase activity.<sup>56</sup> A recent crystallographic study with ATPase type HypB (HypB<sub>AT</sub>) from *Thermococcales* demonstrated that ATP-dependent association of HypB<sub>AT</sub> with HypA leads to the formation of a square-planar nickel site with nanomolar affinity ( $K_d = 7\text{nM}$ )<sup>57</sup>, which is tighter than HypA alone ( $K_d = 1\ \mu\text{M}$ )<sup>52, 54</sup>. In *A. fulgidus*, disrupting the residues critical for the interaction between HypA and HypB was shown to abolish hydrogenase activity,<sup>58</sup> and it is proposed that HypA transfers nickel to HypB, followed by binding of GTP and subsequent dissociation of HypA and dimerization of HypB. Nickel and GTP-bound HypB dimer then deliver nickel to the precursor by GTP hydrolysis<sup>58</sup>. In another study, apo-HypA was shown to interact with the immature form of large subunit of NiFe-hydrogenase<sup>28</sup>, although the functional relevance of this interaction is not clear.<sup>59</sup> It would be interesting to know whether the nickel-bound HypA is capable of interaction and insertion of nickel into the active site and would further our understanding of the role of complex formation and GTPase activity of HypB required for nickel insertion into the active site of hydrogenase in the pathogen.

Despite a specific cascade of proteins for maturation of either urease or hydrogenase, some components of hydrogenase maturation pathway, such as HypA and HypB are also critical for the maturation of urease in *H. pylori*.<sup>13, 55</sup> Deletion of its *hypA* or *hypB* genes, causes loss in both urease and hydrogenase activities<sup>13, 60-61</sup> and in fact deletion of *hypA* is lethal to the acid viability of the pathogen<sup>61</sup>. Additionally, interactome analysis of *H. pylori* using Tandem Affinity Purification revealed a direct association of HypB and SlyD with urease maturation complex.<sup>62</sup> However, a complete knowledge of the mechanistic details of how HypA and HypB simultaneously participate and facilitate urease and hydrogenase maturation in *H. pylori* remains

elusive. There are some reports on the *in vitro* interaction between accessory proteins involved in Ni, Fe - hydrogenase and urease maturation. For example, apo-HypA competes with UreG<sup>46</sup> to interact with UreE-dimer<sup>63</sup>, and forms a stable complex with a dissociation constant of 1-2  $\mu\text{M}$ <sup>64</sup>. However, recent calorimetric studies show that interaction of nickel-bound HypA with UreE<sub>2</sub> is tighter and formation of this stable complex between HypA and UreE<sub>2</sub> with or without nickel has been shown to prevent hydrolytic degradation and stabilize the C-terminal motif of UreE<sub>2</sub> dimer that is close to its nickel-binding site.<sup>64</sup> The HypA•UreE<sub>2</sub> complex binds nickel with high affinity, and this site is proposed to be distinct from that of individual HypA or UreE<sub>2</sub><sup>64</sup>, however the exact metric details, its relevance and implication in urease maturation requires further investigation both *in vitro* and *in vivo*.

Based on the aforementioned studies, it seems possible that HypA, which in itself has weaker affinity for nickel, interacts with UreE<sub>2</sub> in urease maturation pathway, and HypB in hydrogenase maturation pathway to form a higher affinity nickel site. It would be interesting to unravel the functional relevance of such a higher affinity nickel site formed by the interaction of HypA with HypB and UreE. Does the UreFGH complex recognize HypA•UreE<sub>2</sub> more efficiently than just nickel-bound UreE<sub>2</sub>? One possible explanation could be that the higher affinity nickel site is critical for downstream recognition and subsequent nickel transfer to urease through UreGFH or to hydrogenase directly. Alternatively, given that under neutral conditions, all urease in *H. pylori* is in apo-state, it is possible that HypA•UreE<sub>2</sub> complex is designed keep nickel away from apo-urease until nickelation of enzyme is needed in an acidic environment. However, the molecular basis of how HypA acquires and differentially distributes nickel to HypB or UreE is an open question that needs further investigation.

## 5.6 Nickel Export

The only nickel exporter reported in *H. pylori* so far is encoded by the gene cluster *cznCBA* that imparts cadmium, zinc and nickel resistance to the organism.<sup>65</sup> Whether this gene cluster is regulated by Ni-NikR or by acid stress is unknown. Deletion of these genes resulted in increased sensitivity to the aforementioned metals, and prevented the gastric colonization in gerbil-based animal models.<sup>65</sup> *H. pylori* mutants lacking *cznC* and *cznA*, particularly, showed increased urease activity due to the increased accumulation of cytoplasmic nickel.<sup>65</sup> Recombinant CznB and CznC was shown to bind nickel, where CznB can additionally bind Cd and Zn also.<sup>65</sup> CznA resembles the inner membrane cation-proton pumps in other organisms, and based on these findings, CznCBA is proposed to be a proton driven nickel exporter<sup>49,65</sup>, but a detailed structure – function analysis of this exporter in *H. pylori* is unknown.

## 5.7 Conclusion

In the present era of increasing microbial resistance to antibiotics, specific drugs targeting specific virulence factors of pathogens are required. This can be achieved by first understanding the details of such specific virulence factors followed by development of specific drugs. Among others, nickel is an essential virulence factor of *H. pylori*, and a detailed understanding of nickel trafficking in the pathogen is critical to effectively target its nickel – dependent pathogenicity. Although much progress has been made, there are still some important questions that need to be answered to completely decode the nickel – dependent virulence of this gastric pathogen. For example, the acquisition and transport mechanism of Ni from the environment into the cytoplasm is unknown. Once Ni is in the cytoplasm, does it form the labile nickel pool from where it is sequestered by distinct chaperones or regulatory sites? In such a case, identity of those labile nickel

pools in *H. pylori* might assist in developing compounds that can target the available nickel in the pathogen.

## 5.8 References

1. Salama, N. R.; Hartung, M. L.; Muller, A., Life in the human stomach: persistence strategies of the bacterial pathogen *Helicobacter pylori*. *Nat. Rev. Microbiol.* **2013**, *11* (6), 385-399.
2. Covacci, A.; Telford, J. L.; Del Giudice, G.; Parsonnet, J.; Rappuoli, R., *Helicobacter pylori* virulence and genetic geography. *Science* **1999**, *284* (5418), 1328-1333.
3. Eusebi, L. H.; Zagari, R. M.; Bazzoli, F., Epidemiology of *Helicobacter pylori* infection. *Helicobacter* **2014**, *19 Suppl 1*, 1-5.
4. Shrivastava, S.; Shrivastava, P.; Ramasamy, J., World health organization releases global priority list of antibiotic-resistant bacteria to guide research, discovery, and development of new antibiotics. *J. Med. Soc.* **2018**, *32* (1), 76-77.
5. Camilo, V.; Sugiyama, T.; Touati, E., Pathogenesis of *Helicobacter pylori* infection. *Helicobacter* **2017**, *22* (S1), e12405.
6. Gressot, P.; Frossard, J. L.; Grosгурin, O.; Marti, C., [First line eradication treatment of *Helicobacter pylori* in 2019]. *Rev. Med. Suisse* **2019**, *15* (667), 1854-1858.
7. Yang, J. C.; Lu, C. W.; Lin, C. J., Treatment of *Helicobacter pylori* infection: current status and future concepts. *World J. Gastroenterol.* **2014**, *20* (18), 5283-5293.
8. Ge, R. G.; Wang, D. X.; Hao, M. C.; Sun, X. S., Nickel trafficking system responsible for urease maturation in *Helicobacter pylori*. *World J. Gastroenterol.* **2013**, *19* (45), 8211-8218.
9. Maroney, M. J.; Ciurli, S., Nonredox nickel enzymes. *Chem. Rev.* **2014**, *114* (8), 4206-4228.
10. Jones, M. D.; Li, Y.; Zamble, D. B., Acid-responsive activity of the *Helicobacter pylori* metalloregulator NikR. *Proc. Natl. Acad. Sci. U. S. A.* **2018**, *115* (36), 8966-8971.



11. Hu, L. T.; Mobley, H. L., Purification and N-terminal analysis of urease from *Helicobacter pylori*. *Infect. Immun.* **1990**, *58* (4), 992-998.
12. Stingl, K.; De Reuse, H., Staying alive overdosed: how does *Helicobacter pylori* control urease activity? *Int. J. Med. Microbiol.* **2005**, *295* (5), 307-315.
13. Olson, J. W.; Mehta, N. S.; Maier, R. J., Requirement of nickel metabolism proteins HypA and HypB for full activity of both hydrogenase and urease in *Helicobacter pylori*. *Mol. Microbiol.* **2001**, *39* (1), 176-182.
14. Olson, J. W.; Maier, R. J., Molecular hydrogen as an energy source for *Helicobacter pylori*. *Science* **2002**, *298* (5599), 1788-1790.
15. Wang, G.; Romero-Gallo, J.; Benoit, S. L.; Piazuelo, M. B.; Dominguez, R. L.; Morgan, D. R.; Peek, R. M., Jr.; Maier, R. J., Hydrogen Metabolism in *Helicobacter pylori* Plays a Role in Gastric Carcinogenesis through Facilitating CagA Translocation. *MBio* **2016**, *7* (4).
16. Macomber, L.; Hausinger, R. P., Mechanisms of nickel toxicity in microorganisms. *Metallomics : integrated biometal science* **2011**, *3* (11), 1153-1162.
17. Vannini, A.; Pinatel, E.; Costantini, P. E.; Pellicciari, S.; Roncarati, D.; Puccio, S.; De Bellis, G.; Peano, C.; Danielli, A., Comprehensive mapping of the *Helicobacter pylori* NikR regulon provides new insights in bacterial nickel responses. *Sci. Rep.* **2017**, *7*, 45458.
18. Muller, C.; Bahlawane, C.; Aubert, S.; Delay, C. M.; Schauer, K.; Michaud-Soret, I.; De Reuse, H., Hierarchical regulation of the NikR-mediated nickel response in *Helicobacter pylori*. *Nucleic Acids Res.* **2011**, *39* (17), 7564-7575.
19. Wolfram, L.; Haas, E.; Bauerfeind, P., Nickel represses the synthesis of the nickel permease NixA of *Helicobacter pylori*. *J. Bacteriol.* **2006**, *188* (4), 1245-1250.

20. Ernst, F. D.; Kuipers, E. J.; Heijens, A.; Sarwari, R.; Stoof, J.; Penn, C. W.; Kusters, J. G.; van Vliet, A. H., The nickel-responsive regulator NikR controls activation and repression of gene transcription in *Helicobacter pylori*. *Infect. Immun.* **2005**, *73* (11), 7252-7258.
21. Carpenter, B. M.; West, A. L.; Gancz, H.; Servetas, S. L.; Pich, O. Q.; Gilbreath, J. J.; Hallinger, D. R.; Forsyth, M. H.; Merrell, D. S.; Michel, S. L., Crosstalk between the HpArsRS two-component system and HpNikR is necessary for maximal activation of urease transcription. *Front. Microbiol.* **2015**, *6*, 558.
22. Abraham, L. O.; Li, Y.; Zamble, D. B., The metal- and DNA-binding activities of *Helicobacter pylori* NikR. *J. Inorg. Biochem.* **2006**, *100* (5-6), 1005-1014.
23. Dian, C.; Schauer, K.; Kapp, U.; McSweeney, S. M.; Labigne, A.; Terradot, L., Structural basis of the nickel response in *Helicobacter pylori*: crystal structures of HpNikR in Apo and nickel-bound states. *J. Mol. Biol.* **2006**, *361* (4), 715-730.
24. Zambelli, B.; Bellucci, M.; Danielli, A.; Scarlato, V.; Ciurli, S., The Ni<sup>2+</sup> binding properties of *Helicobacter pylori* NikR. *Chem. Commun. (Camb.)* **2007**, (35), 3649-3651.
25. Delany, I.; Ieva, R.; Soragni, A.; Hilleringmann, M.; Rappuoli, R.; Scarlato, V., In vitro analysis of protein-operator interactions of the NikR and fur metal-responsive regulators of coregulated genes in *Helicobacter pylori*. *J. Bacteriol.* **2005**, *187* (22), 7703-7715.
26. Contreras, M.; Thiberge, J. M.; Mandrand-Berthelot, M. A.; Labigne, A., Characterization of the roles of NikR, a nickel-responsive pleiotropic autoregulator of *Helicobacter pylori*. *Mol. Microbiol.* **2003**, *49* (4), 947-963.
27. Benanti, E. L.; Chivers, P. T., An intact urease assembly pathway is required to compete with NikR for nickel ions in *Helicobacter pylori*. *J. Bacteriol.* **2009**, *191* (7), 2405-2408.

28. Fischer, F.; Robbe-Saule, M.; Turlin, E.; Mancuso, F.; Michel, V.; Richaud, P.; Veyrier, F. J.; De Reuse, H.; Vinella, D., Characterization in *Helicobacter pylori* of a Nickel Transporter Essential for Colonization That Was Acquired during Evolution by Gastric *Helicobacter* Species. *PLoS Pathog.* **2016**, *12* (12), e1006018.
29. Schauer, K.; Gouget, B.; Carriere, M.; Labigne, A.; de Reuse, H., Novel nickel transport mechanism across the bacterial outer membrane energized by the TonB/ExbB/ExbD machinery. *Mol. Microbiol.* **2007**, *63* (4), 1054-1068.
30. Fulkerson, J. F., Jr.; Garner, R. M.; Mobley, H. L., Conserved residues and motifs in the NixA protein of *Helicobacter pylori* are critical for the high affinity transport of nickel ions. *J. Biol. Chem.* **1998**, *273* (1), 235-241.
31. Shaik, M. M.; Cendron, L.; Salamina, M.; Ruzzene, M.; Zanotti, G., *Helicobacter pylori* periplasmic receptor CeuE (HP1561) modulates its nickel affinity via organic metallophores. *Mol. Microbiol.* **2014**, *91* (4), 724-735.
32. Mobley, H. L.; Garner, R. M.; Bauerfeind, P., *Helicobacter pylori* nickel-transport gene nixA: synthesis of catalytically active urease in *Escherichia coli* independent of growth conditions. *Mol. Microbiol.* **1995**, *16* (1), 97-109.
33. Hendricks, J. K.; Mobley, H. L., *Helicobacter pylori* ABC transporter: effect of allelic exchange mutagenesis on urease activity. *J. Bacteriol.* **1997**, *179* (18), 5892-5902.
34. Jones, M. D.; Ademi, I.; Yin, X.; Gong, Y.; Zamble, D. B., Nickel-responsive regulation of two novel *Helicobacter pylori* NikR-targeted genes. *Metallomics : integrated biometal science* **2015**, *7* (4), 662-673.
35. Chivers, P. T., Nickel recognition by bacterial importer proteins. *Metallomics : integrated biometal science* **2015**, *7* (4), 590-595.

36. Chivers, P. T.; Benanti, E. L.; Heil-Chapdelaine, V.; Iwig, J. S.; Rowe, J. L., Identification of Ni-(L-His)<sub>2</sub> as a substrate for NikABCDE-dependent nickel uptake in *Escherichia coli*. *Metallomics : integrated biometal science* **2012**, *4* (10), 1043-1050.
37. Vinella, D.; Fischer, F.; Vorontsov, E.; Gallaud, J.; Malosse, C.; Michel, V.; Cavazza, C.; Robbe-Saule, M.; Richaud, P.; Chamot-Rooke, J.; Brochier-Armanet, C.; De Reuse, H., Evolution of *Helicobacter*: Acquisition by Gastric Species of Two Histidine-Rich Proteins Essential for Colonization. *PLoS Pathog.* **2015**, *11* (12), e1005312.
38. Bury-Mone, S.; Thiberge, J. M.; Contreras, M.; Maitournam, A.; Labigne, A.; De Reuse, H., Responsiveness to acidity via metal ion regulators mediates virulence in the gastric pathogen *Helicobacter pylori*. *Mol. Microbiol.* **2004**, *53* (2), 623-638.
39. Saylor, Z.; Maier, R., *Helicobacter pylori* nickel storage proteins: recognition and modulation of diverse metabolic targets. *Microbiology* **2018**, *164* (8), 1059-1068.
40. Volland, P.; Weeks, D. L.; Marcus, E. A.; Prinz, C.; Sachs, G.; Scott, D., Interactions among the seven *Helicobacter pylori* proteins encoded by the urease gene cluster. *Am. J. Physiol. Gastrointest. Liver Physiol.* **2003**, *284* (1), G96-g106.
41. Farrugia, M. A.; Macomber, L.; Hausinger, R. P., Biosynthesis of the urease metallocenter. *J. Biol. Chem.* **2013**, *288* (19), 13178-13185.
42. Fong, Y. H.; Wong, H. C.; Yuen, M. H.; Lau, P. H.; Chen, Y. W.; Wong, K. B., Structure of UreG/UreF/UreH complex reveals how urease accessory proteins facilitate maturation of *Helicobacter pylori* urease. *PLoS Biol.* **2013**, *11* (10), e1001678.
43. Yuen, M. H.; Fong, Y. H.; Nim, Y. S.; Lau, P. H.; Wong, K. B., Structural insights into how GTP-dependent conformational changes in a metallochaperone UreG facilitate urease maturation. *Proc. Natl. Acad. Sci. U. S. A.* **2017**, *114* (51), E10890-e10898.

44. Yang, X.; Koochi-Moghadam, M.; Wang, R.; Chang, Y. Y.; Woo, P. C. Y.; Wang, J.; Li, H.; Sun, H., Metallochaperone UreG serves as a new target for design of urease inhibitor: A novel strategy for development of antimicrobials. *PLoS Biol.* **2018**, *16* (1), e2003887.
45. Tarsia, C.; Danielli, A.; Florini, F.; Cinelli, P.; Ciurli, S.; Zambelli, B., Targeting *Helicobacter pylori* urease activity and maturation: In-cell high-throughput approach for drug discovery. *Biochim. Biophys. Acta Gen. Subj.* **2018**, *1862* (10), 2245-2253.
46. Benoit, S. L.; McMurry, J. L.; Hill, S. A.; Maier, R. J., *Helicobacter pylori* hydrogenase accessory protein HypA and urease accessory protein UreG compete with each other for UreE recognition. *Biochim. Biophys. Acta* **2012**, *1820* (10), 1519-1525.
47. Benoit, S.; Mehta, N.; Wang, G.; Gatlin, M.; Maier, R. J., Requirement of hydD, hydE, hypC and hypE genes for hydrogenase activity in *Helicobacter pylori*. *Microb. Pathog.* **2004**, *36* (3), 153-157.
48. Cheng, T.; Li, H.; Yang, X.; Xia, W.; Sun, H., Interaction of SlyD with HypB of *Helicobacter pylori* facilitates nickel trafficking. *Metallomics : integrated biometal science* **2013**, *5* (7), 804-807.
49. Maier, R. J.; Benoit, S. L.; Seshadri, S., Nickel-binding and accessory proteins facilitating Ni-enzyme maturation in *Helicobacter pylori*. *Biometals* **2007**, *20* (3-4), 655-664.
50. de Reuse, H.; Vinella, D.; Cavazza, C., Common themes and unique proteins for the uptake and trafficking of nickel, a metal essential for the virulence of *Helicobacter pylori*. *Front. Cell Infect. Microbiol.* **2013**, *3*, 94.
51. Xia, W.; Li, H.; Sze, K. H.; Sun, H., Structure of a nickel chaperone, HypA, from *Helicobacter pylori* reveals two distinct metal binding sites. *J. Am. Chem. Soc.* **2009**, *131* (29), 10031-10040.

52. Hu, H. Q.; Johnson, R. C.; Merrell, D. S.; Maroney, M. J., Nickel Ligation of the N-Terminal Amine of HypA Is Required for Urease Maturation in *Helicobacter pylori*. *Biochemistry* **2017**, *56* (8), 1105-1116.
53. Spronk, C.; Zerko, S.; Gorka, M.; Kozminski, W.; Bardiaux, B.; Zambelli, B.; Musiani, F.; Piccioli, M.; Basak, P.; Blum, F. C.; Johnson, R. C.; Hu, H.; Merrell, D. S.; Maroney, M.; Ciurli, S., Structure and dynamics of *Helicobacter pylori* nickel-chaperone HypA: an integrated approach using NMR spectroscopy, functional assays and computational tools. *J. Biol. Inorg. Chem.* **2018**, *23* (8), 1309-1330.
54. Herbst, R. W.; Perovic, I.; Martin-Diaconescu, V.; O'Brien, K.; Chivers, P. T.; Pochapsky, S. S.; Pochapsky, T. C.; Maroney, M. J., Communication between the zinc and nickel sites in dimeric HypA: metal recognition and pH sensing. *J. Am. Chem. Soc.* **2010**, *132* (30), 10338-10351.
55. Mehta, N.; Olson, J. W.; Maier, R. J., Characterization of *Helicobacter pylori* nickel metabolism accessory proteins needed for maturation of both urease and hydrogenase. *J. Bacteriol.* **2003**, *185* (3), 726-734.
56. Xia, W.; Li, H.; Yang, X.; Wong, K. B.; Sun, H., Metallo-GTPase HypB from *Helicobacter pylori* and its interaction with nickel chaperone protein HypA. *J. Biol. Chem.* **2012**, *287* (9), 6753-6763.
57. Watanabe, S.; Kawashima, T.; Nishitani, Y.; Kanai, T.; Wada, T.; Inaba, K.; Atomi, H.; Imanaka, T.; Miki, K., Structural basis of a Ni acquisition cycle for [NiFe] hydrogenase by Ni-metallochaperone HypA and its enhancer. *Proc. Natl. Acad. Sci. U. S. A.* **2015**, *112* (25), 7701-7706.
58. Chan, K. H.; Lee, K. M.; Wong, K. B., Interaction between hydrogenase maturation factors HypA and HypB is required for [NiFe]-hydrogenase maturation. *PLoS One* **2012**, *7* (2), e32592.

59. Lacasse, M. J.; Summers, K. L.; Khorasani-Motlagh, M.; George, G. N.; Zamble, D. B., Bimodal Nickel-Binding Site on Escherichia coli [NiFe]-Hydrogenase Metallochaperone HypA. *Inorg. Chem.* **2019**, *58* (20), 13604-13618.
60. Blum, F. C.; Hu, H. Q.; Servetas, S. L.; Benoit, S. L.; Maier, R. J.; Maroney, M. J.; Merrell, D. S., Structure-function analyses of metal-binding sites of HypA reveal residues important for hydrogenase maturation in Helicobacter pylori. *PLoS One* **2017**, *12* (8), e0183260.
61. Johnson, R. C.; Hu, H. Q.; Merrell, D. S.; Maroney, M. J., Dynamic HypA zinc site is essential for acid viability and proper urease maturation in Helicobacter pylori. *Metallomics : integrated biometal science* **2015**, *7* (4), 674-682.
62. Stingl, K.; Schauer, K.; Ecobichon, C.; Labigne, A.; Lenormand, P.; Rouselle, J. C.; Namane, A.; de Reuse, H., In vivo interactome of Helicobacter pylori urease revealed by tandem affinity purification. *Mol. Cell Proteomics* **2008**, *7* (12), 2429-2441.
63. Benoit, S. L.; Mehta, N.; Weinberg, M. V.; Maier, C.; Maier, R. J., Interaction between the Helicobacter pylori accessory proteins HypA and UreE is needed for urease maturation. *Microbiology* **2007**, *153* (Pt 5), 1474-1482.
64. Hu, H. Q.; Huang, H. T.; Maroney, M. J., The Helicobacter pylori HypA.UreE2 Complex Contains a Novel High-Affinity Ni(II)-Binding Site. *Biochemistry* **2018**, *57* (20), 2932-2942.
65. Stahler, F. N.; Odenbreit, S.; Haas, R.; Wilrich, J.; Van Vliet, A. H.; Kusters, J. G.; Kist, M.; Bereswill, S., The novel Helicobacter pylori CznABC metal efflux pump is required for cadmium, zinc, and nickel resistance, urease modulation, and gastric colonization. *Infect. Immun.* **2006**, *74* (7), 3845-3852.

## CHAPTER 6

### CHARACTERIZATION OF THE HIGH-AFFINITY NICKEL BINDING SITE IN THE HYPA•UREE COMPLEX FROM *H. PYLORI*

#### 6.1 Introduction

*H. pylori* is a gastric pathogen which has a unique ability to survive the harsh acidic conditions of human stomach (~ pH 2), and cause gastric ulcers in almost 50% of the world's population, some of which are also associated with gastric carcinomas.<sup>1-2</sup> Acid viability of this pathogen is largely provided by its nickel-dependent enzyme urease, which catalyzes the conversion of urea to ammonia that aids in neutralization of the local pH around the pathogen.<sup>3-4</sup> Maturation of urease in *H. pylori* requires a cascade of accessory proteins, UreEFGH, which ensure proper delivery of cytosolic nickel to the enzyme.<sup>5</sup> Surprisingly, in addition to the urease specific accessory proteins, UreE, UreF, UreG and UreH, maturation of urease in *H. pylori* also requires HypA, a nickel metallochaperone, which is typically critical for the maturation of Ni, Fe – hydrogenase in most bacteria.<sup>6</sup> Biophysical and structural studies revealed that HypA can interact with UreE in *H. pylori*<sup>7-9</sup>, but the details of this interaction and its relevance requires further investigation.

*HpHypA* is a 13.2 kDa monomeric protein and contains two distinct and quasi-rigid metal binding domains – an intrinsic structural zinc-domain and a nickel binding domain (**Figure 6.1**).<sup>10-12</sup> At neutral or acidic pH, the nickel-binding stoichiometry of Zn-HypA is one per protein with an apparent  $K_d$  of 1  $\mu$ M.<sup>12-13</sup> The nickel binding site is located at the N-terminal conserved MHE-motif.<sup>10-12, 14</sup> Previous XAS characterization of the nickel site in WT-HypA identified a six-coordinate nickel-binding site with primarily N/O ligands, one or two of which were modeled as imidazole ligands.<sup>13</sup> Mutagenesis studies further confirmed His2 and the N-terminal amine<sup>12</sup> as two of the six nickel-binding ligands. The other four ligands for nickel binding were identified



from the NMR studies on a modified WT-HypA from *H. pylori*, where nickel was bound to His2, backbone amide N-donor atoms of His2 and Glu3, and Asp40.<sup>10</sup> Recent NMR studies further confirmed the six Ni-coordinating ligands as N-terminal amine, amide N-atoms from His2 and Glu3, the His2 imidazole side chain bound via N $\delta$ 1, and carboxylate side chains of Glu3 and Asp40.<sup>11</sup>

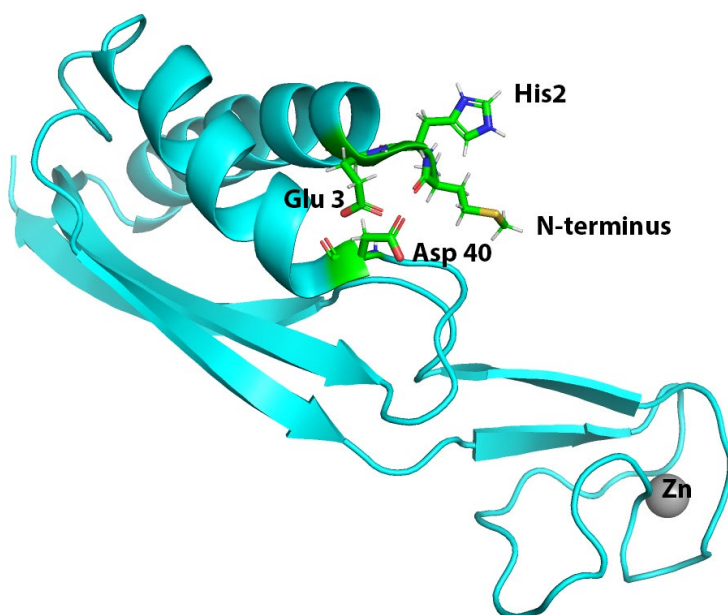


**Figure 6.1: Solution NMR structure of apo, Zn – WT HypA from *H. pylori* (PDB ID: 6G81): Zn- is shown as grey sphere and Ni binding site residues are shown in green color.**

*H. pylori* apo-UreE is a homodimer with a disordered C-terminal region, which is stabilized with the binding of Ni<sup>2+</sup> or Zn<sup>2+</sup>.<sup>15</sup> It binds one nickel per dimer with a binding affinity of 0.15  $\mu$ M.<sup>15</sup> X - ray Absorption spectroscopy on nickel-bound *H. pylori* UreE revealed a pseudo-octahedral arrangement of six N/O-donor ligands, with four N-donor atoms being contributed by four histidine ligands from UreE.<sup>15</sup> Crystallographic and site directed mutagenesis studies on the nickel site corroborated the XAS studies and identified the ligands as the two His102 residues, one

from each UreE monomer, His152 ligand from the C-terminal segment of UreE monomer, while His152 from other monomer was disordered, Glu4 and a water - molecule.<sup>15</sup>

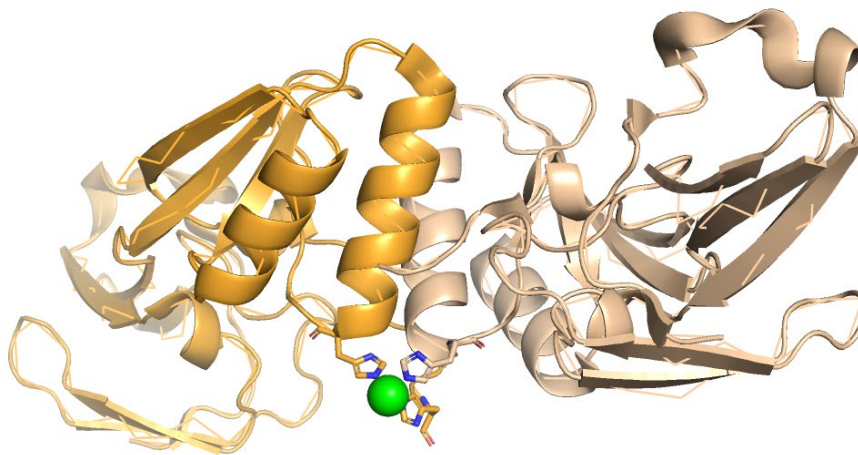


**Figure 6.2: Crystal structure of UreE-dimer from *H. pylori* (PDB ID: 3TJ8): green sphere shows the nickel bound to three histidine ligands. The fourth histidine ligand is disordered and not shown here.**

At neutral pH, HypA and UreE<sub>2</sub> form stable complexes as apo-proteins<sup>12, 16</sup> or in presence of metals<sup>16-17</sup> and it is postulated that such a protein-protein interaction improves nickel availability for urease maturation in *H. pylori*, either by tighter binding of nickel to preformed HypA•UreE<sub>2</sub> complex or enhancement of the HypA-UreE interaction in presence of nickel, especially under acid shock conditions.<sup>9</sup> Isothermal Titration Calorimetry (ITC) revealed that nickel binding to a complex of apo, Zn-HypA•UreE<sub>2</sub> is tighter than nickel binding to either apo,Zn-HypA or apo-UreE<sub>2</sub>.<sup>9</sup> Alternatively, titration of Ni, Zn-HypA to UreE<sub>2</sub> was accompanied by two binding events, that were pH independent – a low affinity binding event, similar to that observed for apo-Zn, HypA with UreE<sub>2</sub>, and a higher affinity binding event, ( $K_d = 0.6$  nM), not observed for apo-Zn, HypA with UreE<sub>2</sub>.<sup>9</sup> These studies revealed a novel high-affinity binding site of nickel in HypA•UreE<sub>2</sub>

complex. However, the coordination environment of this high-affinity nickel site in this complex is unknown and requires further investigation.

This chapter deals with characterizing the novel high-affinity binding site of nickel in HypA•UreE<sub>2</sub> complex under neutral and acidic pH conditions. The main objective of this characterization is to examine and understand the differences in coordination of nickel in the complex as compared to either HypA or UreE.

## **6.2 Experimental Procedures**

### **6.2.1 XAS data Collection**

XAS data on the frozen samples were collected at the Stanford Synchrotron Radiation Lightsource (SSRL) at the SLAC National Accelerator Laboratory using dedicated ring conditions (3 GeV and 450-500 mA) on beamline 9-3 with a Si (220) double crystal monochromator. The frozen samples in kapton-taped holders were immobilized on aluminium prongs and cooled to ~10K using liquid helium cryostat (Oxford instruments). A 100-element Ge detector (Canberra) was used for collecting X-ray fluorescence data. To minimize scattering, a 3  $\mu\text{m}$  Z-1 filter and Soller slits were installed between the detector and sample. X-ray fluorescence data on Ni K-edge of the Ni, Zn-HypA-UreE<sub>2</sub> complex were collected concurrently with spectra of a Ni metal foil in transmission mode for energy calibration. Extended X-ray Absorption Fine Structure (EXAFS) were collected to 15k above the K-edge for both metals.

**6.2.2 XAS Data Reduction and Analysis.** Data reduction and analyses were performed according to previously published procedures, adjusted for Ni and Zn K-edge XAS data.<sup>18</sup> The Sixpack<sup>19</sup> software package was used to process and normalize the XAS data. Fluorescence channels from each scan were visually checked for bad channels, which were deleted. For each scan, Ni K-edge

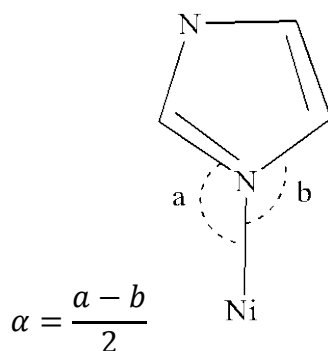
energy calibration was performed by assigning the first maximum in the first derivative spectrum of the Ni-foil to 8331.6 eV. The energy calibrated XAS data for Ni is an average of 8-9 scans that was normalized and corrected for background. For normalization and background correction, the K-edge energy of Ni was set to 8340 eV with a  $R_{\text{bkg}}$  of 1. The edge jump was normalized by setting the difference between the corrected pre-edge and post-edge baselines to 1. A linear function was used for fitting the pre-edge range of -200 to -50eV and quadratic polynomial functions with 7 spline points were used to fit the post-edge range of +150 to +880 eV relative to  $E_0$ . The EXAFS data were converted to k-space using the relationship  $[2m_e (E-E_0)/\hbar^2]^{1/2}$ , where  $m_e$  is the mass of electron and  $\hbar$  is the Plank's constant divided by  $2\pi$ . The  $k^3$ -weighted EXAFS data were Fourier-transformed over the k-range 2-12.5  $\text{\AA}^{-1}$  using a Hanning window and fit in r-space using an  $S_0$  value of 0.9. The r-space data shown in the figures were not corrected for phase shifts.

Similarly, for each scan, Zn K-edge energy calibration was performed by assigning the first maximum in the first derivative spectrum of the Zn-foil to 9660.7 eV. The energy calibrated XAS data for Zn is an average of 6 scans that was normalized and corrected for background. For normalization and background correction, the K-edge energy of Zn was set to 9670 eV with a  $R_{\text{bkg}}$  of 1. The edge jump was normalized by setting the difference between the corrected pre-edge and post-edge baselines to 1. A Gaussian function was used for fitting the pre-edge range of -200 to -50eV and quadratic polynomial functions with 7 spline points were used to fit the post-edge range of +150 to +880 eV relative to  $E_0$ . The EXAFS data were converted to k-space using the relationship  $[2m_e (E-E_0)/\hbar^2]^{1/2}$ , where  $m_e$  is the mass of electron and  $\hbar$  is the Plank's constant divided by  $2\pi$ . The  $k^3$ -weighted EXAFS data were Fourier-transformed over the k-range 2-14.5  $\text{\AA}^{-1}$  using a Hanning window and fit in r-space using an  $S_0$  value of 0.9. The r-space data shown in the figures were not corrected for phase shifts.

The Artemis software program<sup>19</sup> with FEFF6 and the IFEFFIT algorithm was used to generate and fit single and multiple scattering paths for each data as described previously<sup>15</sup>. Single-scattering fits were generated over an r-space of both 1-2.5 Å and 1- 4.0 Å, while multiple -scattering fits were carried out over 1- 4 Å. For each Ni-imidazole FEFF calculation, scattering paths with amplitudes greater than 16% were selected, which were used to model the EXAFS arising from scattering atoms in the imidazole ligand. The EXAFS fitting equation used was:

$$\chi(k) = \sum_i \frac{N_i f_i(k) e^{-2k^2 \sigma_i^2}}{k r_i^2} \sin[2k r_i + \delta_i(k)]$$

where  $f(k)$  is the scattering amplitude,  $\delta(k)$  is the phase-shift,  $N$  is the number of neighboring atoms,  $r$  is the distance to the neighboring atoms, and  $\sigma^2$  is a Debye-Waller factor reflecting the mean square deviation in the distance to the nearest neighbor (thermal and static disorder). The position of the imidazole ring with respect to metal center was fit in terms of metal-ligand bond distance ( $R_{\text{eff}}$ ) and the rotation angle ( $\alpha$ ) defined as below:



To compare the fits of different models to the data set, ifeffit utilizes three goodness of fit parameters:  $\chi^2$ , reduced  $\chi^2$  and the R-factor.  $\chi^2$  is given by equation 1, where  $N_{\text{idp}}$  is the number of independent data points,  $N_e^2$  is the number of uncertainties to minimize,  $\text{Re}(f_i)$  is the real part of EXAFS function and  $\text{Im}(f_i)$  is the imaginary part of the EXAFS fitting function.

$$\chi^2 = \frac{N_{idp}}{N_{\epsilon 2}} \sum_{i=1}^N \{[Re(f_i)^2] + [Im(f_i)^2]\} \quad (1)$$

Reduced  $\chi^2$  represents the degree of freedom in the fit and is given by equation (2)

$$red. \chi^2 = \frac{\chi^2}{N_{idp} - N_{var}} \quad (2)$$

where  $N_{var}$  is the number of refining parameters and  $N_{var}$  is the number of adjustable parameters.

Additionally, ifeffit calculates the R-factor for the fit, which is given by equation (3), and is scaled to the magnitude of the data making it proportional to  $\chi^2$ .

$$R = \frac{\sum_{i=1}^N \{[Re(f_i)^2] + [Im(f_i)^2]\}}{\sum_{i=1}^N \{[Re(xdata_i)]^2 + [Im(xdata_i)]^2\}} \quad (3)$$

In comparing different models, the R-factor and reduced  $\chi^2$  parameter were used to determine the model(s) that was the best fit for the data, from fits with acceptable  $\sigma^2$  parameters. The R-factor will generally improve with increasing number of adjustable parameters, while reduced  $\chi^2$  will go through a minimum and then increase, indicating that the model is overfitting the data. The resolution of the data for Zn and Ni was 0.15 and 0.18 determined by equation (4), using  $\Delta k$ -value of 12.5 and 10.5, respectively.

$$Resolution = \frac{\pi}{2 \times \Delta k} \quad (4)$$

## 6.3 Results

### 6.3.1 XANES and EXAFS analysis of Ni-site

*Ni site:* Ni K-edge X-ray Absorption Spectroscopy (XAS) was used to probe the structure of the Ni(II) site in the HypA•UreE<sub>2</sub> complex at pH 7.2 and pH 6.3. X-ray absorption near edge

structure (XANES) analysis can provide information about the coordination number and oxidation state of the metal-complexes.<sup>20</sup> Ni(II) complexes potentially show features associated with high-energy electronic transitions in the pre-edge XANES region of XAS spectra.<sup>20</sup> These transitions involve the promotion of one 1s electron to either the 3d manifold ( $1s \rightarrow 3d$ ), which occurs near 8331 eV, or to a  $4p_z$  orbital ( $1s \rightarrow 4p_z$ ), which occurs near 8336 eV.<sup>20</sup> XANES analysis of the nickel site in the HypA•UreE<sub>2</sub> complex show a small  $1s \rightarrow 3d$  feature at 8331.6 eV (**Figure 6.3A**) with a peak area of  $0.035 (\pm 0.002)$  eV<sup>2</sup>. This peak area coupled with the absence of any feature near 8336 eV is consistent with a 6-coordinate distorted octahedral geometry.

Analysis of the Extended X-ray Absorption Fine Structure (EXAFS) region of the XAS spectra of metal-complexes provides information on the identity of ligand-donor atoms ( $Z \pm 1$ ) around the metal center, the M-L distances ( $\pm 0.02 \text{ \AA}$ ), as well as a second measure of coordination number ( $\pm 20\%$ ). The Ni K-edge EXAFS spectrum of the Ni (II) site in the HypA•UreE<sub>2</sub> complex is shown in **Figure 6.3B**, with the fits leading to the best fit model of the Ni site structure summarized in **Table 1**. Single-scattering analysis of the EXAFS data of this complex indicates a nickel site with mainly N/O atoms in a 6-coordinate fashion (**Appendix B, Table B.1**), which is also consistent with the coordination number/geometry determined from the XANES analysis (*vide supra*). Systematic splitting of the single shell of 6-coordinate N/O atoms into two different shells corresponding to N/O atoms at two different distances did not improve the fit (**Appendix B, Table B.1**).

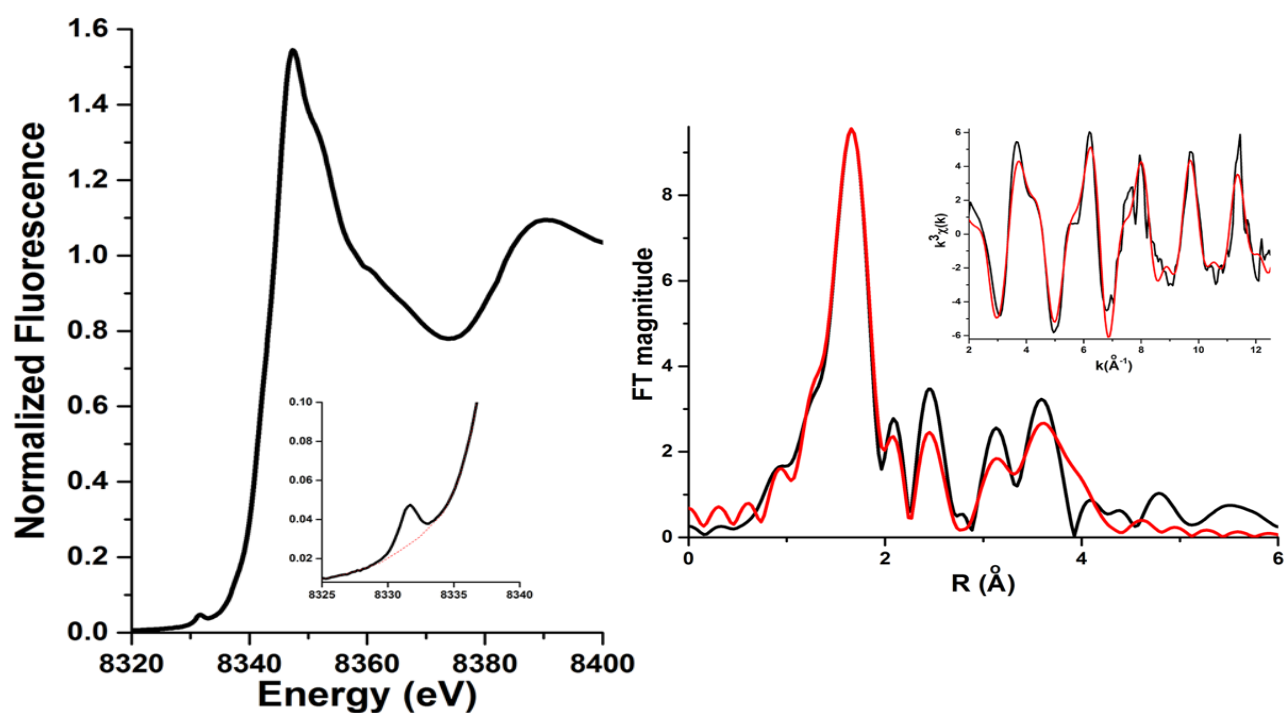


Figure 6.3: A) Ni K-edge XANES spectrum of Ni,Zn-WT-HypA•WT-UreE<sub>2</sub> complex at pH 7.2; the inset shows the 1s→3d transition (black) at 8330 eV and the baseline (dotted red line) used to measure the associated peak area B) Fourier transformed EXAFS ( $k = 2 - 12.5 \text{ \AA}^{-1}$ ) data (black) uncorrected for phase shifts and the best fit model (red) for Ni,Zn-WT-HypA•WT-UreE<sub>2</sub> complex at pH 7.2; the inset shows the  $k^3$ - weighted unfiltered EXAFS data (black) and best fit model (red).



**Table 6.1: Selected EXAFS fits for the Ni-site in the HypA-UreE<sub>2</sub> complex at pH 7.2**

Shell	r (Å)	$\sigma^2$ ( $\times 10^{-3} \text{ \AA}^{-2}$ )	$\Delta E_0$	R-factor	Red. $\chi^2$
<b>6 N/O</b>	2.08(1)	4(0)	1(2)	17.2	214.18
<b>5 N/O</b>	2.08(1)	6(1)	0(1)	10.2	144.00
<b>1Im0°</b>	2.09(1)	neg			
<b>4 N/O</b>	2.07(1)	5(2)	1(1)	8.1	114.11
<b>2Im0°</b>	2.09(1)	2(2)			
<b>3 N/O</b>	2.08(1)	2(1)	1(1)	6.6	93.18
<b>3Im0°</b>	2.09(2)	6(2)			
<b>2N/O</b>	2.08(1)	0(1)	0(1)	5.4	76.39
<b>4Im0°</b>	2.08(2)	8(1)			
<b>1N/O</b>	2.08(1)	neg	0(1)	5.3	76.04
<b>5Im0°</b>	2.08(1)	8(1)			
<b>3 N/O</b>	2.06(1)	2(1)	0(1)	6.5	91.57
<b>3Im5°</b>	2.10(2)	5(2)			
<b>3 N/O</b>	2.04(1)	4(1)	0(1)	5.3	74.76
<b>3Im10°</b>	2.10(1)	2(0)			
<b>3N/O</b>	<b>2.03(1)</b>	<b>7(2)</b>	<b>2(1)</b>	<b>3.6</b>	<b>59.44</b>
<b>1Im0°</b>	<b>2.07(1)</b>	<b>1(2)</b>			
<b>2Im10°</b>	<b>2.09(1)</b>	<b>1(1)</b>			

Multiple-scattering scaffolds were then added to account for the features in the FT-EXAFS spectra arising from second and third coordination sphere scattering atoms resulting from the coordination of His imidazole ligands using a rigid 5-membered ring with a single adjustable Ni-N distance, as previously described<sup>12, 15, 21</sup>. Addition of multiple-scattering pathways from single shells of one to five His imidazole ligands with  $\alpha = 0^\circ, 5^\circ$  or  $10^\circ$ , along with one shell of 1-5 N/O donors, and totaling six ligands, resulted in lower R-factors and  $\chi^2$  values, and gave acceptable Debye-Waller factors ( $\sigma^2$ ) for fits with three or four imidazole ligands. However, none produced a fit with  $R < 5\%$ , a criterion for a good model. Splitting the single shell of N/O scatterers in models with 3-4 His ligands resulted in modest improvements in R-factor but produced negative values of  $\sigma^2$  for N/O shells (**Appendix B, Table B.1**). In contrast, splitting the shell of imidazoles into shells with different  $\alpha$  angles dramatically improved the fits and produced fits with acceptable R-factors ( $< 5\%$ ) and Debye-Waller factors, with the fit containing three N/O-donors and three His ligands producing the best fit. This progression is shown in **Table 6.1** for the model with 3 His ligands that leads to the best fit model. Similar attempts to split the single shell of four imidazoles into two or three different shells resulted in unacceptable Debye -Waller factors (**Appendix B, Table B.1**).

The Ni K-edge XAS spectrum of the Ni (II) site in the HypA-UreE<sub>2</sub> complex at pH 6.3 is superimposable with that obtained at pH 7.2, indicating that the structure of the site is not greatly altered by this pH change. The XANES of the Ni (II) site in the HypA-UreE<sub>2</sub> complex at pH 6.3 also shows a small  $1s \rightarrow 3d$  feature at 8331.6 eV (**Appendix B, Figure B.1**) with a peak area of  $0.036 (\pm 0.002) \text{ eV}^2$ , indistinguishable from the value found at pH 7.2 and also consistent with a 6-coordinate nickel site. Comparison of the EXAFS data for the Ni(II) sites at two pHs, also reveals similar structures. The analysis of the EXAFS for the Ni-site in the HypA-UreE<sub>2</sub> complex at pH 6.3 (**Appendix B, Figure B.2**) as described for the pH 7.2 sample (*vide supra*), also reveals six

N/O-donor ligands (**Appendix B, Table B.2 & B.3**) and leads to a best fit model featuring three N/O scatterers and three imidazoles at similar distances. However, unlike the fits to the spectra obtained at pH 7.2, splitting the shell of three imidazoles did not improve the fit and resulted in negative Debye-Waller factors (**Appendix B, Table B.3**). The best model featured three N/O scatterers at 2.04 Å and a single shell of three imidazoles with Ni-N bond distance of 2.13 Å at an  $\alpha$ -angle 10°, and R=4.9%.

### **6.3.2 XANES and EXAFS analysis of Zn-site**

*Zn-site:* Zn K-edge X-ray Absorption Spectroscopy was used to analyze the Zn (II)-site of HypA in the Ni-HypA•UreE<sub>2</sub> complex at pH 7.2 (**Appendix B, Figure B.7 & B.8; Table B.4**) and 6.3 (**Appendix B, Figure B.9 & B.10; Table B. 5**). The best fits from the EXAFS analysis on the Zn-site results in Zn-S distances of 2.32(2) Å at both pH 7.2 and 6.3 with R<5% and is consistent with four sulfur ligands observed for WT-HypA.

## **6.4 Discussion**

Examination of the high- affinity nickel site in in the HypA-UreE complex at pH 7.2 by X-ray Absorption Spectroscopy reveals a distinct nickel binding site from either Ni,Zn-HypA (**Appendix B, Figure B.3**) or Ni-UreE<sub>2</sub> (**Appendix B, Figure B.4**). In Ni,Zn-WT-HypA, the nickel site is coordinated to the N-terminal amine, the imidazole and backbone amide from His2, and carboxylate groups from the side chains of Glu3 and Asp40. In Ni-UreE<sub>2</sub>, four histidine residues (two histidines - His 102 and His 152 from each monomeric subunit) of different angles at two shells of different distances, one N/O from Glu 4 and a water molecule coordinates the nickel atom. In the Ni, Zn-WT-HypA•UreE<sub>2</sub>, three N/O ligands and three distinct histidine ligands at two different distances coordinate the nickel atom. Two of these histidine ligands are at 10° and

one is oriented at 0°. The structure of this nickel site is similar at pH 6.3, with three N/O ligands and three histidine ligands, which, unlike that at 7.2, are all in a similar angular orientation of 10°. The Zn-site in the complex is similar to that of WT-HypA and is independent of pH changes, suggesting that the protein interactions does not alter this structural site in the complex.

From these results, it is clear that ligands from both HypA and UreE<sub>2</sub> contribute towards binding nickel in the HypA•UreE<sub>2</sub> complex with a physiologically relevant nickel-binding affinity<sup>12</sup>. As *H. pylori* WT-HypA alone has a lower binding affinity for nickel<sup>12</sup>, it may serve as a proteinaceous labile metal pool in *H. pylori*, and act as the primary acceptor of nickel from the nickel-importers in the pathogen. It is likely that after nickel acquisition, based on the cellular signals and/or demands of the pathogen, nickel-bound HypA interacts with either UreE<sub>2</sub> for urease maturation or HypB for H<sub>2</sub>ase maturation.

## 6.5 Conclusion

The nickel site in Ni, Zn-WT-HypA•UreE<sub>2</sub> complex is distinct from either Ni, Zn-WT-HypA or Ni-WT-UreE<sub>2</sub>. The high-affinity nickel site in this chaperone complex is octahedral and is composed of nickel ligands provided by both HypA and UreE. It will be interesting to further identify the ligands provided by these two nickel chaperones that form the distinct high-affinity nickel site in the complex.

## 6.6 References

1. Eusebi, L. H.; Zagari, R. M.; Bazzoli, F., Epidemiology of *Helicobacter pylori* infection. *Helicobacter* **2014**, *19 Suppl 1*, 1-5.
2. Marshall, B. J.; Warren, J. R., Unidentified curved bacilli in the stomach of patients with gastritis and peptic ulceration. *Lancet* **1984**, *1* (8390), 1311-1315.
3. Camilo, V.; Sugiyama, T.; Touati, E., Pathogenesis of *Helicobacter pylori* infection. *Helicobacter* **2017**, *22* (S1), e12405.
4. Sachs, G.; Weeks, D. L.; Wen, Y.; Marcus, E. A.; Scott, D. R.; Melchers, K., Acid acclimation by *Helicobacter pylori*. *Physiology (Bethesda)* **2005**, *20*, 429-438.
5. Maier, R. J.; Benoit, S. L.; Seshadri, S., Nickel-binding and accessory proteins facilitating Ni-enzyme maturation in *Helicobacter pylori*. *Biometals* **2007**, *20* (3-4), 655-664.
6. Olson, J. W.; Mehta, N. S.; Maier, R. J., Requirement of nickel metabolism proteins HypA and HypB for full activity of both hydrogenase and urease in *Helicobacter pylori*. *Mol. Microbiol.* **2001**, *39* (1), 176-182.
7. Benoit, S. L.; Mehta, N.; Weinberg, M. V.; Maier, C.; Maier, R. J., Interaction between the *Helicobacter pylori* accessory proteins HypA and UreE is needed for urease maturation. *Microbiology* **2007**, *153* (Pt 5), 1474-1482.
8. Yang, X.; Li, H.; Cheng, T.; Xia, W.; Lai, Y. T.; Sun, H., Nickel translocation between metallochaperones HypA and UreE in *Helicobacter pylori*. *Metallomics : integrated biometal science* **2014**, *6* (9), 1731-1736.
9. Hu, H. Q.; Huang, H. T.; Maroney, M. J., The *Helicobacter pylori* HypA.UreE2 Complex Contains a Novel High-Affinity Ni(II)-Binding Site. *Biochemistry* **2018**, *57* (20), 2932-2942.

10. Xia, W.; Li, H.; Sze, K. H.; Sun, H., Structure of a nickel chaperone, HypA, from *Helicobacter pylori* reveals two distinct metal binding sites. *J. Am. Chem. Soc.* **2009**, *131* (29), 10031-10040.
11. Spronk, C.; Zerko, S.; Gorka, M.; Kozminski, W.; Bardiaux, B.; Zambelli, B.; Musiani, F.; Piccioli, M.; Basak, P.; Blum, F. C.; Johnson, R. C.; Hu, H.; Merrell, D. S.; Maroney, M.; Ciurli, S., Structure and dynamics of *Helicobacter pylori* nickel-chaperone HypA: an integrated approach using NMR spectroscopy, functional assays and computational tools. *J. Biol. Inorg. Chem.* **2018**, *23* (8), 1309-1330.
12. Hu, H. Q.; Johnson, R. C.; Merrell, D. S.; Maroney, M. J., Nickel Ligation of the N-Terminal Amine of HypA Is Required for Urease Maturation in *Helicobacter pylori*. *Biochemistry* **2017**, *56* (8), 1105-1116.
13. Herbst, R. W.; Perovic, I.; Martin-Diaconescu, V.; O'Brien, K.; Chivers, P. T.; Pochapsky, S. S.; Pochapsky, T. C.; Maroney, M. J., Communication between the zinc and nickel sites in dimeric HypA: metal recognition and pH sensing. *J. Am. Chem. Soc.* **2010**, *132* (30), 10338-10351.
14. Mehta, N.; Olson, J. W.; Maier, R. J., Characterization of *Helicobacter pylori* nickel metabolism accessory proteins needed for maturation of both urease and hydrogenase. *J. Bacteriol.* **2003**, *185* (3), 726-734.
15. Banaszak, K.; Martin-Diaconescu, V.; Bellucci, M.; Zambelli, B.; Rypniewski, W.; Maroney, M. J.; Ciurli, S., Crystallographic and X-ray absorption spectroscopic characterization of *Helicobacter pylori* UreE bound to Ni(2)(+) and Zn(2)(+) reveals a role for the disordered C-terminal arm in metal trafficking. *Biochem. J.* **2012**, *441* (3), 1017-1026.

16. Benoit, S. L.; McMurry, J. L.; Hill, S. A.; Maier, R. J., Helicobacter pylori hydrogenase accessory protein HypA and urease accessory protein UreG compete with each other for UreE recognition. *Biochim. Biophys. Acta* **2012**, *1820* (10), 1519-1525.
17. Yang, X.; Li, H.; Lai, T. P.; Sun, H., UreE-UreG complex facilitates nickel transfer and preactivates GTPase of UreG in Helicobacter pylori. *J. Biol. Chem.* **2015**, *290* (20), 12474-12485.
18. Higgins, K. A.; Hu, H. Q.; Chivers, P. T.; Maroney, M. J., Effects of select histidine to cysteine mutations on transcriptional regulation by Escherichia coli RcnR. *Biochemistry* **2013**, *52* (1), 84-97.
19. Webb, S. M., SIXPack a Graphical User Interface for XAS Analysis Using IFEFFIT. *Physica Scripta* **2005**, 1011-1014.
20. Colpas, G. J.; Maroney, M. J.; Bagyinka, C.; Kumar, M.; Willis, W. S.; Suib, S. L.; Mascharak, P. K.; Baidya, N., X-ray spectroscopic studies of nickel complexes, with application to the structure of nickel sites in hydrogenases. *Inorg. Chem.* **1991**, *30* (5), 920-928.
21. Martin-Diaconescu, V.; Bellucci, M.; Musiani, F.; Ciurli, S.; Maroney, M. J., Unraveling the Helicobacter pylori UreG zinc binding site using X-ray absorption spectroscopy (XAS) and structural modeling. *J. Biol. Inorg. Chem.* **2012**, *17* (3), 353-361.

## CHAPTER 7

### PERTURBATION OF PROTEIN DYNAMICS BY GLYCINE MUTATIONS IN HYPA: THE ROLE OF HYPA CONFORMATIONS IN UREASE AND HYDROGENASE MATURATION IN *H. PYLORI*

#### 7.1 Introduction

*H. pylori* is a human pathogen responsible for gastritis and is associated with gastric cancers.<sup>1-2</sup> This pathogen has a unique ability to colonize and survive the harsh acidic conditions of human stomach, and nickel largely contributes to its acid acclimation.<sup>3</sup> Nickel forms the cofactor of urease, which catalyzes the hydrolysis of urea to ammonia and carbamate, thus neutralizing the pH around the pathogen.<sup>2</sup> In addition to urease, *H. pylori* has another nickel – dependent, membrane-bound enzyme – Ni, Fe- hydrogenase, which catalyzes the reversible oxidation of hydrogen. It functions as a hydrogen-uptake hydrogenase in the pathogen and is required for efficient colonization of *H. pylori* in mouse models.<sup>4-6</sup> Recent studies reveal that Ni, Fe-hydrogenase enzyme provides compact and high-energy substrate for respiratory-based energy generation which is utilized by the pathogen to translocate the of CagA cytotoxin through the T4SS pathway in to the host cells.<sup>7</sup> Maturation of two nickel - dependent enzymes in *H. pylori* requires proper delivery of nickel to the respective active sites of these enzymes.<sup>8</sup> High - fidelity nickel delivery is achieved by a cascade of accessory proteins for each of these two nickel enzymes – UreEFGH cascade for urease<sup>2,9</sup> and HypABCDEF for Ni, Fe- hydrogenase<sup>8,10-11</sup>. The *hyp* cascade of accessory proteins in other bacteria such as, *E. coli* is usually involved in the maturation of Ni, Fe- hydrogenase, but surprisingly, in *H. pylori*, it is also critical to the delivery of nickel to urease.<sup>12</sup> Deletion of *hypA* in *H. pylori* strains causes loss of activity in both these enzymes.<sup>12</sup> Ureolytic



inactivation due to *hypA* deletion compromises the acid viability of *H. pylori*<sup>13</sup> but loss of its hydrogenase activity does not affect its acid viability.<sup>1</sup> How *HpHypA* carries out differential delivery of nickel to both enzymes in *H. pylori* is unknown.

*HpHypA* is a 13.2 kDa monomeric protein and contains two distinct metal binding sites – an intrinsic structural zinc-domain and a nickel binding domain (**Figure 7.1**).<sup>3, 14-15</sup> The Zn - site is coordinated to two conserved CXXC motifs provided by Cys71, Cys 77, Cys91 and Cys 94 in *HpHypA*.<sup>14</sup> In addition to the conserved CXXC motifs in the structural Zn-site, *H. pylori* HypA also has His residues (His 75 and His 95) closely flanking the conserved motifs.<sup>14</sup> Extensive X-ray Absorption Spectroscopic (XAS) characterization of *H. pylori* HypA Zn - site show that this metal binding site is dynamic.<sup>16</sup> At neutral pH (7.2), the average Zn coordination is Zn(Cys)<sub>4</sub>, which changes to Zn(Cys)<sub>2</sub>(His)<sub>2</sub> at pH 6.3 (the estimated internal pH of *H. pylori* under acid shock conditions).<sup>16</sup> However, no evidence for a pH induced structural change in the Zn(II) coordination environment of *HpHypA* was found from its recent room temperature high resolution NMR structure.<sup>15</sup> Substitution of any of the four conserved Cys residues to Ala or Asp causes the loss of the dynamic nature of the Zn - site and locks it in a Zn(Cys)<sub>2</sub>(His)<sub>2</sub> structure.<sup>16</sup> Mutation of histidines (His 79 and 95), however, retains the Zn(Cys)<sub>4</sub> structure. Interestingly, only the Cys variants and not the His variants of *HpHypA* show moderate (Cys 71 and 77) to severe impairment (Cys 91 and Cys 94) in acid viability of the pathogen.<sup>13</sup>

At neutral or acidic pH, the nickel-binding stoichiometry of Zn-HypA is one per protein with an apparent  $K_d$  of 1  $\mu$ M.<sup>3, 16</sup> The nickel binding site in HypA has long been associated with the N-terminal conserved MHE-motif. Mutation of His2 residue in *HpHypA* and extension of the N-terminal amine (L2\*-variant of *HpHypA*) caused a loss of Ni binding, with the latter also affecting the acid viability of the pathogen.<sup>3, 11</sup> NMR studies on a modified WT-HypA (reminiscent

of affinity purification with two additional residue (GS-) preceding the N-terminus of *HpHypA*) from *H. pylori* identified a diamagnetic four-coordinate nickel- site with backbone amide N-donor atoms of His2 and Glu3, and Asp 40, along with His 2 as nickel-binding ligands.<sup>14</sup> XAS characterization and magnetic susceptibility measurements of the nickel site in WT-*HpHypA*, on the other hand, identified a paramagnetic six-coordinate nickel-binding site with primarily N/O ligands, one or two of which were modeled as imidazole ligands.<sup>16</sup> Recent NMR studies confirmed that the Ni-site in *HpHypA* is six-coordinate with N-terminal amine, amide N-atoms from His2 and Glu3, the His2 imidazole side chain bound via N $\delta$ 1, and carboxylate side chains of Glu3 and Asp40 as nickel-ligands in the chaperone (**Figure 7.1, inset**).<sup>15</sup>

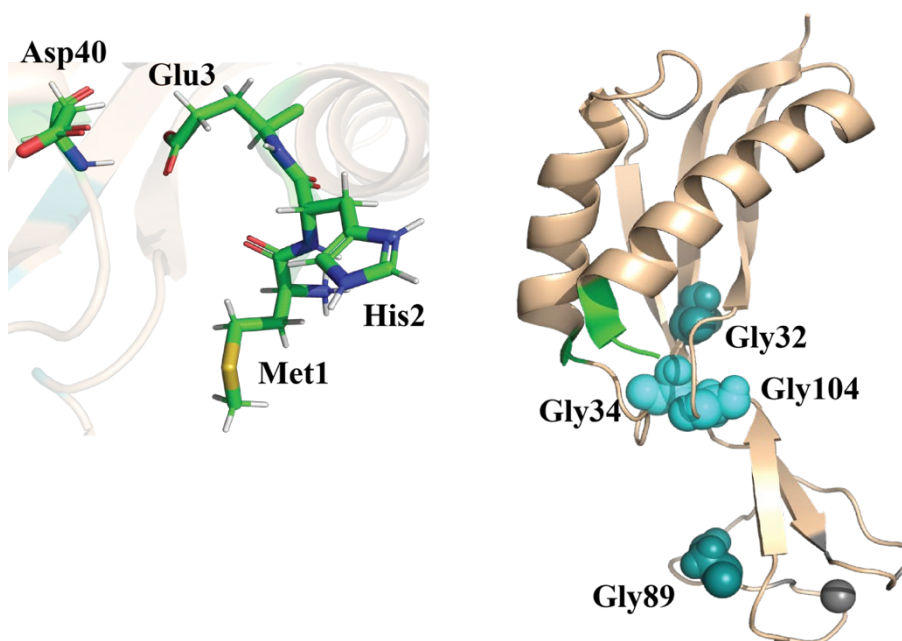


**Figure 7.1: Solution NMR structure of nickel metallochaperone HypA from *H. pylori* (PDB: 6G81<sup>15</sup>) showing Zn- (grey sphere) and Ni- binding site (green). Glycine residues are shown as space-filling spheres (conserved, Gly34 and Gly104 are shown in cyan and non-conserved, Gly32 and Gly89 are shown in teal); *Inset* shows the Ni-binding site residues at the N-terminus of *HpHypA*.**

The recent solution structure of *HpHypA* revealed variable orientation of the metal binding domains connected by a flexible linker.<sup>15</sup> Flexibility in proteins is an intrinsic part of protein structure and is important for molecular recognition.<sup>17</sup> It is defined as concerted conformational changes in the proteins that affect its few degrees of freedom, without modifying its structure or destroying it, and encompasses different kinds of conformational changes corresponding to the mobility of rigid part of the protein, e.g. domain motions (ii) deformability of the protein backbone, e.g. crankshaft motions or (iii) both.<sup>17-18</sup> It is possible that owing to such intrinsic flexibility, *HpHypA* exists in distinct conformational states in solution, some of which may interact differentially with UreE and HypB, thereby mediating the maturation of urease and Ni, Fe - hydrogenase, respectively in *H. pylori*. The primary aim of this research was to perturb *HpHypA* flexibility and dynamics, which in turn may disrupt critical structural changes around its Zn- and/or Ni-site or its overall tertiary structure in a way that affects the interactions between HypA and proteins in the urease and/or hydrogenase maturation pathways, thus hampering its function as a nickel chaperone and hence survival of *H. pylori*.

To interrogate the flexibility and dynamics of *HpHypA*, the flexibility hot-spot residues in this metallochaperone, i.e., the glycine residues (**Figure 7.1**), both conserved (Gly34 and Gly 104), and non-conserved (Gly32 and Gly 89) were mutated to a more constrained Alanine. Glycine is the smallest amino acid residue with no side chains, possess the highest degree of rotational freedom, and is shown to impart backbone flexibility in enzyme active sites, and transmembrane helices.<sup>17</sup> The effect of these mutations on acid viability of the pathogen, and the *in vitro* urease and hydrogenase activities were studied. Changes in coordination of metal sites (Zn-site and Ni-site) were examined using X-ray Absorption Spectroscopy. Changes in secondary structure of these HypA variants were monitored by Circular Dichroism Spectroscopy.

## 7.2 Experimental Procedures

### 7.2.1 Site-Directed mutagenesis of Glycine residues in HypA from *H. pylori*

Polymerase chain reaction (PCR) was used to introduce the desired glycine to alanine mutations in HypA. A pET22b (+) vector encoding the wild type *hypA* sequence from *H. pylori* was used as the template DNA for single point mutations, and PCR primers (listed in **Table 7.1**) were designed to incorporate the desired mutations. For each 50  $\mu$ L volume of PCR reaction mixture, 0.5  $\mu$ M of each primer was used for 2 ng of template DNA. For inserting G34A/G104A double point mutation in HypA, primers for G34A HypA were used with the G104A HypA plasmid as the template. Similarly, for inserting G32A/G89A double point mutation in HypA, the G32A HypA plasmid was used as the template with G89A HypA primers. Successful PCR amplifications were determined using a 0.8% agarose gel and the amplicons were subsequently digested with DpnI for 1 hr at 37 °C to remove any methylated template DNA. The digested PCR mixture was then transformed into Novablue competent cells with an ampicillin resistance gene (Fisher Scientific) for selection and the transformed cells were plated on LB-agar plates containing ampicillin (100mg/ml). Single colonies were grown to saturation in 5ml LB-miller broth supplemented with ampicillin at 37 °C. Cells were pelleted at 13,000 g for 5 minutes and the plasmids were isolated using a GeneJET plasmid miniprep kit (Thermo Fisher Scientific). Plasmid sequencing (Genewiz, Inc.) confirmed the successful mutations.

**Table 7.1: Primers and plasmids used in this study**

Plasmid	Description	Reference
pET22b-HypA(G34A)	pET22b(+) vector with hypA G34A coding sequence	This study
pET22b-HypA(G104A)	pET22b(+) vector with hypA G104A coding sequence	This study
pET22b-HypA(G34/G10A)	pET22b(+) vector with hypA G34A/G104A coding sequence	This study
pET22b-HypA(G32A)	pET22b(+) vector with hypA G32A coding sequence	This study
pET22b-HypA(G89A)	pET22b(+) vector with hypA G89A coding sequence	This study
pET22b-HypA(G32/G89A)	pET22b(+) vector with hypA G32A/G89A coding sequence	This study
Primers	Sequence (5' to 3')	Reference
HypA_G34A_F	GTGGTCGGTATTG <u>CT</u> GAAAGAAG	This study
HypA_G34A_R	CATAGCACTTCTTT <u>CAG</u> CAATACCGACCAC	This study
HypA_G104A_F	TGTTATTATCACTCAAG <u>CCA</u> TGAAATGC	This study
HypA_G104A_R	CATTT <u>CATTGG</u> CTTGAGTGATAATAACATTCTTGC	This study
HypA_G32A_F	GAAAGAGTCGTGGT <u>CGC</u> ATTGGTGAAAGAAGTGCT	This study
HypA_G32A_R	ATCCATAGCACTTCTTT <u>CACCA</u> TGGCGACCACGAC	This study
HypA_G89A_F	GCGCTAGATTATG <u>CGG</u> TCTGTGAGAAATGCCAC	This study
HypA_G89A_R	GCTGTCGCATTTCTCACAC <u>ACC</u> GATAATCTAG	This study

\*The changed nucleotides are underlined.

### 7.2.2 Expression & Purification of *HpHypA* glycines,

Each glycine variant of HypA was expressed as previously described<sup>1</sup> with some modification in time and temperature to maximize the protein expression (**Table 7.2**). Purification of each HypA variant was performed as previously described<sup>1</sup> and the mass of each HypA variant was determined by ESI-MS and was found to be consistent with predicted mass (**Table 7.2**).

**Table 7.2: Optimized conditions used for maximal expression of glycine variants of HypA and the corresponding mass of purified proteins**

HypA variant	Time and Temperature after induction for maximal expression	Theoretical mass (Da)	Experimental mass (Da)
G34A	6 hours at 25°C	13216.25	13214.85
G104A	3 hours at 37°C	13216.25	13214.93
G34A/G104A	6 hours at 25°C	13230.28	13230.05
G32A	6 hours at 25°C	13216.25	13214.87
G89A	6 hours at 25°C	13216.25	13214.90
G32A/G89A	3 hours at 37°C	13230.28	13230.12

### 7.2.3 Acid Viability Assays

The plasmids with the desired glycine to alanine mutations in the *hypA* coding sequence were used by Prof. Douglas S. Merrell (The Uniformed Services University, Bethesda MD) to insert the mutant DNA of interest into the *H. pylori* chromosomal DNA as described previously.<sup>13</sup> These genetic manipulations resulted in mutant *H. pylori* strains that expressed only the HypA variants, as listed in **Table 7.3**. In order to control any defects arising as a result of these manipulations, a *hypA*-restorant strain was also made where the *kan-sac* cassette is replaced by wild type *hypA* gene.<sup>13</sup> Other controls (WT,  $\Delta$ *ureB*,  $\Delta$ *hydB*) were created as previously described.<sup>13</sup>

The acid resistance of each of the six mutant *H. pylori* strains containing glycine to alanine mutations in *hypA* were tested in the Merrell lab using the method described previously. Wild type

*H. pylori* strain, *hypA::kan-sac* strain, *hypA*-restorant strain and *ureB::kan-sac* (or  $\Delta ureB$ ) strain were used as controls. Three biological replicates were performed for each strain.

**Table 7.3: Strain of *H. pylori* used in this study**

Strain	Description	Reference
DSM 1	G27 WT	1, 2
DSM 43	G27 $\Delta ureB$ ( <i>ureB::kan</i> ), Kan <sup>R</sup>	1,2
DSM 1570	G27 $\Delta hydB$ ( <i>hydB::kan</i> ), Kan <sup>R</sup>	2
DSM 1283	G27 $\Delta hypA$ ( <i>hypA::kan-sac</i> ) Kan <sup>R</sup> , Sac <sup>S</sup>	1,2
DSM 1295	G27 <i>hypA</i> restorant	1-2, This study
DSM 1476	G27 <i>hypA</i> G34A	This study
DSM 1477	G27 <i>hypA</i> G104A	This study
DSM 1478	G27 <i>hypA</i> G34A/G104A	This study
DSM 1649	G27 <i>hypA</i> G32A	This study
DSM 1650	G27 <i>hypA</i> G389A	This study
DSM 1651	G27 <i>hypA</i> G32A/G89A	

#### 7.2.4 *In vitro* Urease Activity Assay

For urease activity assays, an overnight culture of each of the six mutant *H. pylori* strains along with the controls (Wild type, *hypA::kan-sac*, *hypA*-restorant,  $\Delta ureB$ ) were made by Prof. Douglas S. Merrell (The Uniformed Services University, Bethesda MD). Briefly, each of the cultures were diluted to an OD<sub>600</sub> of 0.05, and the cells were grown for 20 hours, after which the OD<sub>600</sub> was measured and 1.0 ODU (optical density units) of bacteria were pelleted for 2 minutes at 2000 x g. The medium was aspirated off, and the pellets were frozen at -80°C. The frozen cells were then transferred to University of Massachusetts Amherst for the *in vitro* assays described as

follows. The frozen cells were thawed, re-suspended in 750 $\mu$ L of ice-cold lysis buffer (50mM HEPES, pH 7.0, 1mM phenylmethanesulfonic acid (PMSF) and 1X protease cocktail inhibitor from Sigma-Aldrich) and then lysed by pulsed sonication (500Hz) at 40% amplitude for 12 seconds (2 seconds each pulse) on ice. The lysed cells were centrifuged at 14,000 x g for 15 minutes at 4 °C to remove insoluble particles from the soluble whole cell extract. Total protein concentration in the soluble whole cell extract was determined using Bradford assay with Coomassie Protein Assay kit (Thermo Scientific).

A modified phenol-hypochlorite method was used to assay the ammonia released from the soluble whole cell extract of *H pylori* strains in the presence of urea.<sup>13,16</sup> Briefly, 5 $\mu$ L of the soluble whole cell extract of each strain was added to 245  $\mu$ L of urease reaction buffer (50 mM HEPES, 25 mM urea, pH 7.0) and the mixture was incubated for 20 minutes at 37 °C to allow production of ammonia in solution. The reaction was quenched with sequential addition of 375  $\mu$ L of Quenching Buffer A (100 mM phenol, 167.8  $\mu$ M sodium nitroprusside) and 375  $\mu$ L of Quenching Buffer B (125 mM phenol, 0.044% NaClO). The assay samples were quickly vortexed with each buffer addition and then incubated at 37 °C for 30 minutes to allow for color development (conversion of ammonia to indophenol). The absorbance of each assay sample was measured at 625 nm using a UV-visible spectrophotometer (Hewlett-Packard 8453). The ammonia released from each assay mixture was quantified using a standard curve (**Appendix C, Figure C.1**) prepared using known amounts of ammonium chloride (0.2-500 nmol) solution in place of whole cell extracts. The urease activity of *ΔureB* strain was treated as background and subtracted from the urease activity of other strains. The urease activity of mutant *hypA* strains was normalized to *hypA* - restorant strain (*hypA-R*, DSM1295) whose urease activity was treated as 100%. All assays were conducted in triplicate for two independently grown cultures.



### 7.2.5 *In vitro* Hydrogenase Activity Assay

For hydrogenase activity assays, hydrogen oxidation activity was measured at room temperature (~23 °C) using the whole cell lysates of the various *H. pylori* strains (*vide supra*). Cells were grown as previously described<sup>13</sup> by Prof. Douglas S. Merrell (The Uniformed Services University, Bethesda MD), and approximately  $10^8$  cells were pelleted and frozen at -80 °C prior to lysis. The cells were thawed on ice and then resuspended in 750  $\mu$ L of ice-cold *H. pylori* lysis buffer (50 mM HEPES at pH 7.0 with 1 mM phenylmethanesulfonyl fluoride (PMSF)). The resuspended cells were then kept on ice during lysis by pulsed sonication (500 Hz) at 40% amplitude for 14 seconds. H<sub>2</sub> consumption was measured as previously described<sup>19</sup> with slight modifications. Briefly, an aliquot of whole cell lysate was used to test H<sub>2</sub> oxidation activity by monitoring the reduction of methyl viologen (MV) inside an anaerobic chamber (COY Labs, Grass Lake, MI) with a consistent atmosphere of primarily N<sub>2</sub> with 3–4% H<sub>2</sub> and 0–20 ppm O<sub>2</sub>. Oxidized-MV (colorless) is the electron acceptor in the H<sub>2</sub> oxidation reaction catalyzed by hydrogenase in the lysate resulting in formation of reduced-MV (blue). The appearance of reduced-MV was monitored at  $A_{578 \text{ nm}}$  ( $\epsilon = 9.78 \text{ mM}^{-1} \cdot \text{cm}^{-1}$ )<sup>20</sup> using a UV-Visible spectrophotometer (UV-1280, Shimadzu). The reaction was initiated by adding 30  $\mu$ L of whole cell lysate to 1 mL of deoxygenated H<sub>2</sub>ase Reaction Buffer (50 mM Tris-HCl, 2 mM methyl viologen, pH 8.0) in a glass vial. After an initial lag time, the reaction mixture was transferred to a quartz cuvette and the appearance of reduced methyl viologen was monitored at  $A_{578 \text{ nm}}$  for 45–150 minutes. The slope of the linear increase in absorbance over time (**Appendix C, Figure C.2**) was taken as the rate of reduction, where two reduced-MV were expected for every H<sub>2</sub> oxidized.<sup>19</sup> The lag is due to anaerobic activation that occurs upon exhaustion of trace oxygen

levels.<sup>4</sup> Reaction initiated by lysis buffer alone was used to correct for background activity/instrument drift, which is in the same order of magnitude ( $\sim 10^{-8}$   $\mu\text{mol}/\text{min}$ ) as the  $\Delta\text{hyd}B$  strain (where no activity was expected) and less than 1% of any other strains tested. The specific  $\text{H}_2$ -oxidation activity was obtained by normalizing against the total protein in the whole cell lysate. Three biological replicates were tested for each strain (unless otherwise noted) and the specific  $\text{H}_2$ -oxidation activity of each strain was normalized against the activity of the wild-type strain to obtain percent hydrogenase activity relative to wild-type.

### **7.2.6 Circular Dichroism Spectroscopy**

The purified proteins were buffer exchanged in CD Buffer (10mM Tris, 100mM NaCl, 0.5mM TCEP, pH 7.2 or 6.3) and served as the apo-protein. The protein stock solutions were incubated with 2 equivalents of nickel for 1 hour on ice and then chelexed to remove excess metal. The samples were buffer exchanged with CD buffer (pH 7.2 or pH 6.3). 15 $\mu\text{M}$  of each these protein sample was used to obtain their CD spectrum on Jasco J-1500 Circular Dichroism Spectrophotometer.

### **7.2.7 XAS data Collection, Data Reduction and Analysis**

XAS data on the frozen samples were collected at the Stanford Synchrotron Radiation Lightsource (SSRL) at the SLAC National Accelerator Laboratory using dedicated ring conditions (3 GeV and 450-500 mA) on beamline 9-3 with a Si (220) double crystal monochromator. The frozen samples were immobilized on aluminium prongs and cooled to  $\sim 10\text{K}$  using liquid helium cryostat (Oxford instruments). A 100-element Ge detector (Canberra) was used for collecting X-ray fluorescence data. To minimize scattering, a 3  $\mu\text{m}$  Z-1 filter and Soller slits were installed between the detector and sample. X-ray fluorescence data on Zn K-edge of the Zn- and Ni, Zn-

Gly-to-Ala HypA complexes were collected concurrently with spectra of Zn metal foil in transmission mode for energy calibration. X-ray fluorescence data on Ni K-edge of the Ni, Zn-Gly-to-Ala HypA complexes were collected concurrently with spectra of Ni metal foil in transmission mode for energy calibration. Extended X-ray Absorption Fine Structure (EXAFS) were collected to 15k above the K-edge for both metals.

Data reduction and analyses were performed according to previously published procedures adjusted for Ni and Zn K-edge XAS data.<sup>21</sup> The Sixpack<sup>22</sup> software package was used to process and normalize the XAS data. Fluorescence channels from each scan were visually checked for bad channels, which were deleted. For each scan, Ni K-edge energy calibration was performed by assigning the first maximum in the first derivative spectrum of the Ni-foil to 8331.6 eV. The energy calibrated XAS data for Ni is an average of 8-9 scans that was normalized and corrected for background. For normalization and background correction, the K-edge energy of Ni was set to 8340 eV with a  $R_{\text{bkg}}$  of 1. A linear function was used for fitting the pre-edge range of -200 to -50eV and quadratic polynomial functions with 7-8 spline points were used to fit the post-edge range of +150 to +880 eV relative to  $E_0$ . The edge jump was normalized by setting the difference between the corrected pre-edge and post-edge baselines to 1. The EXAFS data were converted to k-space using the relationship  $[2m_e (E-E_0)/\hbar^2]^{1/2}$ , where  $m_e$  is the mass of electron and  $\hbar$  is the Plank's constant divided by  $2\pi$ . The  $k^3$ -weighted EXAFS data were Fourier-transformed over the k-range 2-12.5  $\text{\AA}^{-1}$  using a Hanning window and fit in r-space using an  $S_0$  value of 0.9. The r-space data shown in the figures were not corrected for phase shifts.

Similarly, for each scan, Zn K-edge energy calibration was performed by assigning the first maximum in the first derivative spectrum of the Zn-foil to 9660.7 eV. The energy calibrated XAS data for Zn is an average of 6 scans that was normalized and corrected for background. For

normalization and background correction, the K-edge energy of Zn was set to 9670 eV with a  $R_{\text{bkg}}$  of 1. A Gaussian function was used for fitting the pre-edge range of -200 to -50eV and quadratic polynomial functions with 7-8 spline points were used to fit the post-edge range of +150 to +880 eV relative to  $E_0$ . The edge jump was normalized by setting the difference between the corrected pre-edge and post-edge baselines to 1. The EXAFS data were converted to k-space using the relationship  $[2m_e (E-E_0)/\hbar^2]^{1/2}$ , where  $m_e$  is the mass of electron and  $\hbar$  is the Plank's constant divided by  $2\pi$ . The  $k^3$ -weighted EXAFS data were Fourier-transformed over the k-range 2-14.5  $\text{\AA}^{-1}$  using a Hanning window and fit in r-space using an  $S_0$  value of 0.9. The r-space data shown in the figures was not corrected for phase shifts.

The Artemis software program<sup>22</sup> with FEFF6 and IFEFFIT algorithm was used to generate and fit single and multiple scattering paths for each data as described previously<sup>3</sup>. Single - scattering fits were generated over an r-space of both 1-2.5  $\text{\AA}$  and 1- 4.0  $\text{\AA}$ , while multiple - scattering fits were carried out over 1- 4  $\text{\AA}$ . For each Ni-imidazole FEFF calculation, scattering paths with amplitudes greater than 16% were selected, which were used to model the EXAFS arising from scattering atoms in the imidazole ligand. The EXAFS fitting equation used was:

$$\chi(k) = \sum_i \frac{N_i f_i(k) e^{-2k^2 \sigma_i^2}}{k r_i^2} \sin[2k r_i + \delta_i(k)]$$

where  $f(k)$  is the scattering amplitude,  $\delta(k)$  is the phase-shift,  $N$  is the number of neighboring atoms,  $r$  is the distance to the neighboring atoms, and  $\sigma^2$  is a Debye-Waller factor reflecting the mean square deviation in the distance to the nearest neighbor (thermal and static disorder). The position of the imidazole ring with respect to the metal center was fit in terms of the metal-N bond distance ( $R_{\text{eff}}$ ) and the rotation angle ( $\alpha$ ) as defined previously<sup>23</sup>.

To compare the different models fit to the data set, ifeffit utilizes three goodness of fit parameters:  $\chi^2$ , reduced  $\chi^2$  and the R-factor.  $\chi^2$  is given by equation 1, where  $N_{idp}$  is the number of independent data points,  $N_{\epsilon^2}$  is the number of uncertainties to minimize,  $Re(fi)$  is the real part of EXAFS function and  $Im(fi)$  is the imaginary part of the EXAFS fitting function.

$$\chi^2 = \frac{N_{idp}}{N_{\epsilon^2}} \sum_{i=1}^N \{ [Re(f_i)]^2 + [Im(f_i)]^2 \} \quad (1)$$

Reduced  $\chi^2$  represents the degree of freedom in the fit and is given by equation (2)

$$red. \chi^2 = \frac{\chi^2}{N_{idp} - N_{var}} \quad (2)$$

where  $N_{var}$  is the number of refining parameters and  $N_{var}$  is the number of adjustable parameters. Additionally, ifeffit calculates the R-factor for the fit, which is given by equation (3), and is scaled to the magnitude of the data making it proportional to  $\chi^2$ .

$$R = \frac{\sum_{i=1}^N \{ [Re(f_i)]^2 + [Im(f_i)]^2 \}}{\sum_{i=1}^N \{ [Re(xdata_i)]^2 + [Im(xdata_i)]^2 \}} \quad (3)$$

In comparing different models, the R-factor and reduced  $\chi^2$  parameter were used to determine the model that was the best fit for the data. The R-factor will generally improve with increasing number of adjustable parameters, while reduced  $\chi^2$  will go through a minimum and then increase, indicating that the model is overfitting the data. The resolution of the Zn- and Ni- data was 0.13 and 0.15 which was determined by equation (4), using  $\Delta k$ -value of 12.0 and 10.5 for Zn and Ni, respectively.

$$Resolution = \frac{\pi}{2 \times \Delta k} \quad (4)$$

## 7.3 Results

### 7.3.1 Gly to Ala substitutions in HypA do not affect the acid viability of *H. pylori* or urease activity.

To examine the physiological importance of the flexibility of the linker region in *H. pylori* HypA, mutant strains of *H. pylori* expressing HypA variants with Gly-to-Ala substitutions at each Gly residue in the HypA protein, as well as for pairs of conserved (G34A/G104A) and non-conserved (G32A/G89A) Gly residues were made, and the mutant strains were assessed for acid viability<sup>15</sup>, and *in vitro* urease activity<sup>15</sup>. The results of acid viability assays of the mutant strains of *H. pylori* are summarized in **Figure 7.2A**.

At pH 2.3 in the presence of urea (**Figure 7.2A**), the wild-type strain (WT) survived, due to its utilization of urea to neutralize the low pH. Under the same conditions, the survival of the  $\Delta ureB$  mutant, which does not have a functional urease, was significantly impaired. The  $\Delta hypA$  mutant, which carries a *kan-sacB* cassette in the *hypA* coding region, was acid sensitive, as observed previously<sup>1, 13</sup>. The *hypA* restorant (*hypA-R*), as well as all of the Gly-to-Ala variants studied, did not show differences in survival from the WT strain under these conditions. Similarly, the results of *in vitro* urease assays on cell lysates from mutant strains of *H. pylori* expressing the Gly-to-Ala variants showed that urease activity in the variants was generally indistinguishable from the restorant strain (**Figure 7.2B**).

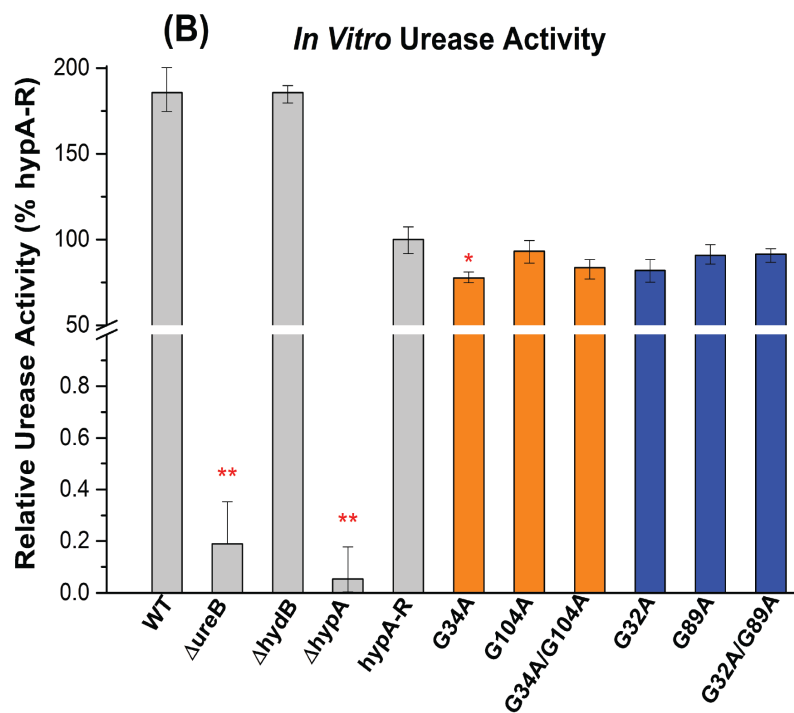
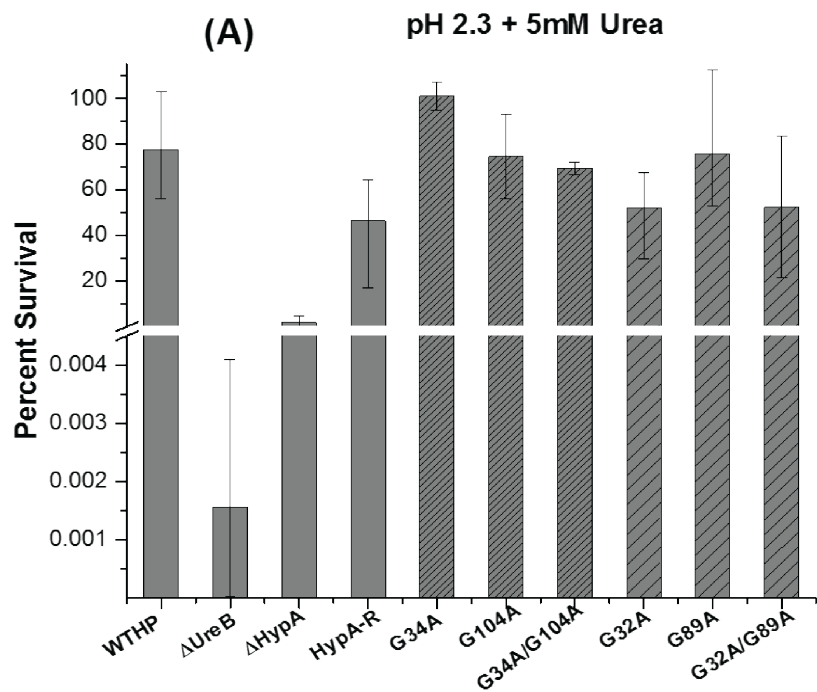


**Figure 7.2: (A) Acid viability assay and (B) *In vitro* urease activity assay of Gly-to-Ala HypA variants in *H. pylori* strains**

### 7.3.2 Gly to Ala substitutions in *H. pylori* HypA affects Ni, Fe - Hydrogenase activity

Since HypA is a common nickel chaperone for urease and Ni, Fe – hydrogenase in *H. pylori*<sup>12</sup> and Ni, Fe – hydrogenase is not required for acid adaptation in the pathogen<sup>1</sup>, the effects of Gly-to-Ala substitutions in HypA on hydrogenase activity of the pathogen were also examined. The results of *in vitro* hydrogenase activity assays on crude cell lysates from mutant strains of *H. pylori* expressing the Gly-to-Ala variants of HypA are summarized in **Figure 7.3** and **Table 7.4**.

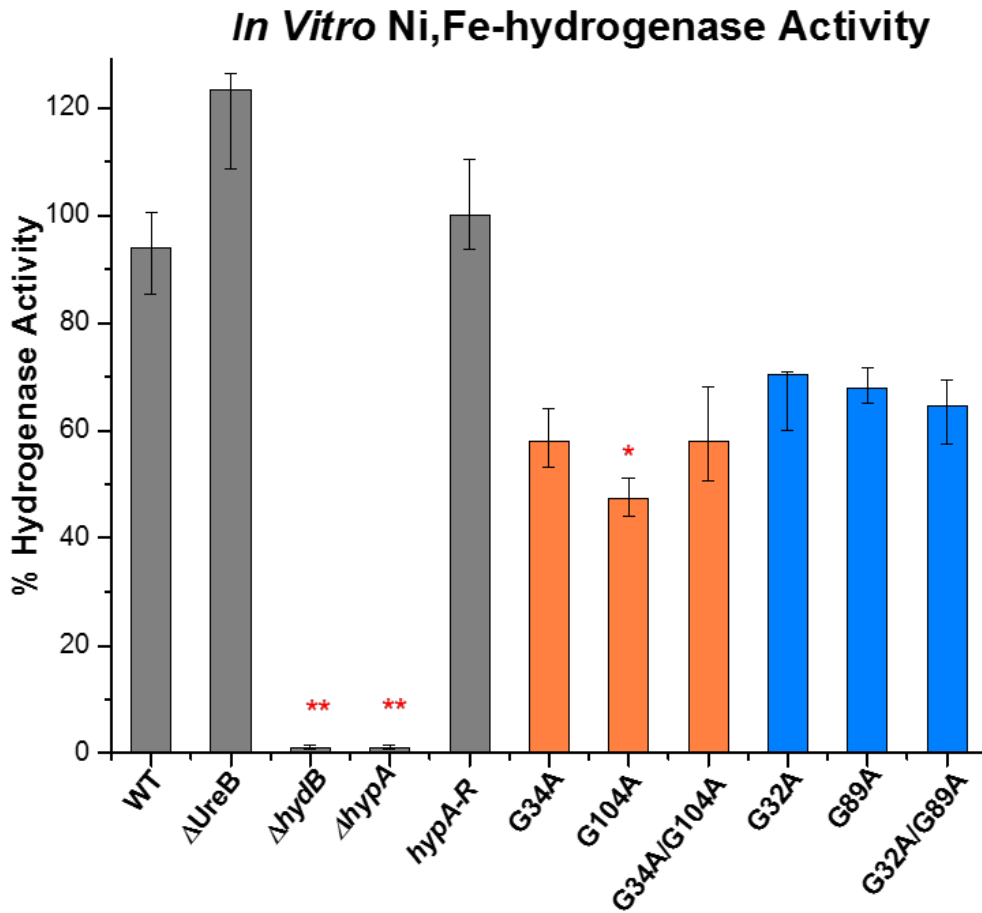


**Figure 7.3:** *In vitro* Ni, Fe- hydrogenase activity of Gly-to-Ala HypA expressing *H. pylori* strains.



**Table 7.4: *In – vitro* hydrogenase activity of *H. pylori* strains**

<b>Strain</b>	<b>Hydrogenase activity (mean <math>\pm</math> SD, %)</b>
WT	94 $\pm$ 7
$\Delta ureB$	115 $\pm$ 6
$\Delta hydB$	0.04 $\pm$ 0.04
<i>hypA:: kan-sacB</i>	7 $\pm$ 5
<i>hypA</i> – R	100 $\pm$ 10
G34A HypA	59 $\pm$ 6
G104A HypA	47 $\pm$ 4
G34A/G104A HypA	58 $\pm$ 10
G32A HypA	70 $\pm$ 9
G89A HypA	67 $\pm$ 6
G32A/G89A HypA	65 $\pm$ 8

The wild-type strain (WT) and  $\Delta ureB$  mutant strain showed the expected hydrogenase activity, due to its fully functional HypA cascade. Under the same conditions, the activity of the  $\Delta hydB$  mutant, which does not have a functional Ni, Fe - hydrogenase, was significantly impaired. The  $\Delta hypA$  mutant, which carries a *kan-sacB* cassette in the *hypA* coding region, also did not show hydrogenase activity, as reported previously<sup>1</sup>, and the hydrogenase activity is similar to  $\Delta hydB$  mutant strain. The *hypA* restorant variant restored the hydrogenase activity comparable to WT- or  $\Delta ureB$  mutant strain. Moderate defect (less than 60%) in hydrogenase activity was observed for

G34A, G104A and G34A/G104A *H. pylori* HypA strains. The hydrogenase activity of G32A, G89A and G32A/G89A *H. pylori* HypA strains was less than WT by only about 30% and is thus comparable. Interestingly, the increase in apparent hydrogenase activity in the  $\Delta hydB$  mutant is comparable to the loss of activity in the HypA mutants. Thus, it can be concluded that the Gly residues, particularly the conserved ones that show a larger variation in its hydrogenase activity might play a role in modulating Ni, Fe- hydrogenase activity in *H. pylori*.

### **7.3.3 Circular Dichroism Spectroscopy: Perturbed secondary structure of selected Gly to Ala HypA variants**

In order to examine the effects of Gly to Ala substitutions on the secondary structure of HypA, circular dichroism (CD) spectroscopy was performed on the purified apo- and Ni-bound Gly to Ala substituted HypA proteins. The CD spectrum of apo- and Ni- bound proteins for conserved and non-conserved Gly to Ala variants of HypA at pH 7.2 (**Figure 7.4**) and pH 6.3 (**Appendix C, Figure C.3**) showed characteristic peaks at 220 nm and 208 nm, which are the signatures of a typical  $\alpha$ -helix secondary structure. Notably, for the apo-HypA proteins of these variants, a significantly higher ellipticity at 208 nm as compared to WT-HypA was observed. Such subtle differences in the CD spectra can be explained by calculating the helix propensity (or helicity, denoted as  $\theta$ ) which is defined as the ratio of CD signals at 222 nm and 208 nm.<sup>24</sup> Helix propensity of protein equal to or greater than 1.0 suggests a coiled-coil  $\alpha$ - helical structure of proteins, while helix propensity less than or equal to 0.86 suggests an isolated  $\alpha$ -helix in the protein structure.<sup>25</sup>

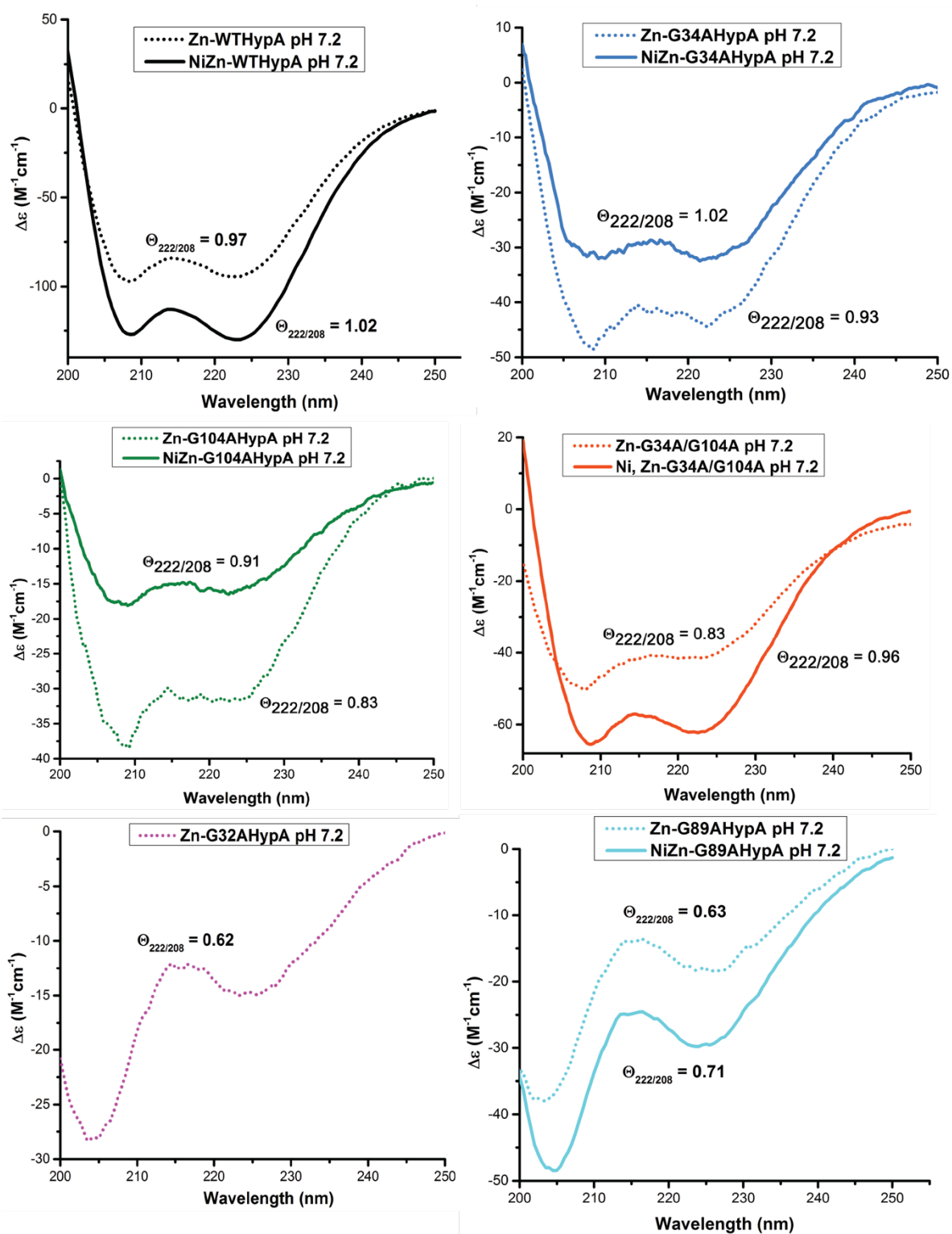


Figure 7.4: CD Spectra of apo (dotted line) and Ni-bound (solid line) conserved and non-conserved Gly -to -Ala *H. pylori* HypA variant proteins at pH 7.2.

The helix propensity for apo- and Ni- bound Gly→Ala HypA proteins were calculated at pH 7.2 and 6.3 and are shown in **Table 7.5**. At neutral pH, the helicity of apo-WT-HypA is 0.97, suggesting a coiled – coil helix and remains the same when Ni is bound to the protein. Such a coiled-coil structure of apo- or Ni-bound WT-HypA is also suggested by its NMR structures.<sup>14-15</sup> For apo-G34A-HypA, helicity was 0.93, which is less than 1.0, but more than the threshold value of 0.86, and hence might indicate a semi-coiled - coil helix structure for this protein. Interestingly, when nickel is bound to G34A-HypA at neutral pH, the helix propensity increases above 1.0 and becomes a fully coiled-coil structure like WT-HypA. On the other hand, the helix propensity for apo-G104AHypA and G34A/G104AHypA at neutral pH is 0.83 and hence might indicate an isolated - helix for these proteins. Binding of nickel to these proteins improves the helix propensity which is 0.91 and 0.96 for G104A-HypA and G34A/G104A-HypA, respectively, and possibly results in semi-coiled - coil helix structure for these variants. For non-conserved apo- Gly-to-Ala HypA variants, there is a drastic decrease in the helix propensity calculated to be 0.62, which does not improve beyond the threshold value of 0.86 upon nickel binding to G89AHypA.

At acidic pH, the feature at 208nm of selected apo-Gly-to-Ala- HypA variant proteins are different than WT-HypA (**Appendix C, Figure C.3**). For apo-G104-AHypA and apo-G34A/G104A HypA the calculated helix propensity is 0.75 and 0.92 respectively and does not change with nickel binding. For apo-G89A HypA and particularly for apo- G32A/G89A, the calculated helix propensity is 0.66 and 0.62, respectively. From these results, it can be concluded subtle changes in the secondary structural elements occur as a result of these Gly→ Ala variants of HypA, as a function of nickel binding and pH change.

**Table 7.5: Calculated helix propensity of conserved Gly→Ala HypA proteins**

Proteins	Helicity ( $\theta_{222}/\theta_{208}$ )			
	pH 7.2		pH 6.3	
	Apo-Zn -	Ni, Zn -	Apo-Zn	Ni, Zn-
WT	0.97	1.03	ND	ND
G34A HypA	0.93	1.02	ND	ND
G104A HypA	0.84	0.91	0.75	0.73
G34A/G104A HypA	0.83	0.96	0.92	0.94
G32A HypA	0.62	ND	ND	ND
G89A HypA	0.63	0.71	0.66	ND
G32A/G89AHypA	ND	ND	0.62	ND

\*ND = Not Determined

### 7.3.4 Unperturbed Zn- or Ni-site of HypA by XAS

The Zn- and Ni-site of apo- or Ni-bound Gly to Ala variants of HypA at pH 7.2 and pH 6.3 were examined using X-ray Absorption spectroscopy. Selected and best fits of Zn-site and Ni-site at pH 7.2 and pH 6.3 are summarized in **Table 7.6 & 7.7** and best fits of each variant at the Zn- and Ni- site are shown in **Appendix C, Figure C.4-C.6 and Figure C.8-C.10**, respectively. No changes in either the Zn-site or the Ni-site structures for these variants were observed, and the metal site structures were similar to those found in WT-HypA at pH 7.2 and pH 6.3, respectively.

**Table 7.6: Best EXAFS fits of Zn- site in non- conserved Gly→Ala HypA variants**

Shell	R (Å)	$\sigma^2$ ( $\times 10^{-3} \text{ \AA}^{-2}$ )	$\Delta E_0$	R-factor(%)	Red. $\chi^2$
<i>Ni, Zn - G32A-HypA, pH 7.2</i>					
4 S	2.33 (0)	2(0)	(-)0(0)	1.6	22.9
3 S	2.33 (0)	1(0)	0(1)	3.9	60.9
1 Im0°	2.98 (1)	<b>52(313)</b>			
2 S	2.34 (0)	<b>0(0)</b>	1(2)	6.5	101.36
2 Im0°	2.14 (3)	4(2)			
<i>Ni, Zn - G32A-HypA, pH 6.3</i>					
4 S	2.33 (0)	3(0)	(-)1(1)	4.5	4.6
3 S	2.34(0)	1(0)	(-)0(1)	3.5	4.0
1 Im0°	2.14 (2)	1(2)			
2 S	2.34(0)	<b>0(0)</b>	1(1)	5.2	6.0
2 Im0°	2.14 (2)	2(1)			
<i>Ni, Zn - G89A-HypA, pH 7.2</i>					
4S	2.32 (1)	3(0)	(-) 2 (2)	4.2	140.2
4S	2.31 (0)	3(0)	(-) 5 (2)	4.9	143.2
1N/O	1.92 (2)	1(2)			
4S	2.34 (0)	4 (0)	(-) 0 (1)	4.7	139.2
1 Im0°	2.16 (1)	<b>neg</b>			
<i>Ni, Zn - G89A-HypA, pH 6.3</i>					
4S	2.33 (0)	3(0)	(-)1(1)	3.6	22.9
<i>Ni, Zn - G32A/G89A-HypA, pH 7.2</i>					
4S	2.33 (0)	3(0)	(-)0(0)	1.7	49.8
3 S	2.34(0)	2(0)	(-)0(1)	2.1	68.0
1 Im0°	2.12 (2)	2(1)			
<i>Ni, Zn - G32A/G89A-HypA, pH 6.3</i>					
4 S	2.33(0)	3(0)	5(0)	1.3	22.7

**Table 7.7: Selected EXAFS fits of Ni- site in non – conserved Gly→Ala HypA variants**

Shell	R (Å)	$\sigma^2$ ( $\times 10^{-3} \text{ \AA}^{-2}$ )	$\Delta E_0$	R-factor(%)	Red. $\chi^2$
<i>Ni, Zn - G32A-HypA, pH 7.2</i>					
<b>4 N/O</b>	2.07(1)	4(1)	3(2)	17.0	93.0
<b>5 N/O</b>	2.08(1)	6(2)	2(3)	18.6	101.8
<b>6 N/O</b>	2.08(1)	8(3)	2(3)	21.0	114.8
<b>3 N/O</b>	2.09(1)	2(1)	7(2)	9.7	70.4
<b>1 N/O</b>	2.30(3)	<b>0(2)</b>			
<b>2 N/O</b>	2.08(1)	<b>neg</b>	7(2)	10.9	79.1
<b>2 N/O</b>	2.25(5)	3(7)			
<b>4 N/O</b>	2.10(1)	4(1)	6(1)	7.4	53.6
<b>1 N/O</b>	2.32(3)	<b>neg</b>			
<b>4 N/O</b>	2.09(1)	3(0)	7(1)	7.9	57.3

<b>2 N/O</b>	2.32(2)	3(2)				
2N/O	<b>2.09 (2)</b>	<b>1(1)</b>	<b>2(2)</b>	<b>4.8</b>	<b>20.5</b>	
1N/O	<b>2.28 (2)</b>	<b>3(1)</b>				
1Im0°	<b>2.07 (1)</b>	<b>3(2)</b>				
1BBAm	<b>1.91 (3)</b>	<b>4(2)</b>				
	<b>1.96 (3)</b>					
<i>Ni, Zn - G32A-HypA, pH 6.3</i>						
<b>4 N/O</b>	2.06(1)	1(0)	1(2)	16.9	56.6	
<b>5 N/O</b>	2.07(1)	3(1)	1(2)	20.8	65.8	
<b>6 N/O</b>	2.07(1)	4(1)	1(2)	26.0	81.7	
<b>3 N/O</b>	2.07(1)	neg	5(4)	11.1	81.3	
<b>1 N/O</b>	2.25(3)	0(7)				
<b>2 N/O</b>	2.06(1)	neg	5(3)	10.9	79.7	
<b>2 N/O</b>	2.25(3)	7(8)				
<b>4 N/O</b>	2.08(1)	1(0)	4(3)	10.9	79.8	
<b>1 N/O</b>	2.28(3)	neg				
<b>4 N/O</b>	2.08(1)	1(0)	5(2)	10.7	77.8	
<b>2 N/O</b>	2.29(2)	3(0)				
2N/O	<b>2.06 (0)</b>	<b>3(2)</b>	<b>2(2)</b>	<b>3.5</b>	<b>43.6</b>	
1N/O	<b>2.26 (2)</b>	<b>2(4)</b>				
1Im0°	<b>2.08 (1)</b>	<b>3(2)</b>				
1BBAm	<b>2.01 (2)</b>	<b>1(3)</b>				
	<b>2.06 (2)</b>					
<i>Ni, Zn - G89A-HypA, pH 7.2</i>						
<b>4 N/O</b>	2.09 (1)	3 (1)	4(2)	13.9	21.9	
<b>5 N/O</b>	2.09 (1)	4 (1)	4(2)	15.9	25.0	
<b>6 N/O</b>	2.09 (1)	5 (1)	4(2)	19.5	30.5	
<b>3 N/O</b>	2.08 (1)	2 (0)	(-)0(2)	9.4	19.4	
<b>1 N/O</b>	1.89 (3)	3 (3)				
<b>2 N/O</b>	2.08 (1)	0 (1)	(-)0(2)	9.8	20.3	
<b>2 N/O</b>	1.89 (3)	10 (7)				
<b>4 N/O</b>	2.07 (1)	4 (1)	(-)0(2)	10.7	22.3	
<b>1 N/O</b>	1.86 (2)	2 (2)				
<b>4 N/O</b>	2.08 (1)	4 (1)	(-)1(2)	12.9	25.9	
<b>2 N/O</b>	1.87 (3)	8 (4)				
2N/O	<b>2.09 (1)</b>	<b>1(1)</b>	<b>(-)2(2)</b>	<b>4.9</b>	<b>5.6</b>	
1N/O	<b>2.21 (2)</b>	<b>1(2)</b>				
1Im10°	<b>2.10 (2)</b>	<b>2(2)</b>				
1BBAm	<b>1.95 (1)</b>	<b>1(1)</b>				
	<b>2.00 (1)</b>					
<i>Ni, Zn - G89A-HypA, pH 6.3</i>						
<b>4 N/O</b>	2.07 (1)	3 (0)	1 (2)	12.4	138.3	
<b>3 N/O</b>	2.08 (1)	1 (0)	7 (1)	6.9	102.1	
<b>1 N/O</b>	2.25 (3)	0 (2)				
<b>2 N/O</b>	2.06 (1)	neg	5 (2)	7.2	105.9	
<b>2 N/O</b>	2.20 (4)	6 (5)				

<b>5 N/O</b>	2.07 (1)	5 (1)	1 (2)	14.7	138.3
<b>4 N/O</b>	2.08 (1)	2 (0)	5 (1)	6.5	96.4
<b>1 N/O</b>	2.28 (2)	neg			
<b>3 N/O</b>	2.07 (1)	2 (0)	5 (1)	6.4	95.0
<b>2 N/O</b>	2.25 (3)	5 (3)			
<b>6 N/O</b>	2.09 (1)	5 (1)	4(2)	18.4	204.5
<b>5 N/O</b>	2.07 (1)	4 (1)	5 (1)	8.2	120.9
<b>1 N/O</b>	2.25 (4)	neg			
<b>4 N/O</b>	2.08 (1)	2 (0)	5 (1)	7.9	115.6
<b>2 N/O</b>	2.25 (4)	4 (3)			
<b>3N/O</b>	2.08 (1)	1(1)	2(1)	3.0	86.2
<b>1N/O</b>	2.24 (2)	2(1)			
<b>1BBAm</b>	1.96 (5)	3(2)			
	2.02 (5)				
<i>Ni, Zn – G32A/G89A-HypA, pH 7.2</i>					
<b>4 N/O</b>	2.06 (1)	7 (1)	2 (2)	10.5	91.7
<b>3 N/O</b>	2.04 (1)	3 (0)	2 (1)	4.8	55.7
<b>1 N/O</b>	2.19 (1)	neg			
<b>2 N/O</b>	2.01 (1)	1 (1)	2 (1)	4.5	51.7
<b>2 N/O</b>	2.15 (1)	2(1)			
<b>5 N/O</b>	2.07 (1)	9 (1)	2 (1)	8.0	70.0
<b>4 N/O</b>	2.05 (1)	5 (1)	2 (1)	4.7	54.5
<b>1 N/O</b>	2.21 (2)	1 (1)			
<b>3 N/O</b>	2.03 (1)	4 (1)	2 (1)	4.6	52.8
<b>2 N/O</b>	2.18 (1)	4 (2)			
<b>6 N/O</b>					
<b>5 N/O</b>	2.06 (1)	8 (1)	2 (1)	6.0	70.3
<b>1 N/O</b>	2.23 (4)	3 (3)			
<b>4 N/O</b>	2.05 (1)	7 (1)	3 (2)	5.8	67.4
<b>2 N/O</b>	2.21 (5)	9 (6)			
<b>3 N/O</b>	2.04 (2)	6 (1)	3 (2)	5.6	64.7
<b>3 N/O</b>	2.19 (4)	13 (6)			
<b>3N/O</b>	2.03 (1)	3(1)	3(1)	3.6	20.8
<b>2N/O</b>	2.20 (1)	1(0)			
<b>1Im10°</b>	2.06 (2)	4(2)			
<i>Ni, Zn – G32A/G89A-HypA, pH 6.3</i>					
<b>4 N/O</b>	2.08 (1)	5(0)	2 (1)	5.9	106.3
<b>3 N/O</b>	2.08 (1)	3 (1)	4 (1)	4.2	101.3
<b>1 N/O</b>	2.24 (5)	5 (5)			
<b>2 N/O</b>	2.07 (1)	2 (1)	4 (1)	4.4	105.3
<b>2 N/O</b>	2.18 (5)	9 (6)			
<b>5 N/O</b>	2.08 (1)	7(0)	2 (1)	5.3	95.9
<b>4 N/O</b>	2.09 (0)	5 (0)	5 (0)	1.9	45.5
<b>1 N/O</b>	2.30 (2)	3 (2)			
<b>3 N/O</b>	2.08 (0)	3 (0)	5 (1)	2.2	53.4
<b>2 N/O</b>	2.25 (3)	11 (4)			



<b>6 N/O</b>	2.09 (1)	<b>9 (1)</b>	2 (1)	6.6	119.0
<b>5 N/O</b>	2.10 (0)	7 (0)	5 (0)	1.3	31.5
<b>1 N/O</b>	2.31 (1)	2 (1)			
<b>4 N/O</b>	2.09 (0)	5 (0)	5 (0)	1.6	38.5
<b>2 N/O</b>	2.30 (2)	9 (2)			
<b>3 N/O</b>	2.08 (0)	4 (0)	5 (1)	1.9	44.5
<b>3 N/O</b>	2.25 (3)	<b>17 (4)</b>			
2N/O	2.12 (1)	2(1)	4(0)	2.5	29.3
1N/O	2.29 (2)	1(1)			
1Im0°	2.10 (2)	5(2)			
1BBAm	2.00 (2)	3(2)			
	2.05 (2)				

\* the red colors denote the unacceptable values

## 7.4 Discussion

Glycine residues, particularly in the loops and linkers of protein structure serve as flexibility hot-spots in some proteins, which include glycines in enzyme active sites, transmembrane helices, and are crucial to the respective function.<sup>26-29</sup> The dynamic nickel-metallochaperone, HypA in *H. pylori*, which stands at the crossroads of nickel delivery to two structurally and functionally distinct enzymes – urease and Ni,Fe-hydrogenase, has four glycine residues (Gly32, Gly34, Gly89 and Gly104) distributed around its Ni- and Zn- binding domains (Figure 7.1). Mutation of glycine residues in *H. pylori* HypA to alanine did not hamper urease maturation as indicated by the intact urease activity of *H. pylori* strains expressing Gly-to-Ala variants, and as the urease activity largely determines the acid viability of *H. pylori*, these variant strains exhibited acid viabilities similar to the WT strain. However, unlike acid viability or *in vitro* urease activity, the hydrogenase activity of the crude cell lysates of *H. pylori* strains expressing Gly -to- Ala HypA variants showed an overall decrease as compared to *hypA* restorant or WT *H. pylori* strain (Figure 7.3, Table 4). Hydrogenase activity in *H. pylori* do not contribute to its virulence but is shown to be important for pathogenic colonization in host.<sup>1, 5-6</sup>

In *Helicobacter* species, Ni, Fe-hydrogenase is the only known hydrogenase.<sup>4</sup> Variant strains of *H. pylori* with no Ni, Fe – hydrogenase ( $\Delta$ hydB) were unable to colonize in gerbil models.<sup>6</sup> Successful colonization of *H. pylori* requires the injection of a cytotoxin CagA from the pathogen into the host cells through T4SS pathway. Recent studies show that the activity of hydrogenase in *H. pylori* fuels the translocation of CagA cytotoxin, thus explaining the colonization inability of null -hydrogenase expressing *H. pylori* variant strains.<sup>7</sup> Ni, Fe-hydrogenase is a heteronuclear, membrane-bound enzyme which utilizes Ni, and Fe at its active site to catalyze the reversible oxidation of molecular hydrogen.<sup>10</sup> There are two subunits in the mature enzyme: a large subunit which accommodates the heteronuclear active site, and a small subunit which harbors the Fe-S clusters.<sup>10</sup> Maturation of this enzyme requires a series of post-translational modifications of the precursor of large subunit, (such as HycE in *E. coli*) which includes sequential insertion of the metals (Fe and then Ni), proteolytic processing of its C-terminal extension by specific protease followed by conformational changes that allows association of small subunit containing Fe-S clusters.<sup>10, 30-33</sup> Membrane insertion of the mature enzyme is dependent on the twin-arginine signal sequence found on small subunit and association between the two subunits and occurs via twin-arginine transporter (TAT) pathway.<sup>34-36</sup> Sequential insertion of the metals into the pre-active site of the precursor is a crucial step and involves the orchestration of several accessory proteins.<sup>31, 37</sup> While HypCDEF ensures delivery of Fe, HypA and HypB are responsible for proper insertion of Ni.<sup>10, 31, 38</sup> HypA interacts and delivers nickel to the GTPase, HypB, which then delivers nickel to the pre-active site of the immature large subunit of Ni,Fe-hydrogenase.<sup>10, 39-40</sup> Direct interaction of HypA with the immature large subunit of Ni, Fe-hydrogenase from *Thermococcus kodakarensis*, HyhL has also been shown recently, although the relevance of this interaction is yet unknown.<sup>41</sup>

A decrease in hydrogenase activity of the Gly-to-Ala HypA expressing *H. pylori* strains is likely associated with perturbations in the Ni, Fe -hydrogenase of these variant *H. pylori* strains, which might arise either due to impaired/incomplete maturation or low expression levels of enzyme. As HypA can interact with HypB or HyhL, impaired maturation of the Ni,Fe-hydrogenase can be attributed to the defects in the HypA conferred by Gly-to Ala mutations. Intriguingly, among these variants, particularly G104AHypA *H. pylori* variant strain, showed a remarkable 60% reduction in its hydrogenase activity which is possibly due to the perturbed secondary structure of this variant, as observed from the CD spectra of apo- or Ni – bound states of purified G104A HypA protein at pH 7.2 and 6.3 (Figure 7.4). It is possible that subtle changes in the secondary structure of these variant proteins hamper its interaction with HypB or large subunit of apo-Ni, Fe-hydrogenase.

It is also important to note that proteins can simultaneously occur in various conformational states in solution or cellular milieu.<sup>42</sup> Recent NMR studies on purified apo- or Ni- bound *H. pylori* WT- HypA indicated the existence of such conformational variations in this protein also.<sup>15</sup> Owing to this feature, it is possible that the mutation of Gly to Ala in *H. pylori* HypA have not affected its ensemble of conformational spaces that are involved in its interaction with UreE, and hence results in unaffected urease activity or acid viability of the pathogen. On the contrary, as the hydrogenase activity of these variants is lowered, these mutations might have caused subtle variations in the ensemble of conformational spaces of HypA that are involved in the interaction with HypB or HyhL. Computational methods can be used to calculate the populations of distinct ensembles that might occur as a result of these mutation in HypA. A structural comparison of protein-protein interaction in HypA•UreE complex and HypA•HypB complex might also reveal useful insights into the differential interaction pattern, if any, of HypA with these two proteins

downstream required for the maturation of urease and Ni, Fe hydrogenase respectively. Alternatively, it is also possible that owing to these mutations, the expression levels of Ni, Fe – hydrogenase in these variant strains itself are less than the controls used in the study and resulted in decreased hydrogenase activity. Whether these Gly-to-Ala- mutations in *H. pylori* HypA have caused changes to the expression of its Ni, Fe - hydrogenase is not known and can be tested further by measuring and comparing the respective transcripts. Furthermore, as hydrogenase activity is required for colonization, it will be interesting to test the colonization profile of the Gly-to-Ala HypA expressing *H. pylori* strains in mouse models.

## 7.5 References

1. Blum, F. C.; Hu, H. Q.; Servetas, S. L.; Benoit, S. L.; Maier, R. J.; Maroney, M. J.; Merrell, D. S., Structure-function analyses of metal-binding sites of HypA reveal residues important for hydrogenase maturation in *Helicobacter pylori*. *PLoS One* **2017**, *12* (8), e0183260.
2. Ge, R. G.; Wang, D. X.; Hao, M. C.; Sun, X. S., Nickel trafficking system responsible for urease maturation in *Helicobacter pylori*. *World J. Gastroenterol.* **2013**, *19* (45), 8211-8218.
3. Hu, H. Q.; Johnson, R. C.; Merrell, D. S.; Maroney, M. J., Nickel Ligation of the N-Terminal Amine of HypA Is Required for Urease Maturation in *Helicobacter pylori*. *Biochemistry* **2017**, *56* (8), 1105-1116.
4. Maier, R. J.; Fu, C.; Gilbert, J.; Moshiri, F.; Olson, J.; Plaut, A. G., Hydrogen uptake hydrogenase in *Helicobacter pylori*. *FEMS Microbiol. Lett.* **1996**, *141* (1), 71-76.
5. Olson, J. W.; Maier, R. J., Molecular hydrogen as an energy source for *Helicobacter pylori*. *Science* **2002**, *298* (5599), 1788-1790.
6. Benoit, S. L.; Maier, R. J., Hydrogen and nickel metabolism in helicobacter species. *Ann. NY Acad. Sci.* **2008**, *1125*, 242-251.
7. Wang, G.; Romero-Gallo, J.; Benoit, S. L.; Piazuelo, M. B.; Dominguez, R. L.; Morgan, D. R.; Peek, R. M., Jr.; Maier, R. J., Hydrogen Metabolism in *Helicobacter pylori* Plays a Role in Gastric Carcinogenesis through Facilitating CagA Translocation. *MBio* **2016**, *7* (4).
8. Boer, J. L.; Mulrooney, S. B.; Hausinger, R. P., Nickel-dependent metalloenzymes. *Arch. Biochem. & Biophys.* **2014**, *544*, 142-152.
9. Farrugia, M. A.; Macomber, L.; Hausinger, R. P., Biosynthesis of the urease metallocenter. *J. Biol. Chem.* **2013**, *288* (19), 13178-13185.

10. Lacasse, M. J.; Zamble, D. B., [NiFe]-Hydrogenase Maturation. *Biochemistry* **2016**, *55* (12), 1689-1701.
11. Mehta, N.; Olson, J. W.; Maier, R. J., Characterization of Helicobacter pylori nickel metabolism accessory proteins needed for maturation of both urease and hydrogenase. *J. Bacteriol.* **2003**, *185* (3), 726-734.
12. Olson, J. W.; Mehta, N. S.; Maier, R. J., Requirement of nickel metabolism proteins HypA and HypB for full activity of both hydrogenase and urease in Helicobacter pylori. *Mol. Microbiol.* **2001**, *39* (1), 176-182.
13. Johnson, R. C.; Hu, H. Q.; Merrell, D. S.; Maroney, M. J., Dynamic HypA zinc site is essential for acid viability and proper urease maturation in Helicobacter pylori. *Metallomics : integrated biometal science* **2015**, *7* (4), 674-682.
14. Xia, W.; Li, H.; Sze, K. H.; Sun, H., Structure of a nickel chaperone, HypA, from Helicobacter pylori reveals two distinct metal binding sites. *J. Am. Chem. Soc.* **2009**, *131* (29), 10031-10040.
15. Spronk, C.; Zerko, S.; Gorka, M.; Kozminski, W.; Bardiaux, B.; Zambelli, B.; Musiani, F.; Piccioli, M.; Basak, P.; Blum, F. C.; Johnson, R. C.; Hu, H.; Merrell, D. S.; Maroney, M.; Ciurli, S., Structure and dynamics of Helicobacter pylori nickel-chaperone HypA: an integrated approach using NMR spectroscopy, functional assays and computational tools. *J. Biol. Inorg. Chem.* **2018**, *23* (8), 1309-1330.
16. Herbst, R. W.; Perovic, I.; Martin-Diaconescu, V.; O'Brien, K.; Chivers, P. T.; Pochapsky, S. S.; Pochapsky, T. C.; Maroney, M. J., Communication between the zinc and nickel sites in dimeric HypA: metal recognition and pH sensing. *J. Am. Chem. Soc.* **2010**, *132* (30), 10338-10351.

17. Janin, J.; Sternberg, M. J., Protein flexibility, not disorder, is intrinsic to molecular recognition. *FI000 Biol. Rep.* **2013**, *5*, 2.
18. Craveur, P.; Joseph, A. P.; Esque, J.; Narwani, T. J.; Noel, F.; Shinada, N.; Goguet, M.; Sylvain, L.; Poulain, P.; Bertrand, O.; Faure, G.; Rebehmed, J.; Ghozlane, A.; Swapna, L.; Bhaskara, R.; Barnoud, J.; Téletchéa, S.; Jallu, V.; Cerny, J.; Schneider, B.; Etchebest, C.; Srinivasan, N.; Gelly, J.-C.; de Brevern, A., Protein flexibility in the light of structural alphabets. *Front. Mol. Biosci.* **2015**, *2* (20).
19. Boyer, M. E.; Stapleton, J. A.; Kuchenreuther, J. M.; Wang, C.-w.; Swartz, J. R., Cell-free synthesis and maturation of [FeFe] hydrogenases. *Biotech. and Bioengin.* **2008**, *99* (1), 59-67.
20. Park, D. H.; Laivenieks, M.; Guettler, M. V.; Jain, M. K.; Zeikus, J. G., Microbial utilization of electrically reduced neutral red as the sole electron donor for growth and metabolite production. *Appl. Environ. Microbiol.* **1999**, *65* (7), 2912-2917.
21. Higgins, K. A.; Hu, H. Q.; Chivers, P. T.; Maroney, M. J., Effects of select histidine to cysteine mutations on transcriptional regulation by Escherichia coli RcnR. *Biochemistry* **2013**, *52* (1), 84-97.
22. Webb, S. M., SIXPack a Graphical User Interface for XAS Analysis Using IFEFFIT. *Physica Scripta* **2005**, 1011-1014.
23. Banaszak, K.; Martin-Diaconescu, V.; Bellucci, M.; Zambelli, B.; Rypniewski, W.; Maroney, M. J.; Ciurli, S., Crystallographic and X-ray absorption spectroscopic characterization of Helicobacter pylori UreE bound to Ni(2)(+) and Zn(2)(+) reveals a role for the disordered C-terminal arm in metal trafficking. *Biochem. J.* **2012**, *441* (3), 1017-1026.
24. Vaidya, S.; Hardy, J. A., Caspase-6 latent state stability relies on helical propensity. *Biochemistry* **2011**, *50* (16), 3282-3287.

25. Zhou, N. E.; Kay, C. M.; Hodges, R. S., Synthetic model proteins. Positional effects of interchain hydrophobic interactions on stability of two-stranded alpha-helical coiled-coils. *J. Biol. Chem.* **1992**, *267* (4), 2664-2670.
26. Yan, B. X.; Sun, Y. Q., Glycine residues provide flexibility for enzyme active sites. *The J. Biol. Chem.* **1997**, *272* (6), 3190-3194.
27. Jacob, J.; Duclouhier, H.; Cafiso, D. S., The role of proline and glycine in determining the backbone flexibility of a channel-forming peptide. *Biophys. J.* **1999**, *76* (3), 1367-1376.
28. Hesperen, C. W.; Bruegger, J. J.; Guo, Y.; Marletta, M. A., Native Alanine Substitution in the Glycine Hinge Modulates Conformational Flexibility of Heme Nitric Oxide/Oxygen (H-NOX) Sensing Proteins. *ACS Chem. Biol.* **2018**, *13* (6), 1631-1639.
29. Hogel, P.; Gotz, A.; Kuhne, F.; Ebert, M.; Stelzer, W.; Rand, K. D.; Scharnagl, C.; Langosch, D., Glycine Perturbs Local and Global Conformational Flexibility of a Transmembrane Helix. *Biochemistry* **2018**, *57* (8), 1326-1337.
30. Senger, M.; Stripp, S. T.; Soboh, B., Proteolytic cleavage orchestrates cofactor insertion and protein assembly in [NiFe]-hydrogenase biosynthesis. *J. Biol. Chem.* **2017**, *292* (28), 11670-11681.
31. Magalon, A.; Blokesch, M.; Zehelein, E.; Bock, A., Fidelity of metal insertion into hydrogenases. *FEBS Lett.* **2001**, *499* (1-2), 73-76.
32. Rossmann, R.; Sauter, M.; Lottspeich, F.; Böck, A., Maturation of the large subunit (HYCE) of Escherichia coli hydrogenase 3 requires nickel incorporation followed by C-terminal processing at Arg537. *Eur. J. Biochem.* **1994**, *220* (2), 377-384.



33. Menon, N. K.; Robbins, J.; Der Vartanian, M.; Patil, D.; Peck, H. D., Jr.; Menon, A. L.; Robson, R. L.; Przybyla, A. E., Carboxy-terminal processing of the large subunit of [NiFe] hydrogenases. *FEBS Lett.* **1993**, *331* (1-2), 91-95.
34. Rodrigue, A.; Chanal, A.; Beck, K.; Müller, M.; Wu, L. F., Co-translocation of a periplasmic enzyme complex by a hitchhiker mechanism through the bacterial tat pathway. *The J. Biol. Chem.* **1999**, *274* (19), 13223-13228.
35. Gross, R.; Simon, J.; Kroger, A., The role of the twin-arginine motif in the signal peptide encoded by the hydA gene of the hydrogenase from wolinella succinogenes. *Arch. Microbiol.* **1999**, *172* (4), 227-232.
36. Dubini, A.; Sargent, F., Assembly of Tat-dependent [NiFe] hydrogenases: identification of precursor-binding accessory proteins. *FEBS Lett.* **2003**, *549* (1-3), 141-146.
37. Theodoratou, E.; Paschos, A.; Magalon, A.; Fritsche, E.; Huber, R.; Bock, A., Nickel serves as a substrate recognition motif for the endopeptidase involved in hydrogenase maturation. *Eur. J. Biochem.* **2000**, *267* (7), 1995-1999.
38. Benoit, S.; Mehta, N.; Wang, G.; Gatlin, M.; Maier, R. J., Requirement of hydD, hydE, hypC and hypE genes for hydrogenase activity in Helicobacter pylori. *Microb. Pathog.* **2004**, *36* (3), 153-157.
39. Xia, W.; Li, H.; Yang, X.; Wong, K. B.; Sun, H., Metallo-GTPase HypB from Helicobacter pylori and its interaction with nickel chaperone protein HypA. *J. Biol. Chem.* **2012**, *287* (9), 6753-6763.
40. Chan, K. H.; Lee, K. M.; Wong, K. B., Interaction between hydrogenase maturation factors HypA and HypB is required for [NiFe]-hydrogenase maturation. *PLoS One* **2012**, *7* (2), e32592.

41. Kwon, S.; Watanabe, S.; Nishitani, Y.; Kawashima, T.; Kanai, T.; Atomi, H.; Miki, K., Crystal structures of a [NiFe] hydrogenase large subunit HyhL in an immature state in complex with a Ni chaperone HypA. *Proc. Natl. Acad. Sci. U. S. A.* **2018**, *115* (27), 7045-7050.
42. Juritz, E.; Palopoli, N.; Fornasari, M. S.; Fernandez-Alberti, S.; Parisi, G., Protein conformational diversity modulates sequence divergence. *Mol. Biol. Evol.* **2013**, *30* (1), 79-87.

APPENDIX A

SUPPORTING INFORMATION FOR THE ROLE OF CYTOPLASMIC LIGANDS IN THE *IN VITRO* MATURATION OF NISOD

Table A.1. Ni K-Edge EXAFS Fits for holo-WT-NiSodN.

Shell	R (Å)	$\sigma^2$ (x10 <sup>-3</sup> Å <sup>-2</sup> )	$\Delta E_0$	R-factor(%)	Red. $\chi^2$
4N/O	2.08(1)	4(0)	3(1)	11.7	100.2
5N/O	2.08(1)	5(0)	2(1)	9.6	82.6
6N/O	2.08(1)	7(0)	2(1)	9.5	83.0
4N/O	2.07(1)	3(1)	4(1)	8.5	82.8
1N/O	2.27(4)	2(4)			
3N/O	2.06(1)	2(1)	3(1)	8.4	81.8
2N/O	2.18(4)	5(5)			
2N/O	2.04(1)	2(1)	4(1)	5.4	61.0
2N/O	2.17(4)	5(5)			
1Im0°	2.11(2)	2(2)			
2N/O	2.06(1)	0(2)	3(1)	5.6	63.4
1N/O	2.18(4)	1(5)			
2Im0°	2.11(3)	7(3)			
2N/O	2.06(1)	0(3)	3(1)	8.2	92.7
1N/O	2.19(3)	1(8)			
1BBAm	2.06 (1)	8(9)			
	2.11(1)				
5N/O	2.08(1)	5(0)	4(1)	8.3	
1N/O	2.28(5)	4(5)			91.6
4N/O	2.07(1)	4(1)	4(2)	8.1	87.8
2N/O	2.22(8)	11(10)			
5N/O	2.08(1)	5(0)	2(1)	8.0	90.0
1S	2.21(1)	19(13)			

<b>4N/O</b>	2.28	4(2)	2(2)	8.4	101.2
<b>2S</b>	2.46(8)	25(10)			
<b>5N/O</b>	2.08(1)	8(1)	2(1)	6.6	64.6
<b>1Im0°</b>	2.08(2)	2(3)			
<b>4 N/O</b>	2.07(1)	4(1)	4(1)	5.1	57.4
<b>1N/O</b>	2.27(3)	3(4)			
<b>1Im0°</b>	2.12(2)	2(3)			
<b>3N/O</b>	2.06(1)	3(1)	4(1)	4.9	55.4
<b>2N/O</b>	2.23(3)	9(5)			
<b>1Im0°</b>	2.12(2)	2(2)			
<b>2N/O</b>	2.04(1)	1(1)	4(1)	4.3	57.9
<b>2N/O</b>	2.17(3)	4(4)			
<b>1Im0°</b>	2.12(2)	1(2)			
<b>1S</b>	2.58(7)	17(10)			
<b>2N/O</b>	2.04(1)	0(1)	4(1)	4.7	62.9
<b>2N/O</b>	2.18(3)	3(4)			
<b>1Im0°</b>	2.12(2)	1(2)			
<b>1Br</b>	2.32(7)	19(10)			
<b>3N/O</b>	2.06(1)	2(1)	4(1)	4.9	65.4
<b>1N/O</b>	2.21(4)	0(3)			
<b>1Im0°</b>	2.12(3)	2(3)			
<b>1Br</b>	2.31(7)	19(11)			
<b>3N/O</b>	2.07(1)	3(1)	3(1)	4.9	55.2
<b>1N/O</b>	2.25(4)	6(6)			
<b>2Im0°</b>	2.11(3)	7(3)			
<b>2N/O</b>	2.06(1)	2(3)	4(1)	4.9	54.7
<b>2N/O</b>	2.18(4)	11(7)			
<b>2Im0°</b>	2.11(3)	7(3)			
<b>2N/O</b>	2.04(1)	0(2)	4(1)	4.3	57.3
<b>1N/O</b>	2.17(3)	0(4)			
<b>2Im0°</b>	2.11(3)	7(3)			
<b>1S</b>	2.54(7)	17(9)			
<b>3N/O</b>	2.11(3)	3(5)	3(2)	7.8	87.7
<b>1N/O</b>	2.26(3)	2(5)			
<b>1 BBAm</b>	1.99(2)	1(2)			

	2.04(2)				
<b>2N/O</b>	2.11(3)	3(5)	3(1)	3.83	
<b>1BBAm</b>	1.99(2)	1(2)			51.2
	2.04(2)				
<b>1N/O</b>	2.26(3)	2(5)			
<b>1Im0°</b>	2.12(2)	Neg			
<b>2N/O</b>	<b>2.08(2)</b>	<b>1(2)</b>	<b>3(1)</b>	<b>4.08</b>	<b>54.5</b>
<b>1BBAm</b>	<b>1.99(3)</b>	<b>4(3)</b>			
	<b>2.04(3)</b>				
<b>1N/O</b>	<b>2.25(4)</b>	<b>1(3)</b>			
<b>1Im5°</b>	<b>2.13(2)</b>	<b>1(2)</b>			

**Table A.2:** Thermodynamic parameters of nickel binding to WT-SodN, H15A-SodN and WT-NiSOD

<b>Protein</b>	<b><math>\Delta G</math> (kcal/mol)</b>	<b><math>\Delta H</math> (kcal/mol)</b>	<b><math>-T\Delta S</math> (kcal/mol)</b>
<b>WT-NiSOD</b>	-8.3	-13.0	+4.7
<b>WT-SodN</b>	-6.2	-8.5	+2.3
<b>H15A-SodN</b>	-6.2	-21.0	+14.8

*WT-SodN*

MLSRLFAPKVTVSAHCDLPCGVYDPAQARIEAESVKAVQEKMAGNDDPHFQTRATVIKEQRAE  
LAKHHVSVLWSDYFKPPHFEKYPELHQLVNDTLKALSAAKGSKDPATGQKALDYIAQIDKIFWE  
TKKA

*P19A-SodN*

MLSRLFAPKVTVSAHCDL**A**CGVYDPAQARIEAESVKAVQEKMAGNDDPHFQTRATVI  
KEQRAELAKHHVSVLWSDYFKPPHFEKYPELHQLVNDTLKALSAAKGSKDPATGQKAL  
DYIAQIDKIFWETKKA

*H15A-SodN*

MLSRLFAPKVTVSA**A**CDLPCGVYDPAQARIEAESVKAVQEKMAGNDDPHFQTRATVIKEQRAE  
LAKHHVSVLWSDYFKPPHFEKYPELHQLVNDTLKALSAAKGSKDPATGQKALDYIAQIDKIFWE  
TKKA

*WT-SodX:*

MMPEQLSQETERARGALPFGPAEVTGPSMVPTLHHGDVLLVHWGARVRPGDVVVLRHPFQQD  
LLVVKRAAERRGAGWWVLGDNAFAGGDSTDYGVVPQDLVLRVFRFRYRPPRAGQRSPLAVVR  
WALSARVPVPADRSASRRLRAR

*S28A-SodX*

MMPEQLSQETERARGALPFGPAEVTGP**A**MVPTLHHGDVLLVHWGARVRPGDVVVLRHPFQQD  
LLVVKRAAERRGAGWWVLGDNAFAGGDSTDYGVVPQDLVLRVFRFRYRPPRAGQRSPLAVVR  
WALSARVPVPADRSASRRLRAR

**Figure A.1. Amino acid sequences generated using Expsy TRANSLATE tool on the corresponding DNA sequences obtained from the sequence analysis of pET-3a plasmids containing WT-*sodN*, H15A-*sodN* or P19A-*sodN*, and pET-22b plasmids containing WT-*sodX* or S28A-*sodX*. Yellow highlights denote the respective mutations.**

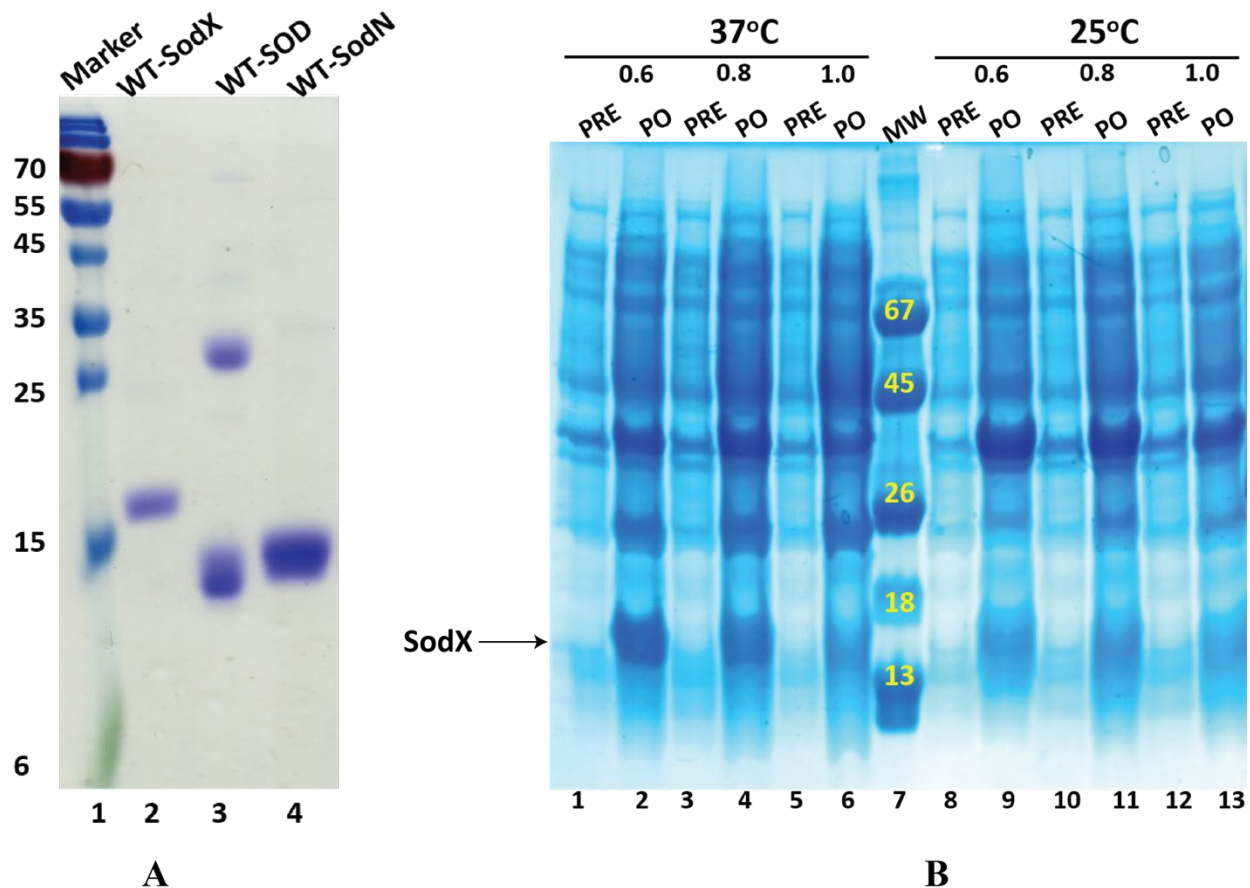
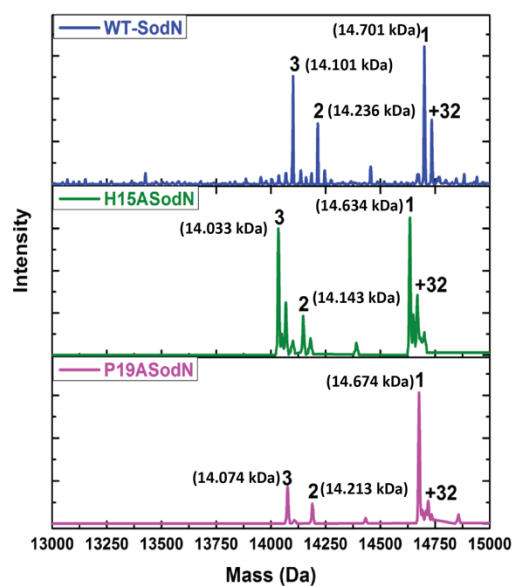
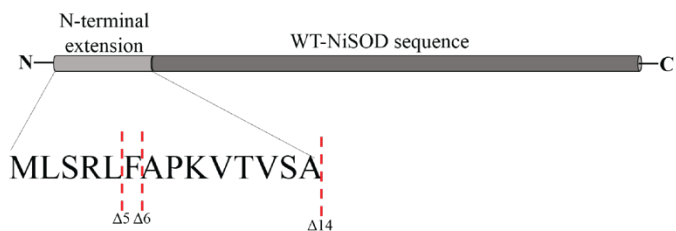


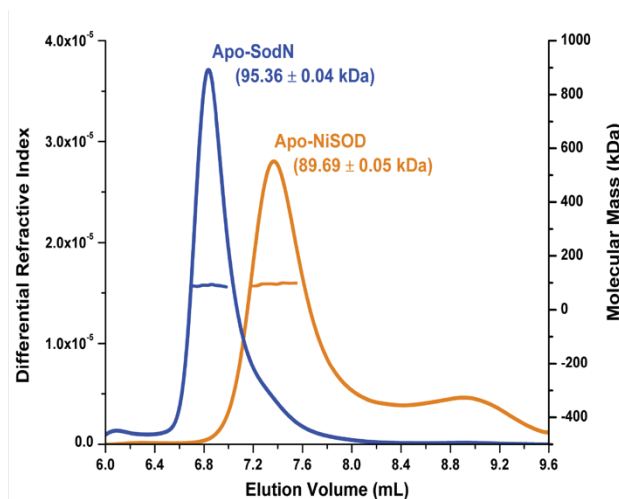
**Figure A.2. SDS - PAGE with Coomassie stain for analysis of protein expression and purification. A)** SDS-PAGE gels with Coomassie stain showing the homogeneity of the purified proteins used in this study: lane 1: Protein MW markers, lane 2: WT-SodX, lane 3: WT-NiSOD (apo-NiSOD runs as a dimer), lane 4: WT-SodN **B)** Overexpression of WT-SodX in *E. coli* BL21(DE3) plysS strain transformed with pET22b plasmid encoding WT-*sodX* grown at 37°C (lanes 1-6) and 25°C (lanes 8-13). Pre-induction cell lysates collected at OD<sub>600</sub> of 0.6 (lanes 1 & 8), 0.8 (lanes 3 & 10) and 1.0 (lanes 5 & 12). Post-induction cell lysates collected at OD<sub>600</sub> of 0.6 (lane 2 & 9), 0.8 (lane 4 & 11) and 1.0 (lane 6 & 13). Molecular weight markers are shown in lane 7.



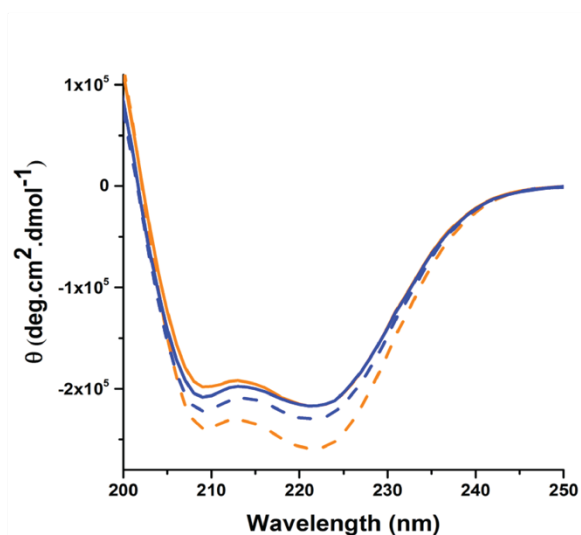
A



B



C



D

**Figure A.3. A.** Deconvoluted ESI-MS traces of WT-SodN, H15A-SodN, P19A-SodN; 1: full-length SodN 2: N $\Delta$ 4-SodN 3: N $\Delta$ 5-SodN **B.** Schematics showing truncated or processed products observed in this study **C.** SEC-MALS data for Apo-WT-SodN (blue) and Apo-WT-SOD (orange) **D.** CD spectra of Apo-WT-SodN (dashed blue line), Ni-WT-SodN (solid blue line), Apo-WT-SOD (dashed orange line), Ni-WT-SOD (solid orange line).



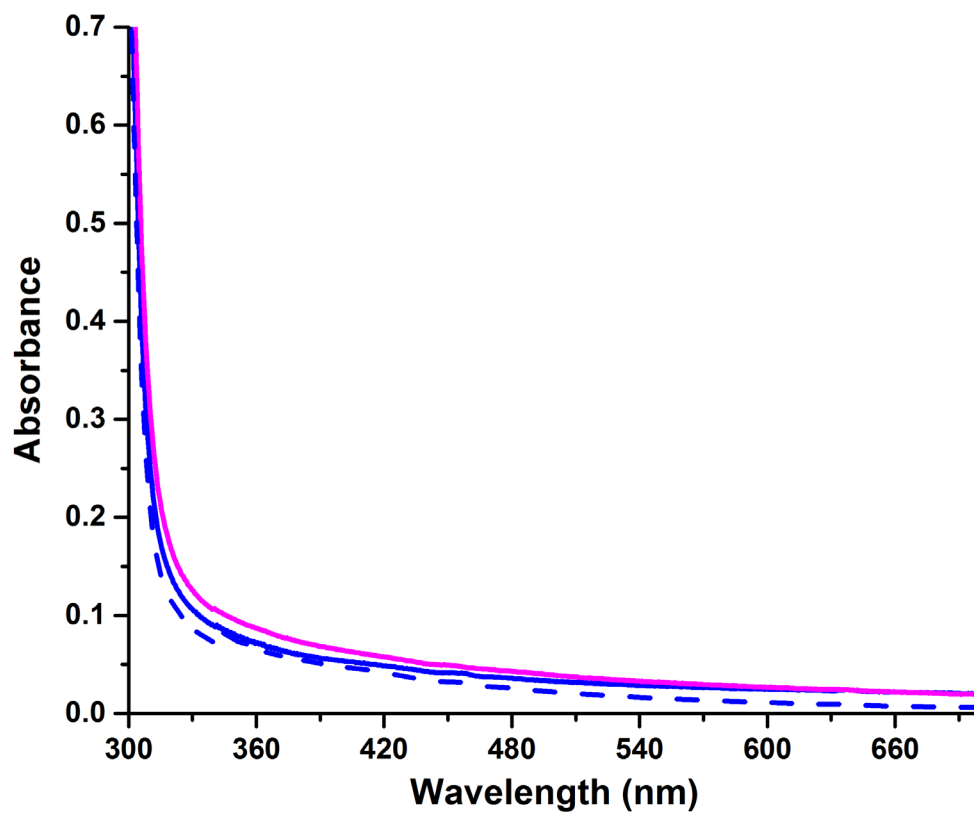


**Figure A.4.** UV-Vis spectra of 100  $\mu$ M apo-WT-SodN (dashed blue line ), Ni-WT-SodN (solid blue line) and Ni-P19A-SodN (solid magenta line)

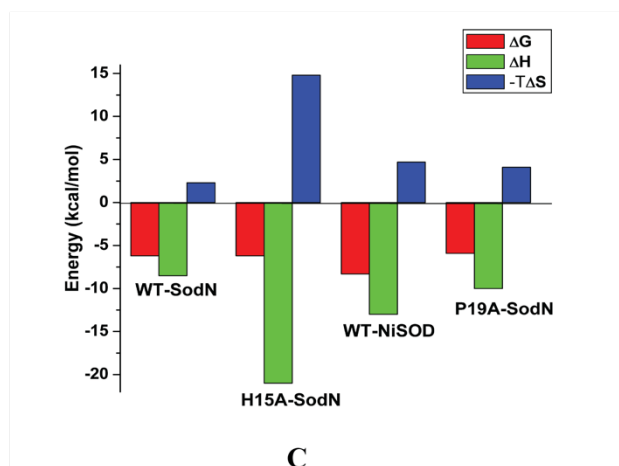
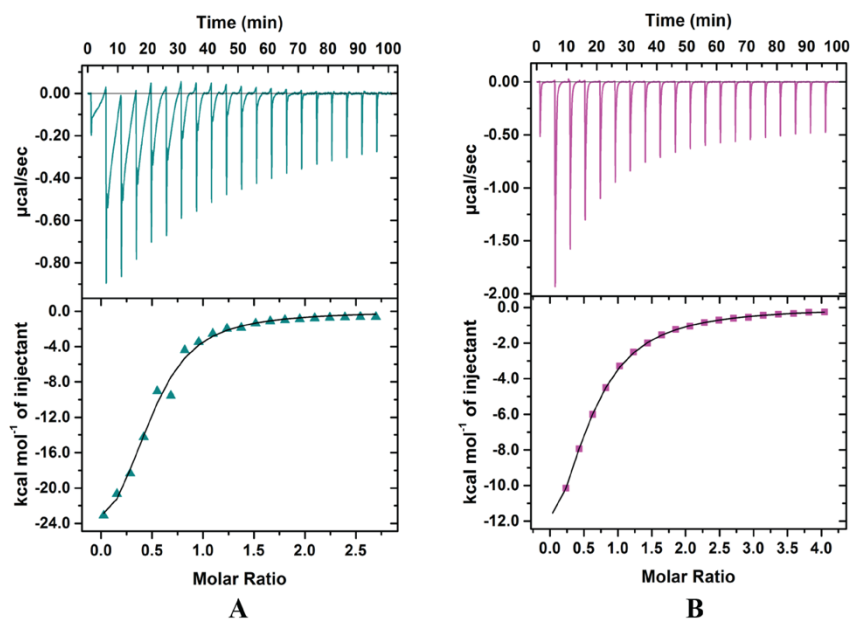


**Figure A.5.** ITC thermograms of A) 0.15 mM apo-H15A-SodN (dark cyan), and B) 0.15 mM of apo-P19A-SodN (magenta) titrated with 2 mM Ni(II) in buffer containing 20 mM Tris, 200 mM NaCl, 1 mM TCEP, pH 8.0. The top panels show the experimental thermogram and the bottom panels show the calculated binding isotherms. A one-site binding model was used to fit (solid black lines) the binding of Ni(II) to H15ASodN ( $K_d = 20$  (2)  $\mu\text{M}$ ,  $n = 0.5$ ) and P19ASodN ( $K_d = 37$  (3)  $\mu\text{M}$ ,  $n = 0.5$ ). C) Analysis of thermodynamic parameters ( $\Delta G$ ,  $\Delta H$ ,  $T\Delta S$ ) of nickel binding to apo-WT-SodN, H15A-SodN, apo-WT-NiSOD, apo-P19A-SodN.

Lep|*E. coli* MANMFALILVIATLVTGILWCVDKFFFAPKRERQAAAQAAAGDSLDKATLKKVAPKPGW  
SodX|*S. coelicolor* -----MMPEQLS  
SodX|*S. seoulensis* -----MPELS  
SodX|*T. erythraeum* -----MIQTIDN  
SodX|*P. marinus* -----MMPTANW  
SodX|*Synechococcus* -----MFSPLAAAGL

Lep|*E. coli* LETGASVFPVLAIVLIVRSFIYEPFQIPSGSMMPDLLIGDFILVEKFAYGIKDPIYQKTL  
SodX|*S. coelicolor* QET-----ERARGALPFGPAEVTGFSMVPTLHHGDVLLVH----W-----  
SodX|*S. seoulensis* QET-----ERGRALPPFGLAEVTGFSMVPTLHHGDRLLLR----Y-----  
SodX|*T. erythraeum* KE-----LLLWLLRLRQRFVCVTGFSMFPILKPGDEVLDTKAYH-----  
SodX|*P. marinus* RS-----LFLLLSGLRRHARVDGDSMSPSLAPGDLVIFQPITRY-----  
SodX|*Synechococcus* QD-----LLLFFCGRRQLLKVQGESMLPHLGPEDRILVN----Q-----

Lep|*E. coli* IETGHPKRGDIVVFKYPEDPKLDYIKKRAVGLPGDKVITYDPVSKELTIQPGCSSGQACENA  
SodX|*S. coelicolor* --GARVRPGDVVLRHPFQQDLLVVKRAAERR-----  
SodX|*S. seoulensis* --GVPVRPGRIVVLRHPFQQDLLVVKRAVERR-----  
SodX|*T. erythraeum* --HCAPEIGDMVVAEHPHRQELKIKKWFVFD-----  
SodX|*P. marinus* --DRRLKAGCVVVRHPLKPATLLIKRLIAIN-----  
SodX|*Synechococcus* --RRRPQPGEVVVAWHPSKPGVRLIKRMHGMD-----

Lep|*E. coli* LPVTYSNVEPSDFVQTFSTRNGGEATSGFFEVPKNETKENGIRLSERKETLGDVTHRILT  
SodX|*S. coelicolor* -----  
SodX|*S. seoulensis* -----  
SodX|*T. erythraeum* -----  
SodX|*P. marinus* -----  
SodX|*Synechococcus* -----

Lep  <i>E. coli</i>	VPIAQDQVGMYYQQPGQQLATWIVPPGQYFMMGDNRDNSADSRYWGFVPEANLVGRATAI
SodX  <i>S. coelicolor</i>	-----GAG-WWVLGDNAFAGGDSTDYGVVPQDLVLGRVRF
SodX  <i>S. seoulensis</i>	-----EGG-WWVLGDNPYAGGDSTDYGVVPEELILGRAVLR
SodX  <i>T. erythraeum</i>	-----EKGDCFLVGENKEESTDSRSFGLVNRKRIIGKVKSK
SodX  <i>P. marinus</i>	-----NSG-LELRGDNEQASTDSRHFGLVNRDSSLGIAEC-
SodX  <i>Synechococcus</i>	-----ANG-MHLLGDNPASASTDSRQLGPIPSGLLIGVATSC
Lep  <i>E. coli</i>	WMSFDKQEG-----EWPTGLRLSRIGGIH-----
SodX  <i>S. coelicolor</i>	YR--PPRAGQRSPLAVVRWALS AVRVPVADRSASRRLRAR
SodX  <i>S. seoulensis</i>	YR--PP-AGRRSPLALVRWVLSAARPLLSDRSAARLRAR
SodX  <i>T. erythraeum</i>	FPT-----
SodX  <i>P. marinus</i>	VWRVPFSA-----
SodX  <i>Synechococcus</i>	LRRSPPTSS-----ATKWHP-----

**Figure A.6: Sequence homology of *S. coelicolor* SodX with *E. coli* SPase I (Lep) and SodX from other organisms expressing NiSOD. Red boxes show the proposed proteolytic residues of Ser-Lys dyad.**

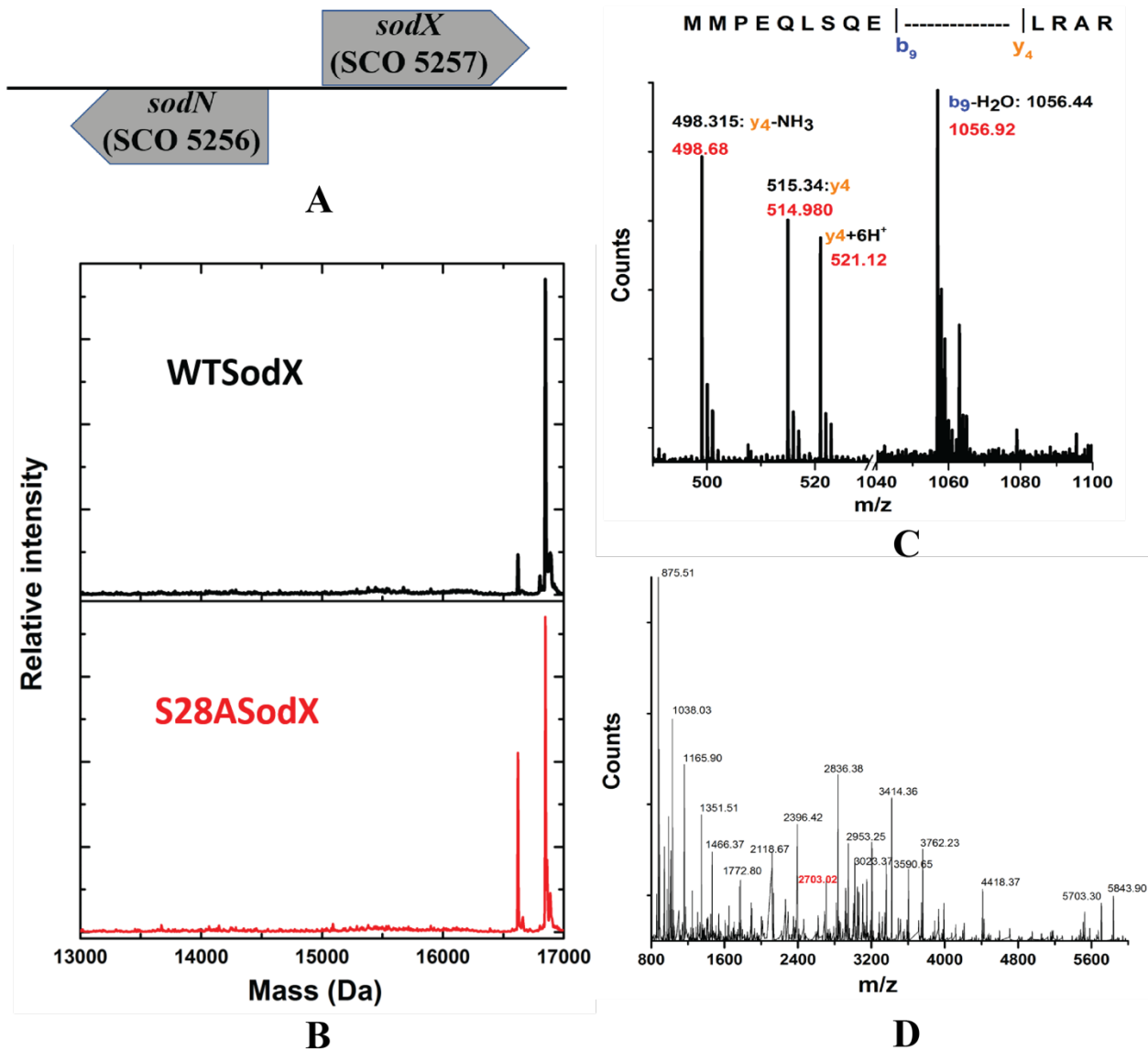
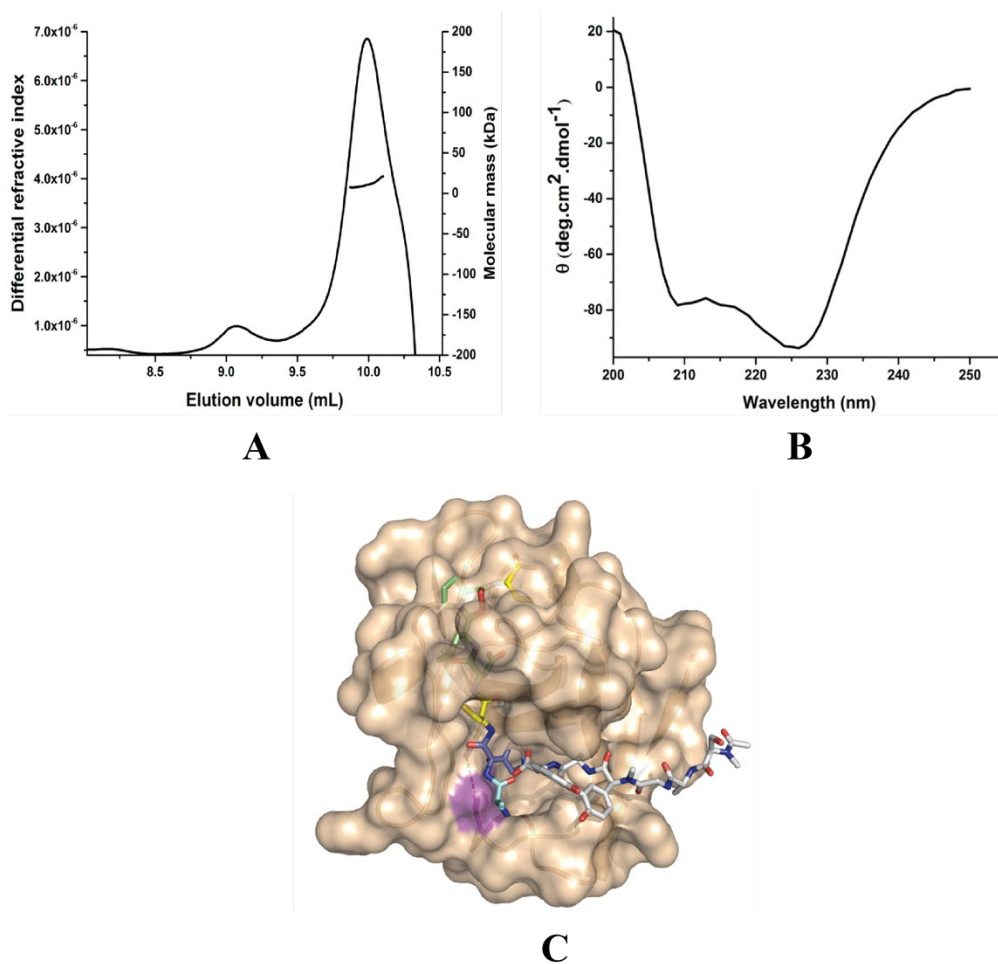


Figure A.7. SodX Protein Characterization. A. *sodN* and *sodX* gene locations in organisms expressing NiSOD *Streptomyces coelicolor*, B. Deconvoluted ESI-MS traces of WT- SodX, and S28A-SodX. C. Collision Induced Dissociation Mass Spectrometry of WT-SodX. Numbers shown in black represent expected masses and that in red show observed masses of N-terminal (blue) and C-terminal (orange) fragments D. Trypsin-digested WT-SodX followed by LC-MS/MS. The modified peptide mass is shown in red.



**Figure A.8. Structural Characterization of WT-SodX** A. SEC-MALS spectra of WT- SodX B. CD spectra of WT- SodX. C. A model of the *S. coelicolor* SodX complex with Ni-hook peptide. The SodX structure is shown in tan, and represented as a surface. The active site Ser28 nucleophile is colored magenta. The inhibitor peptide bound to *E. coli* Signal peptidase (1T7D; not shown) is shown in grey sticks, with heteroatoms colored, and corresponds to the position of the pro- peptide of SodN. The Ni-hook peptide (AHC DLPC; running vertically in the image) is shown in stick form, Ala – cyan, His – blue, Cys – yellow, CPL (Cys6-Pro5-Leu4) – green, with heteroatoms colored.

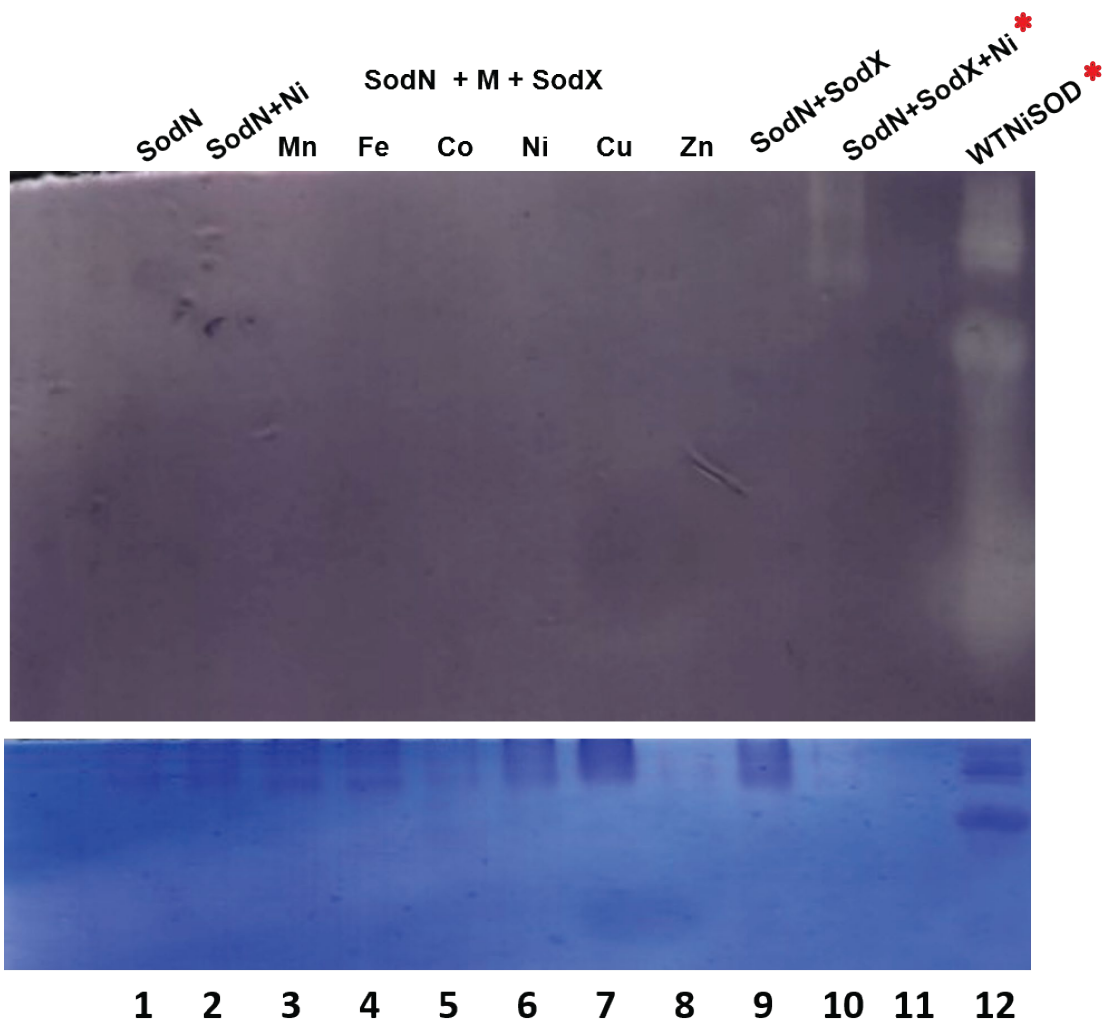
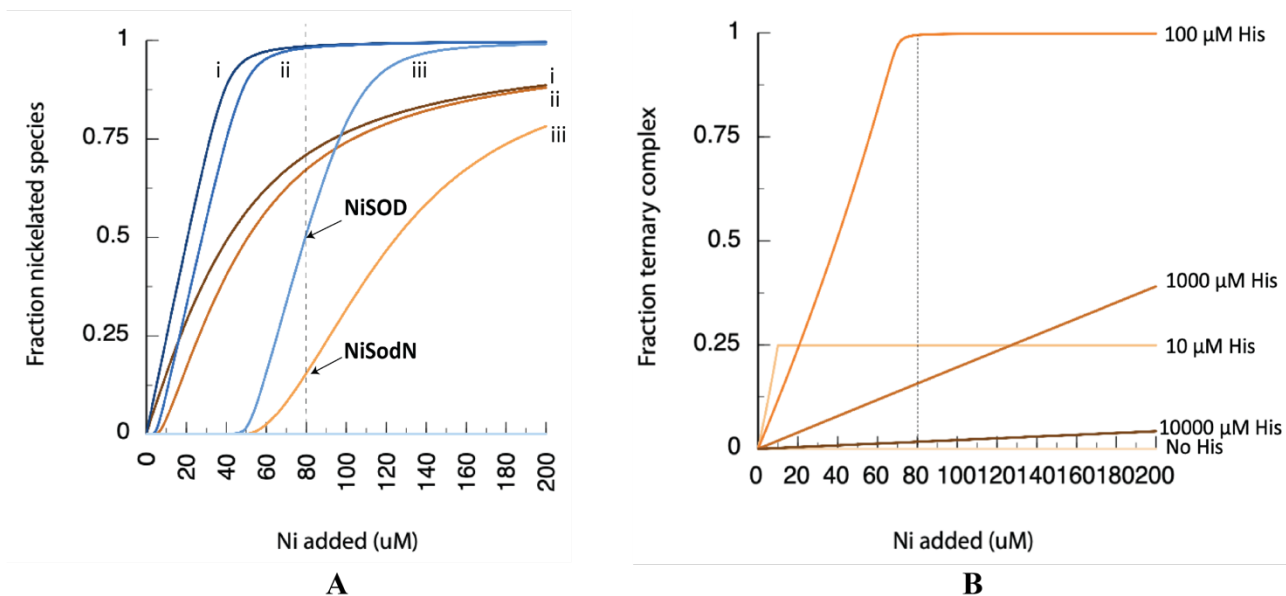
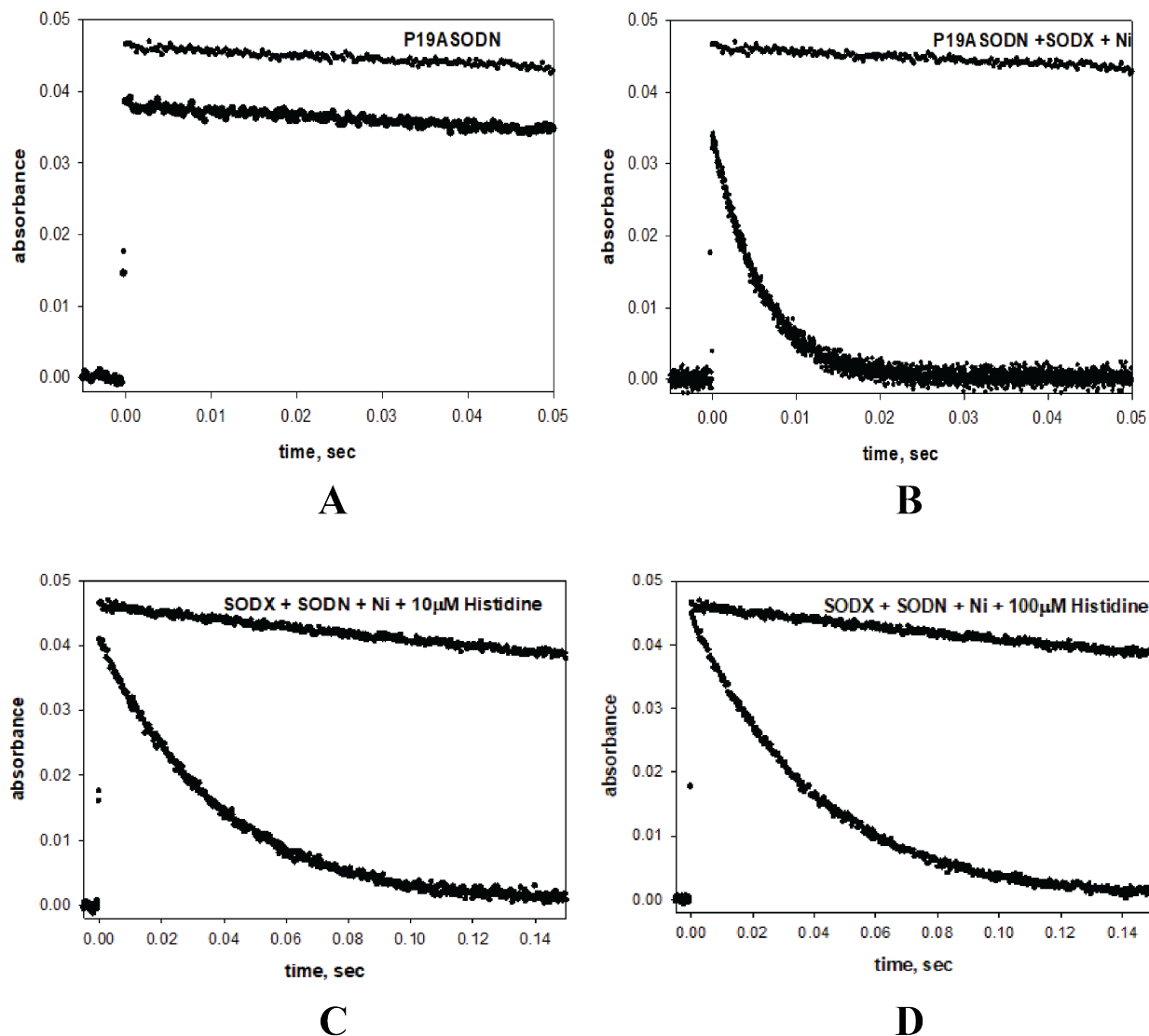


Figure A.9. Top: Native gel with activity stain. Lane 1: WT-SodN. Lane 2: Ni-WT-SodN. Lane 3: WT-SodN +WT-SodX + Mn(II). Lane 4: WT-SodN + WT-SodX + Fe(II). Lane 5: WT-SodN + WT-SodX + Co(II). Lane 6: WT-SodN +WT-SodX + Ni(II). Lane 7: WT-SodN + WT-SodX + Cu(II), Lane 8: WT-SodN +WT-SodX + Zn. Lane 9: WT-SodN +WT-SodX . Lane 10: WT-SodN + WT-SodX + Ni. Lane 11: P19ASodN + WT-SodX + Ni. Lane 12: Ni-WT-SOD. Bottom: The same activity stained gel stained with Coomassie stain to visualize the presence of proteins in each lane. Some regions of SOD-active lanes (except for lane 8), fail to stain for Coomassie possibly because of gel/protein bleaching that might occur after activity stain.



**Figure A.10: Theoretical nickel speciation curves. A. Speciation of nickel in a mixture of 40  $\mu\text{M}$  WT-SodN (brown to orange shades;  $K_d = 21.1 \mu\text{M}$ ) and apo-NiSOD (blue shades;  $K_d = 0.68 \mu\text{M}$ ) in buffers with varying concentrations of histidine (Ni-His,  $K_d = 0.2 \mu\text{M}$ ; Ni-His,  $K_d = 15 \mu\text{M}$ ) - (i) 0  $\mu\text{M}$ , (ii) 10  $\mu\text{M}$ , and (iii) 100  $\mu\text{M}$ . The arrows represent the theoretical fraction of Ni-bound SodN and NiSOD expected in the proteolytic mixture with 1:1 40  $\mu\text{M}$  WT-SodN and WT-SodX and 80  $\mu\text{M}$  nickel. B. Simulation for the formation of SodN•Ni-His ternary complex at different concentrations of L-His and 40  $\mu\text{M}$  WT-SodN, and the dashed line represents the fraction of ternary complex expected to form at 80  $\mu\text{M}$  nickel, which is the nickel concentration used in the proteolytic assays.**





**Figure A.11:** Kinetic traces showing disappearance of pulse-radiolytically generated superoxide radical by monitoring absorbance at 260 nm for buffer (straight line) and A. Ni-P19ASodN, and catalytic curves (hyperbolic) for B. P19A-SodN + WT-SodX + Ni, and WT-SodN + WT-SodX + Ni in C. 0.01 mM ( $[Ni]= 1.8 \mu M$ ) D. 0.1 mM L-His ( $[Ni]= 2.0 \mu M$ ).

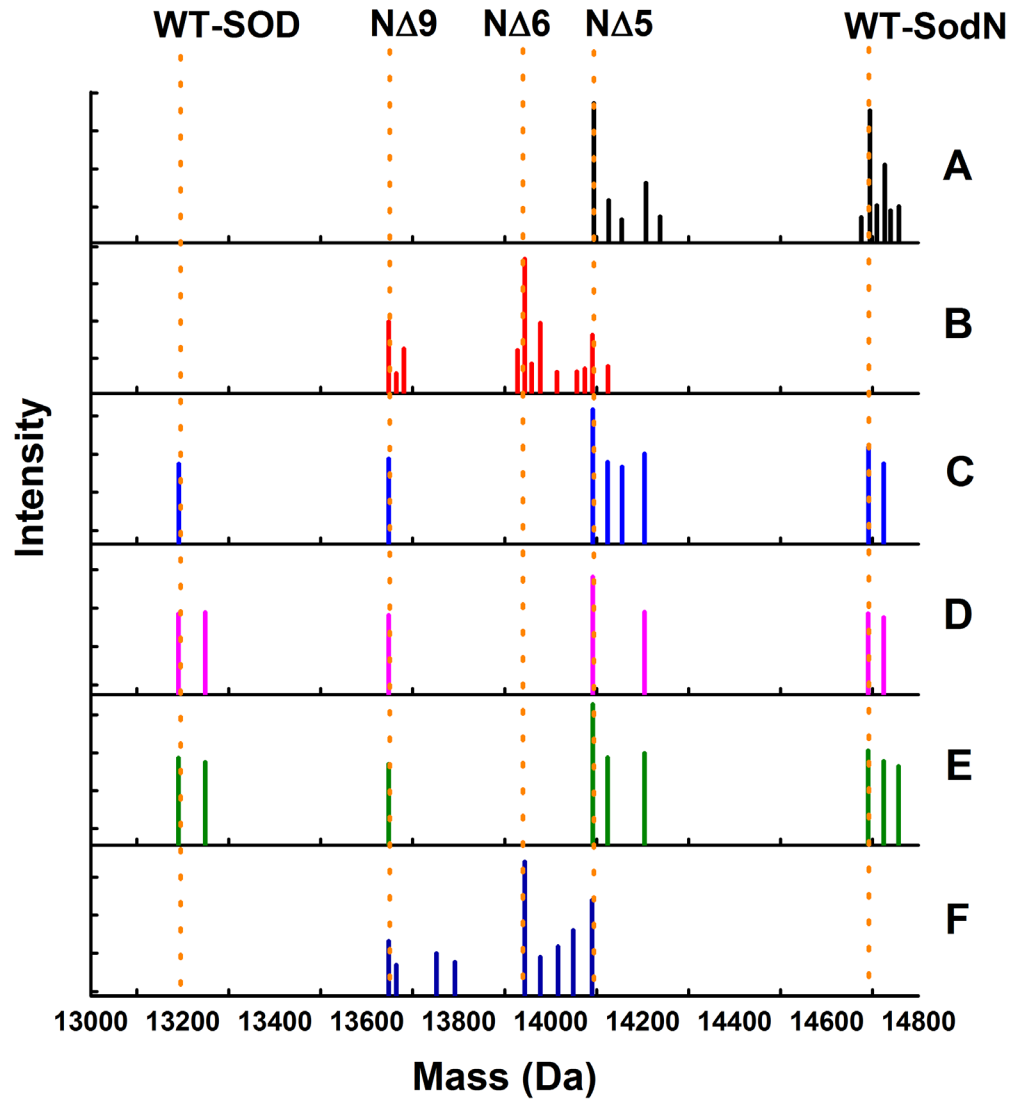


**Figure A.12. High-resolution deconvoluted ESI- MS traces of proteolytic assays containing 40  $\mu$ M WT-SodX and 40  $\mu$ M WT-SodN in assay buffer (50mM Tris, 1mM TCEP, pH 8.0):**  
**A:** apo-WT-SodN incubated with denatured WT-SodX, (SodX was denatured using 1M HCl); **B:** WT-SodX + WT-SodN pre-incubated with 80  $\mu$ M NiCl<sub>2</sub>; **C:** WT-SodX + WT-SodN pre-incubated with 80  $\mu$ M NiCl<sub>2</sub> + 0.01 mM L-Histidine **D:** + 0.1 mM L-Histidine; **E:** + 1.0 mM L-Histidine; **F:** + 10.0 mM L-Histidine

**APPENDIX B**

**SUPPORTING INFORMATION FOR NICKEL BINDING TO HYPA-UREE<sub>2</sub>  
COMPLEX**

**Table B.1: EXAFS fits of Ni-site in HypA-UreE<sub>2</sub> complex at pH 7.2**

Shell	r (Å)	$\sigma^2$ (x10 <sup>-3</sup> Å <sup>-2</sup> )	$\Delta E_0$	R-factor	Red. $\chi^2$
4N/O	2.08(1)	1(0)	1(2)	17.3	214.8
5N/O	2.08(1)	3(0)	2(2)	16.3	202.8
6N/O	2.08(1)	4(0)	1(2)	17.2	214.2
5N/O	2.09(1)	2(0)	3(2)	15.4	217.5
1N/O	2.33(5)	3(7)			
4 N/O	2.08(1)	1(1)	3(3)	15.79	222.9
2N/O	2.13(16)	19(28)			
3 N/O	2.08(1)	0(1)	-2(2)	22.28	222.7
3N/O	2.13(15)	17(10)			
5N/O	2.08(1)	6(1)	0(1)	10.2	144.0
1Im0°	2.09(1)	neg			
4N/O	2.07(1)	5(2)	1(1)	8.1	114.1
2Im0°	2.09(1)	2(2)			
3N/O	2.08(1)	2(1)	1(1)	6.6	93.2
3Im0°	2.09(2)	6(2)			

<b>2N/O</b>	2.08(1)	<b>0(1)</b>	0(1)	5.4	76.4
<b>4Im0°</b>	2.08(1)	8(1)			
<b>1N/O</b>	2.08(1)	<b>neg</b>	0(1)	5.3	76.0
<b>5Im0°</b>	2.08(1)	8(1)			
<b>3N/O</b>	2.06(1)	2(1)	0(1)	6.5	91.6
<b>3Im0°</b>	2.10 (2)	5(2)			
<b>3N/O</b>	2.04(1)	4(1)	0(1)	5.3	74.8
<b>3Im10°</b>	2.10(2)	2(0)			
<b>2N/O</b>	2.07(6)	<b>11(7)</b>	0(1)	5.8	94.1
<b>1N/O</b>	2.08(1)	<b>neg</b>			
<b>3Im0°</b>	2.07(2)	5(2)			
<b>1N/O</b>	2.08(1)	<b>neg</b>	2(1)	5.9	95.7
<b>2 N/O</b>	2.08(5)	<b>11(8)</b>			
<b>3Im0°</b>	2.07(2)	5(2)			
<b>3 N/O</b>	2.07(1)	2(2)	0(1)	5.8	94.4
<b>2Im0°</b>	2.01(3)	5(4)			
<b>1Im5°</b>	2.12(2)	<b>neg</b>			
<b>3 N/O</b>	2.06(1)	2(1)	0(1)	5.4	88.6
<b>1Im0°</b>	1.96(2)	<b>0(2)</b>			
<b>2Im5°</b>	2.10(2)	<b>0(1)</b>			
<b>3N/O</b>	<b>2.03(1)</b>	<b>7(2)</b>	<b>2(1)</b>	<b>3.6</b>	<b>59.44</b>
<b>1Im0</b>	<b>2.07(1)</b>	<b>1(2)</b>			
<b>2Im10</b>	<b>2.09(1)</b>	<b>1(1)</b>			

---

<b>3 N/O</b>	2.03(1)	6(2)	0(1)	3.8	63.3
<b>1Im5°</b>	2.07(2)	1(1)			
<b>2Im10°</b>	2.09(1)	1(1)			
<b>3N/O</b>	2.04(1)	6(1)	0(1)	2.8	54.1
<b>1Im0°</b>	2.05(2)	neg			
<b>1Im5°</b>	2.19(1)	2(5)			
<b>1Im10°</b>	2.09(1)	1(2)			
<b>2N/O</b>	2.03(2)	3(2)	0(1)	3.4	55.9
<b>2Im0°</b>	2.09(3)	7(3)			
<b>2Im10°</b>	2.09(1)	0(1)			
<b>2N/O</b>	2.03(1)	2(2)	0(1)	3.7	61.1
<b>2Im5°</b>	2.11(4)	9(4)			
<b>2Im10°</b>	2.09(1)	0(1)			
<b>2N/O</b>	2.07(1)	3(2)	1(1)	2.3	44.5
<b>2Im0°</b>	2.07(2)	2(2)			
<b>1Im5°</b>	2.23(3)	2(5)			
<b>1Im10°</b>	2.10(1)	neg			
<b>1N/O</b>	2.03(2)	neg	0(1)	3.4	65.9
<b>2Im0°</b>	2.09(2)	3(3)			
<b>1Im5°</b>	1.94(3)	3(3)			
<b>2Im10°</b>	2.10(1)	1(1)			

---

**Table B.2: Selected EXAFS fits of Ni-site in HypA-UreE<sub>2</sub> complex at pH 6.3**

Shell	r (Å)	$\sigma^2$ ( $\times 10^{-3} \text{ \AA}^{-2}$ )	$\Delta E_0$	R-factor	Red. $\chi^2$
<b>6 N/O</b>	2.09(1)	4(0)	2(1)	16.1	483.0
<b>5 N/O</b>	2.08(1)	5(1)	1(1)	9.6	326.4
<b>1Im0°</b>	2.11(2)	neg			
<b>4 N/O</b>	2.08(1)	5(1)	1(1)	7.1	243.6
<b>2Im0°</b>	2.11(1)	2(2)			
<b>3 N/O</b>	2.08(1)	3(1)	2(1)	6.1	206.8
<b>3Im0°</b>	2.11(1)	4(1)			
<b>2N/O</b>	2.08(1)	1(1)	1(1)	5.9	202.8
<b>4Im0°</b>	2.10(2)	6(1)			
<b>1N/O</b>	2.09(1)	neg	1(1)	6.9	234.0
<b>5Im0°</b>	2.09(1)	6(1)			
<b>3 N/O</b>	2.06(1)	3(1)	1(1)	5.8	196.5
<b>3Im5°</b>	2.12(1)	3(1)			
<b>3 N/O</b>	<b>2.04(1)</b>	<b>1(1)</b>	<b>1(0)</b>	<b>4.9</b>	<b>169.1</b>
<b>3Im10°</b>	<b>2.13(1)</b>	<b>1(1)</b>			

**Table B.3: EXAFS fits of Ni-site in HypA-UreE<sub>2</sub> complex at pH 6.3**

Shell	r (Å)	$\sigma^2$ ( $\times 10^{-3} \text{ \AA}^{-2}$ )	$\Delta E_0$	R-factor	Red. $\chi^2$
4 N/O	2.09(1)	1(0)	2(2)	19.9	600.1
5 N/O	2.09(1)	3(0)	2(2)	17.0	512.02
6 N/O	2.09(1)	4(0)	2(1)	16.1	483.0
5 N/O	2.06(2)	4(3)	0(2)	15.8	540.0
1N/O	2.14(5)	neg			
4 N/O	2.05(4)	4(4)	0(2)	16.0	546.5
2N/O	2.13(4)	0(3)			
3 N/O	2.12(2)	neg	0(2)	15.9	544.6
3N/O	2.02(3)	1(4)			
5 N/O	2.08(1)	5(1)	1(1)	9.6	326.4
1Im0°	2.11(2)	neg			
4 N/O	2.08(1)	5(1)	1(1)	7.1	243.6
2Im0°	2.11(1)	2(2)			
3 N/O	2.08(1)	3(1)	2(1)	6.1	206.8
3Im0°	2.11(1)	4(1)			
2N/O	2.08(1)	1(1)	1(1)	5.9	202.8
4Im0°	2.10(2)	6(1)			
1N/O	2.09(1)	neg	1(1)	6.9	234.0
5Im0°	2.09(1)	6(1)			

---

<b>1N/O</b>	2.09(1)	neg	0(1)	4.7	183.4
<b>2N/O</b>	2.05(4)	11(8)			
<b>3Im0°</b>	2.10(2)	10(1)			
<b>3 N/O</b>	2.06(1)	3(1)	1(1)	5.8	196.5
<b>3Im5°</b>	2.12(1)	3(1)			
<b>3 N/O</b>	<b>2.04(1)</b>	<b>1(1)</b>	<b>1(0)</b>	<b>4.9</b>	<b>169.1</b>
<b>3Im10°</b>	<b>2.13(1)</b>	<b>1(1)</b>			
<b>3 N/O</b>	2.07(1)	2(1)	0(1)	3.8	149.7
<b>2Im0°</b>	2.03(2)	2(1)			
<b>1Im5°</b>	2.16(1)	neg			
<b>3 N/O</b>	2.06(1)	1(1)	0(0)	3.6	143.7
<b>1Im0°</b>	1.99(2)	neg			
<b>2Im5°</b>	2.14(1)	neg			
<b>3 N/O</b>	2.04(1)	2(1)	1(0)	3.0	118.9
<b>2Im0°</b>	2.10(1)	3(1)			
<b>1Im10°</b>	2.14(1)	neg			
<b>3 N/O</b>	2.03(1)	2(1)	1(0)	2.9	116.0
<b>1Im0°</b>	2.11(2)	neg			
<b>2Im10°</b>	2.14(1)	0(1)			
<b>3 N/O</b>	2.03(1)	2(1)	1(1)	3.1	122.9
<b>1Im5°</b>	2.11(2)	neg			
<b>2Im10°</b>	2.14(1)	1(1)			

---



---

<b>3 N/O</b>	2.04(1)	2(1)	0(1)	3.1	123.3
<b>2Im5°</b>	2.11(2)	3(1)			
<b>1Im10°</b>	2.14(1)	neg			
<b>2 N/O</b>	2.03(1)	1(1)	0(1)	3.3	131.5
<b>2Im0°</b>	2.09(2)	4(2)			
<b>2Im10°</b>	2.14(1)	0(1)			
<b>3 N/O</b>	2.05(1)	1(1)	0(1)	2.5	118.7
<b>1Im0°</b>	2.00(1)	0(1)			
<b>1Im5°</b>	2.13(1)	neg			
<b>1Im10°</b>	2.16(3)	0(1)			

---

**Table B.4: EXAFS fits of Zn-site in HypA-UreE<sub>2</sub> complex at pH 7.2**

Shell	r (Å)	$\sigma^2$ (x10 <sup>-3</sup> Å <sup>-2</sup> )	$\Delta E_0$	R-factor	Red. $\chi^2$
4S	2.32(0)	5(0)	1(0)	2.1	14.5
2S	2.38(1)	2(1)	1(1)	1.7	18.0
2S	2.28(1)	1(1)			

**Table B.5: EXAFS fits of Zn-site in HypA-UreE<sub>2</sub> complex at pH 6.3**

Shell	r (Å)	$\sigma^2$ (x10 <sup>-3</sup> Å <sup>-2</sup> )	$\Delta E_0$	R-factor	Red. $\chi^2$
4S	2.33(0)	3(0)	-1(1)	4.7	131.7

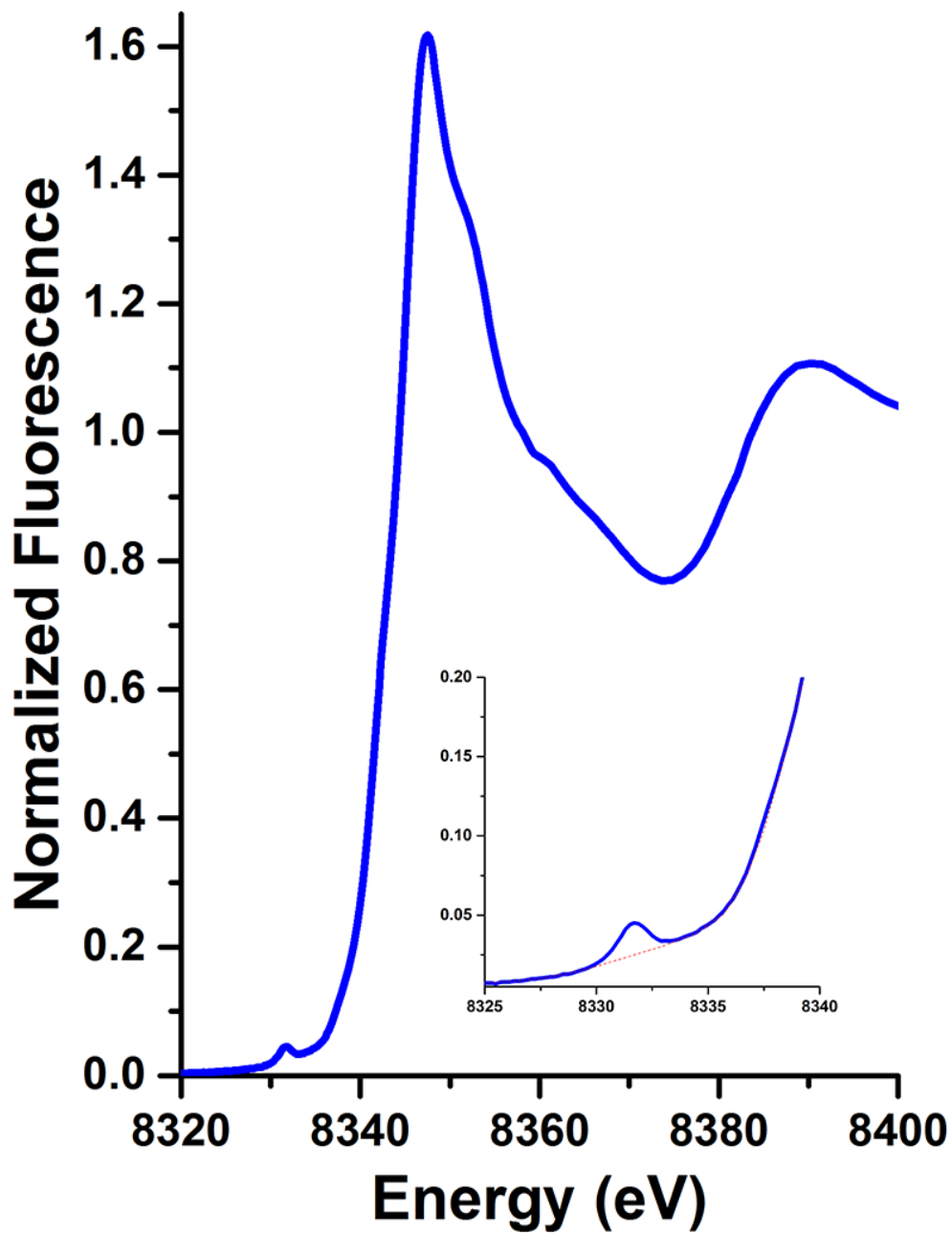


Figure B.1: Ni K-edge XANES spectrum of Ni,Zn-WT-HypA•WT-UreE<sub>2</sub> complex at pH 6.3; the inset shows the 1s→3d transition (blue) at 8330 eV and the baseline (dotted red line) used to measure the associated peak area.

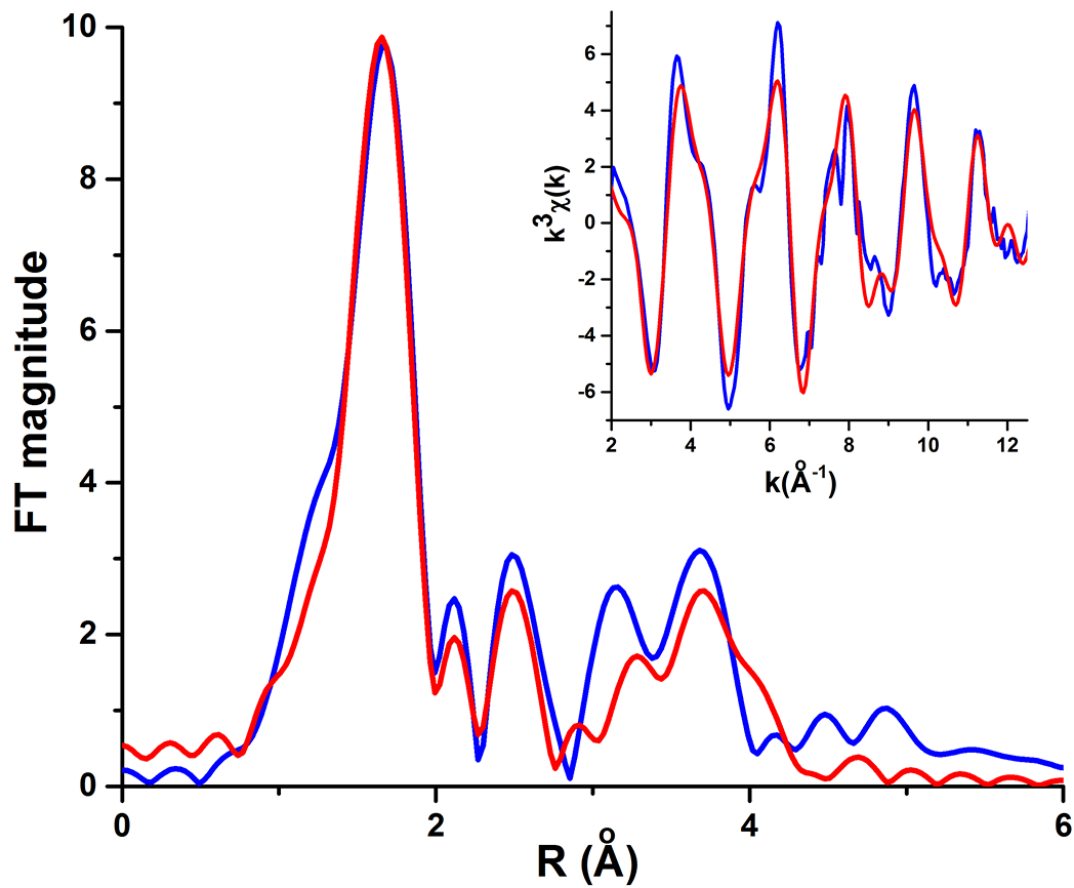


Figure B.2. Fourier transformed EXAFS ( $k = 2 - 12.5 \text{ \AA}^{-1}$ ) data (blue) uncorrected for phase shifts and the best fit model (red) for Ni,Zn-WT-HypA•WT-UreE<sub>2</sub> complex at pH 6.3; the inset shows the  $k^3$ - weighted unfiltered EXAFS data (blue) and best fit model (red).

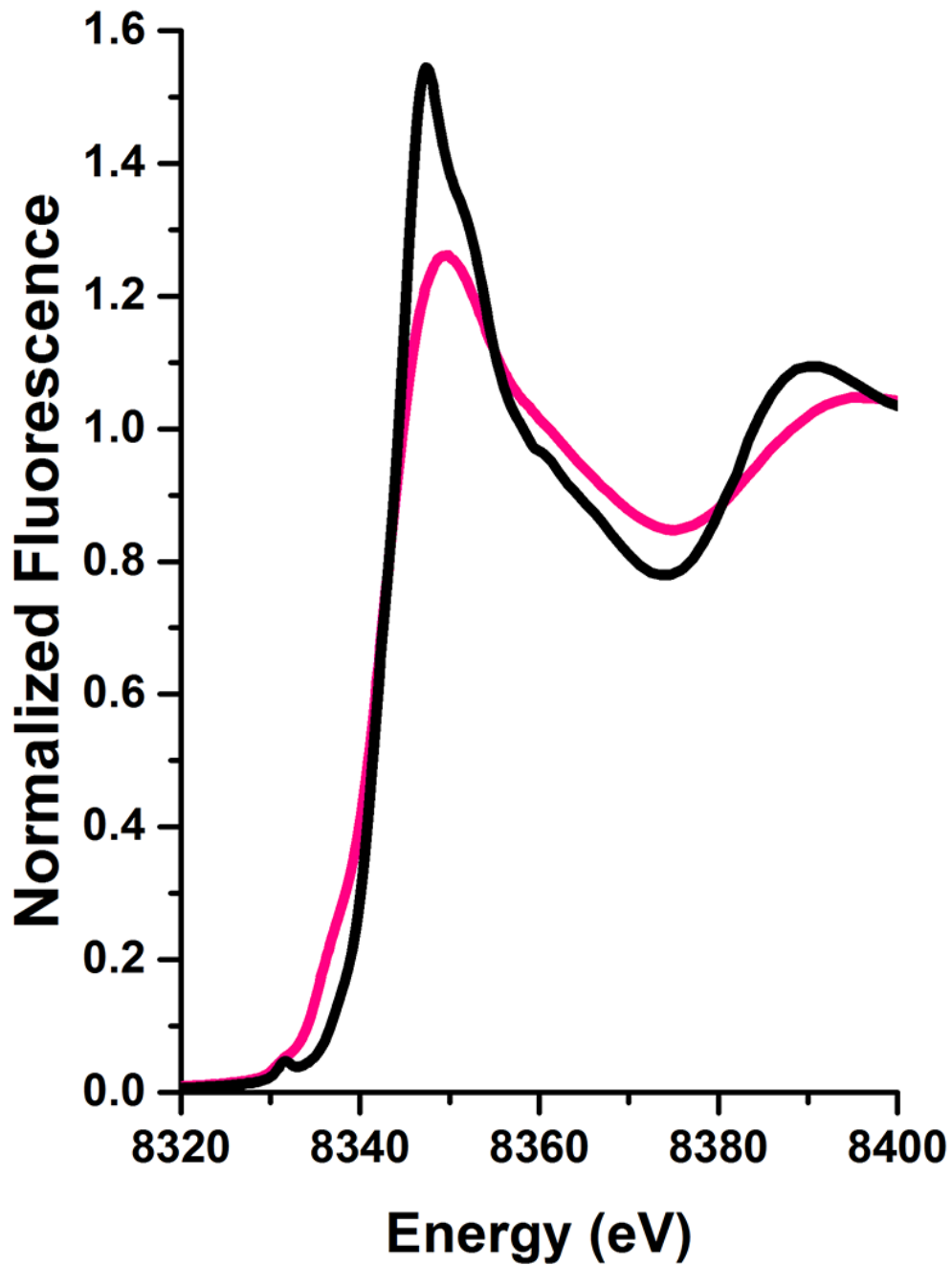
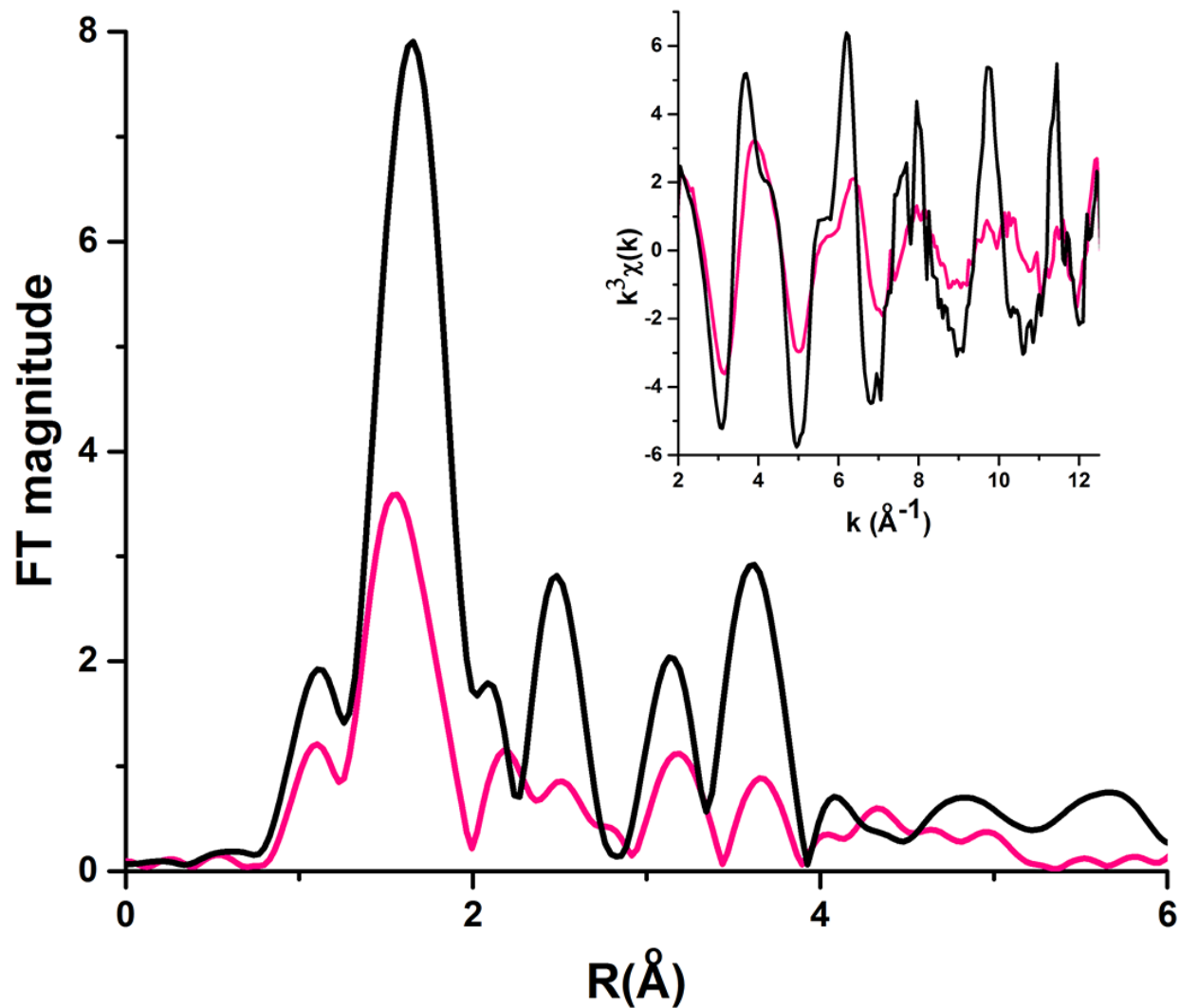


Figure B.3: Overlay of A) Ni K-edge XANES spectrum of Ni,Zn-WT-HypA (pink) and Ni,Zn-WT-HypA•WT-UreE<sub>2</sub> (black) complex at pH 7.2.



**Figure B.4.** Fourier transformed EXAFS ( $k = 2 - 12.5 \text{ \AA}^{-1}$ ) data for Ni,Zn-WT-HypA (pink) and Ni,Zn-WT-HypA•WT-UreE<sub>2</sub> complex (black) at pH 7.2 uncorrected for phase shifts; the inset shows the  $k^3$ - weighted unfiltered EXAFS data for Ni,Zn-WT-HypA (pink) and Ni,Zn-WT-HypA•WT-UreE<sub>2</sub> complex (black).

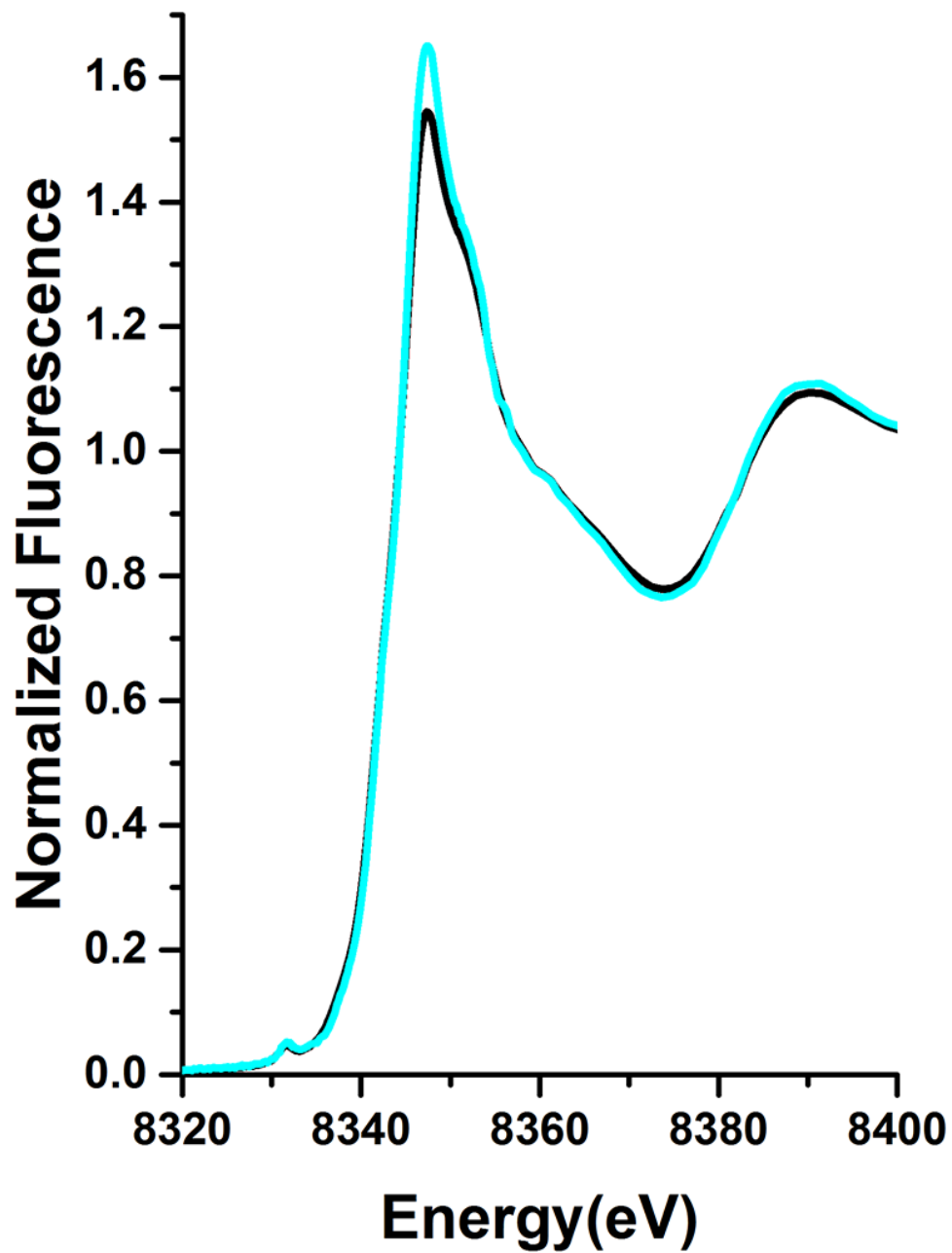


Figure B.5 Overlay of Ni K-edge XANES of Ni-UreE<sub>2</sub> (blue) and Ni, Zn-WT-HypA•WT-UreE<sub>2</sub> complex (black) at pH 7.2.

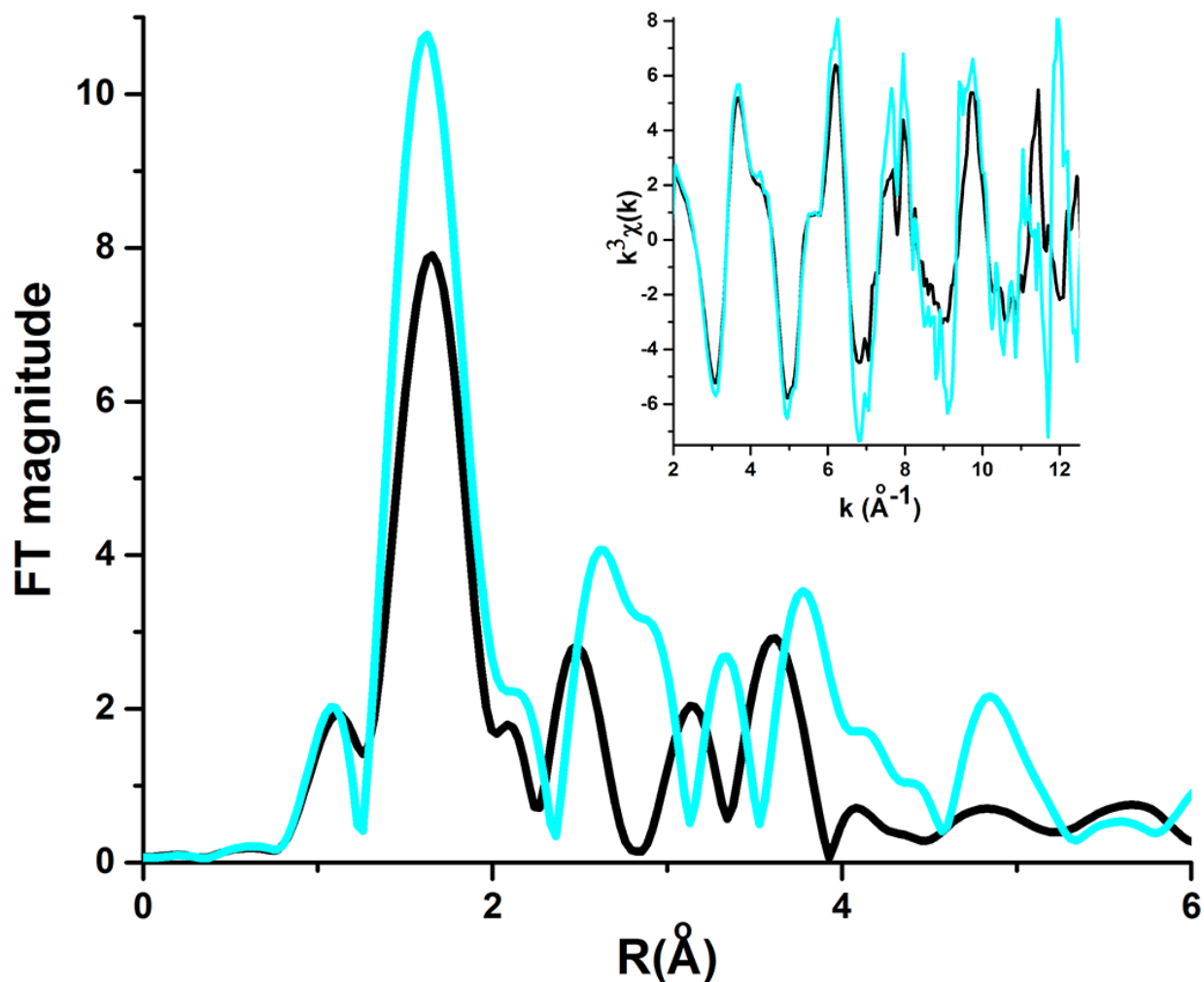


Figure B.6: Overlay of the Fourier transformed EXAFS ( $k = 2 - 12.5 \text{ \AA}^{-1}$ ) data for Ni,Zn-WT-HypA•WT-UreE<sub>2</sub> complex (black) and Ni-UreE<sub>2</sub> (blue) at pH 7.2 uncorrected for phase shifts; the inset shows the  $k^3$ - weighted unfiltered EXAFS data for Ni,Zn-WT-HypA•WT-UreE<sub>2</sub> complex (black) and Ni-UreE<sub>2</sub> (blue).



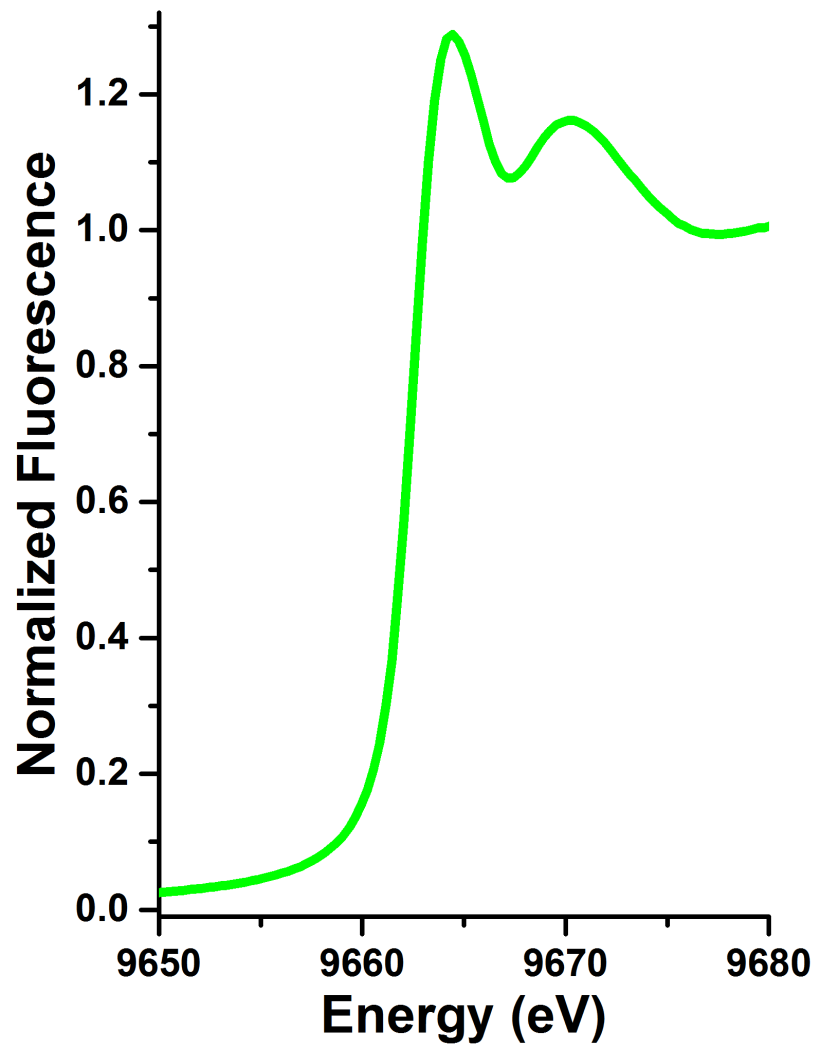


Figure B.7. Zn K-edge XANES of Ni, Zn-WT-HypA•WT-UreE<sub>2</sub> complex (green) at pH 7.2 .

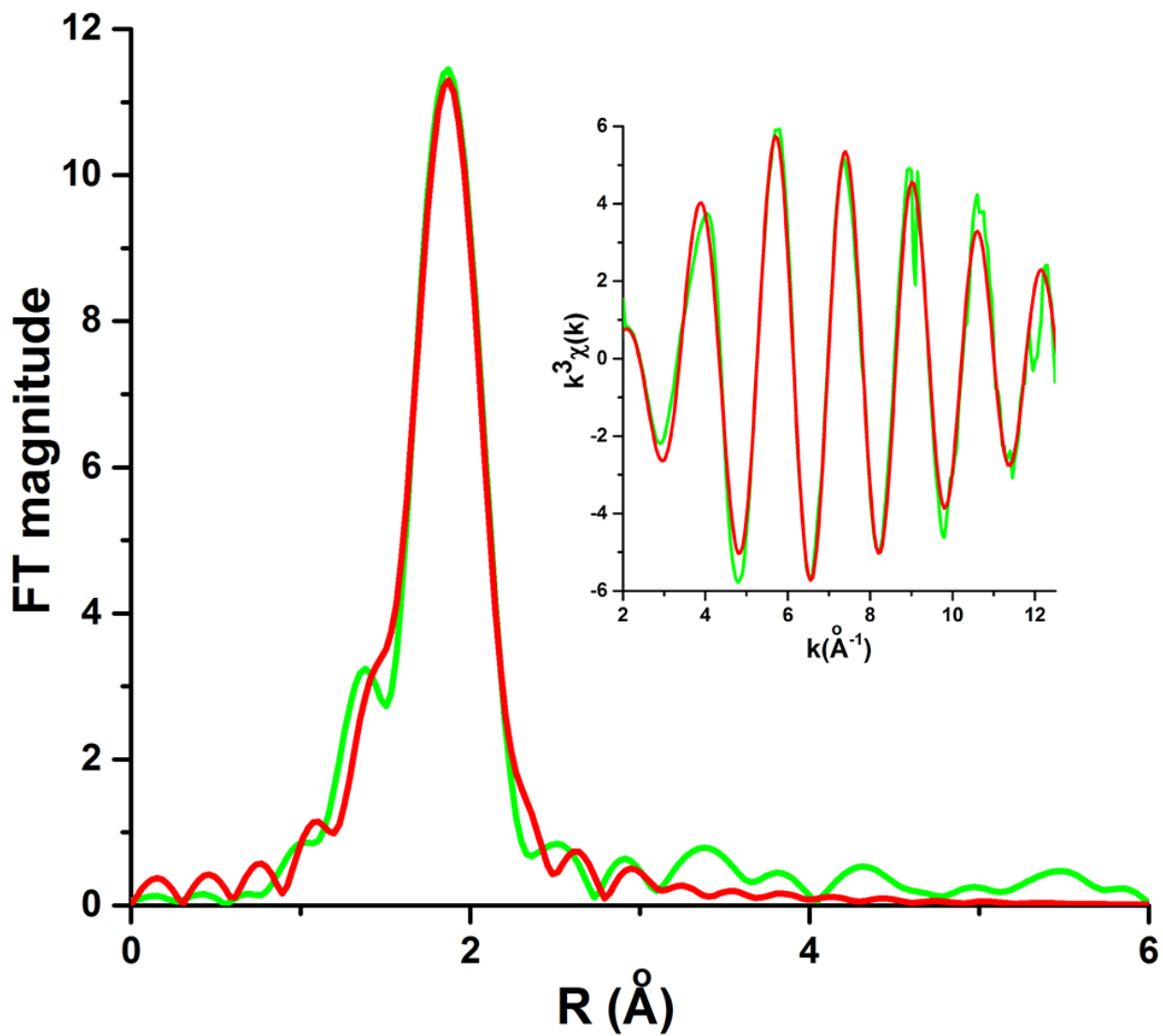


Figure B.8. Zn K-edge EXAFS of Ni, Zn-WT-HypA-WT-UreE<sub>2</sub> complex (green) and fits (red) at pH 7.2.

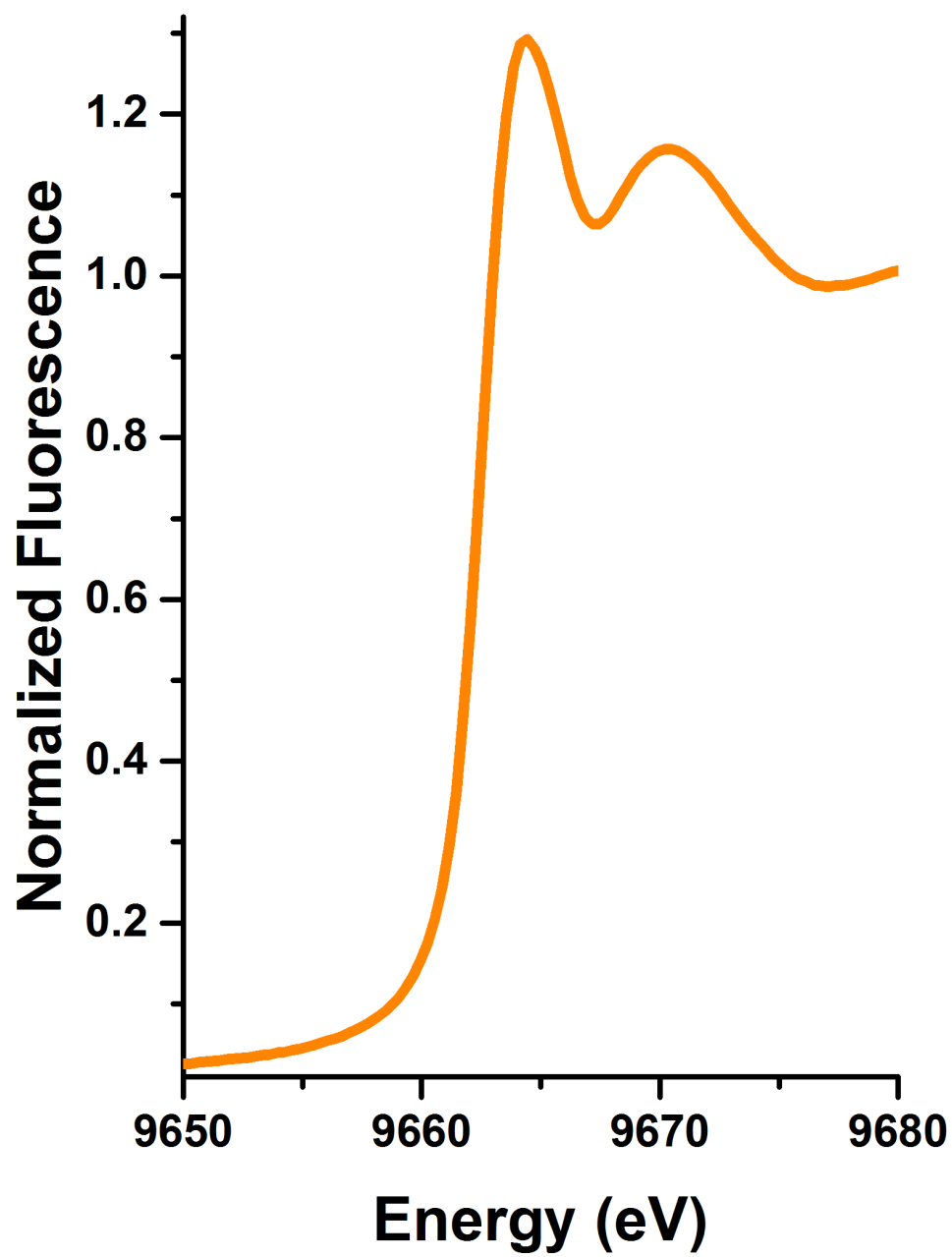


Figure B.9. Zn K-edge XANES of Ni, Zn-WT-HypA-WT-UreE<sub>2</sub> complex (orange) at pH 6.3

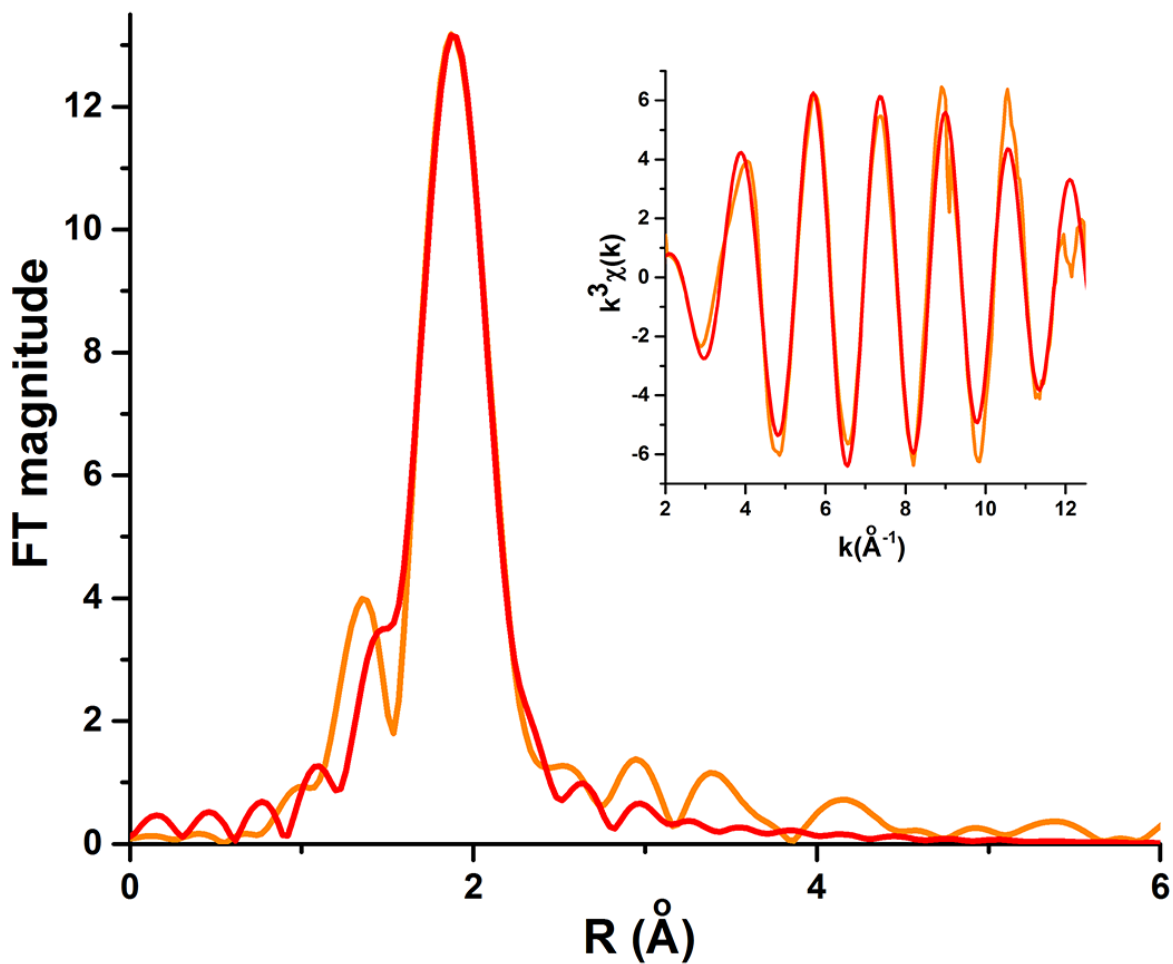
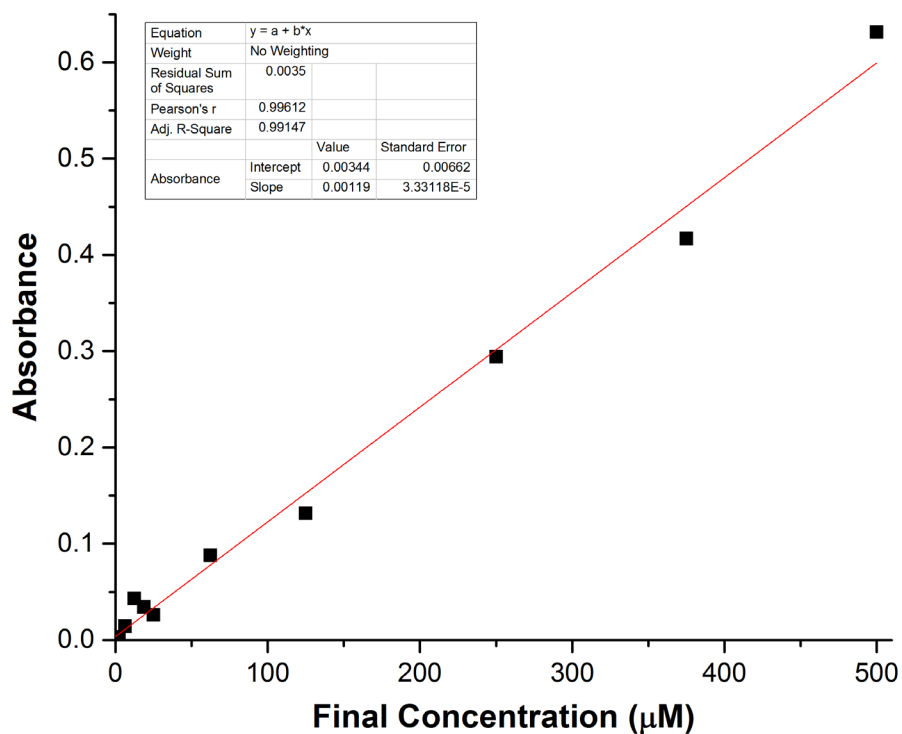


Figure B.10. Zn K-edge EXAFS of Ni, Zn-WT-HypA-WT-UreE<sub>2</sub> complex (orange) and fits (red) at pH 6.3.

## APPENDIX C

### SUPPORTING INFORMATION FOR ROLE OF GLYCINE TO ALANINE MUTATION IN HYPA FOR THE MATURATION OF UREASE AND NI, FE-HYDROGENASE IN *H.PYLORI*



**Figure C.1: Standard Curve used to quantify the ammonia released in the *in vitro* Urease assay. Absorbance (Y-axis) of the solutions containing known amounts of ammonium chloride (X-axis) are plotted and fitted with a linear curve, the parameters of which was used to determine the concentration of ammonia released from the *H. pylori* cell lysates.**

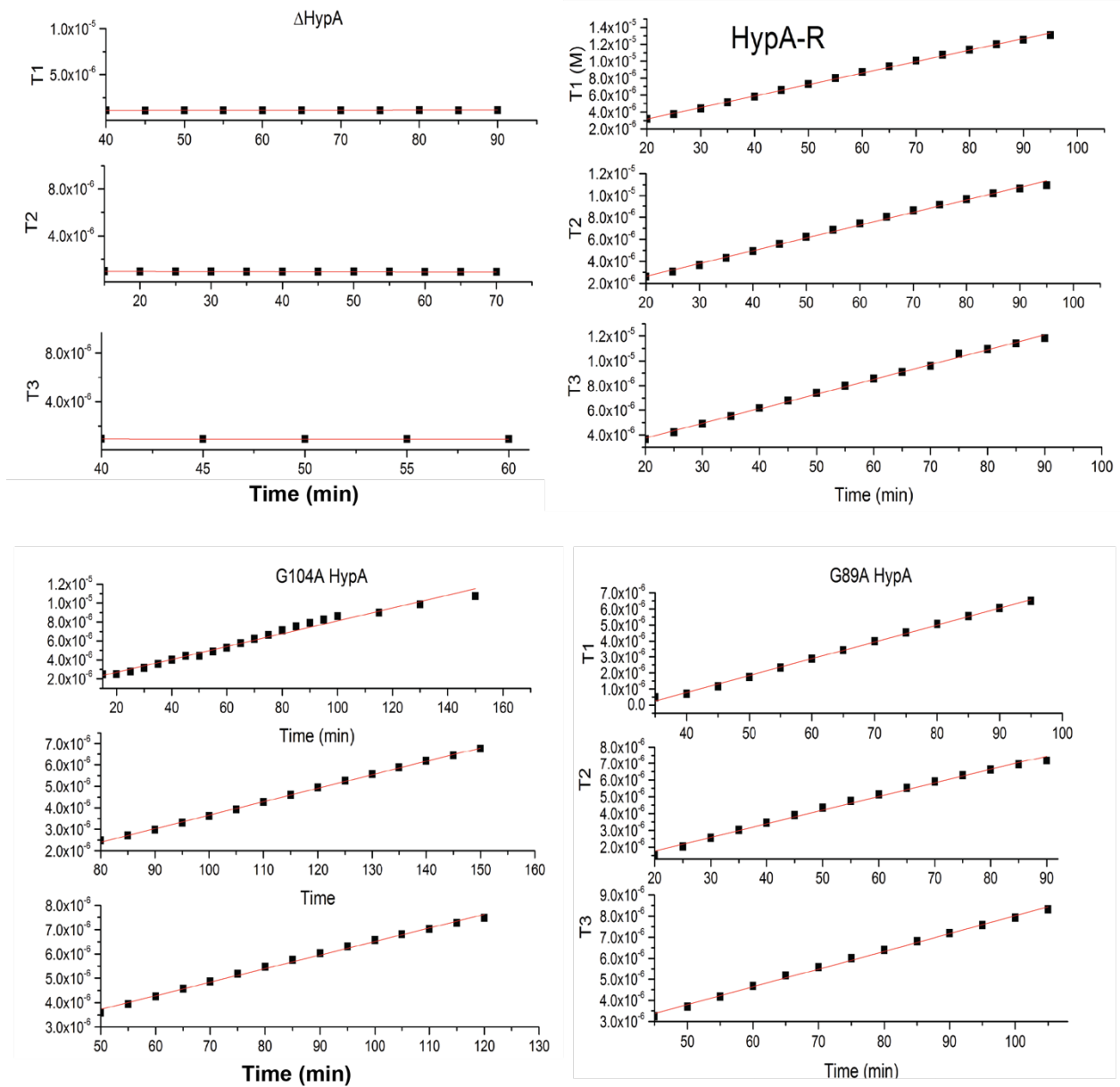


**Figure C.2:** Selected plots showing the absorbance of reduced methyl viologen (Y-axis) from *H. pylori* cell lysates monitored at A578 nm for 45–150 minutes (X-axis). The slope of the linear increase in absorbance over time was taken as the rate of reduction and three replicates ( $T_i$ ) of each strain was used to obtain an average of the rate of reduction.

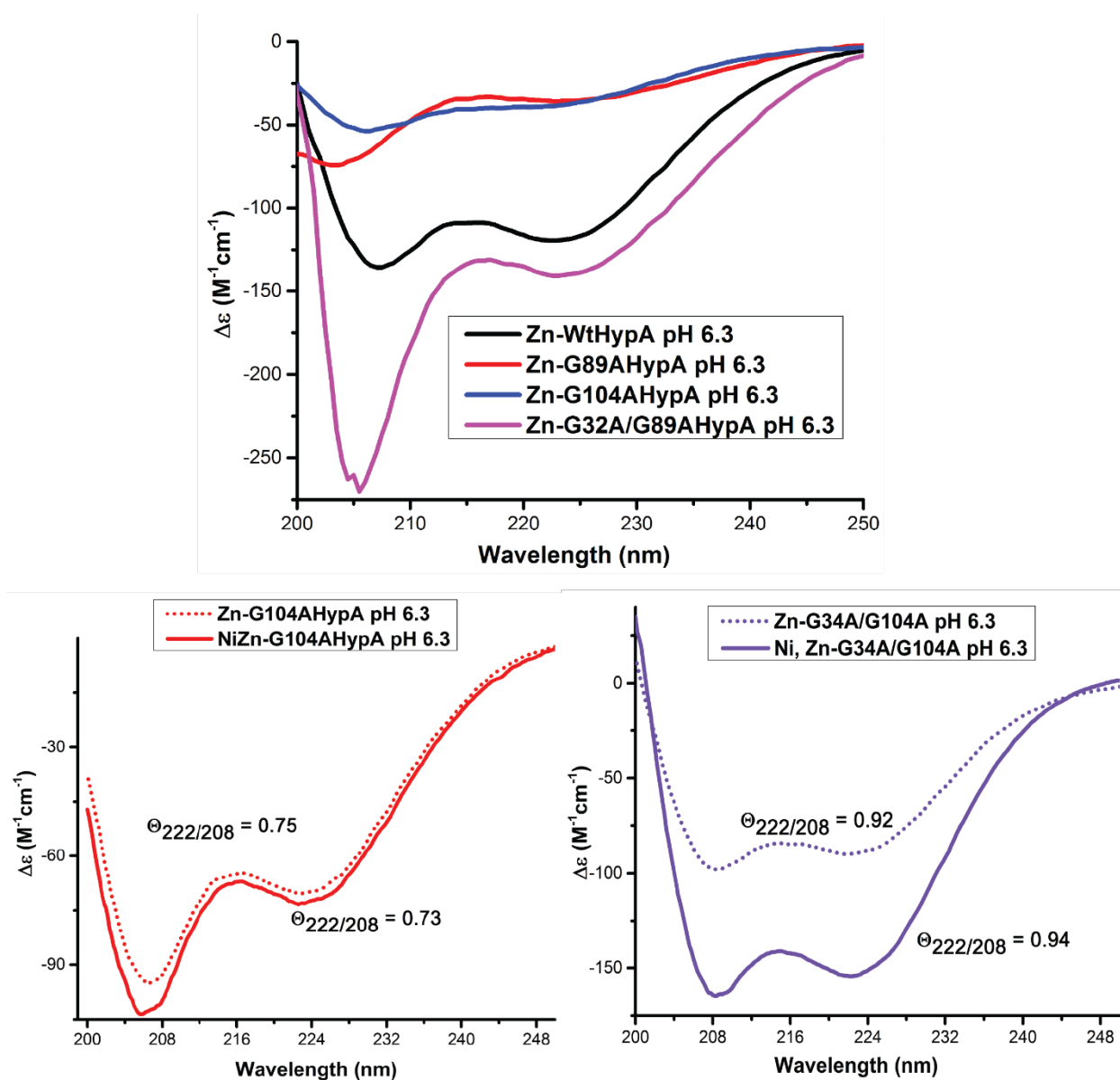


**Figure C.3: Overlay of CD spectra of selected apo-conserved and non-conserved Gly -to -Ala *H. pylori* HypA variant proteins at pH 6.3 (Top); Overlay of CD spectra of apo-(dotted line) and Ni-bound (solid line) G104A HypA (left) and G34A/G104A HypA (right) variant proteins at pH 6.3.**

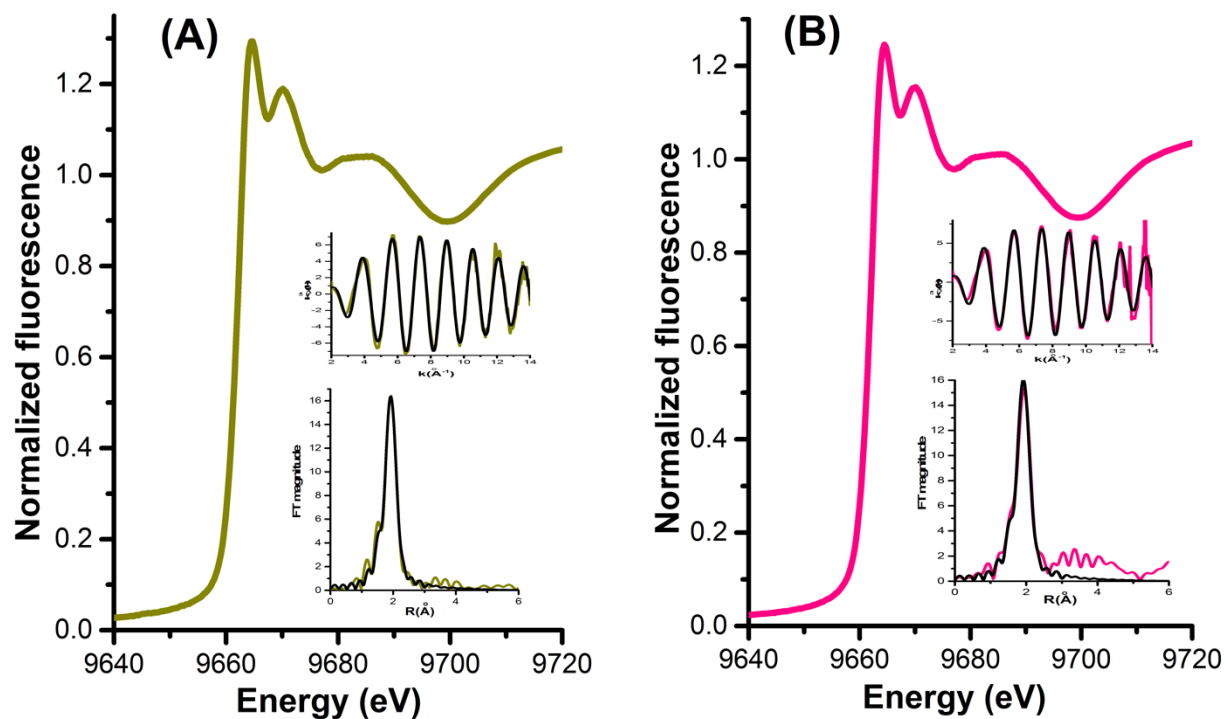
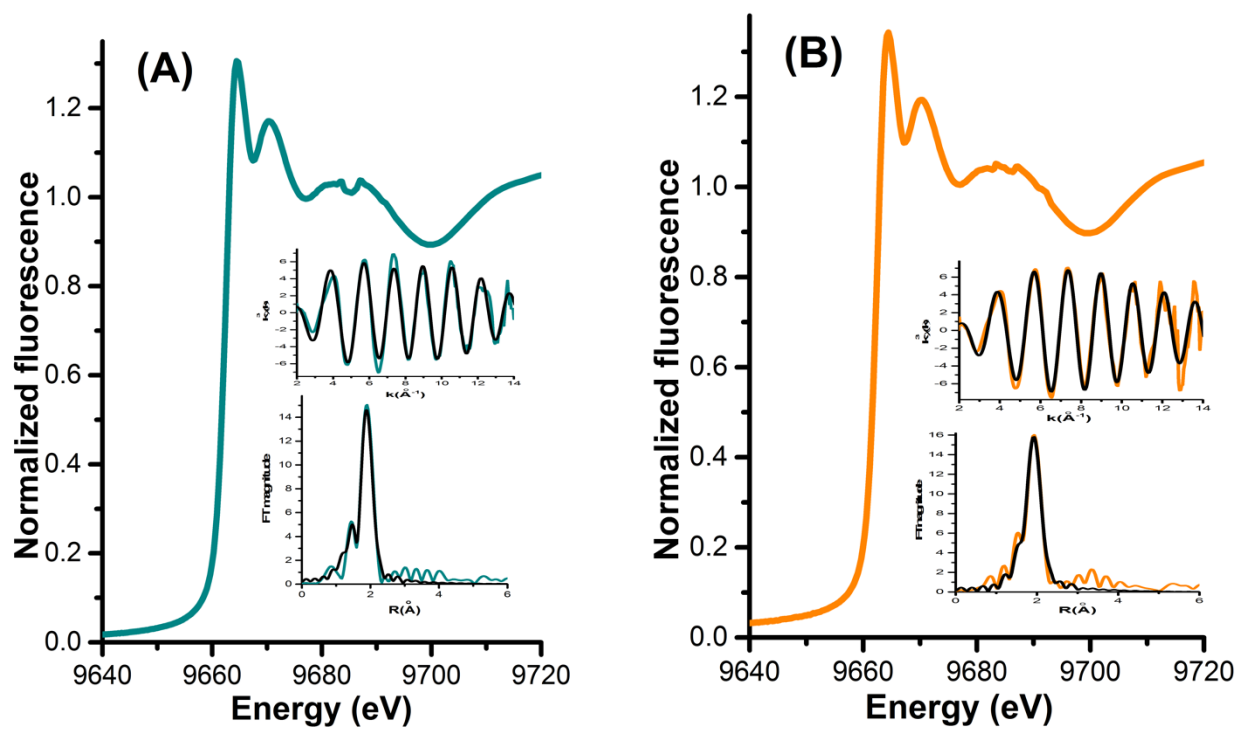


Figure C.4: Zn K-edge XANES spectrum of Ni, Zn-G32A HypA at A) pH 7.2 B) pH 6.3; the top inset shows the  $k^3$ - weighted unfiltered EXAFS data (colored) and best fit model (black), the bottom inset shows the Fourier transformed EXAFS ( $k = 2 - 14.0 \text{ \AA}^{-1}$ ) data (colored) uncorrected for phase shifts and the best fit model (black) for Ni, Zn-G32A HypA





**Figure C.5: Zn K-edge XANES spectrum of Ni, Zn-G89A HypA at A) pH 7.2 B) pH 6.3; the top inset shows the  $k^3$ - weighted unfiltered EXAFS data (colored) and best fit model (black), the bottom inset shows the Fourier transformed EXAFS ( $k = 2 - 14.0 \text{ \AA}^{-1}$ ) data (colored) uncorrected for phase shifts and the best fit model (black) for Ni, Zn-G89A HypA**

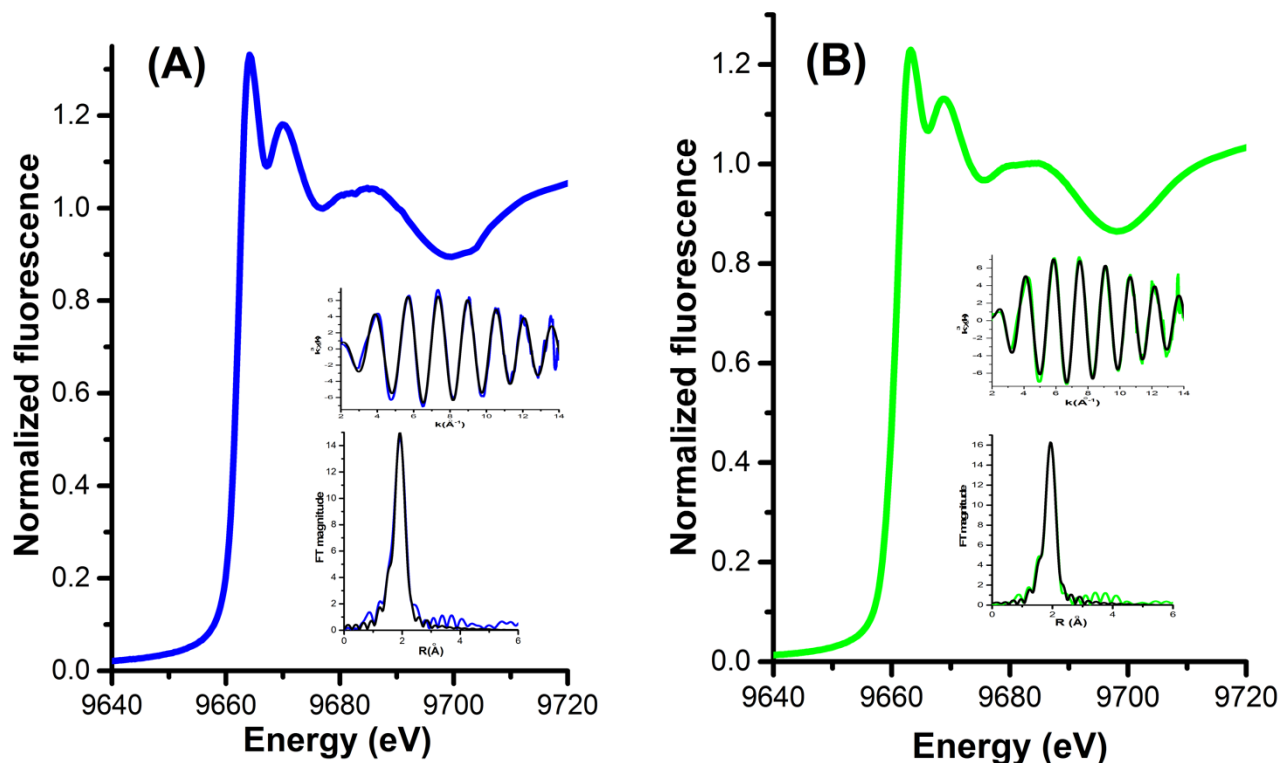
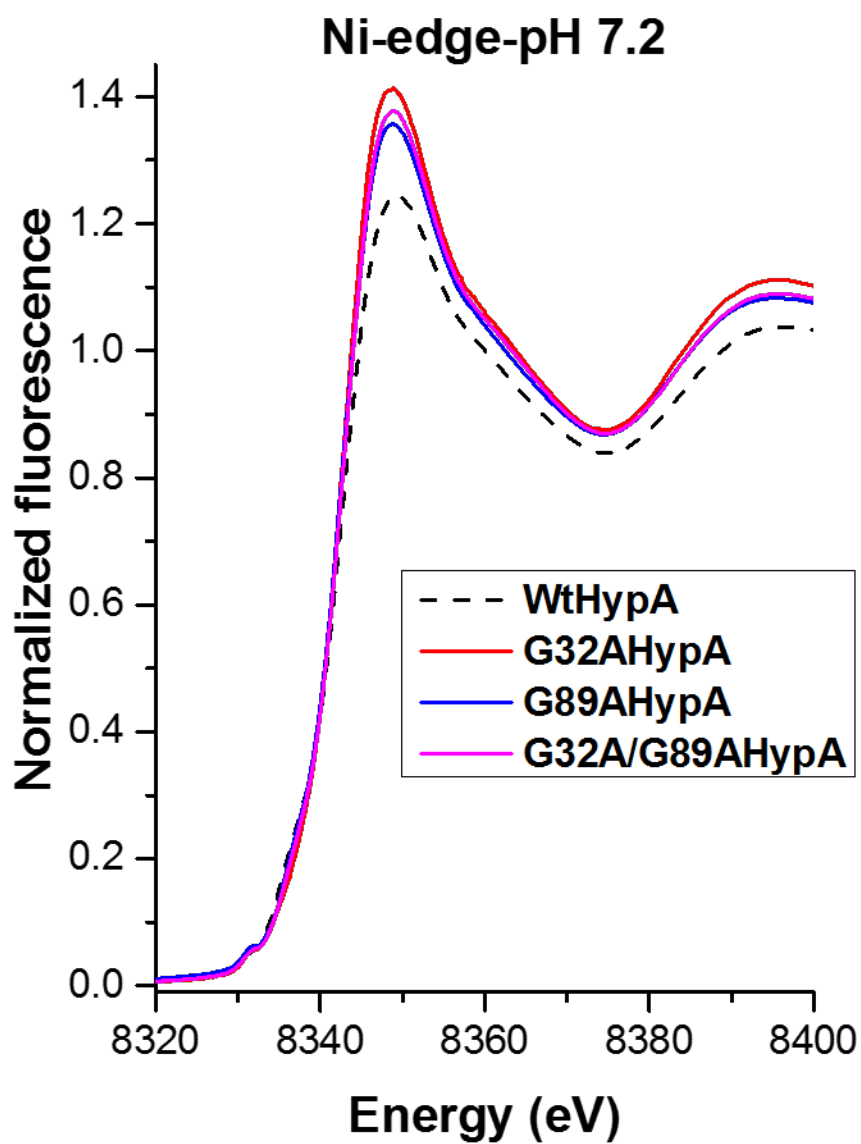


Figure C.6: Zn K-edge XANES spectrum of Ni, Zn-G32A/G89A HypA at A) pH 7.2 B) pH 6.3; the top inset shows the  $k^3$ - weighted unfiltered EXAFS data (colored) and best fit model (black), the bottom inset shows the Fourier transformed EXAFS ( $k = 2 - 14.0 \text{ \AA}^{-1}$ ) data (colored) uncorrected for phase shifts and the best fit model (black) for Ni, Zn-G32A/G89A HypA.



**Figure C.7: Overlay of Ni K-edge XANES spectrum of non-conserved Ni, Zn- Gly-to-Ala HypA variant proteins at pH 7.2**

## BIBLIOGRAPHY

Abraham, L. O.; Li, Y.; Zamble, D. B., The metal- and DNA- binding activities of *Helicobacter pylori* NikR. *J. Inorg. Biochem.* **2006**, *100* (5-6), 1005-1014.

Abreu, I. A.; Cabelli, D. E., Superoxide dismutases – a review of metal associated mechanistic variations. *Biochim. & Biophys. acta* **2010**, *1804* (2), 263-274.

Ahn, B. E.; Cha, J.; Le, E. J., Han, A. R.; Thompson, C. J.; Roe, J. H., Nur, a nickel-responsive regulator of the Fur family, regulates superoxide dismutases and nickel transport in *Streptomyces coelicolor*. *Mol. Microbiol.* **2006**, *59* (6), 1848-1858.

Alfano, M.; Cavazza, C., Structure, function and biosynthesis of nickel-dependent enzymes. *Protein Sci.* **2020**, *29* (5), 1071-1089.

Alfano, M.; Perard, J.; Miras, R.; Catty, P.; Cavazza, C., Biophysical and structural characterization of the putative nickel chaperone CooT from *Carboxythermus hydrogenoformis*. *J. Biol. Inorg. Chem.* **2018**, *23*(5), 809-817.

Alfano, M.; Veronesi, G.; Musiani, F.; Zambelli, B.; Signor, L.; Proux, O.; Rovezzi, M.; Ciurli, S.; Cavazza, C., A solvent exposed cysteine forms peculiar Ni(II)-binding site in the metallochaperone CooT from *Rhodospirillum rubrum*. *Chemistry* **2019**, *25* (67), 15351-15360.

Atanassova, A.; Zamble, D. B., Escherichia Coli HypA is a zinc metalloprotein with a weak affinity for nickel. *J. Bacteriol.* **2005**, *187* (14), 4689-4697.

Banaszak, K.; Martin-Diaconescu, V.; Bellucci, M.; Zambelli, B.; Rypniewski, W.; Maroney, M. J.; Ciurli, S., Crystallographic and X-ray absorption spectroscopic characterization of *Helicobacter*

*pylori* UreE bound to Ni<sup>2+</sup> and Zn<sup>2+</sup> reveals a role for the disordered C-terminal arm in metal trafficking. *Biochem. J.* **2012**, *441*(3), 1017-1026.

Barondeau D. P.; Kassmann, C. J.; Bruns, C. K.; Tainer, J. A., Getzoff, E. D., Nickel Superoxide Dismutase structure and mechanism. *Biochemistry*, **2004**, *43* (25), 8038-8047.

Benoit, S.; Maier, R. J., Dependence of *Helicobacter pylori* urease activity on the nickel-sequestering ability of UreE accessory protein. *J. Bacteriol.* **2003**, *185* (16), 4787-4795.

Benoit, S.; Mehta, N.; Wang, G.; Gatlin, M.; Maier, R. J., Requirement of *hydD*, *hydE*, *hypC* and *hypE* genes for hydrogenase activity in *Helicobacter pylori*. *Microb. Pathog.* **2004**, *36* (3), 153-157

Benoit, S. L.; Maier, R. J., Hydrogen and nickel metabolism in *Helicobacter* species. *Ann. N Y Acad. Sci.* **2008**, *1125*, 242-251.

Benoit, S. L.; McMurry J. L.; Hill, S. A.; Maier, R. J., *Helicobacter pylori* hydrogenase accessory protein HypA and urease accessory protein UreG compete with each other for ureE recognition. *Biochim. & Biophys. acta* **2012**, *1820* (10), 1519-1525.

Benoit, S. L.; Mehta N.; Weinberg, M. V.; Maier, C.; Maier, R. J., Interaction between *Helicobacter pylori* accessory proteins HypA and UreE is needed for urease maturation. *Microbiology* **2007**, *153* (Pt 5), 1474-1482.

Benoit, S. L.; Zbell. A. L.; Maier, R. J., Nickel enzyme maturation in *Helicobacter hepaticus*: roles of accessory proteins in hydrogenase and urease activities. *Microbiology* **2007**, *153* (Pt 11), 3748-3756.

Blum, F. C.; Hu, H. Q.; Servetas, S. L.; Benoit, S. L.; Maier, R. J.; Maroney, M. J.; Merrell, D. S., Structure-function analyses of metal-binding sites of HypA reveal residues important for hydrogenase maturation in *Helicobacter pylori*. *PLoS One* **2017**, *12* (8), e0183260.

Boer, J. L.; Mulrooney, S.B.; Hausinger, R. P., Nickel-dependent metalloenzymes. *Arch. Biochem. & Biophys.* **2014**, *544*, 142-152.

Boiteau, R. M.; Till, C. P.; Ruacho, A.; Bundy, R. M.; Hawco, N. J.; McKenna, A. M.; Barbeau, K. A.; Bruland, K.W.; Saito, M. A.; Repeta, D. J., Structural Characterization of natural Nickel and Copper binding ligands along the US GEOTRACES Eastern Pacific Zonal Transect. *Front. in Marine Sci.* **2016**, *3* (243), 1-16.

Broering, E. P.; Dillon, S.; Gale, E. M.; Steiner, R. A.; Telsler, J.; Brunold, T. C.; Harrop, T. C., Accessing Ni(III)-thiolate versus Ni(II)-thiyl bonding in a family of Ni-N<sub>2</sub>S<sub>2</sub> synthetic models of NiSOD. *Inorg. Chem.* **2015**, *54* (8), 3815-3828.

Broering, E. P.; Truong, P. T.; Gale, E. M.; Harrop, T. C., Synthetic analogues of nickel superoxide dismutase: a new role for nickel in biology. *Biochemistry* **2013**, *52* (1), 4-18.

Bryngelson, P. A.; Arobo, S. E.; Pinkham, J. L.; Cabelli, D. E.; Maroney, M. J., Expression, reconstitution, and maturation of recombinant *Streptomyces coelicolor* NiSOD. *J. Am. Chem. Soc.* **2004**, *126* (2), 460-461.

Bury-Mone, S.; Thiberge, J. M.; Contreras, M.; Maitournam, A.; Labigne, A.; De Reuse, H., Responsiveness to acidity via metal ion regulators mediates virulence in gastric pathogen *Helicobacter pylori*. *Mol. Microbiol.* **2004**, *53* (2), 623-638.

Callahan, D. L.; Roessner, U.; Dumontet, V.; Perrier, N.; Wedd, A. G.; O'Hair, R. A.; Baker, A. J.; Kolev, S. D., LC-MS and GC-MS metabolite profiling of nickel complexes in the latex of nickel-hyperaccumulating tree *Sebertia acuminata* and identification of methylated aldaric acid as a new nickel(II) ligand. *Phytochemistry* **2008**, *69* (1), 240-251.

Camilo, V.; Sugiyama, T.; Touati, E., Pathogenesis of *Helicobacter pylori* infection. *Helicobacter* **2017**, *22* (S1), e12405.

Campecino, J. O.; Dudycz, L. W.; Tumelty, D.; Berg, V.; Cabelli, D. E.; Maroney, M. J., A semisynthetic strategy leads to alteration of the backbone amidate ligands in the NiSOD active site. *J. Am. Chem. Soc.* **2015**, *137* (28), 9044-9052.

Campecino, J. O.; Maroney, M. J., Reinventing the Wheel: The NiSOD Story. *The Biological Chemistry of Nickel*, Deborah Zamble, M. R.-Z., Henryk Kozlowski, Ed. Royal Society of Chemistry: Metallobiology Series No. 10, **2017**; Vol. 10, Ch. 9.

Carpenter, B. M.; West, A. L.; Gancz, H.; Servetas, S. L.; Pich, O. Q.; Gilbreath, J. J.; Hallinger, D. R.; Forsyth, M. H.; Merrell, D. S.; Michael, S. L., Crosstalk between the *HpArsRS* two-component system and *HpNikR* is necessary for maximal activation of urease transcription. *Front. Microbiol.* **2015**, *6*, 558-576.

Carr, C. E. Relationship between structure and function of in nickel proteins and enzymes, **2017**, *Doctoral Dissertations 948* In Department of Chemistry, University of Massachusetts Amherst.

Carr, C. E.; Musiani, F.; Huang, H. T.; Chivers, P. T.; Ciurli, S.; Maroney, M. J., Glutamate ligation in the Ni(II)- and Co(II)- responsive *Escherichia coli* transcriptional regulator, RcnR. *Inorg. Chem.* **2017**, *56* (11), 6459-6476.

Cavazza, C.; Martin, L.; Laffly, E.; Lebrette, H.; Cherrier, M. V.; Zeppieri, L. Richaud, P; Carrière, M.; Fontecilla-Camps, J. C., Histidine 416 of the periplasmic binding protein NikA is essential for nickel uptake in *Escherichia coli*, *FEBS Lett.*, **2011**, *585* (4), 711-715.

Chan, K. H.; Lee, K. M.; Wong, K. B., Interaction between hydrogenase maturation factors HypA and HypB is required for [NiFe]-hydrogenase maturation. *PloS One* **2012**, *7* (2), e32592.

Chatterjee, S. K.; Maji, R. C.; Barman, S. K.; Olmstead, M. M.; Patra, A. K., Hexacoordinate nickel(II)/(III) complexes that mimic the catalytic cycle of nickel superoxide dismutase. *Angew. Chem.* **2014**, *53* (38), 10184-10189.

Cheng, T.; Li, H.; Yang, X.; Xia, W.; Sun, H., Interaction of SlyD with HypB of *Helicobacter pylori* facilitates nickel trafficking. *Metallomics* **2013**, *5* (7), 804-807.

Chiang, C. W.; Chu, Y. L.; Chen, H. L.; Kuo, T. S.; Lee, W. Z., Synthesis and characterization of Ni(III)N<sub>3</sub>S<sub>2</sub> complexes as active site models for the oxidized form of nickel superoxide dismutase. *Chemistry* **2014**, *20* (21) 6283-6286.

Chivers, P. T.; Benanti, E. L.; Heil-Chapdelaine, V.; Iwig, J. S.; Rowe, J. L., Identification of Ni-(L-His)<sub>2</sub> as a substrate for NikABCDE-dependent nickel uptake in *Escherichia coli*. *Metallomics* **2012**, *4* (10), 1043-1050.

Choudhury, S. B.; Lee, J. W.; Davidson, G.; Yim, Y. I.; Bose, K.; Sharma, M. L.; Kang, S. O.; Cabelli, D. E.; Maroney, M. J., Examination of the nickel site structure and reaction mechanism in *Streptomyces seoulensis* superoxide dismutase. *Biochemistry* **1999**, *38* (12), 3744-3752.

Colpas, G. J.; Kumar, M.; Day, R. O.; Maroney, M. J., Structural investigations of nickel complexes with nitrogen and sulfur donor ligands. *Inorg. Chem.* **1990**, *29* (23), 4779-4788.



Colpas, G. J.; Maroney, M. J.; Bagyinka, C.; Kumar, M.; Willis, W. S.; Suib, S. L.; Mascharak, P. K.; Baidya, N., X-ray spectroscopic studies of nickel complexes with application to the structure of nickel sites in hydrogenases. *Inorg. Chem.* **1991**, 30 (5), 920-928.

Covacci, A.; Telford, J. L.; Del Giudice, G.; Parsonnet, J.; Rappuoli, R., *Helicobacter pylori* virulence and genetic geography. *Science* **1999**, 284 (5418), 1328-1333.

Culotta, V. C.; Yang, M.; O'Halloran, T. V., Activation of superoxide dismutases: putting the metal to the pedal. *Biochim. Biophys. acta* **2006**, 1763 (7), 747-758.

Dalton, D. A.; Russell, S. A.; Evans, H. J., Nickel as a micronutrient for plants. *Biofactors* **1988**, 1(1), 11-16.

De Ruse, H.; Vinella, D.; Cavazza, C., Common themes and unique proteins for the uptake and trafficking of nickel, a metal essential for the virulence of *Helicobacter pylori*. *Front. Cell. Infect. Microbiol.* **2013**, 3, 94-100.

Zamble, D.; Rowinska-Zyrek, M.; Kozlowski, H. *The Biological Chemistry of Nickel*. Royal Society of Chemistry: Cambridge, U.K., **2017**.

Dian, C.; Schauer, K.; Kapp, U.; McSweeney, S. M.; Labigne, A.; Terradot, L., Structural basis of the nickel response in *Helicobacter pylori*: crystal structures of HpNikR in apo and nickel-bound states. *J. Mol. Biol.* **2006**, 361 (4), 715-730.

Dupont, C. L.; Neupane, K.; Shearer, J.; Palenik, B., Diversity, function and evolution of genes coding for putative Ni-containing superoxide dismutases. *Environ. Microbiol.* **2008**, 10 (7) 1831-1843.

Echevarria, G.; Massoura, S. T.; Sterckeman, T.; Becquer, T.; Schwartz, C.; Morel, J. L., Assessment and control of the bioavailability of nickel in soils. *Environ. Toxicol. Chem.* **2006**, *25* (3) 643-651.

Eitinger, T., In vivo production of active nickel superoxide dismutase from *Prochlorococcus marinus* MIT9313 is dependent on its cognate peptidase. *J. Bacteriol.* **2004**, *186* (22), 7821-7825.

Ernst, F. D.; Kuipers, E. J.; Heijens, A.; Sarwari, R.; Stoof, J.; Penn, C. W.; Kusters, J. G.; van Vliet, A. H., The nickel responsive regulator NikR controls activation and repression of gene transcription in *Helicobacter pylori*. *J. Bacteriol.* **2005**, *73* (11), 7252-7258.

Eskew, D. L.; Welch, R. M.; Cary, E. E., Nickel: an essential micronutrient for legumes and possibly all higher plants. *Science* **1983**, *222* (4624), 621-623.

Eusebi, L. H.; Zagari, R. M.; Bazzoli, F., Epidemiology of *Helicobacter pylori* infection. *Helicobacter* **2014**, *19* (Suppl 1), 1-5.

Farcasanu, I. C.; Mizunuma, M.; Nishiyama, F.; Miyakawa, T., Role of L-histidine in conferring tolerance to Ni<sup>2+</sup> in *Saccharomyces cerevisiae*. *Biosci. Biotech. & Biochem.* **2005**, *69* (12), 2343-2348.

Farrugia, M. A.; Macomber, L.; Hausinger, R. P., Biosynthesis of the urease metallocentre. *J. Biol. Chem.* **2013**, *288* (19), 13178-13185.

Fernandez-Bravo, A.; Lopez-Fernandez, L.; Figueras, M. J., The metallochaperone encoding gene hypA is widely distributed among pathogenic *Aeromonas* spp and its expression is increased under acidic pH within macrophages. *Microorganisms* **2019**, *7* (10), 415-428.

Fiedler, A. T.; Bryngelson, P. A.; Maroney M. J.; Brunold, T. C., Spectroscopic and computational studies of Ni<sup>3+</sup> complexes with mixed S/N ligation: implications for the active site of nickel superoxide dismutase. *Inorg. Chem.* **2007**, *46* (21), 8511-8523.

Fiedler, A. T.; Bryngelson, P. A.; Maroney M. J.; Brunold, T. C., Spectroscopic and computational studies of Ni superoxide dismutase: electronic structure contributions to enzymatic function. *J. Am. Chem. Soc.* **2005**, *127* (15), 5449-5462.

Finney, L. A.; O'Halloran, T. V., Transition metal speciation in the cell: insights from the chemistry of metal ion receptors. *Science* **2003**, *300* (5621), 931-936.

Fischer, F.; Robbe-Saule, M.; Turlin, E.; Mancuso, F.; Michael, V.; Richaud, P.; Veyrier, F. J.; DeReuse, H.; Vinella, D., Characterization in *Helicobacter pylori* of a nickel transporter essential for colonization that was acquired during evolution by gastric *Helicobacter* species. *PloS Pathog.* **2016**, *12*(12), e1006018.

Fong, Y. H.; Wong, H. C.; Yuen, M. H.; Lau, P. H.; Chen, Y. W.; Wong, K. B., Structure of UreG/UreF/UreH complex reveals how urease accessory proteins facilitate maturation of *Helicobacter pylori* urease. *PloS Biol.* **2013**, *11* (10), e1001678.

Forgacs, Z.; Nemethy, Z.; Revesz, C.; Lazar, P., Specific amino acids moderate the effects on Ni<sup>2+</sup> on the testosterone production of mouse leydig cells in vitro. *J. Toxicol. Environ. Health A* **2001**, *62* (5), 325-358.

Foster, A. W.; Osman, D.; Robinson, N. J., Metal preferences and metalation. *J. Biol. Chem.* **2014**, *289* (41), 28095 - 28103.

Foster, A. W.; Pernil, R.; Patterson, C. J.; Scott, A. J. P.; Palsson, L. O.; Pal, R.; Cummins, I.; Chivers, P. T.; Pohl, E.; Robinson, N. J., A tight tunable range for Ni(II) sensing and buffering in cells. *Nat. Chem. Biol.* **2017**, *13* (4), 409 - 414.

Fraser, K. A.; Harding, M. M., The crystal and molecular structure of bis(histidinato)nickel(II) monohydrate. *J. Chem. Soc. A* **1967**, (0), 415-420.

Fulkerson, J. F., Jr.; Garner, R. M.; Mobley, H. L., Conserved residues and motifs in NixA protein of *Helicobacter pylori* are critical for the high affinity transport of nickel ions. *J. Biol. Chem.* **1998**, *273* (1), 235-241.

Gale, E. M.; Cowart, D. M.; Scott, R. A.; Harrop, T. C., Dipeptide-based models of nickel superoxide dismutase: solvent effects highlight a critical role to Ni-S bonding and active site stabilization. *Inorg. Chem.* **2011**, *50* (20), 10460-10471.

Gale, E. M.; Narendrapurapu, B. S.; Scott, R. A.; Harrop, T. C., Exploring the effects of H-bonding in synthetic analogues of nickel superoxide dismutase (NiSOD): experimental and theoretical implications for protection of Ni-SCys bond. *Inorg. Chem.* **2010**, *49* (15), 7080-7096.

Gale, E. M.; Patra, A. K.; Harrop, T. C., Versatile methodology towards NiN(2)S(2) complexes as nickel superoxide dismutase models: structure and proton affinity. *Inorg. Chem.* **2009**, *48* (13), 5620-5622.

Ge, R. G.; Wang, D. X.; Hao, M.C.; Sun, X. S., Nickel trafficking system responsible for urease maturation in *Helicobacter pylori*. *World J. Gastroenterol.* **2013**, *19* (45), 8211-8218.

Gennari, M.; Orio, M.; Pecaut, J.; Neese, F.; Collomb, M. N.; Duboc, C., Reversible apical coordination of imidazole between the Ni(III) and Ni(II) oxidation states of a dithiolate complex: a process related to the Ni superoxide dismutase. *Inorg. Chem.* **2010**, *49* (14), 6399-6401.

Glennon, J. D.; Sarkar, B., Nickel(II) transport in human blood serum. Studies of nickel(II) binding to human albumin and to native sequence peptide, and ternary-complex formation with L-histidine. *Biochem. J.* **1982**, *203* (1), 15-23.

Greening, C. Cook, G. M., Integration of hydrogenase expression and hydrogen sensing in bacterial cell physiology. *Curr. Opin. Microbiol.* **2014**, *18*, 30-38.

Gressot, P.; Frossard, J. L.; Grosgurin, O.; Marti, C., First line eradication treatment of *Helicobacter pylori* in 2019. *Rev. Med. Suisse* **2019**, *15* (667), 1854-1858.

Hendricks, J. K.; Mobley, H. L., *Helicobacter pylori* ABC transporter: effect of allelic exchange mutagenesis on urease activity. *J. Bacteriol.* **1997**, *179* (18), 5892-5902.

Herbst, R. W.; Guce, A.; Bryngelson, P. A.; Higgins, K. A.; Ryan, K. C.; Cabelli, D. E.; Garman, S. C.; Maroney, M. J., Role of conserved tyrosine residues in NiSOD catalysis: a case of convergent evolution. *Biochemistry* **2009**, *48* (15), 3354-3369.

Herbst, R. W.; Perovic, I.; Martin-Dianconescu, V.; O'Brien, K.; Chivers, P. T.; Pochapsky, S. S.; Pochapsky, T. C.; Maroney, M. J., Communication between the zinc and nickel sites in dimeric HypA; metal recognition and pH sensing. *J. Am. Chem. Soc.* **2010**, *132* (30), 10338-10351.

Herd, D. R.; Grapperhaus, C. A., Kinetic study of nickel-thiolate oxygenation by hydrogen peroxide. Implications for nickel-containing superoxide dismutase. *Dalt. Trans.* **2012**, *41* (2), 364-366.

Higgins, K.A.; Carr, C. E.; Maroney, M. J., Effects of select histidine to cysteine mutations on transcriptional regulation by *Escherichia coli* RcnR. *Biochemistry* **2013**, *52* (1), 84-97.

Hu, H. Q.; Huang, H. T.; Maroney, M. J., Nickel ligation of the N-terminal amine of HypA is required for urease maturation in *Helicobacter pylori*. *Biochemistry* **2017**, *56* (8), 1105-1116.

Hu, H. Q., The role of the metallochaperone HypA in the acid survival and activities of nickel enzymes in *Helicobacter pylori*, **2018**, *Doctoral Dissertations 1174*, in Department of Biochemistry and Molecular Biology, University of Massachusetts Amherst.

Huang, H. T.; Dillon, S.; Ryan, K. C., Campecino, J. O.; Watkins, O. E.; Cabelli, D. E.; Brunold, T. C.; Maroney, M. J., The role of mixed amine/amide in Nickel Superoxide Dismutase. *Inorg. Chem.* **2018**, *57* (20), 12521-12535.

Ingle, R.A.; Mugford, S. T.; Rees, J. D.; Campbell, M. M.; Smith, J. A. C., Constitutively high expression of the histidine pathway contributes to nickel tolerance in hyperaccumulator plants. *The Plant Cell* **2005**, *17*(7), 2089-2106.

Jenkins, R. M.; Singleton, M. L.; Alamaraz, E.; Reibenspies, J. H.; Darensbourg, M. Y., Imidazole containing (N3S)-Ni(II) complexes relating to nickel containing biomolecules. *Inorg. Chem.* **2009**, *48* (15), 7280-7293.

Jesu Jaya Sudan, R.; Lesitha Jeeva Kumari, J.; Sudandiradoss, C., Ab initio coordination chemistry for nickel chelation motifs. *PloS One* **2005**, *10* (5), e0126787.

Spectroscopic and computational investigation of three Cys-to-Ser mutants of nickel superoxide dismutase; insight into the roles played by the Cys2 and Cys6 active site residues. *J. Biol. Inorg. Chem.* **2010**, *15* (5), 777-793.

Johnson, R. C.; Hu, H. Q.; Merrell, D. S.; Maroney, M. J., Dynamic HypA zinc site is essential for acid viability and proper urease maturation in *Helicobacter pylori*. *Metallomics* **2015**, *7* (4), 674-684.

Joho, M.; Ishikawa, Y.; Kunikane, M.; Inouhe, M.; Tohyama, H.; Murayama, T., The subcellular distribution of nickel in Ni-sensitive and Ni-resistant strains of *Saccharomyces cerevisiae*. *Microbios* **1992**, *71* (287), 149-159.

Jones, M. D.; Ademi, I.; Yin, X.; Gong, Y.; Zamble, D. B., Nickel-responsive regulation of two novel *Helicobacter pylori* NikR-targeted genes. *Metallomics* **2015**, *7* (4), 662-673.

Jones, M. D.; Li, Y.; Zamble, D. B., Acid-responsive activity of the *Helicobacter pylori* metalloregulator NikR. *Proc. Natl. Acad. Sci. U.S.A.* **2018**, *115* (36), 8966-8971.

Khorasani-Motlagh, M.; Noroozifar, M.; Kerman, K.; Zamble, D. B., Complex formation between the *Escherichia coli* [NiFe]-hydrogenase nickel maturation factors. *Biometals* **2019**, *32* (3), 521-532.

Kim, E. J.; Chung, H. J.; Suh, B.; Hah, Y. C.; Roe, J. H., Expression and regulation of the sodF gene encoding iron- and zinc- containing superoxide dismutase in *Streptomyces coelicolor* Muller. *J. Bacteriol.* **1998**, *180* (8), 2014-2020.

Kim, E. J.; Chung, H. J.; Suh, B.; Hah, Y. C.; Roe, J. H., Transcriptional and post-transcriptional regulation of nickel by sodN gene encoding nickel-containing superoxide dismutase from *Streptomyces coelicolor* Muller. *Mol. Microbiol.* **1998**, *27* (1), 187-195.

Kim, E. J.; Kim, H. P.; Hah, Y. C.; Roe, J. H., Differential expression of superoxide dismutases containing Ni and Fe/Zn in *Streptomyces coelicolor*. *Eur. J. Biochem.* **1996**, *241* (1), 178-185.

Kim, E. J.; Ahn, B. E.; Lee, J. H.; Roe, J. H., Regulation of a nickel-cobalt efflux system and nickel homeostasis in soil actinobacterium *Streptomyces coelicolor*. *Metallomics* **2015**, *7* (4), 702-709.

Kim, I. -K.; Yim, Y. -I.; Lee, J. -W.; Yim, H.-S.; Kang, S. -O, CbiX-homologous protein (CbiXhp), a metal-binding protein from *Streptomyces seoulensis* is involved in expression of nickel-containing superoxide dismutase. *FEMS Microbio. Lett.* **2003**, *228* (1), 21-26.

Kim, J. S.; Jang J. H.; Lee, J. W.; Kang, S. -O; Kim, K. S.; Lee, J. K., Identification of cis site involved in nickel-responsive transcriptional repression of sodF gene coding for Fe- and Zn-containing superoxide dismutase of *Streptomyces griseus*. *Biochim. Biophys. Acta* **2000**, *1493* (1), 200-207.

Krause, M. E.; Glass, A. M.; Jackson, T. A.; Laurence, J. S., Mapping the chiral inversion and structural transformation of metal-tripeptide complex having nickel superoxide dismutase activity. *Inorg. Chem.* **2011**, *50* (6), 2479-2487.

Krause, M. E.; Glass, A. M.; Jackson, T. A.; Laurence, J. S., Novel tripeptide model of nickel superoxide dismutase. *Inorg. Chem.* **2010**, *49* (2), 362-364.

Krezel, A.; Szczepanik, W.; Sokolowska, M.; Jezowska-Bojczuk, M.; Bal, W., Correlations between complexation modes and redox activities of Ni(II)-GSH complexes. *Chem. Res. Toxicol.* **2003**, *16* (7), 855-864.

Kwon, S.; Watanabe, S.; Nishitani, Y.; Kawashima, T.; Kanai, T.; Atomi, H.; Miki, K., Crystal structures of a [NiFe] hydrogenase large subunit HyhL in an immature state in complex with a Ni chaperone HypA. *Proc. Natl. Acad. Sci. U.S.A.* **2018**, *115* (27), 7045-7050.



Lacasse, M. J.; Douglas, C. D.; Zamble, D. B., Mechanism of Selective Nickel Transfer from HypB to HypA, Escherichia coli [NiFe]-Hydrogenase Accessory Proteins. *Biochemistry* **2016**, *55* (49), 6821-6831.

Lacasse, M. J.; Summers, K. L.; Khorasani-Motlagh, M.; George, G. N.; Zamble, D. B., Bimodal Nickel-Binding Site on Escherichia coli [NiFe]-Hydrogenase Metallochaperone HypA. *Inorg. Chem.* **2019**, *58* (20), 13604-13618.

Lacasse, M. J.; Zamble, D. B., [NiFe]-Hydrogenase Maturation. *Biochemistry* **2016**, *55* (12), 1689-1701.

Lebrette, H.; Borezée-Durant, E.; Martin, L.; Richaud, P.; Boeri Erba, E.; Cavazza, C., Novel insights into nickel import in Staphylococcus aureus: the positive role of free histidine and structural characterization of a new thiazolidine-type nickel chelator. *Metallomics* **2015**, *7* (4), 613-621.

Lebrette, H.; Iannello, M.; Fontecilla-Camps, J. C.; Cavazza, C., The binding mode of Ni-(L-His)<sub>2</sub> in NikA revealed by X-ray crystallography. *J. Inorg. Biochem.* **2013**, *121*, 16-18.

Leclere, V.; Boiron, P.; Blondeau, R., News & notes: diversity of superoxide-dismutases among clinical and soil isolates of Streptomyces species. *Curr. Microbiol.* **1999**, *39* (6), 365-368.

Lee, H. I.; Lee, J. W.; Yang, T. C.; Kang, S. O.; Hoffman, B. M., ENDOR and ESEEM investigation of the Ni-containing superoxide dismutase. *J. Biol. Inorg. Chem.* **2010**, *15* (2), 175-182.

Lee, J. W.; Roe, J. H.; Kang, S. O., Nickel-containing superoxide dismutase. *Methods in Enzymology* **2002**, *349*, 90-101.

Lee, W. Z.; Chiang, C. W.; Lin, T. H.; Kuo, T. S., A discrete five-coordinate Ni(III) complex resembling the active site of the oxidized form of nickel superoxide dismutase. *Chemistry* **2012**, *18 (1)*, 50-53.

Lihí, N.; Csire, G.; Szakacs, B.; May, N. V.; Varnagy, K.; Sovago, I.; Fabian, I., Stabilization of the Nickel Binding Loop in NiSOD and Related Model Complexes: Thermodynamic and Structural Features. *Inorg. Chem.* **2019**, *58 (2)*, 1414-1424.

Lihí, N.; Kelemen, D.; May, N. V.; Fábíán, I., The Role of the Cysteine Fragments of the Nickel Binding Loop in the Activity of the Ni(II)-Containing SOD Enzyme *Inorg. Chem.* **2020**, *59 (7)*, 4772-4780.

Liu, Y.; Wang, Q.; Wei, Y.; Lin, Y. W.; Li, W.; Su, J. H.; Wang, Z.; Tian, Y.; Huang, Z. X.; Tan, X., Functional conversion of nickel-containing metalloproteins via molecular design: from a truncated acetyl-coenzyme A synthase to a nickel superoxide dismutase. *Chem. Comm.* **2013**, *49 (14)*, 1452-1454.

M. Cempel, G. N., Nickel: A Review of its sources and environmental toxicology. *Pol. J. Environ. Stud.* **2006**, *15 (3)*, 375-382.

M.Sivasankar Nair, P. T. A., M. Sankaranarayana Pillai, Chidambaram Natarajan, Mixed-ligand complexes involving sulfur-containing ligands. Part I. Nickel(II) ternary complexes of L-cysteine, D-penicillamine and L-cysteic acid with imidazoles *Dalt. Trans.* **1993**, *6*, 917-921.

Macomber, L.; Hausinger, R. P., Mechanisms of nickel toxicity in microorganisms. *Metallomics* **2011**, *3 (11)*, 1153-1162.

Magalon, A.; Blokesch, M.; Zehelein, E.; Bock, A., Fidelity of metal insertion into hydrogenases. *FEBS Lett.* **2001**, *499 (1-2)*, 73-76.

Maier, R. J., Use of molecular hydrogen as an energy substrate by human pathogenic bacteria. *Biochem. Soc. Trans.* **2005**, *33* (Pt 1), 83-85.

Maier, R. J.; Benoit, S. L.; Seshadri, S., Nickel-binding and accessory proteins facilitating Ni-enzyme maturation in *Helicobacter pylori*. *Biometals* **2007**, *20* (3-4), 655-664.

Maier, R. J.; Fu, C.; Gilbert, J.; Moshiri, F.; Olson, J.; Plaut, A. G., Hydrogen uptake hydrogenase in *Helicobacter pylori*. *FEMS Microbio. Lett.* **1996**, *141* (1), 71-76.

Maroney, M. J.; Ciurli, S., Nonredox nickel enzymes. *Chem. Rev.* **2014**, *114* (8), 4206-4228.

Martin-Diaconescu, V.; Bellucci, M.; Musiani, F.; Ciurli, S.; Maroney, M. J., Unraveling the *Helicobacter pylori* UreG zinc binding site using X-ray absorption spectroscopy (XAS) and structural modeling. *J. Biol. Inorg. Chem.* **2012**, *17* (3), 353-361.

Mathrubootham, V.; Thomas, J.; Staples, R.; McCracken, J.; Shearer, J.; Hegg, E. L., Bisamidate and mixed amine/amidate NiN<sub>2</sub>S<sub>2</sub> complexes as models for nickel-containing acetyl coenzyme A synthase and superoxide dismutase: an experimental and computational study. *Inorg. Chem.* **2010**, *49* (12), 5393-5406.

Mehta, N.; Olson, J. W.; Maier, R. J., Characterization of *Helicobacter pylori* nickel metabolism accessory proteins needed for maturation of both urease and hydrogenase. *J. Bacteriol.* **2003**, *185* (3), 726-734.

Mobley, H. L.; Garner, R. M.; Bauerfeind, P., *Helicobacter pylori* nickel-transport gene nixA: synthesis of catalytically active urease in *Escherichia coli* independent of growth conditions. *Mol. Microbio.* **1995**, *16* (1), 97-109.

Muller, C.; Bahlawane, C.; Aubert, S.; Delay, C. M.; Schauer, K.; Michaud-Soret, I.; De Reuse, H., Hierarchical regulation of the NikR-mediated nickel response in *Helicobacter pylori*. *Nucleic Acids Res.* **2011**, *39* (17), 7564-7575.

Mullins, C. S.; Grapperhaus, C. A.; Frye, B. C.; Wood, L. H.; Hay, A. J.; Buchanan, R. M.; Mashuta, M. S., Synthesis and sulfur oxygenation of a (N<sub>3</sub>S)Ni complex related to nickel-containing superoxide dismutase. *Inorg. Chem.* **2009**, *48* (21), 9974-9976.

Musiani, F.; Zambelli, B.; Bazzani, M.; Mazzei, L.; Ciurli, S., Nickel-responsive transcriptional regulators. *Metallomics* **2015**, *7* (9), 1305-1318.

Nair, M. S.; Arasu, P. T.; Pillai, M. S.; Natarajan, C., Mixed-ligand complexes involving sulfur-containing ligands. Part 1. Nickel(II) ternary complexes of L-cysteine, D-penicillamine and L-cysteic acid with imidazoles. *Dalt. Trans.* **1993**, *6*, 917-921.

Nakane, D.; Kuwasako, S. I.; Tsuge, M.; Kubo, M.; Funahashi, Y.; Ozawa, T.; Ogura, T.; Masuda, H., A square-planar Ni(II) complex with an N<sub>2</sub>S<sub>2</sub> donor set similar to the active centre of nickel-containing superoxide dismutase and its reaction with superoxide. *Chem. Comm. (Camb.)* **2010**, *46* (12), 2142-2144.

Nakane, D.; Wasada-Tsutsui, Y.; Funahashi, Y.; Hatanaka, T.; Ozawa, T.; Masuda, H., A novel square-planar Ni(II) complex with an amino-carboxamido-dithiolato-type ligand as an active-site model of NiSOD. *Inorg. Chem.* **2014**, *53* (13), 6512-6523.

Neupane, K. P.; Gearty, K.; Francis, A.; Shearer, J., Probing variable axial ligation in nickel superoxide dismutase utilizing metalloprotein-based models: insight into the superoxide disproportionation mechanism. *J. Am. Chem. Soc.* **2007**, *129* (47), 14605-14618.

Neupane, K. P.; Shearer, J., The influence of amine/amide versus bisamide coordination in nickel superoxide dismutase. *Inorg. Chem.* **2006**, *45* (26), 10552-10566.

Novelli, E. L.; Rodrigues, N. L.; Ribas, B. O., Superoxide radical and toxicity of environmental nickel exposure. *Human & experimental Toxicol.* **1995**, *14* (3), 248-251.

Oakley, F.; Horn, N. M.; Thomas, A. L., Histidine-stimulated divalent metal uptake in human erythrocytes and in the erythroleukaemic cell line HEL.92.1.7. *J. Physiol.* **2004**, *561* (Pt 2), 525-534.

Olson, J. W.; Maier, R. J., Molecular hydrogen as an energy source for *Helicobacter pylori*. *Science* **2002**, *298* (5599), 1788-1790.

Olson, J. W.; Mehta, N. S.; Maier, R. J., Requirement of nickel metabolism proteins HypA and HypB for full activity of both hydrogenase and urease in *Helicobacter pylori*. *Mol. Microbiol.* **2001**, *39* (1), 176-182.

Ose, D. E.; Fridovich, I., Superoxide dismutase. Reversible removal of manganese and its substitution by cobalt, nickel or zinc. *J. Biol. Chem.* **1976**, *251* (4), 1217-1218.

Pelmenschikov, V.; Siegbahn, P. E., Nickel superoxide dismutase reaction mechanism studied by hybrid density functional methods. *J. Am. Chem. Soc.* **2006**, *128* (23), 7466-7475.

Pirzadeh, S.; Shahpiri, A., Functional characterization of a type 2 metallothionein isoform (OsMTI-2b) from rice. *Int. J. Biol. Macromol.* **2016**, *88*, 491-496.

Prabhakar, R.; Morokuma, K.; Musaev, D. G., A DFT study of the mechanism of Ni superoxide dismutase (NiSOD): role of the active site cysteine-6 residue in the oxidative half-reaction. *J. Comput. Chem.* **2006**, *27* (12), 1438-1445.

Rodrigue, A.; Chanal, A.; Beck, K.; Müller, M.; Wu, L. F., Co-translocation of a periplasmic enzyme complex by a hitchhiker mechanism through the bacterial tat pathway. *J. Biol. Chem.* **1999**, *274* (19), 13223-13228.

Rose, T. L.; Seyse, R. J., Determination of the stability constants of nickel (II)-cysteine. *J. Chem. Edu.* **1976**, *53* (11), 728-729.

Rossmann, R.; Sauter, M.; Lottspeich, F.; Böck, A., Maturation of the large subunit (HYCE) of Escherichia coli hydrogenase 3 requires nickel incorporation followed by C-terminal processing at Arg537. *Eur. J. Biochem.* **1994**, *220* (2), 377-384.

Ryan, K. C.; Guce, A. I.; Johnson, O. E.; Brunold, T. C.; Cabelli, D. E.; Garman, S. C.; Maroney, M. J., Nickel superoxide dismutase: structural and functional roles of His1 and its H-bonding network. *Biochemistry* **2015**, *54* (4), 1016-1027.

Ryan, K. C.; Johnson, O. E.; Cabelli, D. E.; Brunold, T. C.; Maroney, M. J., Nickel superoxide dismutase: structural and functional roles of Cys2 and Cys6. *J. Biol. Inorg. Chem.* **2010**, *15* (5), 795-807.

Sachs, G.; Weeks, D. L.; Wen, Y.; Marcus, E. A.; Scott, D. R.; Melchers, K., Acid acclimation by Helicobacter pylori. *Physiology (Bethesda)* **2005**, *20*, 429-438.

Saito, M. A.; Moffett, J. W.; DiTullio, G. R., Cobalt and nickel in the Peru upwelling region: A major flux of labile cobalt utilized as a micronutrient. *Glob. Biogeochem. Cycles* **2004**, *18* (4), GB4030-GB4044.

Salama, N. R.; Hartung, M. L.; Muller, A., Life in the human stomach: persistence strategies of the bacterial pathogen Helicobacter pylori. *Nat. Rev. Microbiol.* **2013**, *11* (6), 385-399.

Saylor, Z.; Maier, R., Helicobacter pylori nickel storage proteins: recognition and modulation of diverse metabolic targets. *Microbiology* **2018**, *164* (8), 1059-1068.

Schauer, K.; Gouget, B.; Carriere, M.; Labigne, A.; de Reuse, H., Novel nickel transport mechanism across the bacterial outer membrane energized by the TonB/ExbB/ExbD machinery. *Mol. Microbiol.* **2007**, *63* (4), 1054-1068.

Schmidt, A.; Gube, M.; Schmidt, A.; Kothe, E., In silico analysis of nickel containing superoxide dismutase evolution and regulation. *J. Basic Microbiol.* **2009**, *49* (1), 109-118.

Schmidt, M.; Zahn, S.; Carella, M.; Ohlenschlager, O.; Gorlach, M.; Kothe, E.; Weston, J., Solution structure of a functional biomimetic and mechanistic implications for nickel superoxide dismutases. *Chembiochem* **2008**, *9* (13), 2135-2146.

Shahzad, B.; Tanveer, M.; Rehman, A.; Cheema, S. A.; Fahad, S.; Rehman, S.; Sharma, A., Nickel; whether toxic or essential for plants and environment - A review. *Plant Physiol. Biochem.* **2018**, *132*, 641-651.

Shaik, M. M.; Cendron, L.; Salamina, M.; Ruzzene, M.; Zanotti, G., Helicobacter pylori periplasmic receptor CeuE (HP1561) modulates its nickel affinity via organic metallophores. *Mol. Microbiol.* **2014**, *91* (4), 724-735.

Shearer, J., Dioxygen and superoxide stability of metallopeptide based mimics of nickel containing superoxide dismutase: the influence of amine/amidate vs. bis-amidate ligation. *J. Inorg. Biochem.* **2013**, *129*, 145-149.

Shearer, J., Insight into the structure and mechanism of nickel-containing superoxide dismutase derived from peptide-based mimics. *Acc. Chem. Res.* **2014**, *47* (8), 2332-2341.

Shearer, J., Use of a metallopeptide-based mimic provides evidence for a proton-coupled electron-transfer mechanism for superoxide reduction by nickel-containing superoxide dismutase. *Angew. Chem. (International ed. in English)* **2013**, *52* (9), 2569-2572.

Shearer, J.; Dehestani, A.; Abanda, F., Probing variable amine/amide ligation in Ni(II)N<sub>2</sub>S<sub>2</sub> complexes using sulfur K-edge and nickel L-edge X-ray absorption spectroscopies: implications for the active site of nickel superoxide dismutase. *Inorg. Chem.* **2008**, *47* (7), 2649-2660.

Shearer, J.; Long, L. M., A nickel superoxide dismutase maquette that reproduces the spectroscopic and functional properties of the metalloenzyme. *Inorg. Chem.* **2006**, *45* (6), 2358-2360.

Shearer, J.; Neupane, K. P.; Callan, P. E., Metallopeptide based mimics with substituted histidines approximate a key hydrogen bonding network in the metalloenzyme nickel superoxide dismutase. *Inorg. Chem.* **2009**, *48* (22), 10560-10571.

Shearer, J.; Peck, K. L.; Schmitt, J. C.; Neupane, K. P., Cysteinate protonation and water hydrogen bonding at the active-site of a nickel superoxide dismutase metallopeptide-based mimic: implications for the mechanism of superoxide reduction. *J. Am. Chem. Soc.* **2014**, *136* (45), 16009-16022.

Shearer, J.; Schmitt, J. C.; Clewett, H. S., Adiabaticity of the proton-coupled electron-transfer step in the reduction of superoxide effected by nickel-containing superoxide dismutase metallopeptide-based mimics. *J. Phys. Chem. B* **2015**, *119* (17), 5453-5461.

Shearer, J.; Zhao, N., [Me<sub>4</sub>N](Ni(II)(BEAAM)): a synthetic model for nickel superoxide dismutase that contains Ni in a mixed amine/amide coordination environment. *Inorg. Chem.* **2006**, *45* (24), 9637-9639.

Silaghi-Dumitrescu, R., Superoxide interaction with nickel and iron superoxide dismutases. *J. Molecular Graphics & Modelling* **2009**, *28* (2), 156-161.

Smith, R. M., Martell, A. E., *Critical Stability Constants*. Plenum: New York, 1989; Vol. 6, p20, p32, p356.

Snider, V. G.; Farquhar, E. R.; Allen, M.; Abu-Spetani, A.; Mukherjee, A., Design and reactivity of Ni-complexes using pentadentate neutral-polypyridyl ligands: Possible mimics of NiSOD. *J. Inorg. Biochem.* **2017**, *175*, 110-117.

Spronk, C.; Zerko, S.; Gorka, M.; Kozminski, W.; Bardiaux, B.; Zambelli, B.; Musiani, F.; Piccioli, M.; Basak, P.; Blum, F. C.; Johnson, R. C.; Hu, H.; Merrell, D. S.; Maroney, M.; Ciurli, S., Structure and dynamics of *Helicobacter pylori* nickel-chaperone HypA: an integrated approach



using NMR spectroscopy, functional assays and computational tools. *J. Biol. Inorg. Chem.* **2018**, *23* (8), 1309-1330.

Stahler, F. N.; Odenbreit, S.; Haas, R.; Wilrich, J.; Van Vliet, A. H.; Kusters, J. G.; Kist, M.; Bereswill, S., The novel *Helicobacter pylori* CznABC metal efflux pump is required for cadmium, zinc, and nickel resistance, urease modulation, and gastric colonization. *Infect. Immun.* **2006**, *74* (7), 3845-3852.

Steiner, R. A.; Dzul, S. P.; Stemmler, T. L.; Harrop, T. C., Synthesis and speciation-dependent properties of a multimetallic model complex of NiSOD that exhibits unique hydrogen-bonding. *Inorg. Chem.* **2017**, *56* (5), 2849-2862.

Stingl, K.; Schauer, K.; Ecobichon, C.; Labigne, A.; Lenormand, P.; Rousselle, J. C.; Namane, A.; de Reuse, H., In vivo interactome of *Helicobacter pylori* urease revealed by tandem affinity purification. *Mol. Cell. Proteomics* **2008**, *7* (12), 2429-2441.

Szilagyi, R. K.; Bryngelson, P. A.; Maroney, M. J.; Hedman, B.; Hodgson, K. O.; Solomon, E. I., S K-edge X-ray absorption spectroscopic investigation of the Ni-containing superoxide dismutase active site: new structural insight into the mechanism. *J. Am. Chem. Soc.* **2004**, *126* (10), 3018-3019.

Tarsia, C.; Danielli, A.; Florini, F.; Cinelli, P.; Ciurli, S.; Zambelli, B., Targeting *Helicobacter pylori* urease activity and maturation: In-cell high-throughput approach for drug discovery. *Biochim. Biophys. Acta Gen. Subj.* **2018**, *1862* (10), 2245-2253.

Theodoratou, E.; Paschos, A.; Magalon, A.; Fritsche, E.; Huber, R.; Bock, A., Nickel serves as a substrate recognition motif for the endopeptidase involved in hydrogenase maturation. *Eur. J. Biochem.* **2000**, *267* (7), 1995-1999.

180. Tietze, D.; Breitzke, H.; Imhof, D.; Kothe, E.; Weston, J.; Buntkowsky, G., New insight into the mode of action of nickel superoxide dismutase by investigating metallopeptide substrate models. *Chemistry* **2009**, *15* (2), 517-523.
181. Tietze, D.; Koley Seth, B.; Brauser, M.; Tietze, A. A.; Buntkowsky, G., Ni(II) Complex Formation and Protonation States at the Active Site of a Nickel Superoxide Dismutase-Derived Metallopeptide: Implications for the Mechanism of Superoxide Degradation. *Chemistry* **2018**, *24* (59), 15879-15888.
182. Tietze, D.; Sartorius, J.; Koley Seth, B.; Herr, K.; Heimer, P.; Imhof, D.; Mollenhauer, D.; Buntkowsky, G., New insights into the mechanism of nickel superoxide degradation from studies of model peptides. *Sci. Rep.* **2017**, *7* (1), 17194.
183. Tietze, D.; Tischler, M.; Voigt, S.; Imhof, D.; Ohlenschlager, O.; Gorlach, M.; Buntkowsky, G., Development of a functional cis-prolyl bond biomimetic and mechanistic implications for nickel superoxide dismutase. *Chemistry* **2010**, *16* (25), 7572-7578.
- Timm, J.; Brochier-Armanet, C.; Perard, J.; Zambelli, B.; Ollagnier-de-Choudens, S.; Ciurli, S.; Cavazza, C., The CO dehydrogenase accessory protein CooT is a novel nickel-binding protein. *Metallomics* **2017**, *9* (5), 575-583.
- Trumbo, P.; Yates, A. A.; Schlicker, S.; Poos, M., Dietary reference intakes: vitamin A, vitamin K, arsenic, boron, chromium, copper, iodine, iron, manganese, molybdenum, nickel, silicon, vanadium, and zinc. *J. Am. Diet Assoc.* **2001**, *101* (3), 294-301.
- Truong, P. T.; Gale, E. M.; Dzul, S. P.; Stemmler, T. L.; Harrop, T. C., Steric Enforcement about One Thiolate Donor Leads to New Oxidation Chemistry in a NiSOD Model Complex. *Inorg. Chem.* **2017**, *56* (14), 7761-7780.

- Van Den Berg, C. M. G.; Nimmo, M., Determination of interactions of nickel with dissolved organic material in seawater using cathodic stripping voltammetry. *Science of The Total Environ.* **1987**, *60*, 185-195.
- Vannini, A.; Pinatel, E.; Costantini, P. E.; Pellicciari, S.; Roncarati, D.; Puccio, S.; De Bellis, G.; Peano, C.; Danielli, A., Comprehensive mapping of the *Helicobacter pylori* NikR regulon provides new insights in bacterial nickel responses. *Sci. Rep.* **2017**, *7*, 45458-45472.
- Vinella, D.; Fischer, F.; Vorontsov, E.; Gallaud, J.; Malosse, C.; Michel, V.; Cavazza, C.; Robbe-Saule, M.; Richaud, P.; Chamot-Rooke, J.; Brochier-Armanet, C.; De Reuse, H., Evolution of *Helicobacter*: Acquisition by gastric species of two histidine-rich proteins essential for colonization. *PLoS. Pathog.* **2015**, *11* (12), e1005312.
- Voland, P.; Weeks, D. L.; Marcus, E. A.; Prinz, C.; Sachs, G.; Scott, D., Interactions among the seven *Helicobacter pylori* proteins encoded by the urease gene cluster. *Am. J. Physiol. Gastrointest. & Liver Physiol.* **2003**, *284* (1), G96-G106.
- Vraspir, J. M.; Butler, A., Chemistry of marine ligands and siderophores. *Ann. Rev. Marine Sci.* **2009**, *1*, 43-63.
- Wang, G.; Romero-Gallo, J.; Benoit, S. L.; Piazuolo, M. B.; Dominguez, R. L.; Morgan, D. R.; Peek, R. M., Jr.; Maier, R. J., Hydrogen metabolism in *Helicobacter pylori* plays a role in gastric carcinogenesis through facilitating caga translocation. *mBio* **2016**, *7* (4), e01022-16.
- Watanabe, S.; Kawashima, T.; Nishitani, Y.; Kanai, T.; Wada, T.; Inaba, K.; Atomi, H.; Imanaka, T.; Miki, K., Structural basis of a Ni acquisition cycle for [NiFe] hydrogenase by Ni-metallochaperone HypA and its enhancer. *Proc. Natl. Acad. Sci. U.S.A.* **2015**, *112* (25), 7701-7706.
- Watt, R. K.; Ludden, P. W., Nickel-binding proteins. *Cell. Mol. Life Sci.* **1999**, *56* (7-8), 604-625.

Webb, S. M., SIXPack a Graphical User Interface for XAS Analysis Using IFEFFIT. *Physica Scripta* **2005**, 1011.

Wen, Y.; Marcus, E. A.; Matrubutham, U.; Gleeson, M. A.; Scott, D. R.; Sachs, G., Acid-adaptive genes of *Helicobacter pylori*. *Infect. Immun.* **2003**, *71* (10), 5921-5939.

Wen, Y.; Scott, D. R.; Vagin, O.; Tokhtaeva, E.; Marcus, E. A.; Sachs, G., Measurement of Internal pH in *Helicobacter pylori* by Using Green Fluorescent Protein Fluorimetry. *J. Bacteriol.* **2018**, *200* (14), e00178-18.

Weng, L. P.; Wolthoorn, A.; Lexmond, T. M.; Temminghoff, E. J. M.; van Riemsdijk, W. H., Understanding the Effects of Soil Characteristics on Phytotoxicity and Bioavailability of Nickel Using Speciation Models. *Environ. Sci. & Tech.* **2004**, *38* (1), 156-162.

Wolfram, L.; Haas, E.; Bauerfeind, P., Nickel represses the synthesis of the nickel permease NixA of *Helicobacter pylori*. *J. Bacteriol.* **2006**, *188* (4), 1245-1250.

Wuerges, J.; Lee, J. W.; Kang, S. O.; Djinojic Carugo, K., Crystallization of a nickel-containing superoxide dismutase and preliminary phase determination by MAD at the Ni K edge. *Acta crystallographica. Section D, Biological crystallography* **2002**, *58* (Pt 7), 1220-1223.

Wuerges, J.; Lee, J. W.; Yim, Y. I.; Yim, H. S.; Kang, S. O.; Djinojic Carugo, K., Crystal structure of nickel-containing superoxide dismutase reveals another type of active site. *Proc. Natl. Acad. Sci. U.S.A.* **2004**, *101* (23), 8569-8574.

Wycisk, K.; Kim, E. J.; Schroeder, J. I.; Kramer, U., Enhancing the first enzymatic step in the histidine biosynthesis pathway increases the free histidine pool and nickel tolerance in *Arabidopsis thaliana*. *FEBS Lett.* **2004**, *578* (1), 128-134.

Xia, W.; Li, H.; Sze, K. H.; Sun, H., Structure of a nickel chaperone, HypA, from *Helicobacter pylori* reveals two distinct metal binding sites. *J. Am. Chem. Soc.* **2009**, *131* (29), 10031-10040.

Xia, W.; Li, H.; Yang, X.; Wong, K. B.; Sun, H., Metallo-GTPase HypB from *Helicobacter pylori* and its interaction with nickel chaperone protein HypA. *J. Biol. Chem.* **2012**, *287* (9), 6753-6763.

Yang, J. C.; Lu, C. W.; Lin, C. J., Treatment of *Helicobacter pylori* infection: current status and future concepts. *World J. Gastroenterol.* **2014**, *20* (18), 5283-5293.

Yang, X.; Koochi-Moghadam, M.; Wang, R.; Chang, Y. Y.; Woo, P. C. Y.; Wang, J.; Li, H.; Sun, H., Metallochaperone UreG serves as a new target for design of urease inhibitor: A novel strategy for development of antimicrobials. *PLoS Biol.* **2018**, *16* (1), e2003887.

Yang, X.; Li, H.; Cheng, T.; Xia, W.; Lai, Y. T.; Sun, H., Nickel translocation between metallochaperones HypA and UreE in *Helicobacter pylori*. *Metallomics* **2014**, *6* (9), 1731-1736.

Yang, X.; Li, H.; Lai, T. P.; Sun, H., UreE-UreG complex facilitates nickel transfer and preactivates GTPase of UreG in *Helicobacter pylori*. *J. Biol. Chem.* **2015**, *290* (20), 12474-12485.

Youn, H. D.; Kim, E. J.; Roe, J. H.; Hah, Y. C.; Kang, S. O., A novel nickel-containing superoxide dismutase from *Streptomyces* spp. *Biochem. J.* **1996**, *318* (Pt 3), 889-896.

Youn, H. D.; Youn, H.; Lee, J. W.; Yim, Y. I.; Lee, J. K.; Hah, Y. C.; Kang, S. O., Unique isozymes of superoxide dismutase in *Streptomyces griseus*. *Arch. Biochem. and Biophys.* **1996**, *334* (2), 341-348.

Yuen, M. H.; Fong, Y. H.; Nim, Y. S.; Lau, P. H.; Wong, K. B., Structural insights into how GTP-dependent conformational changes in a metallochaperone UreG facilitate urease maturation. *Proc. Natl. Acad. Sci. U.S.A.* **2017**, *114* (51), e10890-e10898.

Zambelli, B.; Bellucci, M.; Danielli, A.; Scarlato, V.; Ciurli, S., The Ni<sup>2+</sup> binding properties of *Helicobacter pylori* NikR. *Chem. Commun. (Camb.)* **2007**, *35*, 3649-3651.

Zeer-Wanklyn, C. J.; Zamble, D. B., Microbial nickel: cellular uptake and delivery to enzyme centers. *Curr. Opin. Chem. Biol.* **2017**, *37*, 80-88.

Zilbermann, I.; Maimon, E.; Cohen, H.; Meyerstein, D., Redox chemistry of nickel complexes in aqueous solutions. *Chem. Rev.* **2005**, *105* (6), 2609-2625.